Developing new high entropy alloys for high-temperature applications using advanced powder metallurgy routes and additive manufacturing

by

S Venkatesh Kumaran

A dissertation submitted in partial fulfillment of the requirements for the degree of Doctor of Philosophy in

Materials Science and Engineering

Universidad Carlos III de Madrid

Advisor:

José Manuel Torralba

September 2024

To,

Mom, Dad, my brother Yogesh

and my teachers

Preface

This doctoral thesis was carried out in Sustainable Powder Technologies group of IMDEA Materials Institute along with a secondment at Centre for Additive Manufacturing – Metals (CAM2), Chalmers university of technology, Göteburg, Sweden. The PhD was funded internally by IMDEA Materials Institute, and the secondment was funded by Maria de Maetzu grant.

This project fulfils all the necessary criteria for its mention as an International Ph.D. Such recognition is specified in the Ordination of Official University Education, as established in Article 15 of the Royal Decree 99/2011 (B.O.E. No. 35 of January 28, 2011, pp. 13909-13926) and as described in the ´Rules and Regulations´ of Ph.D. studies at Universidad Carlos III de Madrid.

ACKNOWLEDGEMENTS

I traveled so far from my family and friends to become a world class scientist and that has always been my goal which I remind myself every now and then when the going gets tough. In that regard, my PhD journey in IMDEA Materials Institute has been a special experience where I have grown both personally and professionally. I could do a good job here which has won me accolades with the support of my team and I got to start an industrial R&D career which I had always aspired for. I will always remember something that Mariana Huerta told me in the beginning when I kept getting unlucky to find an apartment in Madrid, “Venkatesh, it seems you are getting unlucky every time, but I promise you that you will get lots of luck in Spain moving forward”. And how true it turned out to be. So, thank you, Mariana. Moving to Spain was a big decision for me and my initial period saw a lot of delays and uncertainties due to the Covid-19 pandemic, but things had only improved on and on since then and there are many people to thank in this regard.

I will forever be indebted to my PhD advisor and mentor Prof. José Manuel Torralba, who has been a constant pillar of support, right from the day I received my PhD offer. I would like to thank you for the freedom, trust, patience, and guidance in this journey without which I could not have accomplished what I did. Thank you for everything. I will always remember that you came to pick me up from the airport at 1 am when I landed in Madrid.

I would like to thank our powder suppliers, particularly MIMETE, Italy, who graciously provided us with free Cobalt-Chromium powders for our research.

I would also like to thank Prof. Eduard Hryha, who accepted my proposal to carry out a research stay at Centre for Additive Manufacturing - Metals, Chalmers University of Technology, Göteburg, Sweden. It was a great experience working with Dr. Bala Malladi who put a lot of effort and time to help me with my experiments. It was a fruitful collaboration through which I learned a lot. I also made some good friends in this journey, Ahmed Fardan who was also my gym trainer, Anok Nagaram a.k.a Daddy, and Saahith (F45), who supported me during my stay in Sweden.

A special shoutout to my first host in Spain, my Airbnb family, Elena, and Carlos, who helped me settle, and for a person completely new to the city without knowing the language, this meant

a lot to me. Thanks to Rosa Bazan and Ainhoa Zapatero for their administrative assistance, and to Mariana Huerta, who helped me find an apartment to live in during the difficult times of Covid-19. Among those from IMDEA Materials who supported me at this initial time were Dr. Shruti Banait, Dr. Venkata Sai, and Dr. Chandrashekar Pilgar. Thanks to all of you. I will always remember the times we played badminton, padel and cricket.

I would like to express my gratitude to the technicians who taught and helped me with all my experiments and analysis, Amalia San Roman and Ignacio Escobar for metallography and additive manufacturing, Dr. Javier Garcia for XRD, Dr. Vanesa Martinez for mechanical testing, and Dr. Manuel Avella for SEM and TEM. Thank you all for your kindness.

From IMDEA Materials, there is a long list of people who I want to thank. When I was seated on the first floor, Elaheh Kazemi was a great company to have coffee and lunch chats with. Thanks for your support that time even though I had to move to the ground floor later. At this time, Los Nachos, Nacho Escobar and Nacho Rodriguez became good friends of mine. Thank you Nachete for all the metallography and 3D printing support and thanks for inviting me to lunch every Friday in Getafe even though I had to decline at times as my experiments were going on. And Tetenash, I remember we were bonding over cryogenic temperatures in the 3D printing room, and we have come a long way since then. You have been a caring person who made me feel welcomed and introduced me to a lot of new things in Spain. Thanks to Dr. Clara Galera for teaching me patiently everything related to additive manufacturing during that time.

And then came the second member of the research group, Dr. Alberto Meza (or Mr.?), my bro, who became a great support and a close friend. I can never forget all the fun we have had for the last three years. Thanks for being a constant support and an important part of my Imdea life. Isabel Olaya, we had fun times together along with Alberto in the brief time you were in our group and I still cannot believe how you succeeded in convincing me to run 10 Kms with you and that´s something I am very proud of. Thanks to Ahad Mohammadzadeh for always providing me with good tips to write a research article. And among the newest group member but the first person I came in contact with even before my arrival to Spain, Maria de Nicolas a.k.a Vulture. Thanks for replying promptly to my email that time which actually played a role in making my decision to move to Spain. You have become a close friend of mine in a very short time and I will always cherish the fun times we had. A big thank you for your support. Andrea, la niña, thanks for helping me with my research during your time in Imdea. Diego,

thanks for your support and for always joining me for a coffee/breakfast at the UPM whenever I asked. Adrian, thanks for organizing the Go karting farwell, that is something I have never tried before, and I thoroughly enjoyed it. Mohammad Ali Jaberi, thanks for the insightful discussions we had about life, politics, and for helping me with my CV. Facundo and Alex, thanks for helping me whenever I had to come to UC3M for my experiments.

Again among my IMDEA friends, Jorge and Guille, I can`t put into words how much fun I had with you guys. Thanks for introducing me to Spanish culture and for taking care of me whenever I hung out with you guys. Jose Mancias, my fellow Illini, my padel partner, you and I started exploring Spain at the same time and had loads of fun memories together. One of the unique experiences I had with you all was the casa rural. Thanks to Andrea, Angela, Carmen, Eugenia, Delabat, Alessia, Lola, Miguel, David for being great company during that time and beyond. Davide, thanks for the fun times during weekends and for taking me to some great pizza places, the best one being Chicago pizza. Thomas, thanks for taking me on hikes and accompanying me for padel and dinners in Getafe. Christina, we always had interesting conversations during lunch and thanks for taking me on hikes as well. Cillian, thanks for all the jokes that you shared with me and your crazy stories especially with your tooth. Paul, the guiri from Tenerife, I will always remember the deep as well as the not-so-deep conversations we had that sometimes illuminated Alberto. Patricia and Victoria, thanks for being amazing desk neighbours, and I will terribly miss our wordle times. Blanca and Carlota, the biochicas, thanks for taking my mind off with some random but interesting conversations during work.

In the last year of my PhD, I was lucky to befriend Saumya Sadanand, Carolina Pereira, Keayvan Keramati with who I had some wonderful trips with and who showered me with great care and support. Saumya, thank you for caring about me and for inviting me to the Ibiza trip. Hope I have helped you in understanding jokes better. Carolina, thanks for all your care and support. I learned some great tips and hacks for travel, events and gifts from you. All the fun I had with you guys will remain etched in my memory forever. Thanks to Souvik and Jayachandran, for the good company and fun times and for offering me a place to stay whenever I visited Madrid.

Finally, the most important people in my life, my mom, dad, and brother, to who I dedicate this research to. They have done everything possible and fought all odds to provide me with the best education, health, and wisdom to have come so far.

PUBLISHED AND SUBMITTED CONTENT

1. S Venkatesh Kumaran, JM Torralba, "Laser powder bed fusion processing of low cost $CoCrFeNiMo_xNb_y$ high entropy alloys with promising high-temperature properties via in-situ alloying commercial powders: Inconel, CoCrF75, 316L, and INVAR", Metals, (2024), 14(5), 500, https://doi.org/10.3390/met14050500

   The content from the article is wholly included in Chapter 4 and Section 4.2. The material from this source included in this thesis is not singled out with typographic means and references.

2. S Venkatesh Kumaran, D Garbiec, JM Torralba, "A novel and sustainable method to develop non-equiatomic $CoCrFeNiMo_x$ high entropy alloys via spark plasma sintering using commercial commodity powders and evaluation of its mechanical behavior", Materials Science & Engineering A, (2023), Vol 878, 145207 https://doi.org/10.1016/j.msea.2023.145207

   The content from the article is wholly included in Chapter 4 and Section 4.1. The material from this source included in this thesis is not singled out with typographic means and references.

3. JM Torralba, S Venkatesh Kumaran, "Development of competitive high-entropy alloys using commodity powders", Materials letters, (2021), Vol. 301, 130202 https://doi.org/10.1016/j.matlet.2021.130202

   The content from the article is wholly included in Chapter 4 and Section 4.1. The material from this source included in this thesis is not singled out with typographic means and references.

4. S Venkatesh Kumaran, Bala Malladi, Eduard Hryha, José Manuel Torralba, “Effect of laser process paramaters on non-equiatomic $CoCrFeNiMo_xAl_y$ HEAs manufactured by PBF-LB/M via in-situ alloying”, European powder metallurgy association (EPMA), Euro Powder Metallurgy 2023 proceedings, DOI: 10.59499/EP235762606

   The content from the article is wholly included in Chapter 4 and Section 4.3. The material from this source included in this thesis is not singled out with typographic means and references.

5. JM Torralba, S Venkatesh Kumaran, “Development of High Entropy alloys using field assisted sintering and gas atomized commodity powders as raw materials”, European powder metallurgy association (EPMA), Euro Powder Metallurgy 2021 proceedings, ISBN: 978-189907254-5

   The content from the article is wholly included in Chapter 4 and Section 4.1. The material from this source included in this thesis is not singled out with typographic means and references.

BOOK CHAPTER

- Powder bed fusion techniques: Underlying principles and materials, Alessandro de Nardi, S Venkatesh Kumaran, María de Nicolas, Ahad Mohammadzadeh, Elsevier, In preparation

OTHER RESEARCH MERITS

1. **Keynote presentation,** TMS 2024, March 3-7, 2024, Orlando USA, "A Sustainable Approach to Developing High-Entropy Alloys Using Commodity Powders: A Proof of Concept Using SPS, PBF-LB/M, and MIM", Jose M. Torralba, S. Venkatesh Kumaran, Dariusz Garbiec, Bala Malladi, Eduard Hryha, Alberto Meza
2. **Oral presentation**, 3rd World Congress on High Entropy Alloys, November 12-15, 2023, Pittsburg, USA, "The commodity approach: a novel and sustainable method to develop non-equiatomic CoCrFeNiMox high entropy alloys", Jose M. Torralba, Dariusz Garbiec, S. Venkatesh Kumaran, Alberto Meza
3. **Keynote presentation,** Euro PM 2023, Lisbon, Portugal, **"**Effect of Process Parameters On Non-equiatomic CoCrFeNiMoxAly HEAs Manufactured By PBF-LB/M Via In-situ Alloying", S Venkatesh Kumaran, B Malladi, E Hryha, JM Torralba,
4. **Oral Presentation,** Alloys for additive manufacturing symposium (AAMS), Madrid, Spain, 2023, "Using powder mixtures to develop high entropy alloys via in-situ alloying in PBF-LB/M", S Venkatesh Kumaran, B Malladi, E Hryha, JM Torralba
5. **Oral presentation,** Additive Manufacturing with Powder Metallurgy (AMPM), 2023, Las Vegas, USA, "Role of Al mixing to prepare feedstocks for PBF-LB/M to develop new HEAs via in-situ alloying", S Venkatesh Kumaran, B Malladi, E Hryha, JM Torralba
6. **Oral presentation,** Congreso Español Iberoamericano de Pulvimetalurgia CEIPM2023, Donostia – San Sebastian, Spain, "An alternative route to developing CoCrFeNiMoxAly high entropy alloys by PBF-LB/M via in-situ alloying", S Venkatesh Kumaran, Bala Malladi, Eduard Hryha, José Manuel Torralba, May 30-31, 2023
7. **Keynote presentation,** TMS 2023, 19-23 March, 2023, San Diego, USA, "PM Co base superalloys and PM HEAs: beyond Ni base superalloys for high temperature applications", José M. Torralba, S Venkatesh Kumaran, Alex Mejía, Alberto Meza, Ahad Mohammadzadeh and Mónica Campos
8. **Oral presentation**, WORLDPM 2022, Lyon, France, "Developing competitive High entropy alloys via Selective Laser melting using commercial commodity powders", S Venkatesh Kumaran, JM Torralba

9. **Oral presentation,** Alloys for Additive Manufacturing 2022, Munich, Germany**, "**Using mixes of pre-alloyed commodity powders to develop competitive High Entropy Alloys by Selective Laser Melting", S Venkatesh Kumaran, Alberto Meza, José M Torralba
10. **Oral presentation,** Nano 2022, Seville, Spain, "High Entropy Alloys and Additive Manufacturing", José M Torralba, Monica Campos, Paula Alvaredo, Andrea Garcia-Junceda, Alberto Meza, S Venkatesh Kumaran
11. **Oral presentation,** Congreso Nacional de Materiales (CNMAT 2022), Ciudad Real, Spain, "Developing High Entropy Alloys via Spark Plasma Sintering using commercial commodity powders", S Venkatesh Kumaran, D Garbiec, José M Torralba
12. **Oral presentation,** Congreso Nacional de Materiales (CNMAT 2022), Ciudad Real, Spain, "Developing high entropy alloys using commercial commodity powders via selective laser melting", S Venkatesh Kumaran, José M Torralba
13. **Oral presentation,** Congreso Nacional de Materiales (CNMAT 2022), Ciudad Real, Spain, "Development of novel multiphase High Entropy Alloys", I. Olaya, A Meza, S Venkatesh Kumaran, José M Torralba
14. **Oral presentation,** S. Venkatesh Kumaran, Jose M. Torralba, "Development of Powder Metallurgy High-entropy Alloys by Using Superalloys Commercial Commodity Powders", 2nd World Congress on High Entropy Alloys, 5-8 December 2021, Charlotte, USA
15. **Keynote presentation**, EUROMAT 2021, Virtual conference, "A novel approach to developing high entropy alloys by powder metallurgy: the suitability of using commodity powders", S Venkatesh Kumaran, D Garbiec, JM Torralba
16. **Oral presentation**, FAST-SPS Conference 2021, Poznan, Poland, "Developing competitive high entropy alloys using field-assisted sintering using commodity powders", S Venkatesh Kumaran, D Garbiec, JM Torralba,
17. **Oral presentation**, EUROPM 2021, Virtual conference, "Development of High Entropy alloys using field assisted sintering and gas atomized commodity powders as raw materials", JM Torralba, D Garbiec, S Venkatesh Kumaran
18. **Invited Seminar**, Bundeswehr University Munich, "Developing competitive high entropy alloys via Selective Laser Melting using commercial commodity powders", S Venkatesh Kumaran, JM Torralba, April 2022

RESEARCH STAYS AND PROJECTS

- International research stay, Center for Additive Manufacturing – Metals, Chalmers university of technology, Göteburg, Sweden. From 01/08/2022 – 31/10/2022 (3 months)
- Directed project, Andrea Alonso Romero, Desarrollo de aleaciones de alta entropia FeNiCoCrMo por fusion selectiva por laser, Bachelor thesis, Universidad Carlos III de Madrid, 2023

AWARDS DURING PHD

- Second place, 3 minute thesis talk held by Universidad Carlos III de Madrid, 2021

- Jury´s award, 3 minute thesis talk held by IMDEA Materials, Madrid, 2021

- Keynote paper award, Effect of Process Parameters and Heat Treatments on Non-equiatomic $CoCrFeNiMo_xAl_y$ HEAs Manufactured By PBF-LB/M Via In-situ Alloying, EuroPM 2023, Lisbon, Portugal

- Winner of AMES - Joan Antoni Bas Award, May 2023, For the best R&D powder metallurgy work in Spain that represents a technological advance or progress for industrial technology transfer

ABSTRACT

The discovery of new materials is essential due to population growth and the rising quality of life. One significant advancement in this area is high entropy alloys (HEAs), which break away from the traditional alloying method of using a base element and instead combine four or more elements in equiatomic or near-equiatomic proportions. Since their discovery in 2004, HEA research has rapidly expanded, exploring various combinations of 3D transition, refractory, and lightweight metals. HEAs can be customized for specific applications based on the desired properties. Current HEAs show promising performance, often matching or surpassing traditional alloys in strength at cryogenic, room, and high temperatures, among other properties.

Casting and arc melting have been the most common methods for manufacturing HEAs due to their simplicity and accessibility. However, these methods can lead to inhomogeneities, contamination, and large grains, which degrade mechanical properties and necessitate additional heat treatment and mechanical working. Recently, powder metallurgy has emerged as a promising alternative for producing HEAs, offering better control over composition and microstructure, achieving nanocrystalline structures that enhance mechanical properties, and allowing for the creation of complex geometries and near-net shapes. To date, powder metallurgy high-entropy alloys (PMHEAs) have been developed using three classes of powders: fully pre-alloyed gas-atomized powders, pure elemental powders, and fully pre-alloyed mechanically alloyed powders (also made from elemental powders). Despite their potential, challenges such as cost, availability, and the criticality of pure elemental powders limit HEA development.

This thesis explores a novel approach to developing HEAs through powder metallurgy using blended commercial powders as feedstock. The consolidation techniques employed include field-assisted hot pressing, spark plasma sintering, and laser powder bed fusion for additive manufacturing. The material developed is based on the CoCrFeNi system with additions of Mo, Nb, and Al. Structural, microstructural, and mechanical characterizations were performed on all developed HEAs to identify parameters for achieving a single FCC phase. This method's success paves the way for the cost-effective, efficient, flexible, and sustainable exploration of HEAs.

RESUMEN

La necesidad de descubrir nuevos materiales se ve impulsada por el mayor crecimiento demográfico y el mejor estilo de vida de la población. Una consecuencia de esos esfuerzos son las aleaciones de alta entropía (HEA), que abandonan el concepto de elemento base en las aleaciones tradicionales y pueden tener hasta cuatro o más elementos en proporciones equiatómicas o casi equiatómicas. La investigación sobre HEA ha crecido a un ritmo rápido desde su descubrimiento en 2004 con múltiples combinaciones de elementos con metales de transición 3D, refractarios y ligeros. El desarrollo de las HEA se puede adaptar a una aplicación específica en función de las propiedades requeridas. Las HEA desarrolladas en la actualidad exhiben propiedades prometedoras cercanas o, en algunos casos, superiores a las aleaciones existentes en términos de resistencia a temperaturas criogénicas, ambientales y altas, entre otras propiedades.

Hasta ahora, el método más común para fabricar HEA es el moldeo/fusión por arco eléctrico debido a su simplicidad y disponibilidad. Pero este método genera heterogeneidades, contaminación y crecimiento de granos, lo que disminuye las propiedades mecánicas y requiere de tratamientos térmicos y mecánicos para resolver estos problemas. Recientemente, las rutas pulvimetalurgicas se has mostrado muy prometedoras para fabricar HEA, ya que ofrecen un mejor control sobre la composición y la microestructura, logran microestructuras nanocristalinas que mejoran las propiedades mecánicas, pueden producir geometrías complejas y formas cercanas a la forma final. Las aleaciones de alta entropía pulvimetalurgicas (PMHEA) se han desarrollado utilizando tres clases diferentes de polvos hasta la fecha: polvos atomizados por gas prealeados, polvos elementales puros y polvos prealeados por aleación mecánica (que también se fabrican a partir de polvos elementales). Sin embargo, el coste, la disponibilidad y la criticidad de los polvos elementales puros, están ralentizando el desarrollo de HEA.

En la presente tesis, se explora un enfoque novedoso para desarrollar HEA a través de la ruta pulvimetalurgica utilizando como materia prima polvos comerciales mezclados. Las técnicas de fabricación utilizadas fueron prensado en caliente asistido en campo, sinterización por plasma por chispa y fusión láser en lecho de polvo, y el material desarrollado se basó en el sistema CoCrFeNi con adiciones de Mo, Nb y Al. Se llevaron a cabo caracterizaciones estructurales, microestructurales y mecánicas de todas las HEA desarrolladas que identifican

parámetros para el resultado deseado de una sola fase FCC. El éxito de este método allana el camino para la exploración de HEA de manera rentable, eficiente, flexible y sostenible.

CONTENTS

Acknowledgements……v
Abstract……xii
1. Introduction & motivation……..1
1.1 Background & motivation……..1
1.2 Objective and scope……..3
Bibliography……..6
2. Literature review……..10
2.1 High entropy alloys……..10
2.1.1 Definitions ……..10
2.1.2 The HEA concept ……..11
2.1.3 Core effect of HEAs ……..14
2.1.3.1 The high entropy effect ……..15
2.1.3.2 Lattice distortion effect ……..15
2.1.3.3 Sluggish diffusion effect ……15
2.1.3.4 Cocktail effect ……15
2.1.3.5 The chemical short-range order (CSRO) strengthening……..15
2.1.4 Major HEA alloy families and microstructures……..16
2.1.5 Potential applications……17
2.2 Processing routes……..19
2.2.1 Powder development……..19
2.2.2 Powder consolidation……..21
2.2.3 Additive manufacturing ……..26
2.2.3.1 Laser powder bed fusion (PBF-LB/M)……..26
2.2.3.2 Fabrication of HEAs by PBF-LB/M ……..28
2.2.3.3 Feedstocks for PBF-LB/M: The in-situ alloying approach ……..31
2.3 Use of scraps to produce arc-melted HEAs ……..32
Bibiliography ……33
3. Experimental procedures ……46
3.1 Materials ……..46
3.2 Processing methods …… 49
3.2.1 Field assisted hot pressing …… 49

3.2.2 Spark plasma sintering 50
3.3 Heat treatments 53
3.4 Characterization 53
3.4.1 Density measurement 53
3.4.2 Structural and microstructural characterization 53
3.4.2.1 Metallography 53
3.4.2.2 Scanning electron microscope 53
3.4.2.3 X-ray diffraction 54
3.4.3 Mechanical properties 54
3.4.3.1 Hardness 54
3.4.3.2 Micro-tensile test 54
3.4.3.3 Tensile test 55
3.4.3.4 Hot compression test 55
4. Results & discussion 57
4.1 Fabricating HEAs through Field-Assisted Hot Pressing and Spark Plasma Sintering with Blended Commodity Powders 57
4.1.1 Thermodynamic predictions 58
4.1.2 Powder morphology 59
4.1.3 Field assisted hot pressing 61
4.1.4 Spark plasma sintering 64
4.1.4.1 X-Ray diffraction 65
4.1.4.2 Microstructural analysis 66
4.1.4.3 Mechanical properties 73
4.1.4.3.1 Hardness 73
4.1.4.3.2 Tensile features 74
4.1.4.3.3 Hot compression test 76
4.1.5 Cost analysis 78
4.1.6 Conclusions 83
4.2 Fabrication of HEAs via in-situ alloying commodity powders using laser powder bed fusion 84
4.2.1 Powder flowability 85
4.2.2 Powder morphology 86
4.2.3 Porosity analysis 87
4.2.4 Structural and microstructural analysis 87

4.2.5 Mechanical properties ……...91
4.2.6 Fracture behaviour ……92
4.2.7 Conclusions ……...95
4.3 Role of mixing Al to the commercial feedstocks to fabricate HEAs via in-situ alloying in laser powder bed fusion ……...96
4.3.1 Powder morphology ……..97
4.3.2 Process parameter optimization ……97
4.3.3 Microstructural characterization and mechanical properties ……..100
4.3.4 Conclusions ……101
Bibliography ……..103
5. Conclusions and future work ……111
5.1 Conclusions ……111
5.2 Future work ……...114
5.2.1 Materials ……..114
5.2.2 Methodologies ……114
5.2.3 Properties ……115
Appendix ……..117
Paper 1……119
Paper 2……124
Paper 3……131
Paper 4……150
Paper 5……165

CHAPTER 1

Introduction & motivation

1.1 Background & motivation

High entropy alloys (HEAs) have emerged as a new class of materials, due to its unconventional alloying approach of not having a single major component, thus also known as multi-principal element alloys (MPEAs) or multicomponent alloys or complex concentrated alloys (CCAs). First discovered by Yeh [1] and Cantor [2] in 2004, HEAs are attracting a lot of attention due to the possibility of adding different principal elements to obtain unique structures and the possibility to fine-tune the properties, resulting in exceptional properties in various areas: mechanical strength, ductility, wear, oxidation, and corrosion resistance [3]. This makes HEAs a prospective option in many fields of application, such as aerospace, high temperature, and energy applications. These properties result from the four core effects of HEAs, namely, (i) high entropy, (ii) severe lattice distortion, (iii) sluggish diffusion, and (iv) cocktail effect [4]. More recently, the effect of the chemical short-range order seems to be another factor of strengthening in these alloys, which can be considered as a core effect as well [5]. The definition of HEAs, initially stated as alloys consisting of more than five elements of composition range between 5 and 35 at% [6], has been modified to alloys with a configurational mixing entropy, $\Delta S_{mix} > 1.5R$, where R is the gas constant [7]. Due to such a high mixing entropy, single phase solid solution (SS) structures such as face-centered cubic (FCC), body centered cubic (BCC) or hexagonal close packed (HCP), are favoured to form over intermetallics or amorphous phases [3,4,8,9].

The most widely studied HEA is CoCrFeMnNi, also known as the Cantor alloy, which is an equiatomic FCC phase system. Initial focus on equiatomic and single phase HEAs limiting the compositional scope has gradually transitioned to non-equiatomic and multi-phase HEAs in

search of superior mechanical properties. Typically, an FCC HEA exhibits good ductility at the expense of strength and vice versa for a BCC HEA. In this regard, dual phase or multi-phase HEAs proved to offer a good balance of strength and ductility [10–12]. Particularly, eutectic HEAs (EHEAs) with a lamellar structure consisting of ordered FCC and ordered BCC structures garnered great scientific interest in high temperature properties, like $AlCoCrFeNi_{2.1}$[13,14] and Mo and Al containing HEAs [15,16]. For instance, $AlCoCrFeNi_{2.1}$ EHEA after cold rolling and annealing, exhibits a yield strength of 1.1 GPa and 12% ductility [13]. Thus, multi-phase HEA systems have good potential in high temperature applications to replace the existing Ni based superalloys in aerospace applications.

The most commonly used method to fabricate HEAs is ingot melting. But recently, powder metallurgy (PM) routes have emerged as a promising alternative to develop HEAs due to its ability to avoid segregations, offer significantly higher compositional accuracy, obtain nanocrystalline structures and offer superior microstructural control [17]. Additive manufacturing, which uses powders as the raw material has also been studied intensively to develop HEAs due to its ultra-high cooling rate resulting in fine microstructures and suppression of secondary phases. Powder metallurgy high-entropy alloys (PMHEAs) have been developed using three different classes of powders to date: fully pre-alloyed gas-atomized powders, pure elemental powders, and fully pre-alloyed mechanically alloyed powders (which are also fabricated from elemental powders). However, some of the main limitations in PM routes to fabricate HEAs are the cost and availability of the powders. Firstly, there are no fully pre-alloyed powders in the market to fabricate even the most extensively used HEAs today. Thus, there is always a need to start from expensive elemental powders (>99% purity) to proceed with either mechanical alloying to produce pre-alloyed powders or by using critical metals as raw materials to produce powders by gas atomizing, both of which are time-consuming and expensive. In traditional powder metallurgy techniques, like press and sinter, and in advanced techniques like spark plasma sintering (SPS), the powders are prepared by mixing elemental powders or mechanical alloying whereas additive manufacturing uses powders produced by gas atomization. Mechanical alloying can result in contamination, which may manifest as foreign particles introduced from milling media and process control agents or oxidation from the external environment. These impurities have the potential to be transferred to the final product through SPS, thereby compromising the intended microstructure and properties.

Moreover, excessive temperature elevation during milling can affect the alloying of elements, resulting in unwanted phase formation. Avoiding mechanical alloying or gas atomizing and using pure elemental powders has its own challenges as they can be difficult to handle. For instance, in the most commonly studied Cantor alloy (CoCrFeMnNi), Cr has a high affinity towards oxygen forming chromium oxides, whereas Ni and Co are considered hazardous by the REACH regulations [18,19] and Mn has a high tendency to sublimate. Moreover, a study published by the EU, curates a list of critical raw materials important for the EU economy and are at high risk of supply [20–22], which include Co, Mn, Nb, Ta, Ti, W, V, Ni among others, all of which make up the compositions of a vast number of HEAs studied to date. Furthermore, an important factor stymying the commercialization of HEAs is the high cost as these alloys contain expensive metals at high proportions.

A novel idea is indeed necessary to develop new HEAs, in a cost-effective and high throughput manner for industrialization, with enhanced mechanical properties, and avoiding the direct use of critical metals, which are the main focuses of this thesis.

1.2 Objective and scope

As a solution to the above problems, this research explores a new way of producing HEAs using powder metallurgy routes. Currently, there are plenty of commercial alloy powders on the market, which are mass-produced and therefore cheaper and widely available, which contain many elements that can be used to make a final HEA. Examples include Nickel base superalloys, Co base superalloys, and Fe base alloys like stainless steel, among others. A blend of these commercial powders, termed as commodity, was used as the feedstock for the powder metallurgy routes in this work to study its feasibility in developing different HEAs. A total of five different commodity powders were selected for this work: Ni625, CoCrF75, Invar36, 316L, and Fe49Ni. The selected powders were mixed in appropriate proportions to result in different non-equiatomic HEAs based on CoCrFeNi system, with small additions of Mo and Nb, and exploring the addition of Al to generate dual phase microstructures. This method of blending commercial powders offers a sustainable way to accelerate the discovery of new materials. In addition, this method is cost-effective, efficient as it avoids pre-alloying steps, and flexible due to the many types of commercially available powders in the market. Based on the success of this method, using scraps to produce powders for next-generation materials will be possible, thereby enhancing the rate of scrap recycling.

The aims of this PhD thesis are as follows:

1. To design new compositions based on Co, Cr, Fe, Ni, Mo, Nb and Al to obtain single and dual-phase HEAs using the compositions of available commodity powders.
2. To develop the newly designed HEAs using field assisted sintering methods (field assisted hot pressing (FAHP) and spark plasma sintering (SPS)), and laser powder bed fusion (PBF-LB/M) with high densities and subsequent heat treatment studies.
3. To validate the mechanical properties of the newly developed HEAs at room and high temperatures and correlate them with their microstructures.

1.3 Thesis outline

The thesis is organized as follows:

- Chapter 1 is the introduction section, where a short background of HEAs is provided along with the current challenges that exist in its fabrication. The motivation, scope and objectives of this thesis are also introduced.

- Chapter 2 is the literature review. The basic concept of HEAs is introduced along with its composition designs, core effects and mechanical properties. Then an overview of HEA development by powders is provided, where spark plasma sintering and additive manufacturing techniques are introduced and its corresponding effect on the microstructure and properties of HEAs is reviewed.

- Chapter 3 is the experimental procedure. This chapter summarizes and describes the experimental procedures throughout the entire PhD research, including composition design, alloy fabrication, heat treatment, consolidation processes, laser powder bed fusion process, mechanical properties evaluation and microstructural characterization.

- Chapter 4 presents and discusses the results obtained during this PhD research by using the published content from journal and conference papers. The first segment investigates the fabrication of three FCC HEAs based on CoCrFeNiMoNb system by blending commodity powders and consolidating them by FAHP and SPS and evaluating its tensile and hot compression properties. The section also involves the calculation of empirical parameters, microstructural characterization, evaluation of tensile and hot compression properties of the as-sintered and heat-treated alloys. The next segment presents and discusses the results of developing two FCC HEAs by PBF-LB/M via in-situ alloying commodity powders, starting from optimization of parameters, microstructural characterization, and tensile testing at room temperature, 700°C, 800°C and 900°C. The following segment after that provides an in-depth optimization analysis of adding 3.5wt% and 4.5wt% pure Al powders to the CoCrFeNiMoNb system and printing them via PBF-LB/M and presents the microstructural analysis of the high dense samples.

- Chapter 5 summarizes the overall conclusions of the thesis and suggests several future studies that can be developed further from this work.

Bibliography

[1] J.W. Yeh, S.K. Chen, S.J. Lin, J.Y. Gan, T.S. Chin, T.T. Shun, C.H. Tsau, S.Y. Chang, Nanostructured high-entropy alloys with multiple principal elements: Novel alloy design concepts and outcomes, Adv Eng Mater 6 (2004) 299–303. https://doi.org/10.1002/adem.200300567.

[2] B. Cantor, I.T.H. Chang, P. Knight, A.J.B. Vincent, Microstructural development in equiatomic multicomponent alloys, Materials Science and Engineering A 375–377 (2004) 213–218. https://doi.org/10.1016/j.msea.2003.10.257.

[3] J. Chen, X. Zhou, W. Wang, B. Liu, Y. Lv, W. Yang, D. Xu, Y. Liu, A review on fundamental of high entropy alloys with promising high–temperature properties, J Alloys Compd 760 (2018) 15–30. https://doi.org/10.1016/J.JALLCOM.2018.05.067.

[4] Y. Zhang, T.T. Zuo, Z. Tang, M.C. Gao, K.A. Dahmen, P.K. Liaw, Z.P. Lu, Microstructures and properties of high-entropy alloys, Prog Mater Sci 61 (2014) 1–93. https://doi.org/10.1016/j.pmatsci.2013.10.001.

[5] X. Chen, Q. Wang, Z. Cheng, M. Zhu, H. Zhou, P. Jiang, L. Zhou, Q. Xue, F. Yuan, J. Zhu, X. Wu, E. Ma, Direct observation of chemical short-range order in a medium-entropy alloy, Nature 2021 592:7856 592 (2021) 712–716. https://doi.org/10.1038/s41586-021-03428-z.

[6] J.W. Yeh, S.K. Chen, S.J. Lin, J.Y. Gan, T.S. Chin, T.T. Shun, C.H. Tsau, S.Y. Chang, Nanostructured high-entropy alloys with multiple principal elements: Novel alloy design concepts and outcomes, Adv Eng Mater 6 (2004) 299–303. https://doi.org/10.1002/adem.200300567.

[7] J.W. Yeh, Alloy design strategies and future trends in high-entropy alloys, JOM 65 (2013) 1759–1771. https://doi.org/10.1007/s11837-013-0761-6.

[8] Y.F. Ye, Q. Wang, J. Lu, C.T. Liu, Y. Yang, High-entropy alloy: challenges and prospects, Materials Today 19 (2016) 349–362. https://doi.org/10.1016/j.mattod.2015.11.026.

[9] D.B. Miracle, O.N. Senkov, A critical review of high entropy alloys and related concepts, Acta Mater 122 (2017) 448–511. https://doi.org/10.1016/j.actamat.2016.08.081.

[10] X. Gao, T. Liu, X. Zhang, H. Fang, G. Qin, R. Chen, Precipitation phase and twins strengthening behaviors of as-cast non-equiatomic CoCrFeNiMo high entropy alloys, J Alloys Compd 918 (2022) 165584. https://doi.org/10.1016/j.jallcom.2022.165584.

[11] Y.X. Zhuang, X.L. Zhang, X.Y. Gu, Effect of molybdenum on phases, microstructure and mechanical properties of Al0.5CoCrFeMoxNi high entropy alloys, J Alloys Compd 743 (2018) 514–522. https://doi.org/10.1016/J.JALLCOM.2018.02.003.

[12] Z. Tang, O.N. Senkov, C.M. Parish, C. Zhang, F. Zhang, L.J. Santodonato, G. Wang, G. Zhao, F. Yang, P.K. Liaw, Tensile ductility of an AlCoCrFeNi multi-phase high-entropy alloy through hot isostatic pressing (HIP) and homogenization, Materials Science and Engineering: A 647 (2015) 229–240. https://doi.org/10.1016/J.MSEA.2015.08.078.

[13] I.S. Wani, T. Bhattacharjee, S. Sheikh, Y.P. Lud, S. Chatterjee, P.P. Bhattacharjeea, S. Guo, N. Tsujib, Ultrafine-Grained AlCoCrFeNi2.1 Eutectic High-Entropy Alloy, Http://Mc.Manuscriptcentral.Com/Tmrl 4 (2016) 174–179. https://doi.org/10.1080/21663831.2016.1160451.

[14] Y. Zhang, X. Wang, J. Li, Y. Huang, Y. Lu, X. Sun, Deformation mechanism during high-temperature tensile test in an eutectic high-entropy alloy AlCoCrFeNi2.1, Materials Science and Engineering: A 724 (2018) 148–155. https://doi.org/10.1016/j.msea.2018.03.078.

[15] H. Gasan, A. Ozcan, New Eutectic High-Entropy Alloys Based on Co–Cr–Fe–Mo–Ni–Al: Design, Characterization and Mechanical Properties, Metals and Materials International 26 (2020) 1152–1167. https://doi.org/10.1007/s12540-019-00515-9.

[16] L. Yu, X. Ye, D. Fang, M. Liu, H. Guo, S. Wang, G. Zhao, B. Li, H. Wu, Precise design strategy of FeNiCrMo eutectic high-entropy alloys, Journal of Materials Research and Technology 21 (2022) 3207–3219. https://doi.org/10.1016/J.JMRT.2022.10.101.

[17] J.M. Torralba, P. Alvaredo, A. García-Junceda, High-entropy alloys fabricated via powder metallurgy. A critical review, Powder Metallurgy 62 (2019) 84–114. https://doi.org/10.1080/00325899.2019.1584454.

[18] Nickel Infocard, European Chemicals Agency (n.d.). https://echa.europa.eu/substance-information/-/substanceinfo/100.028.283.

[19] Cobalt Infocard, European Chemicals Agency (n.d.). https://echa.europa.eu/substance-information/-/substanceinfo/100.028.325

[20] European Commission, Study on the Critical Raw Materials for the EU, 2023. https://op.europa.eu/en/publication-detail/-/publication/57318397-fdd4-11ed-a05c-01aa75ed71a1.

[21] European Commission, Proposal for a Regulation of the European Parliament and of the Council establishing a framework for ensuring a secure and sustainable supply of critical raw materials and amending Regulations (EU) 168/2013, (EU) 2018/858, 2018/1724 and (EU) 2019/1020, (2016) 1–23.

[22] European Commission, Proposal for a Regulation of the European Parliament and of the council, for establishing a framework for ensuring a secure and sustainable supply of critical

raw materials and amending Regulations (EU) 168/2013, (EU) 2018/858, 2018/1724 and (EU) 2019/102, 0079 (2023) 1–23. https://doi.org/10.2760/386650.

CHAPTER 2

Literature review

2.1 High Entropy Alloys

2.1.1 Definitions

There have been multiple terms used to describe HEAs, like complex concentrated alloys (CCAs), multi-principal element alloys (MPEAs), and baseless alloys. But the main motivation in the development of those alloys remains the same, which is 'to investigate the unexplored central region of multicomponent alloy phase space, away from the vertices, edges, and faces', as mentioned in one of the founding papers [1]. Several HEA definitions exist which gives some confusion whether some alloys can be called HEAs. Some of the commonly used definitions are based on two concepts: composition and entropy.

The composition-based definition states that HEAs are those alloys having, 'five or more principal elements with the concentration of each element being between 35 and 5 at-%' [2] HEAs may also contain minor elements (less than 5 at%) to modify the properties of the base HEA [3], which expands the number of alloys that can be called as HEAs. This composition-based definition doesn't specify any entropy constraints or the requirement for a single-phase SS.

The entropy-based definition categorizes alloys as low ($S^{SS,ideal} < 0.69R$, where $S^{SS,ideal}$ is the total configurational molar entropy in an ideal SS and R is the gas constant), medium ($0.69R < S^{SS,ideal} < 1.61R$) and high ($S^{SS,ideal} > 1.61R$) entropy alloys [3]. However, there is an ambiguity when both the composition-based and entropy-based definitions are combined. Specifically, the maximum configurational entropy of a 5-element HEA is 1.61R (for the equimolar alloy), but the minimum value is 1.36R (for an alloy with 5% A, 5% B, 20% C, 35% D, and 35% E). This latter alloy is considered as an HEA by the composition-based definition but not by the entropy-based definition. Moreover, some superalloys have configurational entropies as high as 1.37R [4]. So, as a compromise, some have suggested that any alloy with $S^{SS,ideal} \geq 1.5R$ may be considered HEAs [5].

Even though it is not required by the primary definitions, there was a common notion initially that HEAs must be single-phase [6]. Rather than characterizing an alloy based on the maximum possible (i.e., ideal) value of configurational entropy, this notion emphasizes the actual configurational molar entropy of an alloy (S^{SS}), which can be much lower. This raises an issue when an HEA is single phase at high temperature having high configurational entropy (ΔS_{conf}) but forms an ordered compound at a lower temperature thus reducing the ΔS_{conf} of the disordered phase. So, there has been a debate on which ΔS_{conf} should be considered for the HEA definition. Otto et al [7] suggest that ΔS_{conf} of the low temperature state be used while Miracle et al [5] ask to consider the ΔS_{conf} value at the high temperature state, since that is the entropy that is inherent in a system, and which must be overcome if competing phases are to form.

HEA is a relatively new field and hence the definitions are always under constant evolution. For instance, even though the composition-based definition requires five or more elements as mentioned above, simple crystal structures have also been found in alloys composed of less than 5 elements (eg. FeCoCrNi [8]). Even though HEAs started as a study on single phase solid solutions, studies have gradually shifted to HEAs with precipitates [9] or dual phase structures [10] or eutectic structures [11] to form multiphases to overcome the inherent weaknesses of the individual microstructures. The concept of how high entropy favours the formation of simple solid solution phases rather than intermetallic or ordered compounds forms the content of the following sections.

2.1.2 The HEA concept

Minimizing Gibbs energy, G, is the standard method to predict the thermodynamically stable phases in an alloy. There are many competing phases in an alloy, and the phase or combination of phases with the lowest Gibbs energy is the equilibrium state. The following relationship exists for the free energy of mixing (ΔG_{mix}) in a system:

$$\Delta G_{mix} = \Delta H_{mix} - T\Delta S_{mix} \tag{2.1}$$

where ΔH and ΔS are the changes in enthalpy and entropy of a system respectively at a given temperature T.

So, to minimize ΔG_{mix}, the value of ΔS_{mix} needs to be high, which makes up the foundation of HEAs.

The total entropy of a system can be expressed as:

$$\Delta S_{mix} = \Delta S_{mix}^{conf} + \Delta S_{mix}^{vib} + \Delta S_{mix}^{elec} + \Delta S_{mix}^{mag} \quad (2.2)$$

The main contribution for ΔS_{mix} comes from the ideal configurational mixing entropy ΔS_{mix}^{conf}, which, for convenience from now on, will be taken as ΔS_{mix}.

According to Boltzmann's hypothesis, the mixing configurational entropy of an n-element alloy changing from an elemental to a random solution state can be expressed as shown in [3]:

$$\Delta S_{mix} = -R \sum_{i=1}^{n} C_i ln C_i \quad (2.3)$$

where R is the gas constant, 8.314 J $K^{-1}mol^{-1}$, and C_i is the mole fraction of the i^{th} of n components (different chemical elements). Recent research has suggested that high entropy of mixing alone won't suppress the formation of intermetallics since it only considers the number of elements within the metallic system and does not consider the chemical contribution or the size of each element as shown in Eqn (2.3). For instance, it has been noted that HEAs with too positive or too negative ΔH_{mix} will result in phase segregation and thus lead to the formation of multi-phase alloys [7,12]. Thus, recent studies have provided an extensive analysis of the factors that impact the formation of single-phase in high entropy alloys [13] and certain criteria have been introduced to predict its formation [12] which are discussed below.

The enthalpy of mixing for a multi-component alloy system with n elements can be determined using the following equation [14]:

$$\Delta H_{mix} = \sum_{i=1, i \neq j}^{n} 4 \Delta H_{ij}^{mix} C_i C_j \quad (2.4)$$

where ΔH_{mix} is the mixing enthalpy of binary liquid $i_{50}j_{50}$ alloy.

Yang et al. [15] introduced two new parameters namely, Ω, which combines entropy and enthalpy of mixing and δ, which considers the atomic size of each element.

$$\Omega = \frac{T_m \Delta S_{mix}}{\Delta H_{mix}} \quad (2.5)$$

$$\delta = \sqrt{\sum_{i=1}^{n} C_i \left(1 - \frac{r_i}{\bar{r}}\right)^2} \tag{2.6}$$

where T_m is the rule-of-mixtures (ROM) melting point of the alloy, $\bar{r}$ is the average atomic radius in the alloy obtained by ROM and r_i is the atomic radius of the i^{th} element.

The criteria presented in [15] for forming a simple solid solution are $\Omega \geq 1.1$ and $\delta \leq 0.066$. Thus, a simple solid solution forms when the entropy is large relative to the enthalpy and there is a small atomic size difference in the alloy.

In addition, a novel parameter, γ, was proposed by Wang et al [16] as a measure of the atomic size difference. This parameter is expressed as:

$$\gamma = \omega_s/\omega_L = \left(1 - \sqrt{\frac{(r_s + \bar{r})^2 - \bar{r}^2}{(r_s + \bar{r})^2}}\right) \Big/ \left(1 - \sqrt{\frac{(r_L + \bar{r})^2 - \bar{r}^2}{(r_L + \bar{r})^2}}\right) \tag{2.7}$$

where ω_S and ω_L are the solid angles of the smallest and the largest atoms, respectively, with respect to the surrounding atoms. r_s and r_L are the radii of the smallest and largest atoms in the given alloy, respectively. The authors analyzed tens of alloys to determine that a single solid solution (SSS) forms for $\gamma < 1.175$.

Singh et al. [17] proposed another single parameter model by defining $\Lambda = \Delta S_{mix}/\delta^2$. SSS formation was reported to be favored for $\Lambda > 0.96$, i.e., a large configurational entropy and a small atomic size difference. This model is the unique among current models in that the effect of the enthalpy is not considered. Atomic size differences play a central role in this model. The valence electron concentration (VEC) can be used to determine the suitability of an FCC or BCC as an HEA [18], where VEC ≥ 8 favors FCC formation, VEC < 6.87 favors BCC formation, and both these phases co-exist between $6.87 \leq VEC < 8$, as shown in Fig. 2.1 (b).

Guo et al [19] also statistically analyzed the effect of atomic size difference, mixing enthalpy, mixing entropy, electronegativity, valence electron concentration among constituent elements in solid solutions forming high entropy alloys and amorphous alloys. It was concluded in their research that the formation of solid solution requires that these parameters simultaneously satisfy $-22 \leq \Delta H_{mix} \leq 7$ kJ/mol, $0 \leq \delta \leq 8.5$, and $11 \leq \Delta S_{mix} \leq 19.5$ J/(K·mol) as shown in Fig. 2.1 (a).

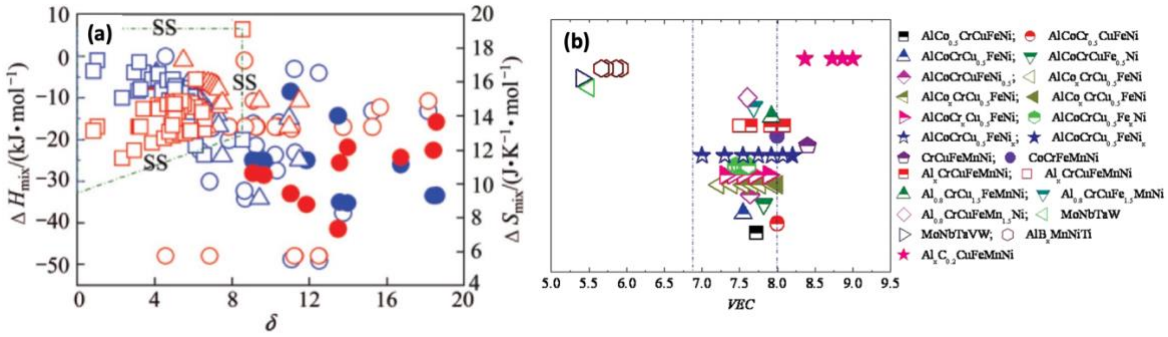

Fig. 2.1: (a) Superimposed effect of all three parameters ΔH_{mix}, ΔS_{mix} and δ on phase stability in HEAs and BMGs where the dashed line marks the boundary for SS formation [19] and (b) prediction of the crystal structure of HEAs based on VEC [18]

Table 2.1 summarizes the threshold values of the aforementioned parameters to form a single-phase SS. So, these values act as a guideline while designing any HEA. The threshold value of the VEC parameter to obtain a single FCC phase has also been included.

TABLE 2.1 : VARIOUS ASSESSMENT PARAMETERS FOR HEAS

Parameter	**Threshold values**	**References**
ΔS_{mix}^{conf}	>1.61R	[3]
ΔH_{mix} (kJ/Mol)	$-11.6 < \Delta H_{mix} < 3.2$	[20]
Ω/1000	≥1.1	[15]
100δ	<6.6	[15]
γ	<1.175	[16]
Λ	>0.96	[15]
VEC	>8 for FCC	[18]

2.1.3 Core effect of HEAs

Four main core effects have been used to describe HEAs: the high entropy effect, the lattice distortion effect, sluggish diffusion, and the cocktail effect [3]. Recently, a feature known as chemical short-range order (CSRO) strengthening has been observed in HEAs which can be classified as a core effect as well [21–23].

2.1.3.1 The high entropy effect

The high entropy effect, as described in the earlier section, describes that an alloy with 5 or more elements in near-equimolar quantities favors formation of solid solution phases compared to competing intermetallic compounds due to higher configurational entropy of mixing.

2.1.3.2 Lattice distortion effect

Since HEAs have multiple elements, the crystal lattice also has a multi-element basis compared to the conventional one or two element basis. This results in severe lattice distortion as the atoms are of different atomic sizes from one another. This lattice distortion effects in HEAs cause high solid solution hardening, thermal resistance, electrical resistance, and x-ray diffuse scattering.

2.1.3.3 Sluggish diffusion effect

Since lattice distortion causes hindrance in the atomic movement, this will limit the effective diffusion rate in HEAs, thus causing the sluggish diffusion effect [2,3]. This claim is based on secondary observations that include formation of nanocrystals and amorphous phases upon solidification.

2.1.3.4 Cocktail effect

The cocktail effect, a phrase first used by Prof. S. Ranganathan [24], is used to describe the unpredictable, synergistic response resulting from the mixture of multi-principal elements. For example, the addition of light elements, such as Al, can decrease the density of HEAs. Furthermore, adding Al [9] increases the hardness of HEAs due to formation of a hard BCC phase, strong cohesive bonding between Al and other elements, and solid solution strengthening in Al-Co-Cr-Fe-Ni alloy system. So, the cocktail effect should be kept in mind when designing new HEAs.

2.1.3.5 The chemical short-range order (CSRO) strengthening

Enthalpic interactions among constituent elements are expected resulting in chemical short-range order in medium and high entropy alloys [21–23]. These short-range orders have been observed in HEAs by energy filtered transmission electron microscopy, which gives rise to higher stacking fault energy and hardness. So, the mechanical properties of medium and high entropy alloys can be improved by tailoring the short-range order by thermomechanical processing, making it an inherent feature in such alloys.

2.1.4 Major HEA alloy families and microstructures

There have been attempts to classify HEAs based on the elements used for alloying irrespective of the processing routes that are used to obtain them. The most common way the HEAs are divided in the literature are 3d transition metals, refractory metals, lightweight materials, and lanthanide HEAs as shown in Fig. 2.2.

3d transition metal HEAs are the most widely studied HEA consisting mostly of Fe, Ni, Cr, and Co, to which the Cantor alloy belongs. A second group of alloying elements is used less frequently: Al, Ti, Cu, and Mn. Most of the HEAs in this family typically exhibit a single-phase FCC microstructure, although certain elements like Al can be added to modify the microstructure from FCC to FCC + BCC or to fully BCC [18]. Most recently, eutectic high entropy alloys (EHEAs) have been reported by many researchers [11], which consists of a lamellar microstructure with FCC and BCC/B2 phases. The commonly studied EHEA is the $AlCoCrFeNi_{2.1}$ system, which was first proposed by Lu et al [25].

The refractory metals HEA (RHEA) family consists of alloys containing at least 4 of the following nine refractory elements, Cr, Hf, Mo, Nb, Ta, Ti, V, W, and Zr, plus Al [26]. The commonly studied RHEA is the Senkov alloy, HfNbTaTiZr. Non-refractory elements like Al or Si are usually included to decrease alloy density and improve properties. This family is studied much less frequently than the 3d transition metal family of alloys. These HEAs were developed in search for high temperature load bearing structures and thermal protection materials for the aerospace industry, among other applications [27]. Since all the elements in this family have a BCC structure, all the refractory HEAs exhibit single phase BCC microstructure.

A third family of HEAs is motivated by the need to develop new structural metals with low density for aerospace and transportation applications. This alloy family is based on mostly lightweight elements such as Al, Be, Li, Mg, Sc, Si, Sn, Ti and Z [28–30]. A broad range of elemental melting and boiling points in this family make processing through ingot metallurgy routes difficult. So, powder metallurgy routes offer a better opportunity to manufacture these types of HEAs.

New alloy families are being devised at a rapid pace, and the current approach for defining alloy families as a small number of elements with a common feature may continue to be useful. However, as the field continues to expand and mature, the definition of an alloy family by the

constituent elements may become less useful, and alloy families based on intended properties or applications may become more useful [26].

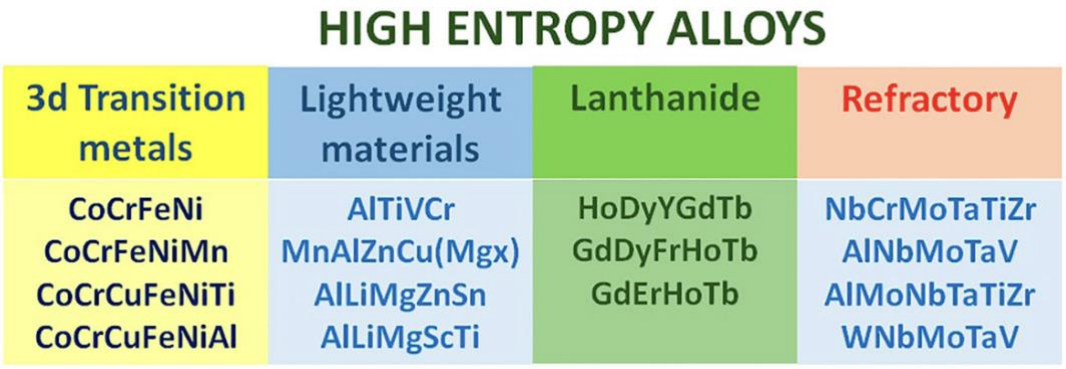

Fig. 2.2: Classification of HEAs [21]

2.1.5 Potential applications

HEAs are still in their early research stages, although significant advancements have been made with respect to the properties using multiple fabrication routes. Thus, it is imperative to discuss about the potential applications of HEAs in the foreseeable future. Due to the numerous possibilities of alloying combinations, the elements can be tailored according to the targeted application based on the requirements as shown in Fig. 2.3 and hence the potential applications vary ranging from structural to functional applications. HEAs are promising for example in engineering applications like aerospace, automotive, machining, boilers, nuclear reactors, among others. It also finds use in functional applications like magnets, hydrogen storage, and energy conversion [31]. Some of these applications are well summarized in [32], listing the alloy, its manufacturing process, and its intended applications.

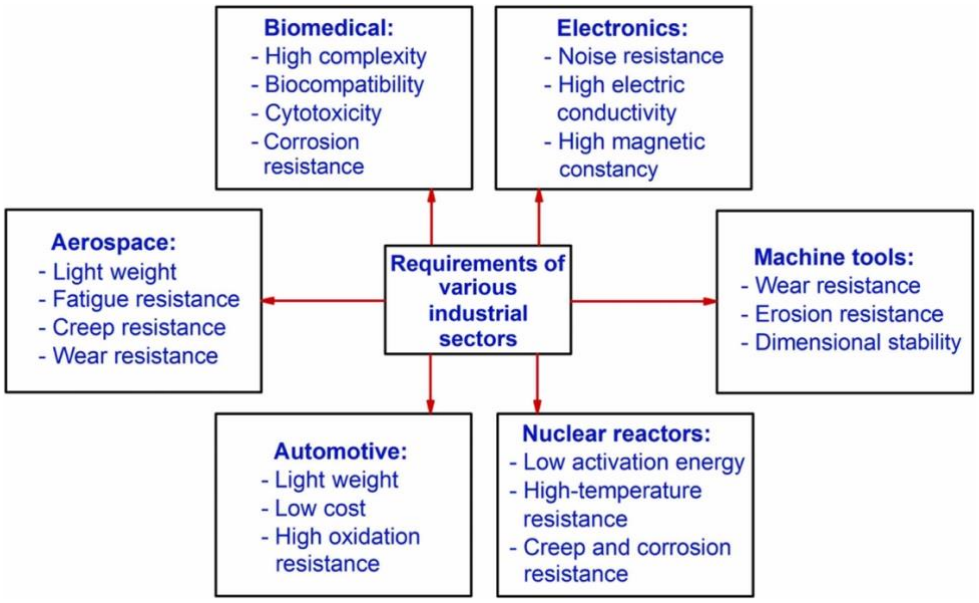

Fig. 2.3: The requirements of HEA properties in various industrial sectors [32]

HEAs have an extremely wide range of temperatures where they are applicable. The well-known cantor alloy, CoCrFeMnNi [33], displays remarkable fracture toughness at cryogenic temperatures making it useful in cryogenic storage tanks. On the other hand, refractory HEAs like TaNbHfZrTi [34], and high entropy superalloys (HESAs) like $AlMo_{0.5}NbTa_{0.5}TiZr$ [35], manifest excellent creep resistance, and can retain their high strengths even at temperatures upto 1400^{o}C, comparable with, or exceeding certain conventional superalloys, such as Inconel 718 and Haynes 230.

Furthermore, certain HEAs exhibit exceptional corrosion resistance, making them highly suitable for various applications involving corrosive environments. These applications span a wide spectrum, such as boilers and heat exchangers operating in high-temperature corrosive conditions and ship propellers exposed to seawater continuously. Examples of corrosion resistant HEAs include $Al_{0.1}CrCoFeNi$ [36], AlCrFeCuCo [37] , and Mo-based HEAs [38–40]. Recently, a report was published by The Minerals, Metals & Materials Society (TMS) written by 15 international experts and funded by two U.S. defense agencies which defines the pathways for harnessing the revolutionary potential of HEAs [41].

However, there is still a long way to go when HEAs can be used in a real-life application mainly due to the cost and the ease of manufacturing, two of the most important factors in commercialization of a material, in addition to structural or functional properties.

2.2 Processing routes

Most of the HEAs have been developed via ingot casting methods. Arc melting is the most common processing method, covering more than half of the production methods, due to its efficiency and low cost. However, when complex compositions must be achieved, ingot metallurgy presents some difficulties that can diminish its potential for fabricating this promising family of alloys. Recently, powder metallurgy (PM) has shown great potential for HEA processing due to its ability to achieve significant compositional accuracy than other methods, while preventing segregation and achieving superior microstructural control (including the formation of nanocrystalline materials) [27]. PM also has two other advantages over other forming techniques: (1) it can be applied when metals with dissimilar densities must be used, which is the case when lightweight HEAs are developed [42]; and (2) it can be applied when many metals with extremely high melting points are involved in the development of the HEA. i.e., refractory HEAs [43]. So, this section focuses on the powder metallurgy routes used to develop HEAs, here after referred to as powder metallurgy HEAs (PMHEAs), and related properties.

2.2.1 Powder development

The first step in any PM process is to obtain suitable powders for the process. Since HEAs have around five different metals, the starting material can be either fully pre-alloyed powders or a conventional mix of powders using pure metals powders.

Based on the literature review, two different methods were used to obtain fully pre-alloyed powders: mechanical alloying (MA) and atomizing, with MA being the most common method. Moreover, these alloys developed so far have been at a lab scale for research purposes.

MA involves loading of the individual elemental powders or pre-alloyed powders along with the grinding medium in a high-energy ball mill, typically maintaining a ball-to-powder weight ratio of 10:1 or higher [44]. The process involves repeated cold welding, fracturing, and rewelding of powder particles. About 1-2 wt.% of a process control agent (PCA) is used, especially when ductile metals are fabricated. The PCA is adsorbed on the surfaces of the powder particles and minimizes excessive cold welding among themselves and/or to the milling container and the grinding medium; this inhibits agglomeration of powder particles. But any possible contamination from the PCA agents should be considered while calculating the final composition of the alloy powders.

In [45], the development of the microstructure in a mechanically alloyed powder when fabricating a high-entropy alloy from elemental powders is analyzed in detail as summarized in Fig. 2.4. Since a HEA contains both hard and soft elements, the brittle-ductile mechanism described in [46] could be followed. Based on the hardness of the elements, they either fragment or flatten during collision as shown in Fig. 2.4.

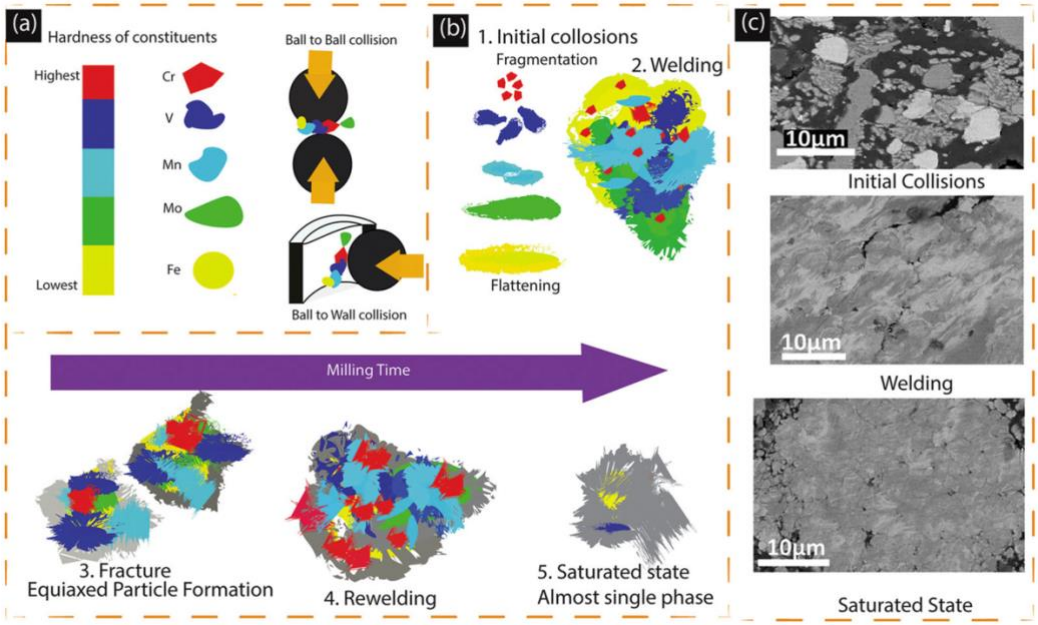

Fig. 2.4: Mechanical alloying process for a multi-principle element system: (a) element hardness and types of collisions, (b) powder processing steps during the mechanical alloying (MA) process, and (c) actual image of the powder during different steps [45]

The second most common method to obtain a fully pre-alloyed powder is atomizing by gas or water. Recently, ultrasonic atomizing has been demonstrated as an interesting alternative for developing HEAs. Gas and ultrasonic atomizing are especially useful for most additive manufacturing methods as it provides almost perfect spherical powders. Atomizing can be considered as the most suitable method to obtain powders to manufacture HEAs due to the better control it offers on both chemical compositions, avoiding undesirable elements such as C, as well as on shape and morphology of the powders. However, due to the wide range of compositional options in HEAs, there are not a lot of tailored powder grades available in the market.

In this regard, this research work uses a blend of pre-alloyed commercial powders, termed as commodity, like Ni superalloys, stainless steel, invar36 and cobalt-chrome, to develop novel HEAs. The selected powders were blended in appropriate proportions and used as a feedstock

in consolidation processes like field assisted hot pressing (FAHP) [47,48], spark plasma sintering (SPS) [49], where the mechanical properties were evaluated, and laser powder bed fusion (PBF-LB/M) where optimizations were carried out to make HEAs via in-situ alloying [50,51].

2.2.2 Powder consolidation

Once the powders are ready by either pre-alloying or conventional mixing, it is necessary to consolidate it to obtain a final bulk part. Omitting additive manufacturing methods which are discussed in the next section, Fig. 2.5 analyses the different PM routes followed in the literature to obtain bulk materials, also showing the percentage of works that use each of these techniques as reviewed by Torralba et al [27]. It is seen that MA is the preferred method to obtain pre-alloyed HEA powders and spark plasma sintering (SPS) is the preferred consolidation step. So, MA + SPS is the most common combination used to obtain a HEA.

Spark plasma sintering (SPS), a field-assisted sintering technique (FAST) is a materials processing technique that uses direct current (DC) with a low pulse voltage current combined with uniaxial force to sinter powder placed in a graphite die (mould). Here, both compaction and sintering are done at the same time unlike the press and sinter route (P&S). During SPS, pressure is applied to compress the powder particles and the pulsed current discharged during the process creates metallurgical bonding between the particles which results in powder densification. For better visualization, a schematic of the SPS technique is shown in Fig 2.6. In addition, Fig. 2.7 shows the schematic illustration of particles transformation stages during sintering. It is seen that spark discharge occurs at the contact points between the particles and causes localized heating which enhances the sintering rate i.e., the full sintering cycle can be developed in very short times, which is one of the main advantages of SPS. These conditions enable full densification of material along with avoiding excessive grain growth. Other methods that also combine pressure and temperature (such as other hot pressing -HP- methods or hot isostatic pressing -HIP- methods) can also attain full density, but these methods usually need higher temperatures and longer times, so grain growth is not fully avoided, and the mechanical properties can be affected [27].

After SPS, the most common method to obtain PM HEAs is by the traditional ´press and sintering´ route. As shown in Fig. 2.5, most of the works use uniaxial pressing while few studies

have used cold isostatic pressing (CIP). Unlike SPS, sintering is done separately on the pressed part and the temperatures are slightly higher than that used for SPS.

The other important processing methods are HP and HIP. In these methods, like in SPS, both pressure and temperature are applied at once but usually the time needed to process is much longer than SPS, leading to significant grain growth. But in one case [52], where the HP method is a ´field assisted hot pressing´ (FAHP) method, the sintering time neared those of SPS. HIP is also a widely used secondary operation to achieve zero defect conditions, especially in additive manufacturing (AM) processes linked to aerospace applications [53].

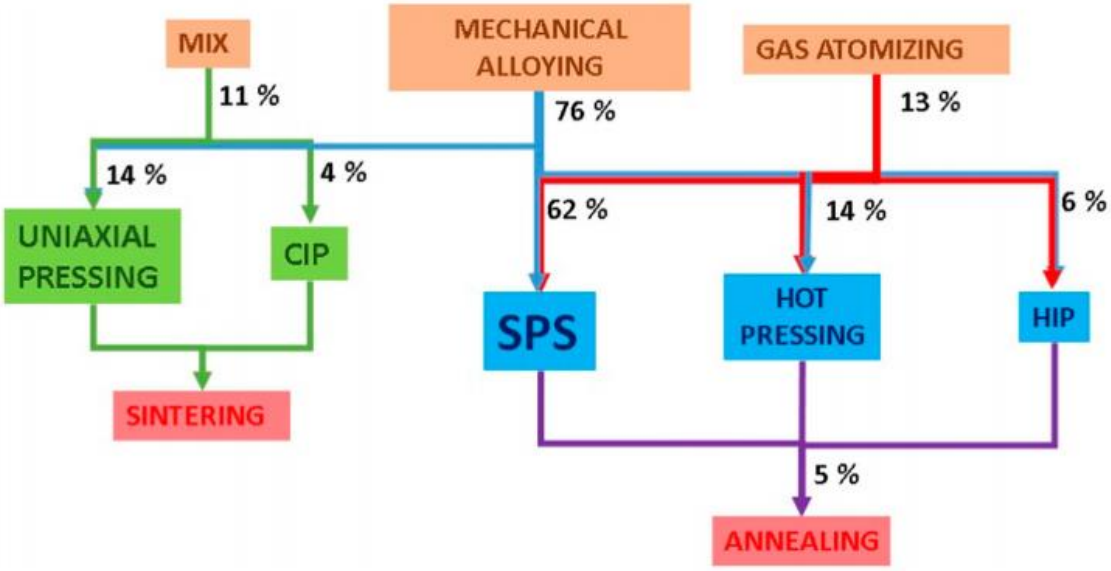

Fig. 2.5: Different PM processing routes to obtain PMHEAs [21]

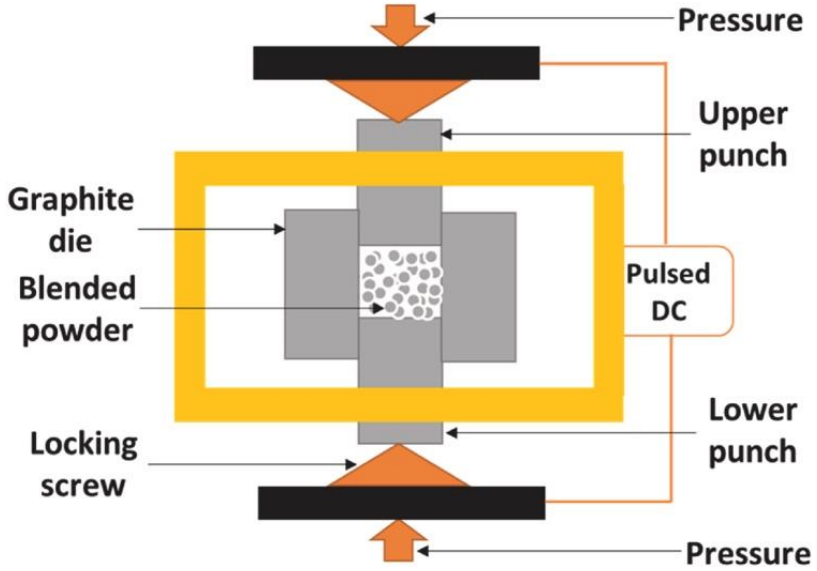

Fig. 2.6: Schematic of SPS technique [54]

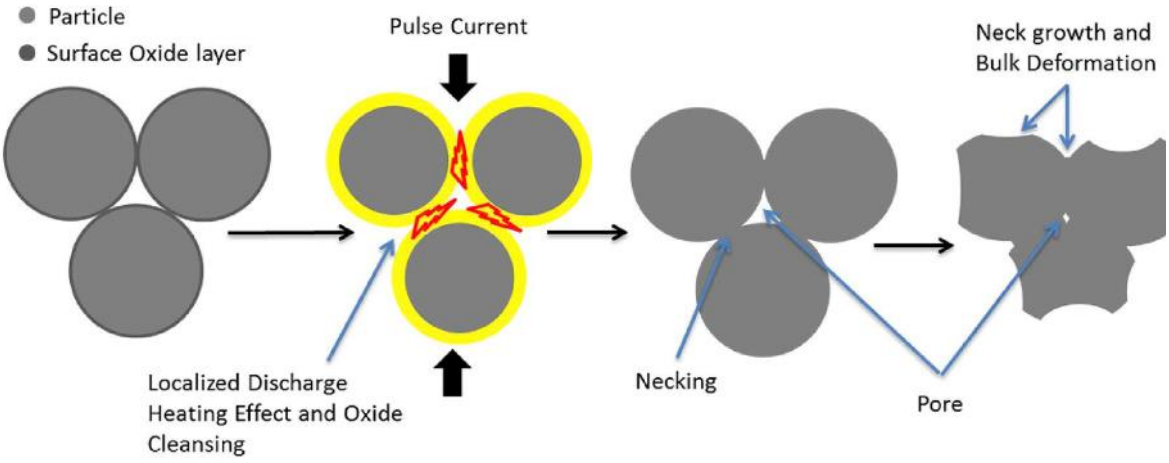

Fig. 2.7: Schematic description of particles transformation stages, a model of three spherical particles [55]

Fabrication of HEAs by SPS

As mentioned before, most of the works use SPS for consolidating HEAs after mechanical alloying (MA) because of its low sintering time, high densification, and grain growth inhibition, among others [56]. So, the microstructures of HEAs processed by SPS are usually refined, having their grain sizes reduced to nanometers giving nanocrystalline microstructures which improves their mechanical properties. A summary of some of the reported HEAs by SPS are listed in Table 2.2. As seen in this table, Cantor based alloys like CoCrFeNi and CoCrFeNiMn have been processed by SPS along with additions with Al, Mo and Nb to introduce new phases and improve the mechanical properties due to their larger atomic size. Typically, in SPS, a higher sintering temperature and pressure reduces the porosity.

For instance, the density of CoCrFeNiMo HEA increased from 7.53 g/cm^3 at a sintering temperature of 850^{o}C to 8.46 g/cm^3 at a sintering temperature of 900^{o}C at the same pressure [57]. When the pressure was increased from 40 MPa to 50 MPa, the density increased from 8.46 g/cm^3 to 8.78 g/cm^3.

Although SPS is promising to produce nanocrystalline microstructures with better mechanical properties than arc melted microstructures, there are still some challenges and concerns to be addressed. Firstly, SPS powders are mostly prepared by mechanical alloying. However, mechanical alloying poses the risk of contamination, which can occur in the form of foreign particles introduced from milling media or oxidation from the external environment. These contaminants may transfer to the final product during SPS, potentially compromising the desired microstructure and properties. Additionally, excessive temperature elevation during milling can influence element alloying, leading to unwanted phase formation. Overcoming these challenges requires careful selection of milling media, milling environment, and milling speed. Ensuring that the milling media, vial, and balls are made of the same material can help prevent contamination. Maintaining a dry protective inert atmosphere can further prevent oxidation of the alloying powder. Thus, proper selection of milling parameters is crucial to achieving the desired alloying outcome. Moreover, the process of mechanical alloying is also time consuming (usually around 60h). Secondly, since HEAs consist of four or more elements in near equiatomic proportions, the entire cost of production is increased as the elemental powders need to be purchased at high purity and then mechanical alloyed or elements have to be ingot melted and then gas atomized before consolidation. Thus, it is difficult to explore new compositions rapidly and efficiently using this method.

Table 2.2: Summary of some HEAs fabricated by SPS

Alloy	Technique	Sintering parameters	Microstructure	Properties
CoCrFeNi [58] CoCrFeNiMn [58]	MA + SPS	900°C, 60 MPa, 5 mins	FCC + Cr_7C_3	-
CoCrFeMnNi [59]	MA + SPS	800°C, 50 MPa, 10 mins	FCC	Compression strength: 1987 MPa Hardness: 646 HV
$Al_xCoCrFeNi_{2.1}$ [60]	MA + SPS	1100°C, 40 MPa, 8 mins	x = 0, 0.3 – FCC x = 0.7, 1, 1.3 – FCC + BCC	x = 1.3, Compression strength: 2333 MPa, Hardness: 563 HV
AlCoCrFeNi [61]	Gas atomized + SPS	1100°C, 30 MPa, 10 mins	B2 + BCC	Compression strength: 2368 MPa, Yield strength tensile: 1287 MPa
$CoCrFeNiMo_{0.2}$ [62]	MA + SPS	900°C, 30 MPa, 5 mins	FCC + μ + σ	Hardness: 620 HV
$CoCrFeNiMo_{0.14}Nb_{0.14}$ [62]	MA + SPS	900°C, 30 MPa, 5 mins	FCC + μ + σ	Hardness: 710 HV
$Fe_{24.1}Co_{24.1}Cr_{24.1}Ni_{24.1}Mo_{3.6}$ [63]	MA + SPS	950°C, 35 MPa, 10 mins	FCC	Hardness: 474 HV
CoCrFeNiMo [57]	MA + SPS	900°C, 50 MPa, 5 min	FCC + μ + σ + Co_3Mo	Hardness: 8.316 GPa

2.2.3 Additive Manufacturing

Additive manufacturing (AM) offers a novel way to produce parts with complex shapes and specific properties due to its layer-by-layer fabrication process. The properties are also better due to higher heating and cooling rates that significantly hinder atomic diffusion and hence suppress phase transition and intermetallic formation during the fabrication process. The main AM technologies involving metals are directed energy deposition (DED), in which focused thermal energy is used to fuse materials by melting as the powders or wires are deposited, and powder bed fusion (PBF), where the thermal energy selectively fuses regions of a powder bed where the powders are spread on the platform using a blade or a roller. The source of the focused thermal energy can be from a laser, electron beam, or plasma arc. Using different methods, one being powder feeding and the other being spreading, may cause different fluid flow and metal evaporation and, consequently, distinct segregation behavior when printing the same alloy by DED or PBF.

Apart from the above-mentioned techniques, recently, binder-based methods are picking up momentum in the domain of metals and also on HEAs [64–66]. Binder jetting (BJT) is a powder-bed-based additive manufacturing technique that selectively dispenses liquid binders on a powder bed layer by layer to fabricate 3D components. The parts are cured after printing to ensure they can hold the geometry during post-processing and are sintered later to achieve the desired density and strength. The advantages of binder jetting are that it can work with virtually any powdered feedstock, can incorporate functionally-graded materials, and has a relatively higher building rate. Due to its strong potential for high-speed and low-cost manufacturing, binder jetting has generated an increased interest in both industry and academia [67].

2.2.3.1 Laser powder bed fusion (PBF-LB/M)

Powder bed fusion of metals with a laser beam is a widely used technique in PBF processes, which employs a full melting mechanism where the powders are fully melted by a high-power laser layer-by-layer. According to ISO/ASTM 52911-1:2019, the term laser powder bed fusion of metals is preferred to the older name selective laser melting (SLM) and is abbreviated as PBF-LB/M (Powder Bed Fusion – Laser Beam/Metals), which will be used in the rest of this thesis to follow the standard norms. PBF-LB/M is regarded as the most versatile additive manufacturing (AM) process because it can process a wide range of materials, including Al-based alloys, Ti-based alloys, Fe-based alloys, Ni-based alloys, Co-based alloys, Cu-based alloys, and their composites.

In a PBF-LB/M process, the powders are spread on the building platform by a recoater (blade or roller), and a focused laser beam selectively melts the powders in the printing layer according to a predefined path, and non-melted powders remain in the powder bed to support subsequent layers. After solidification of the printing layer, the fabrication piston depresses the foundation by the thickness of a single layer to provide space for the new layer, and the powder spreading and melting are repeated. The melting of each layer is followed by rapid solidification at the rate of 10^3–10^8 K/s [68] leading to unique refined microstructures of printed HEA products. The building chamber is usually filled with inert gas like Ar to shield the molten metal from oxidation. A schematic of this process is shown in Fig. 2.7**.**

In PBF-LB/M, the laser process parameters (laser power, scanning speed, hatch distance, layer thickness, and scanning strategy) can greatly determine the overall density and the type of defects in the printed products. Fig. 2.8 summarizes the process parameters of PBF-LB/M which can be changed to optimize the process. These parameters together determine the energy density input and thus the melt pool characteristics [69].

The term 'energy density' (E_v) is generally described by a ratio of process parameters (laser power 'P', scan speed 'v', hatch distance 'h' and layer thickness 't') as:

$$\mathrm{E_v} = \frac{P}{vht}\ \mathrm{J/mm^3} \tag{2.8}$$

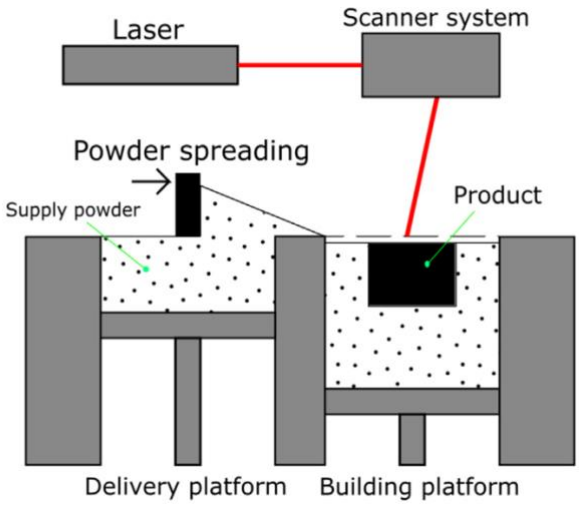

Fig. 2.7: Laser powder bed fusion process schematic [70]

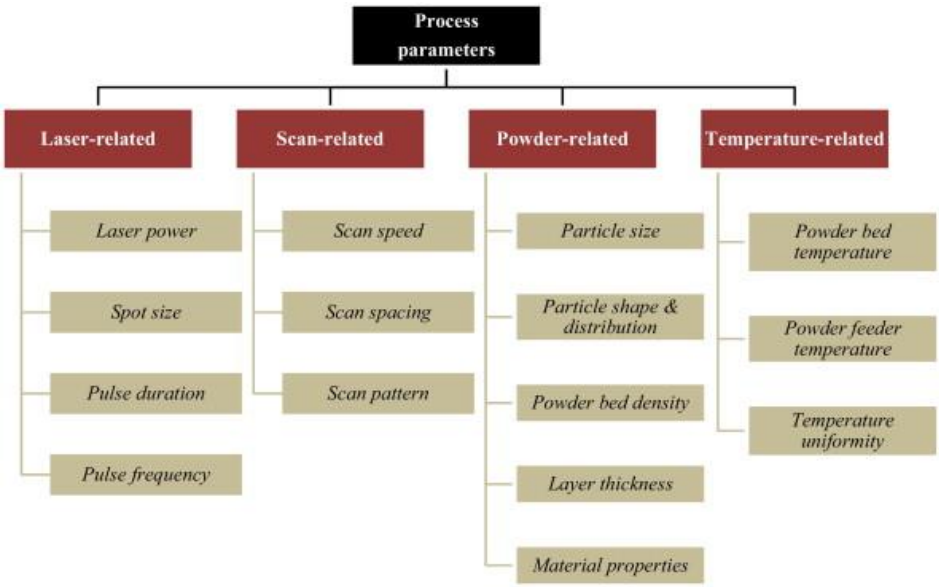

Fig. 2.8 : Process factors involved in an SLM process [71]

2.2.3.2 Fabrication of HEAs by PBF-LB/M

Research efforts on PBF of HEAs have garnered an increased interest, making it a hotspot in both fields of AM and HEAs. CoCrFeNi-based HEAs are the most widely studied HEA system, and other alloying elements are added to this system to improve specific properties based on the desired application. The first PBF-LB/M study of HEA was carried out in 2018 by Brif et al. [8], where an equiatomic CoCrFeNi HEA was successfully produced, having a single solid solution FCC phase. The results were extremely promising and opened a new avenue for manufacturing HEAs. The HEA showed a yield strength of 600 MPa and ductility of 32%, comparable to those of structural materials like stainless steel, whereas the same alloy when arc melted had a yield strength of 188 MPa with an elongation of 50%. CoCrFeMnNi HEA, known as the cantor alloy, is also one of the widely studied HEA systems using PBF-LB/M. The first attempt to print this alloy with PBF-LB/M was carried out by Li et al. [72], where a single solid solution FCC phase was obtained. Hot isostatic pressing (HIP) was performed on the alloy post printing, after which the yield strength increased to 649 MPa, from 600 MPa before HIP. This is almost three times more than that of the yield strength obtained by casting [73]. The elevated strength observed in the additively manufactured materials primarily arises from the formation of fine cellular substructures during the rapid solidification process. These substructures serve as low-angle grain boundaries, impeding dislocation motion and enhancing dislocation storage within the material. In addition, there have been reports of segregation of elements like Cr and Mo at the substructure boundaries, which further enhances the strength

[74]. Mo is added to the CoCrFeNi HEA system to improve the room and high temperature strength and to improve the corrosion properties and hence has attracted strong scientific interest. Recently, the effect of laser powder bed fusion process parameters on the cell substructure size was studied for the $CoCrFeNiMo_{0.2}$ HEA where Mo and Cr was segregated along the boundaries of the cellular substructures [75]. It was reported that as the energy density rises, the temperature gradient (G) and solidification rate (R) decrease. This leads to an increase in the cellular substructure size as shown in Fig. 2.9 as the cooling rate (G x R) reduces, the cellular size increases. The yield strength of this alloy reached up to 707 MPa with a strength contribution of 300 MPa from the compositional segregation.

Columnar grains aligned towards the build direction are the most common morphology in SLM-processed HEAs, such as FeCoCrNi [76], CoCrFeMnNi [77], C-containing FeCoCrNi [78]. The epitaxial growth of the existing grains under rapid cooling of SLM induces columnar grain growth, and competitive growth derived from remelting under the repeated deposition of metal leads to grain orientation selection [79]. To explain further, from the energy point of view, it will save more free energy if nucleation starts from partially melted grains from the previous layer rather than forming a new one. So, the newly formed grains will inherit crystallographic information from existing crystals leading to grain orientation selection [80].

As mentioned in Section 2.1.4, most of the HEAs are based on 3D transition metals that are single-phase with an FCC microstructure. However, there are possibilities to obtain dual-phase microstructures as well, where Al is the most commonly used alloying element as it tends to form BCC/B2 phases in the microstructure due to its larger atomic size [18] [81], enabling the formation of dual-phases in HEAs for a better combination of strength and ductility. It has been studied and reported that a higher Al content favours the formation of BCC/B2 phases due to the effect of valence electron concentration [18]. Zhou et al. [81] prepared an $Al_{0.5}FeCoCrNi$ HEA by PBF-LB/M, which had an FCC phase, whereas the alloy AlCoCrFeNi [82,83], consisted of BCC and B2 phases. The same alloy, when prepared through conventional casting methods, had BCC and FCC phases [84], which shows that higher cooling rate plays an important role in suppressing BCC phase formation. Even though superior properties could be obtained with a dual-phase microstructure, 3D printing of such alloys is prone to cracking during the rapid cooling process [85–87].

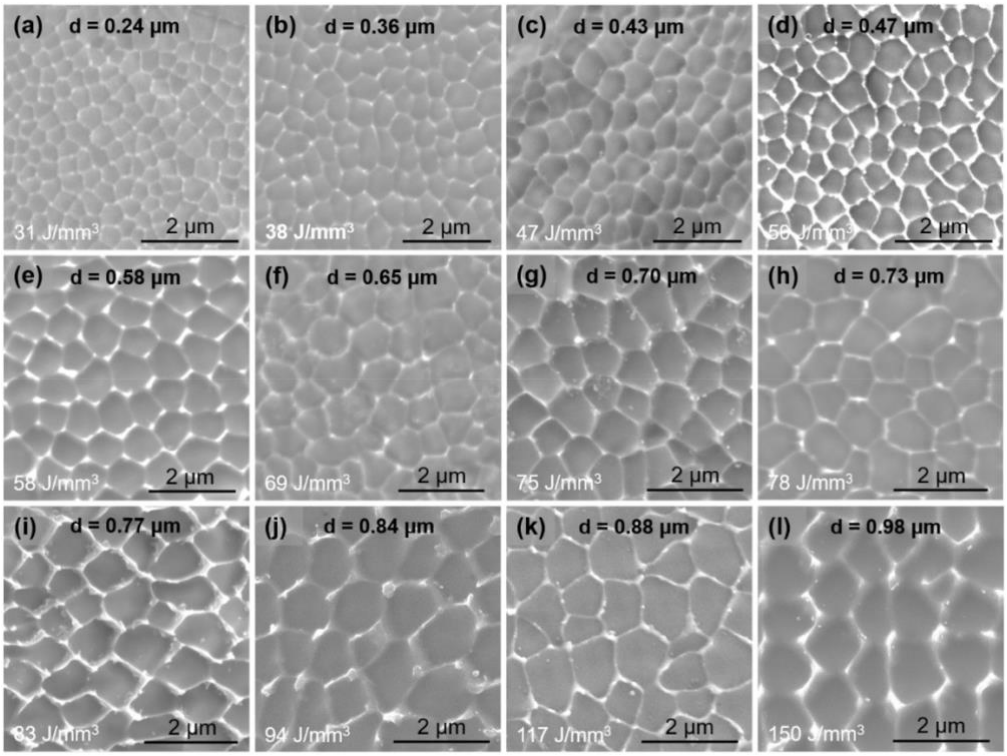

Fig. 2.9: SEM images of the $FeCoCrNiMo_{0.2}$ HEA under different energy densities. (a) 31 J/mm^3, (b) 38 J/mm^3, (c) 47 J/mm^3, (d) 50 J/mm^3, (e) 58 J/mm^3, (f) 69 J/mm^3, (g) 75 J/mm^3, (h) 78 J/mm^3, (i) 83 J/mm^3, (j) 94 J/mm^3, (k) 117 J/mm^3, (l) 150 J/mm^3 (From [75])

To avoid cracking, the base plate is usually pre-heated [88], or the composition is adjusted to change the primary solidification phase [89,90]. Luo et al. [91] successfully printed AlCrCuFeNix (x = 2.0, 2.5, 2,75, 3.0) dual-phase HEAs by PBF-LB/M process, and the micro-cracks reduced as the Ni content increased, as shown in Fig. 2.10. It was found that Ni changed the columnar grains to almost equiaxed and increased the material ductility. This dual-phase microstructure provided a combination of high tensile strength of 957 MPa and ductility of 14.3%. So, dual-phase HEAs developed by PBF-LB/M have great potential for structural applications in the future, provided the cracking issues are resolved.

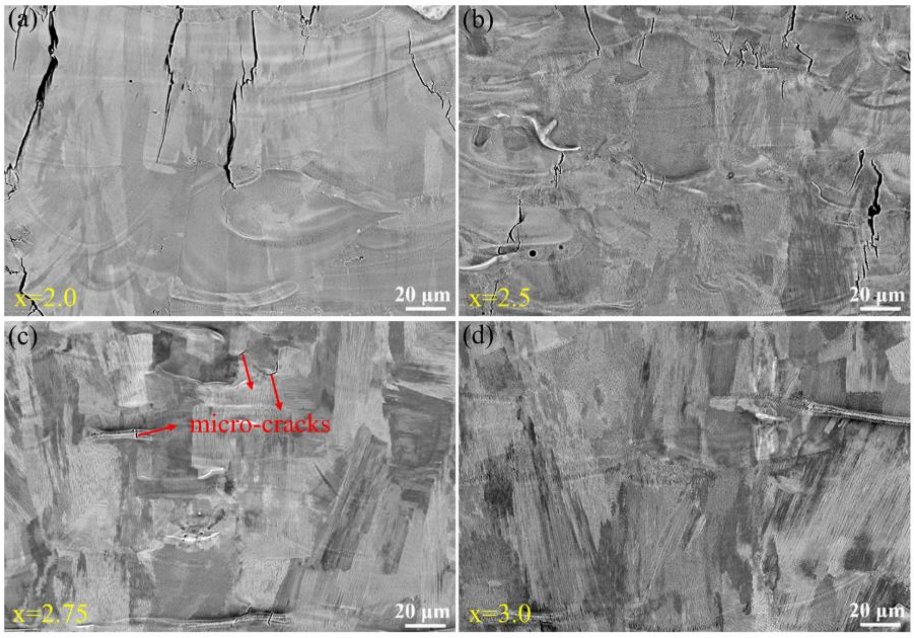

Fig. 2.10: Backscattered SEM images of as-built $AlCrCuFeNi_x$ HEAs: (a) x=2.0; (b) x=2.5; (c) x=2.75; (d) x=3.0 [83]

2.2.3.3 Feedstocks for PBF-LB/M: The in-situ alloying approach

Powder properties determine the quality and performance of AM products. A poor powder quality can produce defects, such as pores, cracks, inclusions, and suboptimal surface roughness. The spherical morphology, smooth surface, and narrow size distribution of the powder feedstock contribute to good flowability which leads to a homogenous spreading and high packing density during the process.

Three approaches to preparing HEA powder feedstock for AM have been reported in the literature, which are mechanical mixing, gas and ultrasonic atomization, and inductively coupled thermal plasma spheroidizing. Gas atomization allows the production of spherical powders, while mechanical alloying produces irregular-shape powder particles that need to be processed to achieve higher degrees of sphericity for good printability. For PBF processes, fully pre-alloyed powders prepared by gas atomization are usually used, as gas atomized powders are spherical which ensures good spreadability during re-coating by the blade/wiper. However, recently a new approach to preparing feedstocks has been introduced where the constituent elements are alloyed simultaneously during melting. This is termed in-situ alloying and provides a rapid means of evaluating new materials while enhancing material processability. For instance, Simonelli et al. explored different feedstocks to print Ti-6Al-4V in PBF-LB/M, by simply mixed elemental powders and by using a novel technique called satellite mixing, where the powders were wet mixed with polyvinyl alcohol [92]. Compared to

the simply mixed feedstock, the segregations were observed to be significantly reduced with the satelliting technique. In a similar work, Ewald et al. used powder blends to produce HEAs based on Al-C-Co-Fe-Mn-Ni to enable rapid alloy development in PBF-LB/M [93]. The effects of process parameters on the homogeneity and mechanical properties were studied, and it was concluded that an optimized energy input results in a homogenous elemental distribution in the printed parts. In the study by Chen et al. [94], Mn powders were blended with pre-alloyed CoCrFeNi powder. Good printability with a nearly homogenous Mn distribution in the as-printed parts was observed with a high VED of 259.3 J/mm^3. Similarly, Sun et al [95] fabricated CoCrFeNiMn by using elemental powders, and it exhibited slightly lower ultimate tensile strength but higher ductility than the HEA fabricated by fully prealloyed CoCrFeNi powder mixed with Mn elemental powders [94]. In another study by Hou et al. [95], the strength and hardness of CoCrFeNi HEA fabricated by pre-alloyed powders and by elemental powders were comparable, even though a higher VED was necessary to obtain excellent performance in the case of elemental powders. Unmelted Cr particles were also observed in the overlapping regions of melt pools due to the very high melting point of Cr compared to the rest of the elements.

Furthermore, Knieps et al. investigated the effect of powder morphology on in-situ alloying in PBF-LB/M to enable the selection of correct powder feedstock [96]. In this work, a blend of commercial alloy powders and elemental powders was used. It was concluded that a multimodal particle size distribution (PSD) increases packing density and enhances process performance. However, no post-processing heat treatments or microstructural studies were carried out. It should be noted that all the above works were based on developing single-phase FCC-based HEAs. But the concept of in-situ alloying in PBF-LB/M is new and needs more intensive research to particularly reduce the elemental segregation during processing of HEAs. And even though the direct use of elemental powders saves time and money by avoiding pre-alloying by gas atomization there is still the problem of high cost of pure elemental powders and their severe segregation during in-situ alloying.

2.3 Use of scraps to produce arc-melted HEAs

Some of the limiting factors in the manufacturing of HEAs is the cost of raw materials, the subsequent manufacturing/processing cost, and the availability of the raw materials as HEAs contain certain critical materials like Co, Ni, Nb, Mo [97,98]. As a solution to this, there has been recent interest in the use of metal scraps to explore new HEAs by vacuum/arc melting and as an effort to commercialize them. Currently, the intricate extraction methods required to

obtain pure elements for producing HEAs contribute to greenhouse gas emissions and their overall carbon footprint [99,100]. In this regard, Hariharan et al [101] showcased a cost-effective method for producing a near-equimolar CrCuFeMnNi HEA utilizing alloy scraps (304-L stainless steel, Nichrome 80, and electrical wire grade copper). This approach yielded a comparable microstructure to the same HEA composition produced from pure elements. Barnett et al [102] proposed a scrap tolerant alloy design using machine learning techniques with compositional flexibility due to impurities in the scrap, based on the high entropy alloy concept. The suggested alloy range (Fe-Cr-Ni-based) encompassed various alloying elements with considerable compositional variability and exhibited plastic and elastic responses within defined parameters. However, these multi-principal FCC alloys demonstrated low yield strength (<300 MPa). Chao et al [103] utilized scrap metals like stainless steel and superalloys to produce dual-phase (FCC + BCC) $Al_xCoCrFeNi$ based HEAs which exhibited similar microstructure and mechanical properties compared with the same HEAs produced from pure elemental ingots. Notably, using a higher impurity scrap led to significant improvement in strength due to presence of hard phases like Laves but limited the ductility. As a first of its kind, motivated by the exponential growth of electronic waste (e-waste) products, Torralba et al [104] used mixtures of such products from smart phones, laptops or Li-ion batteries with stainless steel and cobalt chrome alloys to produce different possible HEAs with BCC, FCC + BCC, FCC + HCP microstructures. The hardness of the developed HEAs reached upto 500 HV. But further mechanical testing must be done to show the viability of this approach.

Bibliography

[1] B. Cantor, I.T.H. Chang, P. Knight, A.J.B. Vincent, Microstructural development in equiatomic multicomponent alloys, Mater. Sci. Eng. A 375–377 (2004) 213–218. https://doi.org/10.1016/j.msea.2003.10.257.

[2] J.W. Yeh, S.K. Chen, S.J. Lin, J.Y. Gan, T.S. Chin, T.T. Shun, C.H. Tsau, S.Y. Chang, Nanostructured high-entropy alloys with multiple principal elements: Novel alloy design concepts and outcomes, Adv. Eng. Mater. 6 (2004) 299–303. https://doi.org/10.1002/adem.200300567.

[3] J.W. Yeh, Recent progress in high-entropy alloys, Ann. Chim. Sci. Mater. 31 (2006) 633–648. https://doi.org/10.3166/acsm.31.633-648.

[4] J.W. Yeh, Alloy design strategies and future trends in high-entropy alloys, JOM 65 (2013) 1759–1771. https://doi.org/10.1007/s11837-013-0761-6.

[5] D.B. Miracle, J.D. Miller, O.N. Senkov, C. Woodward, M.D. Uchic, J. Tiley, Exploration and development of high entropy alloys for structural applications, Entropy 16 (2014) 494–525. https://doi.org/10.3390/e16010494.

[6] R. Kozak, A. Sologubenko, W. Steurer, Single-phase high-entropy alloys - An overview, Z. Krist. 230 (2015) 55–68. https://doi.org/10.1515/zkri-2014-1739.

[7] F. Otto, Y. Yang, H. Bei, E.P. George, Relative effects of enthalpy and entropy on the phase stability of equiatomic high-entropy alloys, Acta Mater. 61 (2013) 2628–2638. https://doi.org/10.1016/j.actamat.2013.01.042.

[8] Y. Brif, M. Thomas, I. Todd, The use of high-entropy alloys in additive manufacturing, Scr. Mater. 99 (2015) 93–96. https://doi.org/10.1016/j.scriptamat.2014.11.037.

[9] C.J. Tong, Y.L. Chen, S.K. Chen, J.W. Yeh, T.T. Shun, C.H. Tsau, S.J. Lin, S.Y. Chang, Microstructure characterization of AlxCoCrCuFeNi high-entropy alloy system with multiprincipal elements, Metall. Mater. Trans. Phys. Metall. Mater. Sci. 36 (2005) 881–893. https://doi.org/10.1007/s11661-005-0283-0.

[10] T. Cao, L. Ma, L. Wang, J. Zhou, Y. Wang, B. Wang, Y. Xue, High temperature deformation behavior of dual-phase Al0.6CoCrFeNi high-entropy alloys, J. Alloys Compd. 836 (2020) 155305. https://doi.org/10.1016/j.jallcom.2020.155305.

[11] Y. Lu, Y. Dong, H. Jiang, Z. Wang, Z. Cao, S. Guo, T. Wang, T. Li, P.K. Liaw, Promising properties and future trend of eutectic high entropy alloys, Scr. Mater. 187 (2020) 202–209. https://doi.org/10.1016/j.scriptamat.2020.06.022.

[12] M.C. Troparevsky, J.R. Morris, P.R.C. Kent, A.R. Lupini, G.M. Stocks, Criteria for predicting the formation of single-phase high-entropy alloys, Phys. Rev. X 5 (2015) 011041. https://doi.org/10.1103/PhysRevX.5.011041.

[13] J.H. Li, M.H. Tsai, Theories for predicting simple solid solution high-entropy alloys: Classification, accuracy, and important factors impacting accuracy, Scr. Mater. 188 (2020) 80–87. https://doi.org/10.1016/j.scriptamat.2020.06.064.

[14] F.R. de Boer, W.C.M. Mattens, R. Boom, A.R. Miedema, A.K. Niessen, Cohesion in metals. Transition metal alloys, 1 (1988). https://www.osti.gov/etdeweb/biblio/5556327 (accessed May 18, 2024).

[15] X. Yang, Y. Zhang, Prediction of high-entropy stabilized solid-solution in multi-component alloys, Mater. Chem. Phys. 132 (2012) 233–238. https://doi.org/10.1016/j.matchemphys.2011.11.021.

[16] Z. Wang, Y. Huang, Y. Yang, J. Wang, C.T. Liu, Atomic-size effect and solid solubility of multicomponent alloys, Scr. Mater. 94 (2015) 28–31. https://doi.org/10.1016/j.scriptamat.2014.09.010.

[17] A.K. Singh, N. Kumar, A. Dwivedi, A. Subramaniam, A geometrical parameter for the formation of disordered solid solutions in multi-component alloys, Intermetallics 53 (2014) 112–119. https://doi.org/10.1016/j.intermet.2014.04.019.

[18] S. Guo, C. Ng, J. Lu, C.T. Liu, Effect of valence electron concentration on stability of fcc or bcc phase in high entropy alloys, in: J. Appl. Phys., 2011. https://doi.org/10.1063/1.3587228.

[19] S. Guo, C.T. Liu, Phase stability in high entropy alloys: Formation of solid-solution phase or amorphous phase, Prog. Nat. Sci. Mater. Int. 21 (2011) 433–446. https://doi.org/10.1016/S1002-0071(12)60080-X.

[20] A. Takeuchi, A. Inoue, Quantitative evaluation of critical cooling rate for metallic glasses, Mater. Sci. Eng. A 304–306 (2001) 446–451. https://doi.org/10.1016/S0921-5093(00)01446-5.

[21] X. Chen, Q. Wang, Z. Cheng, M. Zhu, H. Zhou, P. Jiang, L. Zhou, Q. Xue, F. Yuan, J. Zhu, X. Wu, E. Ma, Direct observation of chemical short-range order in a medium-entropy alloy, Nat. 2021 5927856 592 (2021) 712–716. https://doi.org/10.1038/s41586-021-03428-z.

[22] R. Zhang, S. Zhao, J. Ding, Y. Chong, T. Jia, C. Ophus, M. Asta, R.O. Ritchie, A.M. Minor, Short-range order and its impact on the CrCoNi medium-entropy alloy, Nature 581 (2020) 283–287. https://doi.org/10.1038/s41586-020-2275-z.

[23] H. Li, H. Zong, S. Li, S. Jin, Y. Chen, M.J. Cabral, B. Chen, Q. Huang, Y. Chen, Y. Ren, K. Yu, S. Han, X. Ding, G. Sha, J. Lian, X. Liao, E. Ma, J. Sun, Uniting tensile ductility with ultrahigh strength via composition undulation, Nature 604 (2022) 273–279. https://doi.org/10.1038/s41586-022-04459-w.

[24] S. Ranganathan, Alloyed pleasures: Multimetallic cocktails, Curr. Sci. 85 (2003).

[25] Y. Lu, Y. Dong, S. Guo, L. Jiang, H. Kang, T. Wang, B. Wen, Z. Wang, J. Jie, Z. Cao, H. Ruan, T. Li, A Promising New Class of High-Temperature Alloys: Eutectic High-Entropy Alloys, Sci. Rep. 4 (2014) 6200. https://doi.org/10.1038/srep06200.

[26] D.B. Miracle, O.N. Senkov, A critical review of high entropy alloys and related concepts, Acta Mater. 122 (2017) 448–511. https://doi.org/10.1016/j.actamat.2016.08.081.

[27] J.M. Torralba, P. Alvaredo, A. García-Junceda, High-entropy alloys fabricated via powder metallurgy. A critical review, Powder Metall. 62 (2019) 84–114. https://doi.org/10.1080/00325899.2019.1584454.

[28] V.H. Hammond, M.A. Atwater, K.A. Darling, H.Q. Nguyen, L.J. Kecskes, Equal-Channel Angular Extrusion of a Low-Density High-Entropy Alloy Produced by High-Energy Cryogenic Mechanical Alloying, (n.d.). https://doi.org/10.1007/s11837-014-1113-x.

[29] X. Yang, S.Y. Chen, J.D. Cotton, Y. Zhang, Phase Stability of Low-Density, Multiprincipal Component Alloys Containing Aluminum, Magnesium, and Lithium, JOM 66 (2014) 2009–2020. https://doi.org/10.1007/s11837-014-1059-z.

[30] K.M. Youssef, A.J. Zaddach, C. Niu, D.L. Irving, C.C. Koch, A Novel Low-Density, High-Hardness, High-entropy Alloy with Close-packed Single-phase Nanocrystalline Structures, Http://Mc.Manuscriptcentral.Com/Tmrl 3 (2014) 95–99. https://doi.org/10.1080/21663831.2014.985855.

[31] W. Li, D. Xie, D. Li, Y. Zhang, Y. Gao, P.K. Liaw, Mechanical behavior of high-entropy alloys, Prog. Mater. Sci. 118 (2021) 100777. https://doi.org/10.1016/J.PMATSCI.2021.100777.

[32] M. Slobodyan, E. Pesterev, A. Markov, Recent advances and outstanding challenges for implementation of high entropy alloys as structural materials, Mater. Today Commun. 36 (2023) 106422. https://doi.org/10.1016/J.MTCOMM.2023.106422.

[33] B. Gludovatz, A. Hohenwarter, D. Catoor, E.H. Chang, E.P. George, R.O. Ritchie, A fracture-resistant high-entropy alloy for cryogenic applications, Science 345 (2014) 1153–1158. https://doi.org/10.1126/science.1254581.

[34] S.Y. Chen, Y. Tong, K.K. Tseng, J.W. Yeh, J.D. Poplawsky, J.G. Wen, M.C. Gao, G. Kim, W. Chen, Y. Ren, R. Feng, W.D. Li, P.K. Liaw, Phase transformations of HfNbTaTiZr high-entropy alloy at intermediate temperatures, Scr. Mater. 158 (2019) 50–56. https://doi.org/10.1016/J.SCRIPTAMAT.2018.08.032.

[35] O.N. Senkov, D. Isheim, D.N. Seidman, A.L. Pilchak, Development of a Refractory High Entropy Superalloy, Entropy 2016 Vol 18 Page 102 18 (2016) 102. https://doi.org/10.3390/E18030102.

[36] R.B. Nair, H.S. Arora, S. Mukherjee, S. Singh, H. Singh, H.S. Grewal, Exceptionally high cavitation erosion and corrosion resistance of a high entropy alloy, Ultrason. Sonochem. 41 (2018) 252–260. https://doi.org/10.1016/J.ULTSONCH.2017.09.044.

[37] X.W. Qiu, Y.P. Zhang, L. He, C.G. Liu, Microstructure and corrosion resistance of AlCrFeCuCo high entropy alloy, J. Alloys Compd. 549 (2013) 195–199. https://doi.org/10.1016/J.JALLCOM.2012.09.091.

[38] W. Wang, J. Wang, H. Yi, W. Qi, Q. Peng, Effect of molybdenum additives on corrosion behavior of (CoCrFeNi)100-xMox high-entropy alloys, Entropy 20 (2018). https://doi.org/10.3390/e20120908.

[39] Q. Wang, A. Amar, C. Jiang, H. Luan, S. Zhao, H. Zhang, G. Le, X. Liu, X. Wang, X. Yang, J. Li, CoCrFeNiMo0.2 high entropy alloy by laser melting deposition: Prospective material for low temperature and corrosion resistant applications, Intermetallics 119 (2020) 106727. https://doi.org/10.1016/J.INTERMET.2020.106727.

[40] X. Chen, Q. Wang, Y. Liang, J. Huang, Y. Peng, K. Wang, J. Kong, CoCrFeNiMo0.2 high entropy alloy with excellent mechanical properties and corrosion resistance prepared by laser-powder bed fusion, Intermetallics 163 (2023) 108082. https://doi.org/10.1016/j.intermet.2023.108082.

[41] D. Miracle, D. Brenner, A. Detor, K. Flores, M. Gao, E. George, C. Haines, K. Knipling, J. Lewandowski, T. Pollock, J.R. Scully, A. Strachan, M. Taheri, M. Titus, A. Yiusefiani, Defining Pathways for Realizing the Revolutionary Potential of High Entropy Alloys, (2021). https://www.tms.org/HEApathways.

[42] A. Kumar, M. Gupta, An insight into evolution of light weight high entropy alloys: A review, Metals 6 (2016) 199. https://doi.org/10.3390/met6090199.

[43] O.N. Senkov, G.B. Wilks, D.B. Miracle, C.P. Chuang, P.K. Liaw, Refractory high-entropy alloys, Intermetallics 18 (2010) 1758–1765. https://doi.org/10.1016/j.intermet.2010.05.014.

[44] C. Suryanarayana, Mechanical Alloying: A Novel Technique to Synthesize Advanced Materials, (2019). https://doi.org/10.34133/2019/4219812.

[45] A. Raza, B. Kang, J. Lee, H.J. Ryu, S.H. Hong, Transition in microstructural and mechanical behavior by reduction of sigma-forming element content in a novel high entropy alloy, Mater. Des. 145 (2018) 11–19. https://doi.org/10.1016/J.MATDES.2018.02.036.

[46] J.B. Fogagnolo, F. Velasco, M.H. Robert, J.M. Torralba, Effect of mechanical alloying on the morphology, microstructure and properties of aluminium matrix composite powders, (n.d.). www.elsevier.com/locate/msea.

[47] S.V. Kumaran, D. Garbiec, J.M. Torralba, Development of High Entropy alloys using field assisted sintering and gas atomized commodity powders as raw materials, Eur. Eur. Powder Metall. Assoc. (n.d.).

[48] J.M. Torralba, S.V. Kumarán, Development of competitive high-entropy alloys using commodity powders, Mater. Lett. 301 (2021) 130202. https://doi.org/10.1016/J.MATLET.2021.130202.

[49] S.V. Kumaran, D. Garbiec, J.M. Torralba, A novel and sustainable method to develop non-equiatomic CoCrFeNiMox high entropy alloys via spark plasma sintering using commercial commodity powders and evaluation of its mechanical behaviour, Mater. Sci. Eng. A 878 (2023) 145207. https://doi.org/10.1016/J.MSEA.2023.145207.

[50] S. Venkatesh Kumaran, J.M. Torralba, Laser Powder Bed Fusion Processing of Low Cost CoCrFeNiMoxNby High Entropy Alloys with Promising High-Temperature Properties via In Situ Alloying Commercial Powders, Metals 14 (2024) 500. https://doi.org/10.3390/met14050500.

[51] S. Venkatesh Kumaran, B. Malladi, E. Hryha, J.M. Torralba, Role of Al mixing to prepare feedstocks for PBF-LB/M to develop new HEAs via in-situ alloying, (2023) 756–766.

[52] S. Yadav, S. Sarkar, A. Aggarwal, A. Kumar, K. Biswas, Wear and mechanical properties of novel (CuCrFeTiZn)100-xPbx high entropy alloy composite via mechanical alloying and spark plasma sintering, Wear 410–411 (2018) 93–109. https://doi.org/10.1016/j.wear.2018.05.023.

[53] B. Blakey-Milner, P. Gradl, G. Snedden, M. Brooks, J. Pitot, E. Lopez, M. Leary, F. Berto, A. Du Plessis, Metal additive manufacturing in aerospace: A review, Mater. Des. 209 (2021) 110008. https://doi.org/10.1016/j.matdes.2021.110008.

[54] C.O. Ujah, D.V.V. Kallon, V.S. Aigbodion, High entropy alloys prepared by spark plasma sintering: Mechanical and thermal properties, Mater. Today Sustain. 25 (2024) 100639. https://doi.org/10.1016/J.MTSUST.2023.100639.

[55] M.I. Makena, M.B. Shongwe, M.M. Ramakokovhu, P.A. Olubambi, Effect of sintering parameters on densification, corrosion and wear behaviour of Ni-50Fe alloy prepared by spark plasma sintering, J. Alloys Compd. 699 (2017) 1166–1179. https://doi.org/10.1016/J.JALLCOM.2016.12.368.

[56] P. Cavaliere, B. Sadeghi, A. Shabani, Spark Plasma Sintering: Process Fundamentals, Spark Plasma Sinter. Mater. (2019) 3–20. https://doi.org/10.1007/978-3-030-05327-7_1.

[57] A. Izci, B. Yavas, I. Antoniac, G. Goller, Investigation of the Effects of Spark Plasma Sintering Parameters on Equiatomic CoCrFeNiMo High Entropy Alloy, J. Mater. Eng. Perform. (2023). https://doi.org/10.1007/s11665-023-08872-8.

[58] M. Vaidya, A. Anupam, J.V. Bharadwaj, C. Srivastava, B.S. Murty, Grain growth kinetics in CoCrFeNi and CoCrFeMnNi high entropy alloys processed by spark plasma sintering, J. Alloys Compd. 791 (2019) 1114–1121. https://doi.org/10.1016/J.JALLCOM.2019.03.341.

[59] W. Ji, W. Wang, H. Wang, J. Zhang, Y. Wang, F. Zhang, Z. Fu, Alloying behavior and novel properties of CoCrFeNiMn high-entropy alloy fabricated by mechanical alloying and spark plasma sintering, Intermetallics 56 (2015) 24–27. https://doi.org/10.1016/J.INTERMET.2014.08.008.

[60] G. Liu, Z. Lu, X. Zhang, Nano-Structure Evolution and Mechanical Properties of AlxCoCrFeNi2.1 (x = 0, 0.3, 0.7, 1.0, 1.3) High-Entropy Alloy Prepared by Mechanical Alloying and Spark Plasma Sintering, Nanomaterials 14 (2024). https://doi.org/10.3390/nano14070641.

[61] P.F. Zhou, D.H. Xiao, Z. Wu, M. Song, Microstructure and mechanical properties of AlCoCrFeNi high entropy alloys produced by spark plasma sintering, Mater. Res. Express 6 (2019) 0865e7. https://doi.org/10.1088/2053-1591/AB2517.

[62] S. Praveen, B.S. Murty, R.S. Kottada, Effect of Molybdenum and Niobium on the Phase Formation and Hardness of Nanocrystalline CoCrFeNi High Entropy Alloys, J. Nanosci. Nanotechnol. 14 (2014) 8106–8109.

[63] Y.B. Peng, W. Zhang, X.L. Mei, H.J. Wang, M.Y. Zhang, L. Wang, X.F. Li, Y. Hu, Microstructures and mechanical properties of FeCoCrNi-Mo High entropy alloys prepared by spark plasma sintering and vacuum hot-pressed sintering, Mater. Today Commun. 24 (2020) 101009. https://doi.org/10.1016/J.MTCOMM.2020.101009.

[64] C. Kenel, N.P.M. Casati, D.C. Dunand, 3D ink-extrusion additive manufacturing of CoCrFeNi high-entropy alloy micro-lattices, (n.d.). https://doi.org/10.1038/s41467-019-08763-4.

[65] D. Karlsson, G. Lindwall, A. Lundbäck, M. Amnebrink, M. Boström, L. Riekehr, M. Schuisky, M. Sahlberg, U. Jansson, Binder jetting of the AlCoCrFeNi alloy, Addit. Manuf. 27 (2019) 72–79. https://doi.org/10.1016/J.ADDMA.2019.02.010.

[66] Z. Xu, Z. Zhu, P. Wang, G.K. Meenashisundaram, S.M.L. Nai, J. Wei, Fabrication of porous CoCrFeMnNi high entropy alloy using binder jetting additive manufacturing, Addit. Manuf. 35 (2020) 101441. https://doi.org/10.1016/J.ADDMA.2020.101441.

[67] M. Ziaee, N.B. Crane, Binder jetting: A review of process, materials, and methods, Addit. Manuf. 28 (2019) 781–801. https://doi.org/10.1016/J.ADDMA.2019.05.031.

[68] C. Han, Q. Fang, Y. Shi, S.B. Tor, C.K. Chua, K. Zhou, Recent Advances on High-Entropy Alloys for 3D Printing, Adv. Mater. 32 (2020). https://doi.org/10.1002/adma.201903855.

[69] C.Y. Yap, C.K. Chua, Z.L. Dong, Z.H. Liu, D.Q. Zhang, L.E. Loh, S.L. Sing, Review of selective laser melting: Materials and applications, Appl. Phys. Rev. 2 (2015). https://doi.org/10.1063/1.4935926.

[70] M.Y. Shaheen, A.R. Thornton, S. Luding, T. Weinhart, The influence of material and process parameters on powder spreading in additive manufacturing, Powder Technol. 383 (2021) 564–583. https://doi.org/10.1016/J.POWTEC.2021.01.058.

[71] N.T. Aboulkhair, N.M. Everitt, I. Ashcroft, C. Tuck, Reducing porosity in AlSi10Mg parts processed by selective laser melting, Addit. Manuf. 1–4 (2014) 77–86. https://doi.org/10.1016/J.ADDMA.2014.08.001.

[72] R. Li, P. Niu, T. Yuan, P. Cao, C. Chen, K. Zhou, Selective laser melting of an equiatomic CoCrFeMnNi high-entropy alloy: Processability, non-equilibrium microstructure and mechanical property, J. Alloys Compd. 746 (2018) 125–134. https://doi.org/10.1016/J.JALLCOM.2018.02.298.

[73] J.Y. He, W.H. Liu, H. Wang, Y. Wu, X.J. Liu, T.G. Nieh, Z.P. Lu, Effects of Al addition on structural evolution and tensile properties of the FeCoNiCrMn high-entropy alloy system, Acta Mater. 62 (2014) 105–113. https://doi.org/10.1016/J.ACTAMAT.2013.09.037.

[74] W. Li, Y.Y. Huang, Z.H. Xie, H. Chen, W. Li, B. Liu, B. Wang, Mechanical property and cellular structure of an additive manufactured FeCoNiCrMo0.2 high-entropy alloy at

high-velocity deformation, J. Mater. Sci. Technol. 139 (2023) 156–166. https://doi.org/10.1016/j.jmst.2022.08.013.

[75] A. Fu, Z. Xie, J. Wang, Y. Cao, B. Wang, J. Li, Q. Fang, X. Li, B. Liu, Y. Liu, Controlling of cellular substructure and its effect on mechanical properties of FeCoCrNiMo0.2 high entropy alloy fabricated by selective laser melting, Mater. Sci. Eng. A 901 (2024) 146547. https://doi.org/10.1016/J.MSEA.2024.146547.

[76] D. Lin, L. Xu, H. Jing, Y. Han, L. Zhao, F. Minami, Effects of annealing on the structure and mechanical properties of FeCoCrNi high-entropy alloy fabricated via selective laser melting, Addit. Manuf. 32 (2020) 101058. https://doi.org/10.1016/j.addma.2020.101058.

[77] Y.K. Kim, J. Choe, K.A. Lee, Selective laser melted equiatomic CoCrFeMnNi high-entropy alloy: Microstructure, anisotropic mechanical response, and multiple strengthening mechanism, J. Alloys Compd. 805 (2019) 680–691. https://doi.org/10.1016/J.JALLCOM.2019.07.106.

[78] R. Zhou, Y. Liu, C. Zhou, S. Li, W. Wu, M. Song, B. Liu, X. Liang, P.K. Liaw, Microstructures and mechanical properties of C-containing FeCoCrNi high-entropy alloy fabricated by selective laser melting, Intermetallics 94 (2018) 165–171. https://doi.org/10.1016/J.INTERMET.2018.01.002.

[79] C. Zhang, J. Zhu, H. Zheng, H. Li, S. Liu, G.J. Cheng, A review on microstructures and properties of high entropy alloys manufactured by selective laser melting, Int. J. Extreme Manuf. 2 (2020) 21. https://doi.org/10.1088/2631-7990/ab9ead.

[80] J. Li, X. Zhou, M. Brochu, N. Provatas, Y.F. Zhao, Solidification microstructure simulation of Ti-6Al-4V in metal additive manufacturing: A review, Addit. Manuf. 31 (2020) 100989. https://doi.org/10.1016/J.ADDMA.2019.100989.

[81] P.F. Zhou, D.H. Xiao, Z. Wu, X.Q. Ou, Al0.5FeCoCrNi high entropy alloy prepared by selective laser melting with gas-atomized pre-alloy powders, Mater. Sci. Eng. A 739 (2019) 86–89. https://doi.org/10.1016/J.MSEA.2018.10.035.

[82] P.D. Niu, R.D. Li, T.C. Yuan, S.Y. Zhu, C. Chen, M.B. Wang, L. Huang, Microstructures and properties of an equimolar AlCoCrFeNi high entropy alloy printed by selective laser melting, Intermetallics 104 (2019) 24–32. https://doi.org/10.1016/J.INTERMET.2018.10.018.

[83] D. Karlsson, A. Marshal, F. Johansson, M. Schuisky, M. Sahlberg, J.M. Schneider, U. Jansson, Elemental segregation in an AlCoCrFeNi high-entropy alloy – A comparison between selective laser melting and induction melting, J. Alloys Compd. 784 (2019) 195–203. https://doi.org/10.1016/J.JALLCOM.2018.12.267.

[84] K.S. Lee, B. Bae, J. Kang, K.R. Lim, Y.S. Na, Multi-phase refining of an AlCoCrFeNi high entropy alloy by hot compression, Mater. Lett. 198 (2017) 81–84. https://doi.org/10.1016/J.MATLET.2017.03.181.

[85] S. Luo, P. Gao, H. Yu, J. Yang, Z. Wang, X. Zeng, Selective laser melting of an equiatomic AlCrCuFeNi high-entropy alloy: Processability, non-equilibrium microstructure and mechanical behavior, J. Alloys Compd. 771 (2019) 387–397. https://doi.org/10.1016/J.JALLCOM.2018.08.290.

[86] Y. Wang, R. Li, P. Niu, Z. Zhang, T. Yuan, J. Yuan, K. Li, Microstructures and properties of equimolar AlCoCrCuFeNi high-entropy alloy additively manufactured by selective laser melting, Intermetallics 120 (2020) 106746. https://doi.org/10.1016/J.INTERMET.2020.106746.

[87] M. Zhang, X. Zhou, D. Wang, W. Zhu, J. Li, Y.F. Zhao, AlCoCuFeNi high-entropy alloy with tailored microstructure and outstanding compressive properties fabricated via selective laser melting with heat treatment, Mater. Sci. Eng. A 743 (2019) 773–784. https://doi.org/10.1016/J.MSEA.2018.11.118.

[88] D. Vogiatzief, A. Evirgen, S. Gein, V.R. Molina, A. Weisheit, M. Pedersen, Laser Powder Bed Fusion and Heat Treatment of an AlCrFe2Ni2 High Entropy Alloy, Front. Mater. 7 (2020) 1–12. https://doi.org/10.3389/fmats.2020.00248.

[89] D. Vogiatzief, A. Evirgen, M. Pedersen, U. Hecht, Laser powder bed fusion of an Al-Cr-Fe-Ni high-entropy alloy produced by blending of prealloyed and elemental powder: Process parameters, microstructures and mechanical properties, J. Alloys Compd. 918 (2022) 165658. https://doi.org/10.1016/J.JALLCOM.2022.165658.

[90] P. Niu, R. Li, Z. Fan, P. Cao, D. Zheng, M. Wang, C. Deng, T. Yuan, Inhibiting cracking and improving strength for additive manufactured AlxCoCrFeNi high entropy alloy via changing crystal structure from BCC-to-FCC, Addit. Manuf. 71 (2023) 103584. https://doi.org/10.1016/j.addma.2023.103584.

[91] S. Luo, C. Zhao, Y. Su, Q. Liu, Z. Wang, Selective laser melting of dual phase AlCrCuFeNix high entropy alloys: Formability, heterogeneous microstructures and deformation mechanisms, Addit. Manuf. 31 (2020) 100925. https://doi.org/10.1016/j.addma.2019.100925.

[92] M. Simonelli, N.T. Aboulkhair, P. Cohen, J.W. Murray, A.T. Clare, C. Tuck, R.J.M. Hague, A comparison of Ti-6Al-4V in-situ alloying in Selective Laser Melting using simply-mixed and satellited powder blend feedstocks, Mater. Charact. 143 (2018) 118–126. https://doi.org/10.1016/j.matchar.2018.05.039.

[93] S. Ewald, F. Kies, S. Hermsen, M. Voshage, C. Haase, J.H. Schleifenbaum, Rapid Alloy Development of Extremely High-Alloyed Metals Using Powder Blends in Laser Powder Bed Fusion, Mater. 2019 Vol 12 Page 1706 12 (2019) 1706. https://doi.org/10.3390/MA12101706.

[94] P. Chen, S. Li, Y. Zhou, M. Yan, M.M. Attallah, Fabricating CoCrFeMnNi high entropy alloy via selective laser melting in-situ alloying, J. Mater. Sci. Technol. 43 (2020) 40–43. https://doi.org/10.1016/J.JMST.2020.01.002.

[95] M. Sun, B. Wang, J. Zhang, B. Lu, Intermetallics In-situ synthesis of CoCrFeMnNi high-entropy alloy by selective laser melting, Intermetallics 156 (2023) 107866. https://doi.org/10.1016/j.intermet.2023.107866.

[96] M.S. Knieps, W.J. Reynolds, J. Dejaune, A.T. Clare, A. Evirgen, In-situ alloying in powder bed fusion: the role of powder morphology, Mater. Sci. Eng. A (2021) 140849. https://doi.org/10.1016/j.msea.2021.140849.

[97] Radley-Gardner et al. - 2016 - Fundamental Texts On European Private Law.pdf, (n.d.).

[98] European Commission. Joint Research Centre., Supply chain analysis and material demand forecast in strategic technologies and sectors in the EU: a foresight study., Publications Office, LU, 2023. https://data.europa.eu/doi/10.2760/386650 (accessed May 18, 2024).

[99] D. Raabe, C.C. Tasan, E.A. Olivetti, Strategies for improving the sustainability of structural metals, Nature 575 (2019) 64–74. https://doi.org/10.1038/s41586-019-1702-5.

[100] L. Montanelli, E.R. Homer, E. Olivetti, Factors to Consider When Designing Aluminium Alloys for Increased Scrap Usage, in: A. Lazou, K. Daehn, C. Fleuriault, M. Gökelma, E. Olivetti, C. Meskers (Eds.), REWAS 2022 Dev. Tomorrow's Tech. Cycles Vol. I, Springer International Publishing, Cham, 2022: pp. 465–473. https://doi.org/10.1007/978-3-030-92563-5_48.

[101] K. Hariharan, K. Sivaprasad, Sustainable Low-Cost Method for Production of High-Entropy Alloys from Alloy Scraps, J. Sustain. Metall. (2022). https://doi.org/10.1007/s40831-022-00523-x.

[102] M.R. Barnett, M. Senadeera, D. Fabijanic, K.F. Shamlaye, J. Joseph, S.R. Kada, S. Rana, S. Gupta, S. Venkatesh, A scrap-tolerant alloying concept based on high entropy alloys, Acta Mater. 200 (2020) 735–744. https://doi.org/10.1016/j.actamat.2020.09.027.

[103] Q. Chao, J. Joseph, M. Annasamy, P. Hodgson, M.R. Barnett, D. Fabijanic, AlxCoCrFeNi high entropy alloys from metal scrap: Microstructure and mechanical

properties, J. Alloys Compd. 976 (2024) 173002. https://doi.org/10.1016/j.jallcom.2023.173002.

[104] J. Torralba, D. Iriarte, D. Tourret, J. Meza, Using multicomponent recycled electronic waste alloys to produce high entropy alloys, Intermetallics 164 (2024) 108128. https://doi.org/10.1016/j.intermet.2023.108128.

CHAPTER 3

Experimental procedures

This thesis involved the fabrication of materials using three distinct methods: field-assisted hot pressing (FAHP), spark plasma sintering (SPS), and powder bed fusion with laser beam for metals (PBF-LB/M). The subsequent paragraphs will provide a comprehensive overview of the materials and methodologies employed in this study.

3.1 Materials

The commercial commodity powders used for the FAHP and SPS processes were Ni625, 316L, CoCrF75, Invar, and Fe49Ni. The CoCrF75 powders were sourced from VDM Metals (Germany), while the remaining powders were obtained from Sandvik Osprey (UK). Detailed information regarding the average particle size and composition of these powders can be found in Table 3.1.

TABLE 3.1: PARTICLE SIZE AND CHEMICAL COMPOSITION OF THE POWDERS USED

		wt. (%)				
Alloy	**Size (d50) (µm)**	**Ni**	**Fe**	**Cr**	**Mo**	**Co**
Ni625	60	61.54	5.35	25.26	5.6	-
INVAR 36	3.8	34.8	65.14	-	-	-
CoCrF75	30	0.51	0.8	32.57	3.72	62.41
316L	11.5	11.82	67.77	18.9	1.51	-
Fe49Ni	15	47.76	52.24	-	-	-

For the FAHP and SPS processes, three different alloys were designed, labelled as C1, C2 and C3 by selecting and mixing the available commodity powders in appropriate proportions. The aim was to obtain a reasonably equiatomic CoCrFeNi base HEA alloyed

with Mo and Nb. The proportion of each powder mixed and the final composition of the developed HEAs are shown in Table 3.2.

TABLE 3.2**:** PROPOSED MIXES OF COMMODITY POWDERS USED TO DEVELOP DIFFERENT POSSIBLE HEAs VIA FAHP

Alloy	wt. %					at. %				
	Ni625	**INVAR 36**	**CoCrF75**	**316L**	**Fe49Ni**	**Ni**	**Fe**	**Cr**	**Mo**	**Co**
C1	20	38	42	-	-	25.21	26.92	20.7	1.61	25.56
C2	28	-	38	34	-	21.01	25.03	28.56	2.1	23.28
C3	-	-	48	-	52	24.45	28.22	17.2	1.06	29.07

The commercial powders used for PBF-LB/M were Ni625, Invar36, CoCrF75, and 316L. In this case, Ni625 powders were provided by VDM Metals (Germany), Invar36 by Sandvik Osprey (UK), CoCrF75 by MIMETE (Italy), and 316L by Carpenter additive (UK). The d50 and the composition of the powders are given in Table 3.3. The particle size of the powders ranged from 15 - 53µm.

TABLE 3.3: SIZE AND COMPOSITION OF THE VARIOUS COMMODITY POWDERS USED IN PBF-LB/M

Alloy	Size (d50) (µm)	Role	wt. (%)					
			Ni	**Fe**	**Cr**	**Mo**	**Co**	**Nb**
Ni625	32	Source of Ni, Cr, Fe, Mo	56.87	5	22	10	1	3.8
INVAR 36	29.9	Source of Fe and Ni	36	63.28	-	-	-	-
CoCrF75	30	Source of Co, Cr, and Mo	0.41	0.75	30	7	60.41	-
316L	31.6	Source of Fe, Cr, Ni, Mo	12.55	65.85	17.68	2.33	-	-

Two different HEAs, labelled as C1 and C2, were designed by simply mixing the commodity powders and the proportion of each powders mixed and the corresponding composition of the final HEAs is shown in Table 3.4.

TABLE 3.4: MIXES OF COMMODITY POWDERS USED TO DEVELOP DIFFERENT POSSIBLE HEAs BY PBF-LB/M

Alloy	wt. %				at. %					
	Ni625	INVAR 36	CoCrF75	316L	Ni	Fe	Cr	Mo	Co	Nb
C1	20	38	42	-	25.2	26.6	19.2	3	25.45	1.65
C2	30	-	37	33	21.4	24.8	26.62	3.9	22.6	2.5

To explore alternative materials with dual phases (FCC+BCC), Aluminum (Al) was introduced into the C1 alloy. This research was conducted at the Center for Additive Manufacturing – Metals (CAM2), Chalmers University of Technology, located in Gothenburg, Sweden. The same commercial powders mentioned in Section 3.3.1 were used along with Al powders which were supplied by Toyal Europe. The pure Al powders exhibited a finer particle size distribution (PSD) with a d50 of 20µm and d90 of 44µm. Three distinct compositions were formulated to examine the influence of Al content, specifically 0%, 3.5%, and 4.5% by weight. The combination of powders utilized is outlined in Table 3.5. These powders were homogeneously mixed using a roller mixer for one hour.

TABLE 3.5: PROPOSED MIXES OF COMMODITY AND ALUMINIUM POWDERS USED TO DEVELOP THE HEAS

Alloy	wt. % of powders				at. % of final HEA						
	Ni625	INVAR 36	CoCrF75	Al	Ni	Fe	Cr	Mo	Co	Nb	Al
0Al	20	38	42	0	25.2	26.6	19.2	3	25.45	1.65	0
3.5Al	20	35	41.5	3.5	23.2	23.69	18.27	2.88	24.18	0.46	7.32
4.5Al	20	34	41.5	4.5	22.6	22.8	16.85	2.85	23.92	0.46	9.3

All the powder particles were examined using a FEGSEM (FEI TENEO) for various features, including particle shape and possible satellites. The powders were sprinkled on carbon tape and directly observed under the Scanning electron microscope (SEM). The particle size distribution of powders was measured by a Laser Diffractometer (Mastersizer 2000) following the ISO 13320:2009.

3.2 Processing methods

3.2.1 Field assisted hot pressing (FAHP)

The powders were mixed in a roller mixer in appropriate proportion, as shown in TABLE 3.2 and consolidated via field-assisted hot pressing (FAHP) in Gleeble 3800 (Dynamic Systems Inc, USA).

Gleeble 3800 is a thermal-mechanical physical simulation system capable of exerting as much as 20 tons of static force, heating specimens at a rate exceeding 10,000°C/s, and achieving stroke rates up to 2,000 mm/s. It uses direct resistance heating to heat the powders placed inside the graphite die. The powders were added to a cylindrical graphite die surrounded with W foil to avoid carbon diffusion to the powders. The die was closed at both ends by two graphite punches separated by a W foil between the powders and punches as shown in Both materials, graphite, and tungsten, are excellent electrical conductors in order to heat the die with a current that heats the powder by Joule effect.

The consolidation process was carried out in an argon atmosphere controlling temperature and load. The temperature was achieved by continuous low frequency alternating current (a.c.). It was measured by K type thermocouples placed in the punch and matrix as shown in Fig. 3.1(a), respectively, which were glued with a high temperature cement. The die had a cylindrical shape with 10 mm of diameter.

The parameters used for FAHP are shown in Table 3.6. These parameters were chosen based on the previous works to obtain PMHEAs as reviewed by Torralba et al [1]. The heating rate was 100°C/min and the load was applied in two steps. First, a load of 7 MPa was applied till the temperature reached 400°C. Then, the load was increased to 50 MPa before rising the temperature to 1000°C. After 15 minutes of dwell time, the temperature was cut off while the load was maintained as the sample underwent cooling under Ar atmosphere. The thermo-mechanical cycle used for the FAHP is shown in Fig. 3.1 (b).

TABLE 3.6: PARAMETERS FOR FAHP

Temperature (°C)	Pressure (MPa)	Dwell time (mins)
1000	50	15

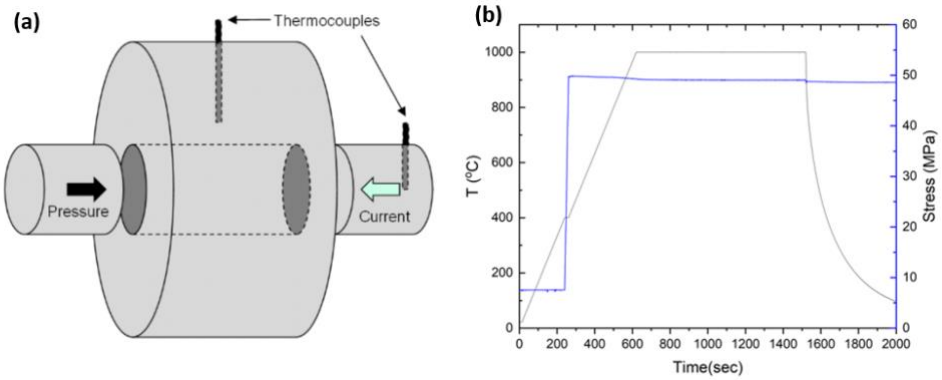

Fig. 3.1: (a) Schematic of a graphite die used in FAHP consolidation and (b) the thermo-mechanical cycle of FAHP process

3.2.2 Spark plasma sintering (SPS)

The SPS consolidation was carried out in HP D 25/3 SPS furnace (FCT system, Germany) at Siec Badawcza Lukasiewicz, Poznan, Poland. The temperature was measured by a pyrometer, which is more sensitive and accurate than a thermocouple. The die had a cylindrical shape with 60 mm diameter and 15 mm height. SPS is similar to FAHP except that in SPS, a pulsed DC current is applied unlike a continuous DC field in FAHP.

The sintering and consolidation were carried out at two different temperatures for each alloy and the parameters are shown in Table 3.7. Initially, based on the previous works in the literature [1], the temperatures were chosen to be 1000°C and 1250°C. When C1 was being consolidated, a liquid phase was formed at around 1140°C and removed from the tools due to which the temperature for C2 and C3 was reduced to 1100°C.

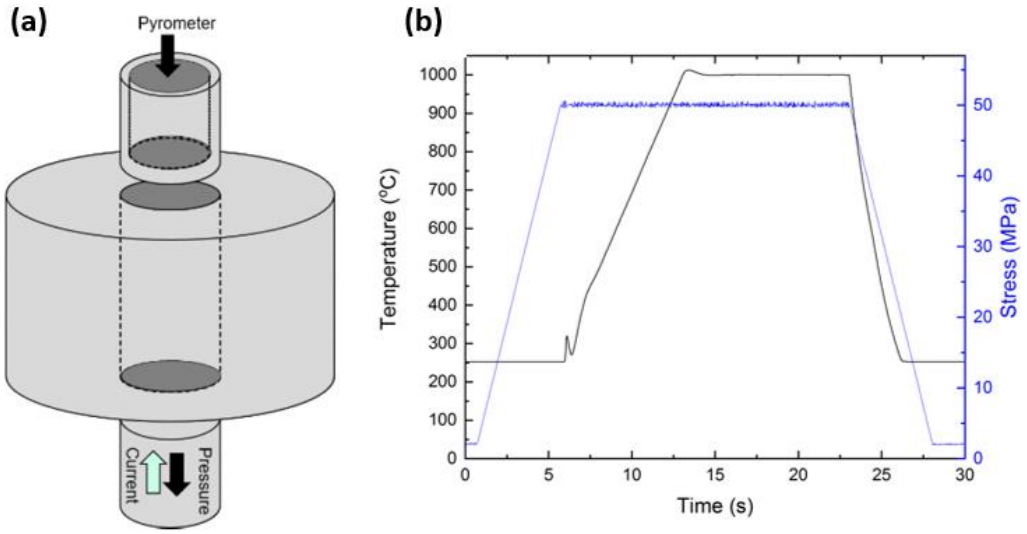

Fig. 3.2: (a) Schematic of a graphite die used in the SPS process and (b) the thermo-mechanical cycle used

TABLE 3.7: PARAMETERS USED FOR SPARK PLASMA SINTERING

Temperature (°C)	**Pressure (MPa)**	**Dwell time (mins)**
1000	50	10
1100 (1250 for C1)	50	10

3.2.3 Powder bed fusion – laser beam/metals (PBF-LB/M)

The fabrication of the bulk samples of C1 and C2 was carried out on a selective laser melting (SLM) system AM 400 with Reduced Build Volume (RBV) from Renishaw, UK. The system has a build volume of 250 mm x 250 mm x 300 mm, with the RBV being 78 mm x 78 mm x 55 mm. The system utilizes a pulsating Yb fibre laser to melt the metal powders. It comprises of a 400 W optical system, which gives out a focused beam of diameter 70 µm. Since it uses a pulsed wave emission, the scanning speed of the laser is calculated in terms of point distance and exposure time. The material of the building plate utilized is S 275 steel.

Choosing appropriate process parameters is critical for any fabrication processes. Based on the literature review of parameters used in SLM for processing commercially available pre-alloyed powders, process parameter optimization for C1 and C2 mix was carried out using a trial-and-error approach starting from a wide range of volumetric energy density (VED). Laser power values ranged from 100 – 370W, hatch distance from 50 - 80µm,

and scan speed from 500 – 1500 mm/s. Cuboidal shapes with dimensions 7 x 7 x 3 mm were printed with a meander scan strategy with 67° rotation per layer and a layer thickness of 30µm. Based on the porosity analysis using an optical microscope, a second trial of fabrication was performed by narrowing the process parameter window used previously. The range of laser power was narrowed down to 150 – 200W and scanning speed to 500 – 1000 mm/s.

In the case of the C1 alloy plus aluminum powder, the samples were manufactured in an EOS M100 machine equipped with a 200W Yb-fiber laser with a spot size of 40µm at Centre for additive manufacturing of metals, Göteburg, Sweden. The build chamber was purged with argon gas to reduce the amount of oxygen to 1000 ppm before process starts. Test samples were printed with a stripe scanning strategy with 5 mm stripe width and with a 0.1 mm overlap with adjacent stripes and a 67o scan rotation between the subsequent layers as shown in Fig. 3.3. Design of experiments (DOE) were carried out using the software JMP pro version 17 by SAS by varying the laser power from 110 - 170W, scan speed from 600 – 1200 mm/s, hatch distance from 0.06 – 0.1 mm and with a constant layer thickness of 30 µm. Based on the porosity percentage of the printed samples, a second DoE was performed by narrowing the process parameter window. In the end, ten cubes of 7mm were built for each material (0Al, 3.5Al, 4.5Al) and for each DoE.

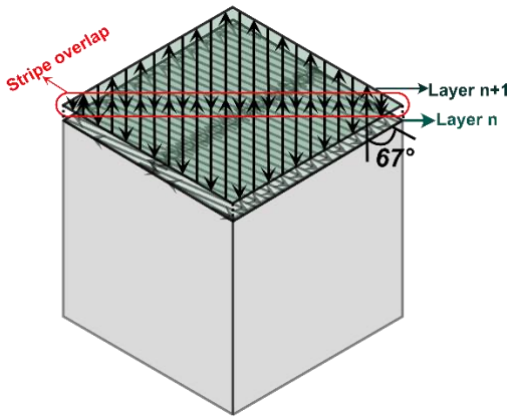

Fig. 3.3: Schematic of stripe scan strategy used in the PBF-LB/M process with a 67° rotation between layers

To analyze these materials, the printed samples were cut from the build plate using a disc-cutting machine and cut longitudinally across the build direction to study the microstructure.

3.3 Heat treatments

To homogenize the microstructure obtained from FAHP and SPS, the samples were subjected to annealing at different temperatures and durations for optimization. In the end, an annealing treatment of 1200°C for 24 hours was chosen as the homogenization treatment.

The heat treatment was carried out in a metal muffle furnace (Carbolite CWF 13/23), equipped with all the protective accessories. To avoid oxidation, all the samples were vacuum encapsulated in a glass tube.

3.4 Characterization

3.4.1 Density measurement

The relative density was calculated by taking images from optical microscope and measuring the porosity using ImageJ software.

3.4.2 Structural and microstructural characterization

3.4.2.1 Metallography

The consolidated samples were manually ground using SiC papers with grit sizes of 320, 600, 1200, and 2500. Subsequently, the samples were manually polished in a Metaserv 250 polishing machine with diamond pastes of 3µm and 1µm and with a final colloidal silica polishing solution (OPS) of size 40nm to achieve a mirror surface revealing the microstructure. In the case of the PBF-LB/M samples, to observe the melt pools, the polished samples were etched in an Aqua regia solution (HNO_3: HCl: H_2O = 1:3:2) for 10 seconds.

3.4.2.2 Scanning electron microscope

A dual beam Scanning Electron Microscope (SEM), Helios Nanolab 600i, equipped with Electron Backscatter Diffraction (EBSD) device and Energy dispersive spectrometer (EDS), was used to observe the microstructure of the samples. The elemental distribution was analyzed by EDS, and the orientation and phases present in the samples were analyzed by EBSD.

3.4.2.3 X-Ray diffraction

To get to know the possible phases present, X-Ray diffraction was carried out on the as-sintered, as-printed, and heat-treated samples. A PANalytical diffractometer with Cu Kα1 radiation source was employed for diffraction. A graph indicating the intensity per counts versus 2θ positions was recorded. Finally, the XRD peaks were analyzed using HighScore plus software.

3.4.3 Mechanical properties

3.4.3.1 Hardness

Both micro and macro-hardness tests were carried out on the as-sintered and heat-treated samples using a Vicker's hardness testing equipment with a load of 0.1 kgf for micro-hardness and 1 kgf for macro-hardness for a period of 25s. The indenter was a quadrilateral diamond pyramid one. After the indentation was made, the diagonals were measured to calculate the final hardness using (3.1).

$$HV = \frac{1.8514F}{d^2} \tag{3.1}$$

where F is the force in kgf and d is the average diagonals of the indentations.

3.4.3.2 Micro-tensile test

Micro-tensile tests of the SPS samples were carried out at room temperature using Kammrath and Weiss GmbH micro-tensile machine which can also be placed inside an SEM for in-situ testing. The tensile speed was 10^{-3} s^{-1} and the samples were machined to a flat dog-bone shape with the dimensions shown in Fig. 3.4. For each material, two tests were carried out and the average was calculated before plotting the stress-strain curve.

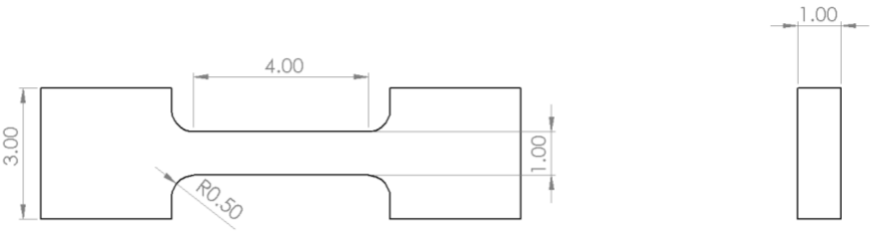

Fig. 3.4: Dimensions of the micro-tensile test sample (in mm)

3.4.3.3 Tensile test

Tensile tests at room and high temperatures were carried out for the samples printed using PBF-LB/M. Solid blocks of samples were printed with the optimized parameters from which flat dog-bone-shaped samples were machined with a wire arc discharge machining. The dimensions of the tensile sample are shown in Fig. 3.5. The tensile tests were performed at room temperature in an Instron 5966 machine at a strain rate of 10^{-3}/s. The high-temperature tensile tests were carried out in a Universal testing machine MTS 810, according to ASTM E21-20 standard at temperatures of 700°C, 800°C, and 900°C. The yield strength was then calculated by 0.2% offset method.

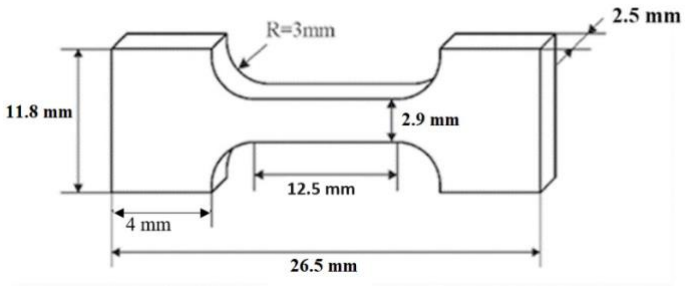

Fig. 3.5: Dimensions of the tensile samples machined from a block printed using PBF-LB/M

3.4.3.4 Hot compression test

For SPS samples, compression tests were performed on both the as-sintered and heat-treated samples at room temperature and at temperatures of 600°C, 700°C, and 750°C in an Instron 3384 machine equipped with a 30kN load cell. The sample dimensions were 2 x 2 x 4 mm. For each material, three tests were performed at a strain rate of 10^{-3}/s and the average was calculated.

CHAPTER 4

Results & discussion

This chapter presents and discusses the results obtained during the course of the PhD research, by linking the contributions from five publications [1–5]. All the publications under the purview of this thesis are attached in the Appendix.

4.1 Fabricating HEAs through Field-Assisted Hot Pressing and Spark Plasma Sintering with Blended Commodity Powders

This section is an extended version of our work presented in Ref. [1–3] (Ref. 1 – Paper 1 in the appendix, Ref. 2 – Paper 2 in the appendix, Ref. 3 – Paper 3 in the appendix). [1,2] deal with the development of HEAs via field assisted hot pressing whereas Ref. [3] deals with processing HEAs via spark plasma sintering.

Processes like FAHP and SPS are a simultaneous compaction and sintering process which falls under the broad category of electric current activated/assisted sintering (ECAS) technologies. The subcategories differ with the type of current that flows through the punches and die, with FAHP utilizing a continuous current and SPS with pulsed doses of current. It enables enhanced densification by superposition of external pressure and direct heating by applying an electric field. Activation of sintering by a combination of pressure and temperature allows high densification with shorter sintering times and higher heating and cooling rates than in conventional sintering situations such as hot pressing or hot isostatic pressing. These shorter sintering times and higher heating and cooling rates result in a clear inhibition of grain growth and a reduction of possible undesired interactions at grain boundaries.

In this work, FAHP was used as a prototype to study the feasibility of using a mix of commodity powders to develop new HEAs. Later after confirming the feasibility, bulk samples of HEAs were manufactured by SPS with different process parameters and mechanical properties were tested including tensile and hot compression tests. The basic methodology hypothesized is shown in Fig. 4.1, where the powders are expected to be sintered well with good densities and later annealed to result in a homogenous microstructure.

The methodology, thermodynamic predictions, powder morphology, and structural characterization are detailed, shedding light on the transformative potential of these fabrication techniques for advanced material development in the following sections.

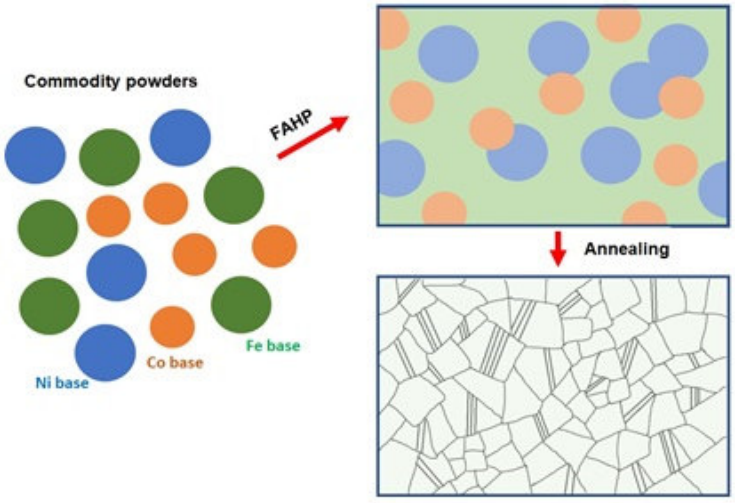

Fig. 4.1: Proposed methodology [1]

4.1.1 Thermodynamic predictions

There are certain empirical rules based on thermodynamics for the phase formation prediction in HEAs which was discussed in Section 2.1.2. The calculated values of the parameters for C1, C2 and C3 alloys along with the threshold values for single solid solution phase formation are shown in Table 4.1. All the alloys fall within the threshold, which shows that the designed composition should result in a solid solution phase. The superimposed effect of $\Delta H_{mix,}$ δ and ΔS_{mix} on phase stability of high entropy alloys is shown in Fig. 4.2 (a), where the dash-dotted line marks the boundary for the solid solution phases to form. Clearly, our proposed alloys fall

well within this region. In Fig. 4.2 (b), the valence electron concentration (VEC) of various HEA systems is plotted which predicts the formation of phases, classified into BCC, FCC + BCC, and FCC regions. C1 and C2 alloy fall in the FCC region whereas C2 is close to the FCC + BCC region.

Since the compositions were predicted to yield a solid solution phase, i.e., a high entropy alloy, the fabrication of all the three alloys were carried out, first with FAHP and then with SPS.

TABLE 4.1: DIFFERENT ASSESSMENT PARAMETERS FOR HEAS

	Obtained value				
Parameter	**C1**	**C2**	**C3**	**Threshold values**	**Reference**
ΔS_{mix}^{conf}	1.44R	1.48R	1.43R	> 1.61R	[6]
ΔH_{mix} (kJ/Mol)	-6.3727	-6.2822	-6.636	$-11.6<\Delta H_{mix}<3.2$	[7]
Ω/1000	3.52	3.7	3.3	≥1.1	[8]
100δ	1.69	2.24	1.85	<6.6	[8]
γ	1.1324	1.1333	1.1328	<1,175	[9]
Λ	4.19	9.58	9.21	>0.96	[10]
VEC	8.32	7.92	8.38	>8 for FCC	[11]

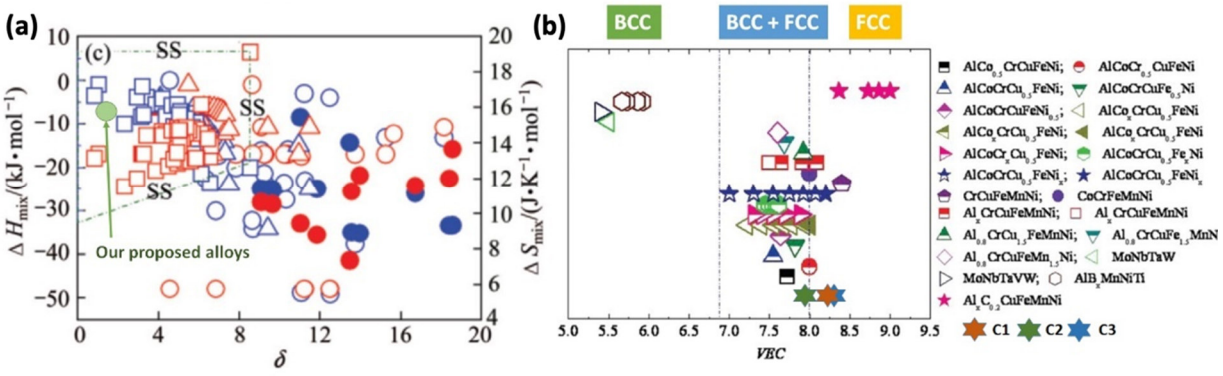

Fig. 4.2: (a) Prediction for forming a single solid solution based on thermodynamical values and the δ parameter [11], and (b) Prediction for forming BCC or FCC phases based on the VEC [12] in C1, C2 and C3 alloys

4.1.2 Powder morphology

The morphology of the C1, C2, and C3 powder mixes are shown in Fig. 4.3 (a). In C1, as shown in Fig. 4.3 (a) and (b), Ni 625 consists of an irregular shape with a d50 of 60µm, which is much larger than the other powder particles. These powders are relatively spherical, but due to a non-

optimized gas atomization process, it has led to clusters of satellites. As seen in Fig. 4.3 (d), the 316L powder particles in the C2 mix are adhered to each other forming large agglomerates. This is attributed to the smaller particle size distribution (PSD) of 316L. In C3, the Fe49Ni particles are highly irregular and adhered to each other and to the CoCrF75 powder particles as shown in Fig. 4.3 (e).

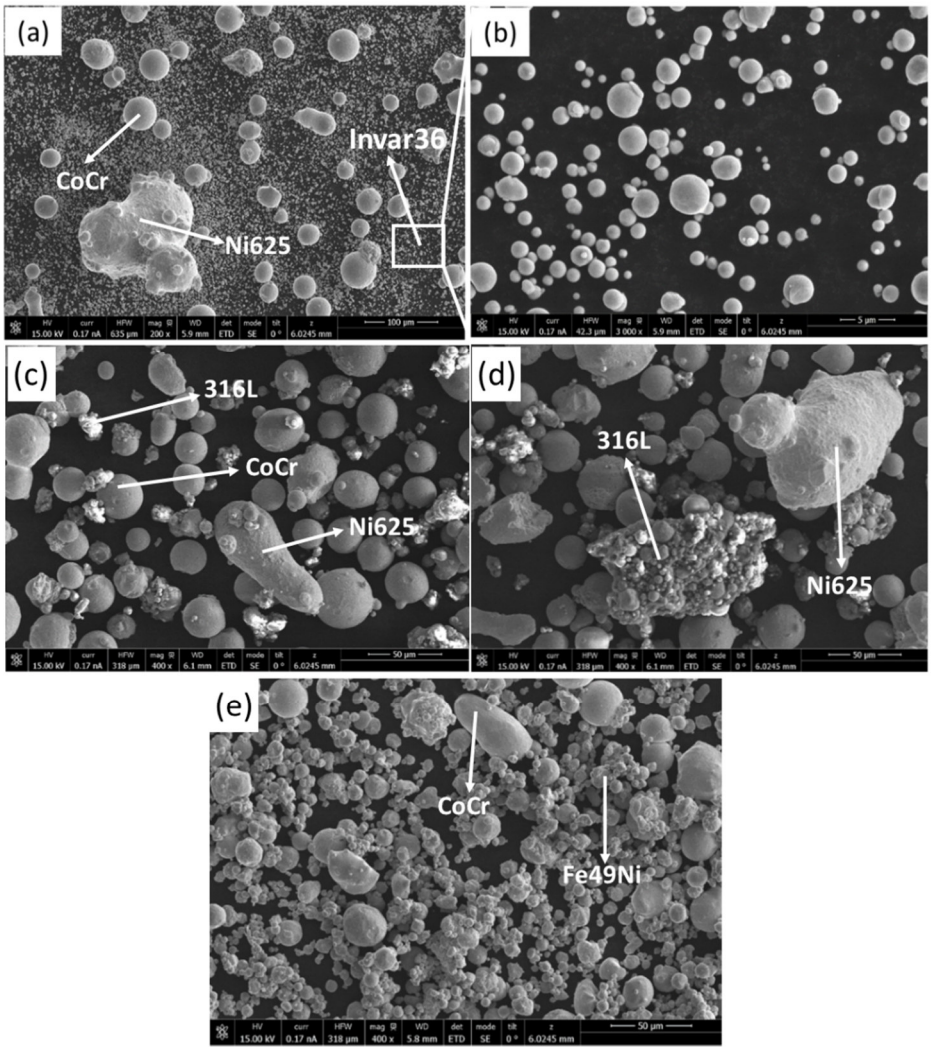

Fig. 4.3: SEM images showing the powder morphology of (a) C1 mix; (b) magnified SEM image of Invar36 powders in the inset; (c) and (d) powder morphology of C2 mix; (e) powder morphology of C3 mix [3]

4.1.3 Field assisted hot pressing

Based on literature review and data gathered by Torralba et al [13], the FAHP parameters to develop the prototype was chosen to be at a temperature of 1000 MPa, pressure of 50 MPa and a dwell time of 15 minutes. All three alloys C1, C2 and C3 were sintered at these parameters and a homogenization treatment was carried out at 1200^{o}C for 24 hours followed by furnace cooling.

To study the phases of the prototype alloys developed using Field Assisted Hot Pressing (FAHP), XRD and EBSD analysis were carried out on both the as-sintered and heat-treated samples. Post sintering, the samples were heat treated at 1200^{o}C for 24 hours. XRD peaks of C1 alloy in the as-sintered state shows FCC, BCC and HCP peaks as shown in Fig. 4.4 (a), which is also confirmed by EBSD phase map shown in Fig. 4.4 (c). The HCP phase corresponds to the CoCr powders in the mix. After the heat treatment, the HEA was fully developed into a single solid solution with a complete FCC phase as seen in the EBSD phase map shown in Fig. 4.4 (d) and confirmed by the XRD peaks seen in Fig. 4.4 (a). The inverse pole figure map in the z direction is shown in Fig. 4.4 (b) for the as-sintered state and in Fig. 4.4 (d) for the heat-treated state, where there is a clear grain growth due to the long annealing times. Similarly, results of C2 and C3 alloys are shown in Fig. 4.5 and Fig. 4.6, respectively. It follows the same pattern as C1, where the as-sintered alloy has FCC, BCC, and HCP phases, whereas the heat-treated samples have only the FCC phase with larger average grain sizes. The C2 alloy was not fully sintered at the given temperature and time as evident by the black spots in Fig. 4.5 (b) and (c). This is probably due to the higher quantity of high melting point elements, Chromium, and Molybdenum in the C2 mixture compared to C1 and C3. So, a higher temperature and/or pressure might be needed to improve the sintering process for the C2 alloy.

The results of this preliminary prototype study showed the feasibility of developing a HEA using a mix of relatively inexpensive commodity powders as raw material.

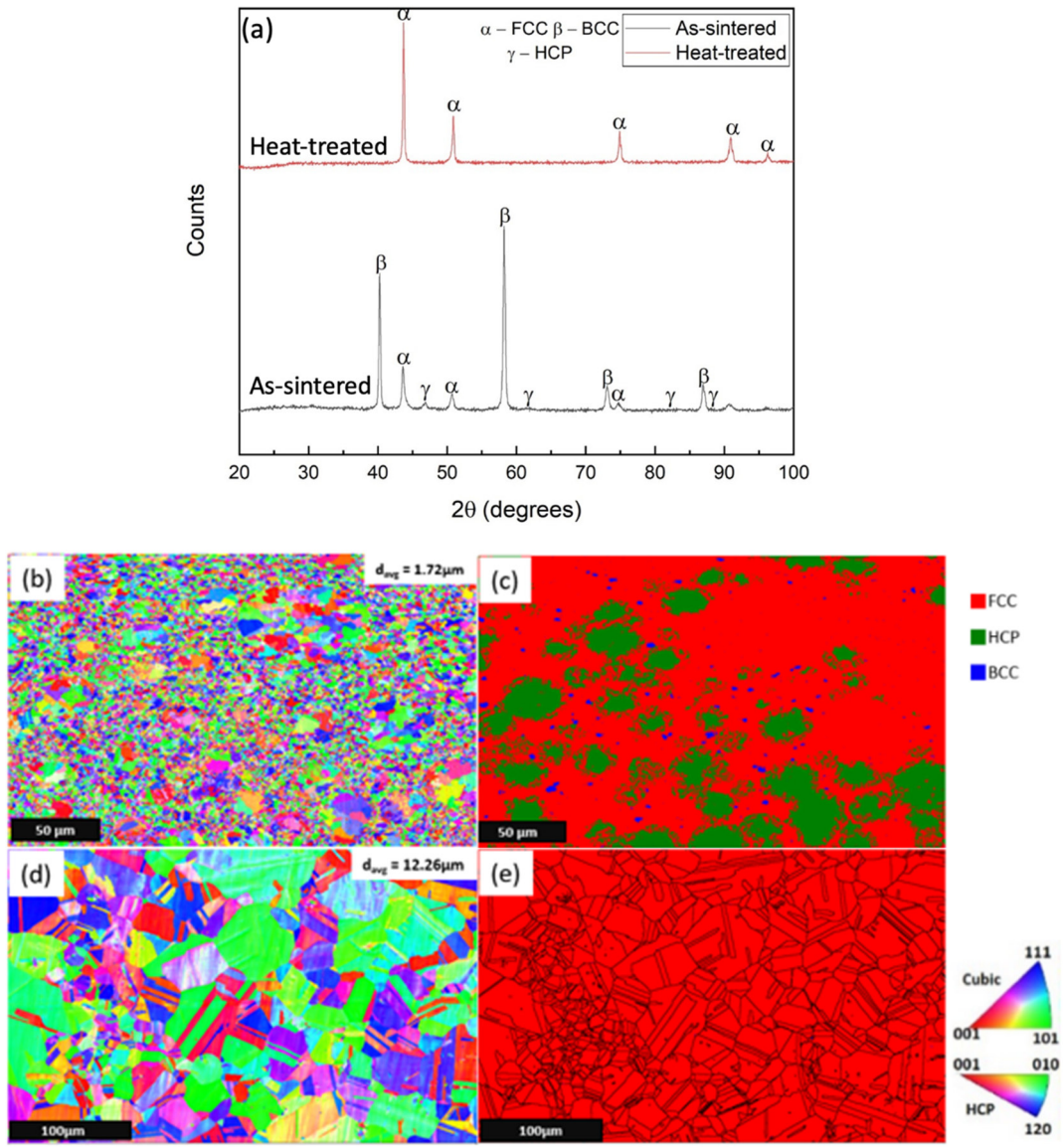

Fig. 4.1: (a) XRD pattern of C1 as-sintered and heat-treated sample, (b) Inverse pole figure (IPF-Z) map and (c) phase map obtained by EBSD of the as-sintered C1 sample and (d) IPF-Z and (e) phase map of heat-treated C1 sample [1]

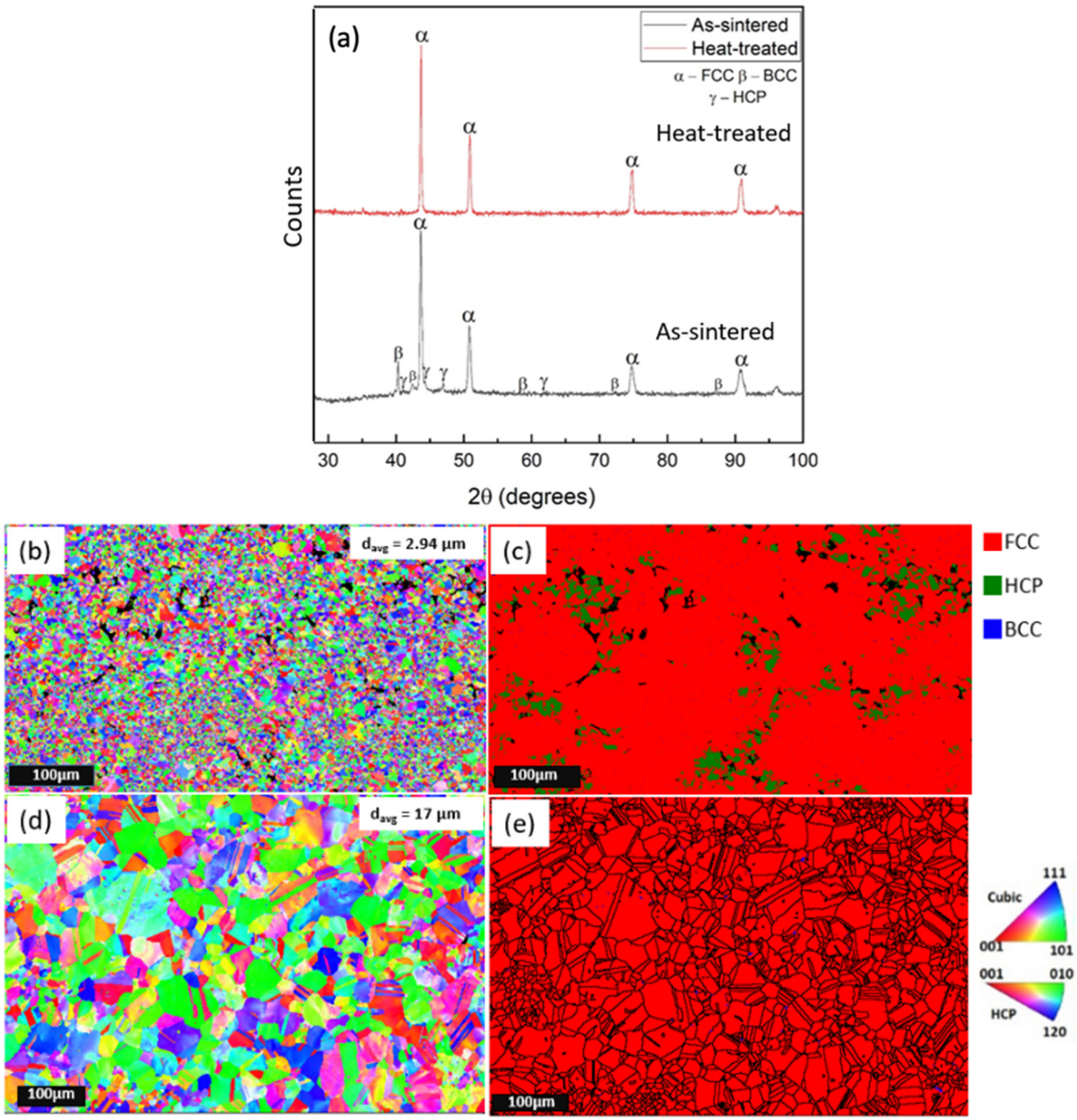

Fig. 4.5: (a) XRD pattern of C2 As-sintered and Heat-treated sample, and (b), (c) EBSD inverse pole figure (IPF-Z) map and EBSD phase map of the as-sintered and (d), (e) heat-treated C2 sample [2]

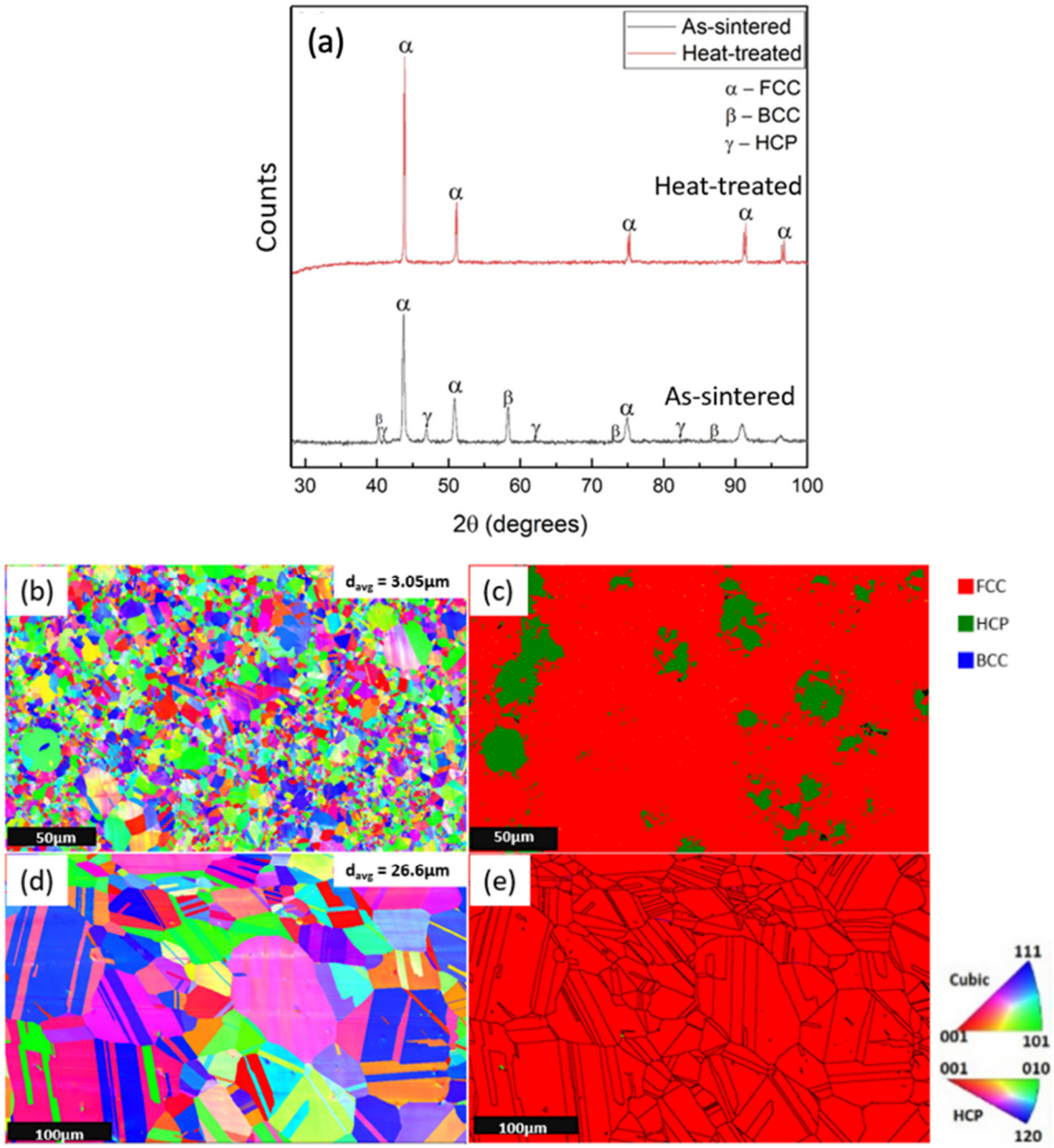

Fig. 4.6: (a) XRD pattern of C3 As-sintered and Heat-treated sample, and (b), (c) EBSD inverse pole figure (IPF-Z) map and EBSD phase map of the as-sintered and (d), (e) heat-treated C3 sample [2]

4.1.4 Spark Plasma Sintering (SPS)

Since the prototypes were successfully manufactured by FAHP, the next step was to fabricate the same alloys using Spark Plasma Sintering (SPS) at 1000°C and 1100°C at 50 MPa for 10 minutes. The C1 alloy was first sintered at 1250°C where a liquid phase was formed due to which the temperature was reduced to 1100°C for C2 and C3 alloy. Again, these parameters were

chosen based on a detailed literature survey carried out by Torralba et al [13] for similar compositions developed by Spark plasma sintering.

4.1.4.1 X-Ray Diffraction

The XRD peaks obtained for C1, C2 and C3 both in the as-sintered and heat-treated state are shown in Fig. 4.7 (a) and (c) respectively. C1 in the as-sintered state contains both Face Centered Cubic (FCC) and Hexagonal Close-Packed (HCP) peaks, whereas after annealing at 1200^{o}C for 24 hours, only FCC peaks remain. The same goes for C2 and C3, except that in C2 alloy sintered at 1100^{o}C and C3 alloy sintered at 1000^{o}C and 1100^{o}C, no HCP peaks were detected in XRD but as shown in Fig. 4.16, Fig. 4.17 and Fig. 4.18, HCP phases were present on the phase maps obtained by EBSD. The HCP phase is linked to the Co base powders and Co is highly concentrated in very specific areas in the as-sintered samples which makes it suitable to be detected by EBSD but not easily by XRD, thus, making the HCP peaks too weak. Both C2 and C3 alloy at both temperatures converted to a single FCC phase after annealing. Since all the alloys in the as-sintered state is just a mix of different commodity powders, there is no single FCC phase throughout with the same lattice parameters. This is the reason why there are multiple peaks as shown in Fig. 4.7 (b), which is the region from the boundary marked in Fig. 4.7 (a), representing FCC phases with different but very close lattice parameters. After the annealing process, the multiple small peaks change to one sharper and narrower peak indicating a single FCC phase with the same lattice parameters. Moreover, as seen in Fig. 4.7 (d), which shows the peaks of alloys after annealing, the slight shift in peaks between C1, C2 and C3 indicate slight change in lattice parameters as expected due to the varying compositions between the alloys.

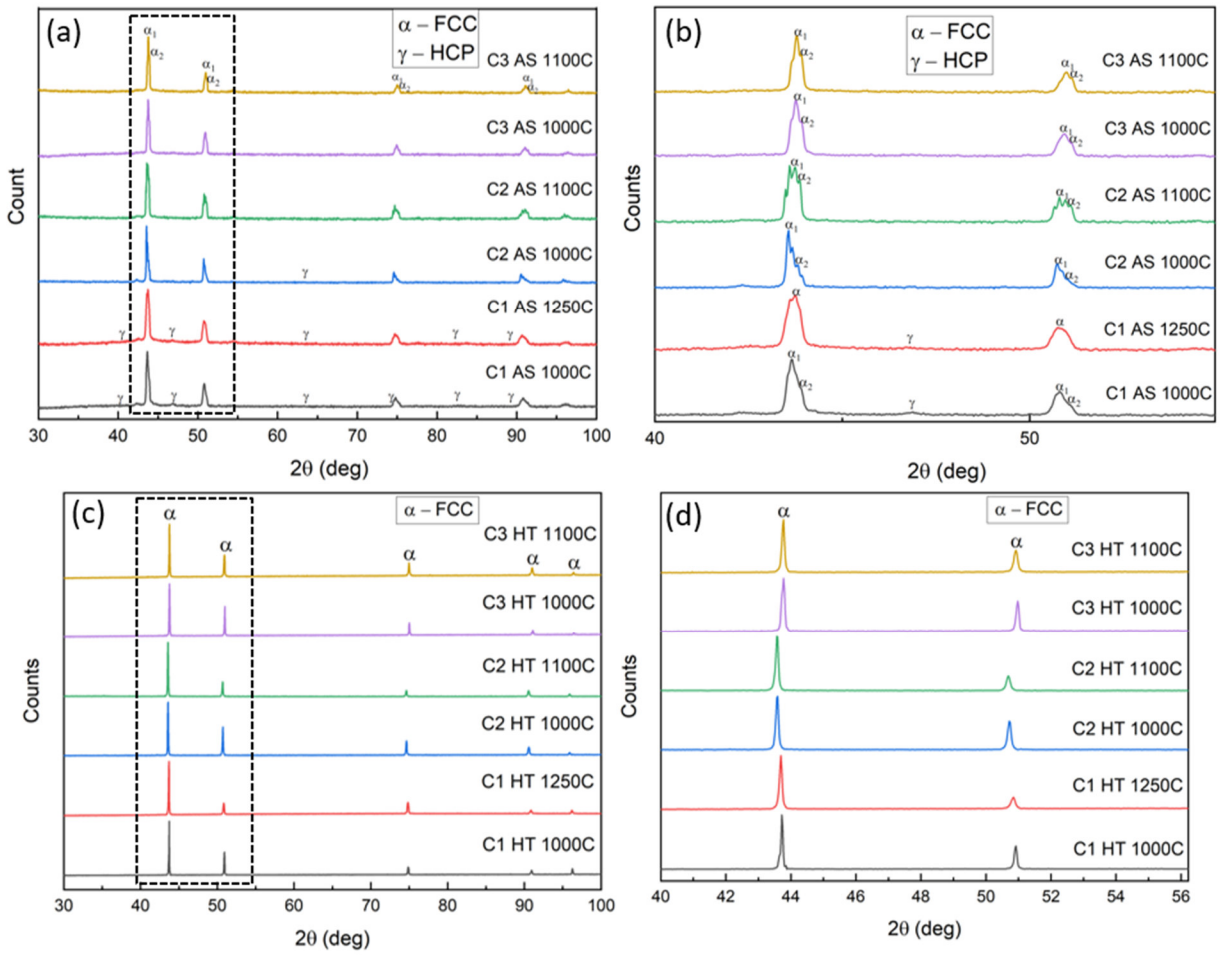

Fig. 4.7: XRD peaks of the alloys in the (a) as-sintered condition sintered at different temperatures and (b) closer view of the marked region from (a), (c) XRD peaks of the alloys sintered at different temperatures after annealing at 1200°C for 24 hours and (d) closer view of the marked region from (c) [3]

4.1.4.2 Microstructural analysis

Fig. 4.8 shows the SEM images of the as-sintered samples via SPS depicting the microstructure evolution of all the three alloys at different sintering temperatures with the average percentage of porosities. It can be observed that the porosity decreases with higher sintering temperatures. The C2 mix of powders are not fully sintered well at the given parameters (1000°C, 50 MPa, 10 mins) due to the higher amount of large particle sized powders, which is Ni625, with a d50 of 60µm. However, the same mix of powders were properly sintered at a temperature of 1100°C. The individual powder particles can be seen in the as-sintered state in Fig. 4.8. To analyze this further, EDS was carried out on C1 alloy sintered at 1000°C to observe the elemental distribution as shown in Fig. 4.9. The individual powder particles of C1, i.e., Ni625, Invar36, and CoCrF75

are clearly visible in the as-sintered state. The Invar36 powders formed the matrix here as its smaller particle size distribution enabled it to achieve higher sinterability.

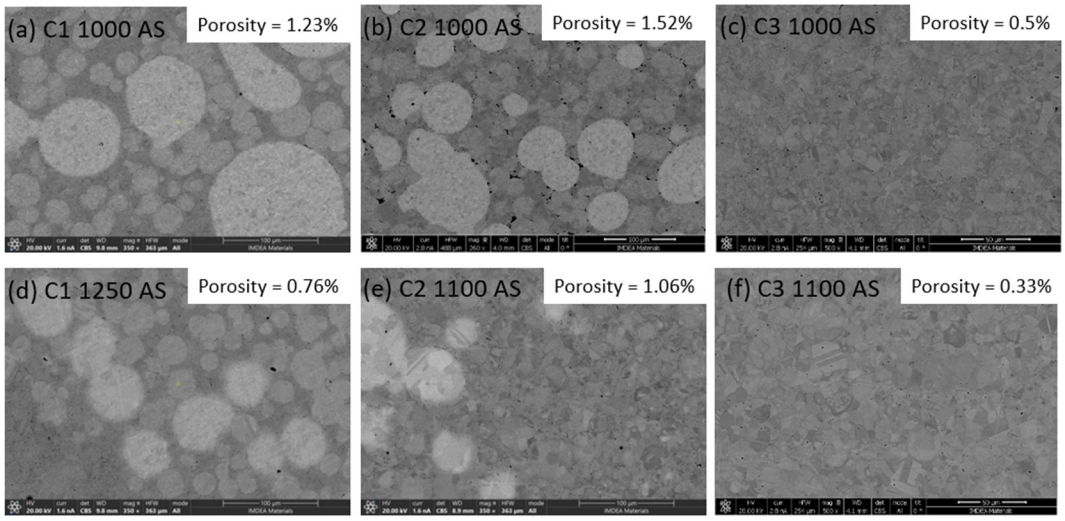

Fig. 4.8: SEM images of as-sintered samples via SPS; C1 sintered at (a) 1000ºC, (d) 1250ºC, and C2 sintered at (b) 1000ºC, (e) 1100ºC, and C3 sintered at (c) 1000ºC, (f) 1100ºC [3]

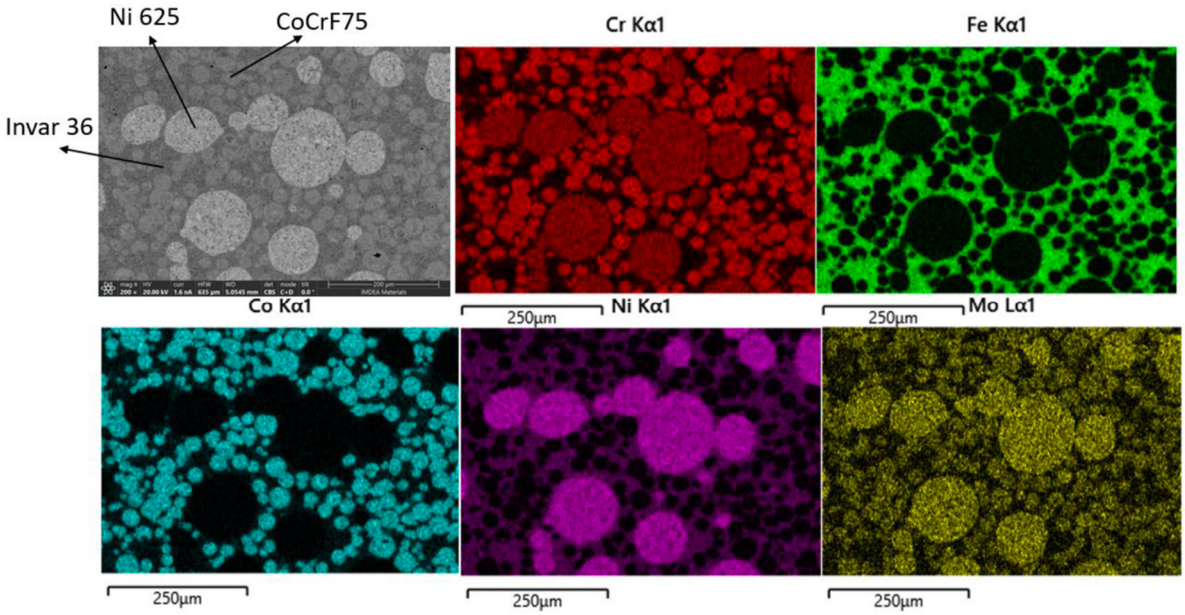

Fig. 4.9. Elemental distribution map of C1 alloy as-sintered via SPS at 1000ºC [3]

Multiple heat treatment trials were carried out to achieve a homogenous microstructure and, in the end, an annealing treatment at 1200ºC for 24 hours yielded a typical HEA microstructure for all the three alloys as shown in Fig. 4.10. An EDS elemental distribution map of C1 alloy sintered at 1000ºC and

annealed is shown in Fig. 4.11 which shows a homogenous distribution of elements as opposed to in the as-sintered state. The same pattern was followed for C2 and C3 alloys as well.

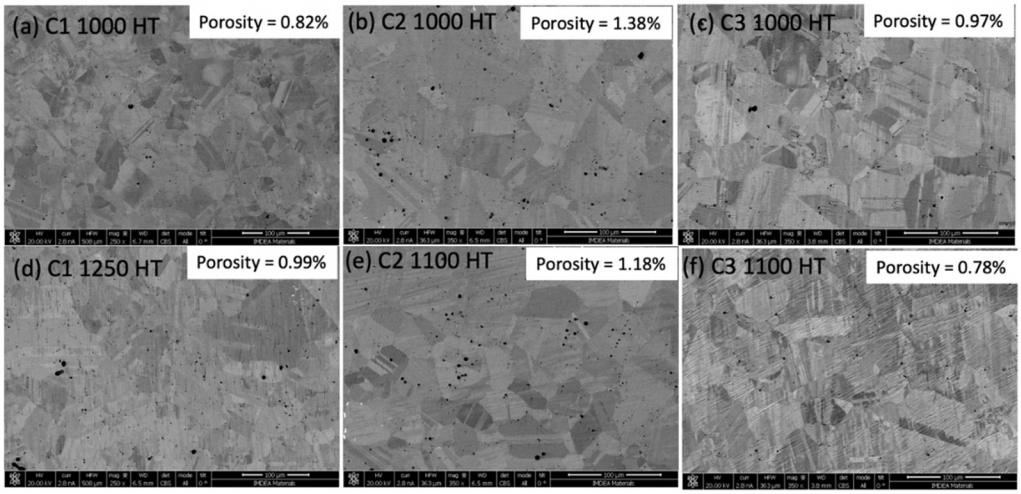

Fig. 4.10: SEM images of samples sintered at various temperatures via SPS and annealed at 1200ºC for 24 hours; C1 sintered at (a) 1000ºC, (d) 1250ºC, and C2 sintered at (b) 1000ºC, (e) 1100ºC, and C3 sintered at (c) 1000ºC, (f) 1100ºC [3]

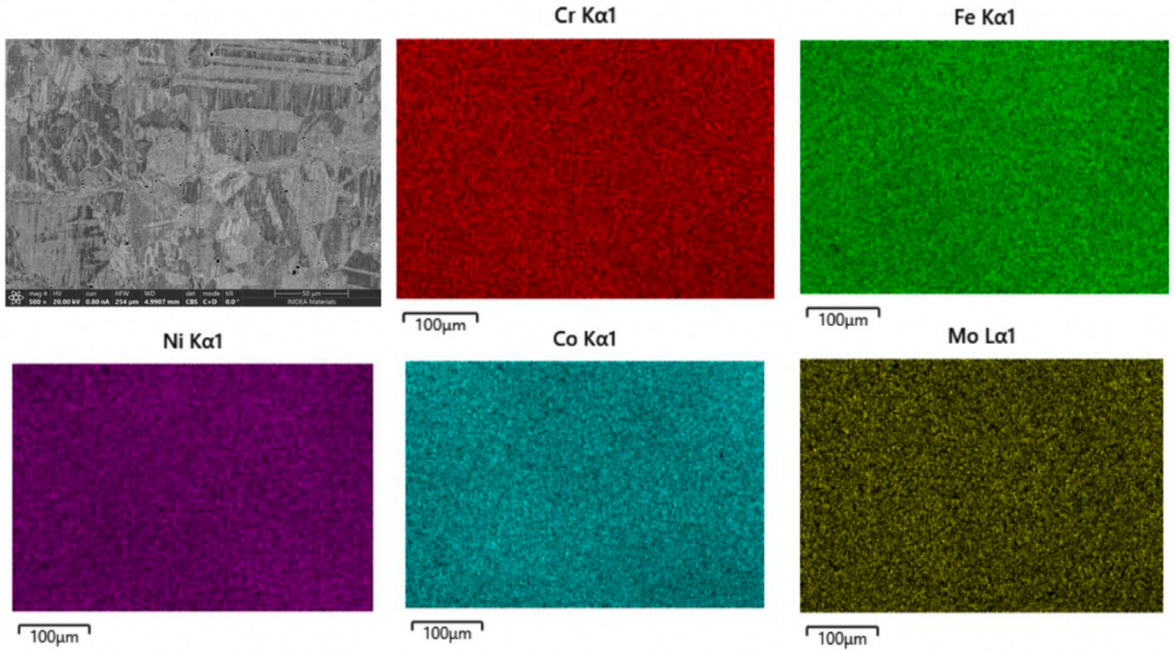

Fig. 4.11: Elemental distribution map of C1 alloy annealed for 24 hours [3]

In highly localized regions, there were small white precipitates in C1 and C2 alloy after annealing but were absent in C3 alloy. A line scan of a precipitate is shown in Fig. 4.12 for C1 alloy sintered at 1000ºC and annealed at 1200ºC for 24 hours which shows that the precipitates are rich in Nb and Mo. As mentioned earlier, Nb is present in Ni625 alloy in small amounts which is mixed in C1 and C2. Due to its very low fraction in the microstructure, perhaps they were not identifiable by XRD. It is known that in Ni625 alloy, many intermetallic phases (like Ni_3Nb) and carbides (MC, M_6C and $M_{23}C_6$) may precipitate after long-time annealing [14–17]. Also shown in Fig. 4.12 are some oxide inclusions which were confirmed by EDS showing chromium and oxygen peaks. As these were absent in the as-sintered alloys, it can be implied that they were picked up during the long-time annealing process. Regardless, these precipitates and oxides did not significantly influence the mechanical properties due to their low volume fraction as discussed in Section 4.1.4.3.

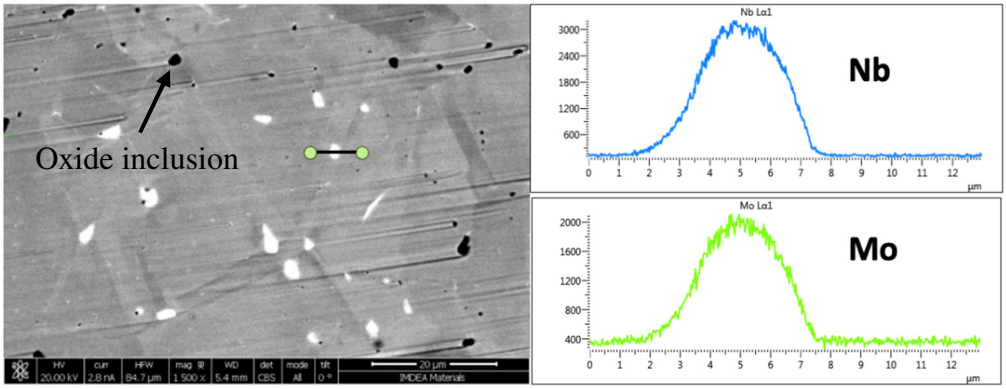

Fig. 4.12: SEM Backscattered image of C1 alloy sintered at 1000ºC and annealed at 1200ºC for 24 hours with a line scan on a precipitate showing the distribution of Nb and Mo [3]

To study the phases after sintering and annealing, EBSD was performed on all the samples. The C1 alloy in the as-sintered state sintered at 1000ºC consists of FCC, HCP and minor amount of body centered cubic (BCC) phases as shown in Fig. 4.13 (b). After annealing at 1200ºC for 24 hours, it results in a single FCC phase as shown in Fig. 4.13 (d). The same C1 alloy when sintered at a higher temperature of 1250ºC, consists of FCC but with much lesser amounts of HCP and BCC phases compared to when it was sintered at 1000ºC as shown in Fig. 4.14 (b). This is attributed to the fact that at higher temperatures, the atomic diffusion is faster which enables more homogeneity to occur. When this alloy was annealed at 1200ºC for 24 hours, a single FCC phase was obtained as shown in Fig. 4.14 (d). The C2 alloy was sintered at 1000ºC

and 1100°C, referred to as C2_1000 and C2_1100 respectively. Both of them consisted of a majority of FCC phase and some amounts of BCC and HCP in the as-sintered condition as shown in Fig. 4.15 (b) and Fig. 4.16 (b), respectively. However, after annealing, a single FCC phase was obtained in both the cases as shown in Fig. 4.15 (d) for C2_1000 and Fig. 4.16 (d) for C2_1100. The C3 alloy was also sintered at 1000°C and 1100°C. In both cases, the as-sintered samples consisted of FCC and HCP phases as shown in Fig. 4.17 (b) and Fig. 4.18 (b), respectively. After annealing at 1200°C for 24 hours, the microstructure changed to a single FCC phase as shown in Fig. 4.17 (c) for C3_1000 and Fig. 4.18 (d) for C3_1100. In all the alloys, after heat treatment, numerous annealing twins can be observed in the inverse pole figure maps suggesting low stacking fault energies as commonly found in recrystallized FCC metals [18].

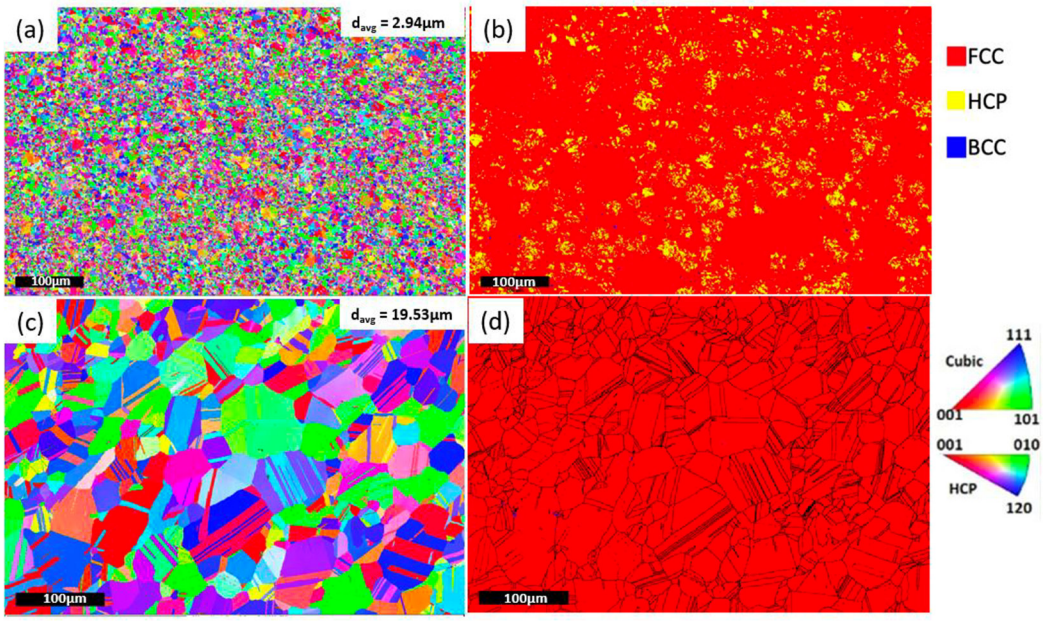

Fig. 4.13: IPF and phase map of C1 alloy sintered at 1000°C in the as-sintered state (a, b) and after annealing at 1200°C for 24hrs (c, d) [3]

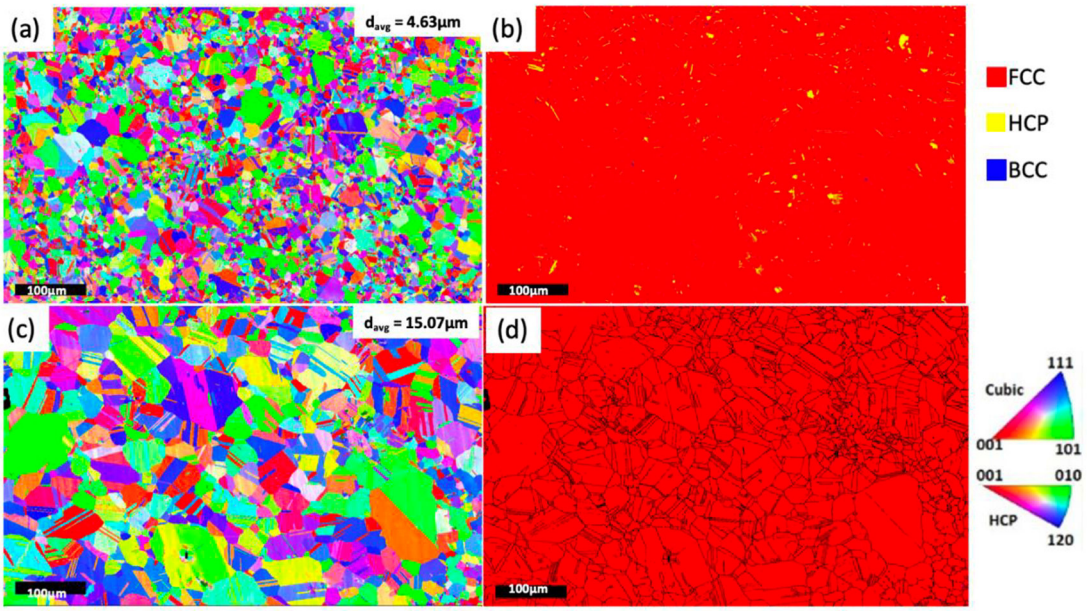

Fig. 4.14: IPF and phase map of C1 alloy sintered at 1250°C in the as-sintered state (a, b) and after annealing at 1200°C for 24hrs (c, d) [3]

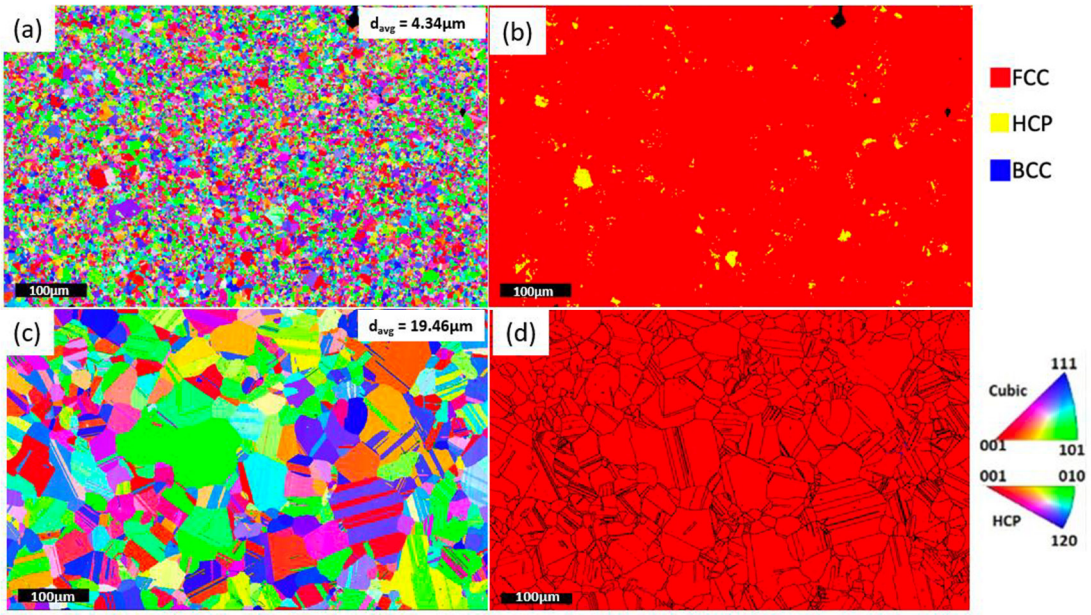

Fig. 4.15: IPF and phase map of C2 alloy sintered at 1000°C in the as-sintered state (a, b) and after annealing at 1200°C for 24hrs (c, d) [3]

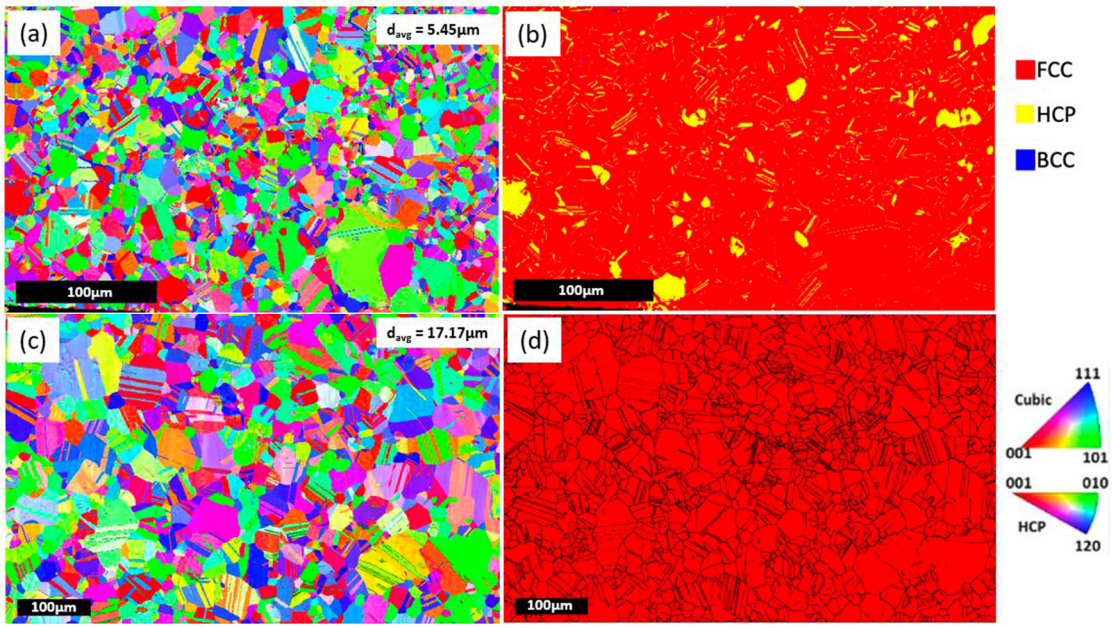

Fig. 4.16: IPF and phase map of C2 alloy sintered at 1100ºC in the as-sintered state (a, b) and after annealing at 1200ºC for 24hrs (c, d) [3]

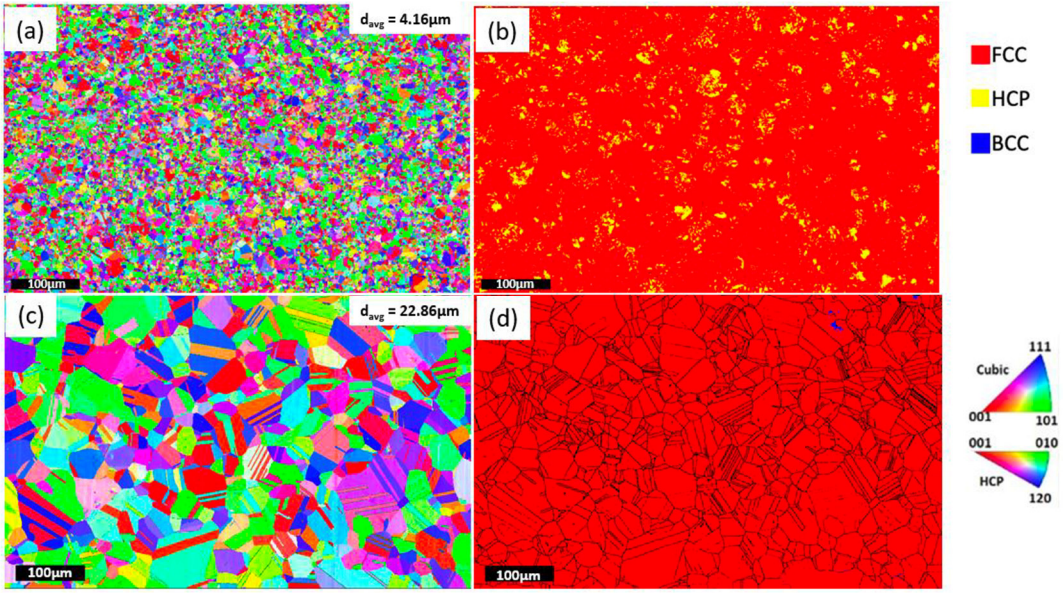

Fig. 4.17: IPF and phase map of C3 alloy sintered at 1000ºC in the as-sintered state (a, b) and after annealing at 1200ºC for 24hrs (c, d) [3]

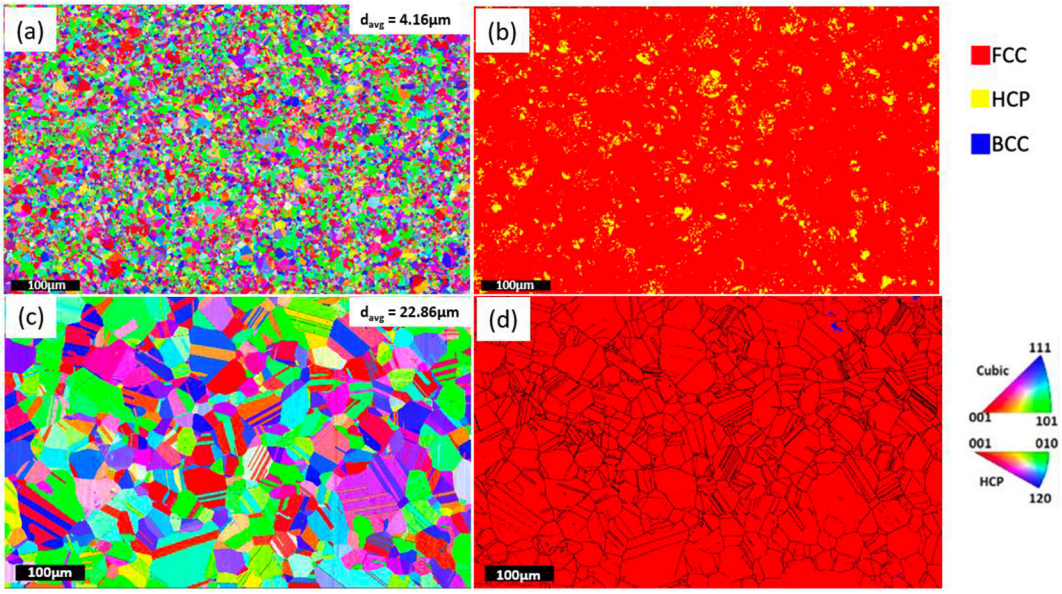

Fig. 4.18: IPF and phase map of C3 alloy sintered at 1100°C in the as-sintered state (a, b) and after annealing at 1200°C for 24hrs (c, d) [3]

It is interesting to note that despite the high temperature and times used for annealing, the grain growth is only slight due to the very small grains obtained due to the fast-heating rates and short dwell times in SPS. The grain sizes obtained after sintering and annealing in all the alloys are shown in Fig. 4.19. These grains are much smaller than the equivalent alloys obtained from ingot casting. For example, $FeCoCrNiMo_{0.1}$ had a grain size of 75µm when annealed at 1050°C for 60 minutes [19] which shows that powder metallurgy routes have great potential in improving the mechanical properties of new alloys.

4.1.4.3 Mechanical properties

The mechanical properties of the samples processed by SPS in both as-sintered and annealed state were evaluated by hardness testing, tensile testing and hot compression testing.

4.1.4.3.1 Hardness

The Vicker's hardness of the annealed alloys is shown in Fig. 4.20. The trend in hardness can be explained by the amount of Mo content. Hardness increases with Mo content as it aids in the local lattice distortion effect in alloys [20]. Thus, C2 has the highest hardness followed by C1 and C3. These values are consistent with other similar PMHEAs like CoCrFeNi, where the obtained hardness was 194 Hv [21].

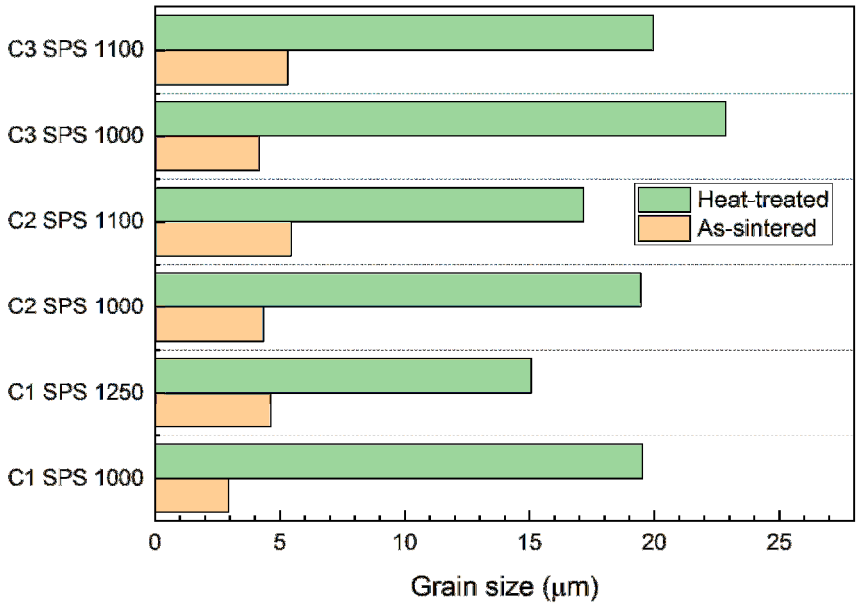

Fig. 4.19: Plot comparing the grain size of as-sintered and annealed samples obtained via SPS and FAHP [3]

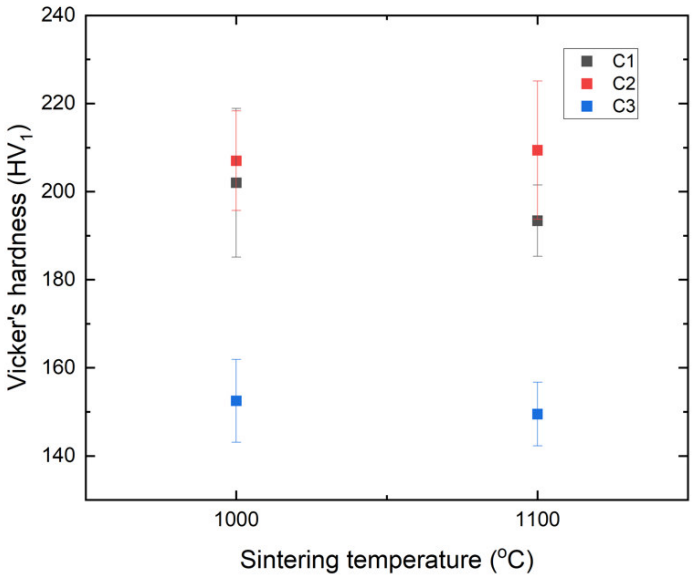

Fig. 4.20: Vicker's hardness values of C1, C2, and C3 alloys processed by SPS at various temperatures and annealed at 1200ºC for 24 hours. It should be noted that the C1 alloy was sintered at 1250ºC instead of 1100ºC [3]

4.1.4.3.2 Tensile features

Micro-tensile tests were performed on the as-sintered and annealed samples. The as-sintered samples do not exactly represent HEAs as they are a mix of different powder particles, and the

composition is not uniform. But for comparative purposes, the tensile results were studied for the as-sintered samples also as shown in Fig. 4.21 (a).

The tensile test results of annealed samples are shown in Fig. 4.21 (b) and the summary of the mechanical properties of both as-sintered and annealed samples are shown in Table 4.2. The ultimate tensile strength (UTS) is lesser, and the ductility is higher for all heat-treated samples compared to the as-sintered ones due to the presence of a single FCC phase and larger grains in the former. All the alloys exhibit a reasonably high UTS and ductility for a single FCC phase, with C2 alloy sintered at 1100^{o}C exhibiting the maximum UTS of 712 MPa due to higher amounts of Mo. As mentioned earlier, the alloying of Mo causes local distortion in the FCC structure [20], which contributes to the strengthening.

Unfortunately, not a lot of work has been reported so far on tensile properties of PMHEAs, especially by SPS. Liu et al [20] investigated the tensile properties of Mo alloyed as-cast CoCrFeNi and reported a UTS of 479 MPa with 51.1% ductility for $CoCrFeNiMo_{0.1}$ and 589.6 MPa with 55.2% ductility for $CoCrFeNiMo_{0.2}$. Similar FCC based alloys like CoCrFeNiMn had a yield strength of 200 MPa and a UTS of 600 MPa after arc-melting and hot rolling [22]. Fig. 4.21(e) shows a comparison plot of tensile strength vs. elongation at fracture of different HEAs developed via powder metallurgy and casting, and other structural alloys. The HEAs developed in this work using commodity powders exhibit a much higher elongation than many other alloys and possess promising tensile strength for a single FCC phase which emphasizes the novelty of this method.

As seen in Table 4.2, in the as-sintered samples, the UTS increases with increasing sintering temperature as there is a shrinkage in porosity, even though there is a slight increase in the grain sizes. Among the heat-treated samples, the C2 alloy shows an expected trend, where the YS and UTS increase with increasing sintering temperatures due to the reduction in porosity, but not in the case of C1 and C3. As mentioned earlier, C1 experienced melting when it was sintered at 1250^{o}C, and produced a liquid phase which resulted in irregular porosities as shown in Fig. 4.22 and might have reduced the strength of the alloy. This is the same trend as seen from the values of Vickers hardness as well where C1 sintered at 1250^{o}C has lesser hardness than the one sintered at 1000^{o}C. It should be noted that C3 alloy has the lowest YS and UTS, due to its lower

quantity of Mo and absence of Nb, which reduced the lattice distortion effect. This shows that Mo and Nb have a significant effect in strengthening HEAs even in small quantities.

The enormous increase in ductility of C2 alloy sintered at 1100°C can be explained as follows. The only difference in C2 mix is the use of 316L powders. Typically, austenitic stainless steels are known for their high work hardening. In the work by Li et al. [23] , the 316L sample exhibited an elongation of 63%. In another work by Yan et al. [24], the ductility of 316L sample was close to 75%. In the C2 alloy in the as-sintered condition, 316L forms the matrix around the Ni625 and CoCr powder particles due to its smaller particle size. The weakest link is the interface between the powder and matrix, where voids initiate, coalesce, and propagate to fracture [25]. Since the matrix is formed by 316L, it may have delayed the propagation of cracks leading to increased ductility and also due to its high work hardening capacity. But C2 alloy sintered at 1000°C shows lesser ductility due to its lower density and the presence of a high number of initial pores in the powder/matrix interface, as shown in Fig. 4.8 (b). However, increasing the sintering temperature to 1100°C increased the density of the C2 alloy, which thereby improved the ductility. The same characteristics were carried on to the annealed samples as well.

Despite the lower ductility of C1 alloy sintered at 1000°C and annealed at 1200°C for 24 hours (10.2%), the fracture surfaces of all samples subjected to the tensile test shown in Fig. 4.23 present a typical micro-ductile fracture. All three samples exhibit micro-fracture with similar small dimples with large ductility signs. As shown in Fig. 4.23 (d), some inclusions are present inside the larger dimples which upon EDS analysis showed two types of oxides, which were Mn-Cr rich and some Si-rich. The commodity powders used consists of trace amounts of Mn and Si which might have resulted in the formation of oxides after the long-time annealing. However, no trends were observed between the oxide volume fraction and mechanical properties which shows that the oxides did not affect the mechanical properties significantly.

4.1.4.3.3 Hot compression test

The ultimate compression strength of the annealed alloys tested at various temperatures up to 750°C obtained by hot compression test is shown in Fig. 4.21(c) for samples sintered at 1000°C and Fig. 4.21 (d) for samples sintered at 1100°C. The summary of the yield strength (YS), ultimate compression strength (UCS) and ductility of both as-sintered (AS) and annealed heat-

treated samples (HT) are tabulated in Table 4.3 and Table 4.4, respectively. The AS alloys in general exhibit better strength and lesser ductility than HT alloys due to the presence of harder and stronger HCP and BCC phases, and the fine grain sizes obtained in the former.

As expected, in all the alloys, the UCS decreases with increasing temperatures as shown in Fig. 4.21 (c) and (d) due to the dynamic softening that occurs at higher temperatures due to the improved thermal activation process [26]. It is to be noted that all the heat-treated samples experienced no fracture at any of the test temperatures even after the strain reached more than 40% indicating a remarkable ductility of the FCC phase. For example, at RT, the C2_HT alloy sintered at 1000^{o}C exhibited a UCS of 1352.5 MPa with a ductility >40%. The same alloy at 750^{o}C, had a UCS of 642.3 MPa with a ductility of >44%. Comparing similar alloys reported in the literature, $CoCrFeNiMo_{0.3}$ developed by casting, showed a UCS of 1269 MPa with a ductility of 58% at room temperature [27]. In another work, $CoCrFeNiMo_{0.2}$ HEA when developed by PM route had a UCS of 500 MPa at 700^{o}C [28] which is lower than that of the HEAs studied in this work.

Various strengthening mechanisms exist in conventional alloys including solid solution strengthening, precipitation strengthening, grain boundary strengthening, and dispersion strengthening. However, in HEAs, strengthening occurs also due to lattice distortion, which is more severe than conventional alloys due to the different atomic sizes of elements and their near-equal proportion, and sluggish diffusion at high temperatures which increases the activation energy. The strengthening due to lattice distortion is more relevant than solid solution strengthening in HEAs, as there are no definite criteria to differentiate a solute from a solvent. For C1 and C2, Mo and Nb contribute to severe lattice distortion due to their large atomic radius compared to the rest of the elements while for C3, it is only Mo. It is also to be noted that C1 and C2 consisted of Mo and Nb rich precipitates in certain localized regions both on the grain boundary and within the grains as shown in Fig. 4.12, which might have also contributed to high compression strength. This is evident by the lower UCS for C3 alloy compared to C1 and C2 at all temperatures. C2 alloy exhibited higher UCS at all temperatures than C1. The atomic size difference, δ defined in [29], was calculated for the alloys from the equation shown below:

$$\delta = \sqrt{\sum_{i=1}^{n} C_i \left(1 - \frac{r_i}{\bar{r}}\right)^2} \quad (1)$$

C_i is the mole fraction of the i^{th} of N components, $\bar{r}$ is the average atomic radius in the alloy obtained by rule of mixtures and r_i is the atomic radius of the i^{th} element. The atomic radii in [30] were used to calculate r_i. C2 had the highest atomic size difference at 2.24 compared to 1.7 for C1 which emphasizes the role played by Mo to distort the lattice and increase the strength by restricting the dislocation movement. Along with being a high radius element, Mo also has a melting point, which has been known to increase the activation energy (Q) for high temperature deformation [28]. In addition, Tsai et al [31] showed that the higher the normalized activation energy (Q/T_m, where T_m is the melting point), the slower the diffusion rate, which implies that Mo enhances the sluggish diffusion effect in HEAs. This corroborates well with the compression test results, as the strength decreases with temperature concerning the amount of Mo, in the order, C2, C1 and C3 in both the sintering temperatures, 1000ºC and 1100ºC.

4.1.5 Cost analysis

A raw materials cost analysis was conducted to compare the fabrication route by pure elemental powders and commercial commodity powders. Based on the quote by raw materials provider Hunan Fushel Technology Limited [32], a bar chart is shown in Fig. 4.24, comparing the cost of C2 alloy. By using commercial powders, there is a 20% reduction in raw material costs than when using pure elemental powders. In addition, it should be noted that when using elemental powders, there are added costs of pre-alloying steps like mechanical alloying or gas atomization, which will add to the total manufacturing cost and time. Hence, this method of using commodity powders offers a feasible way for the commercialization and industrial implementation of HEAs.

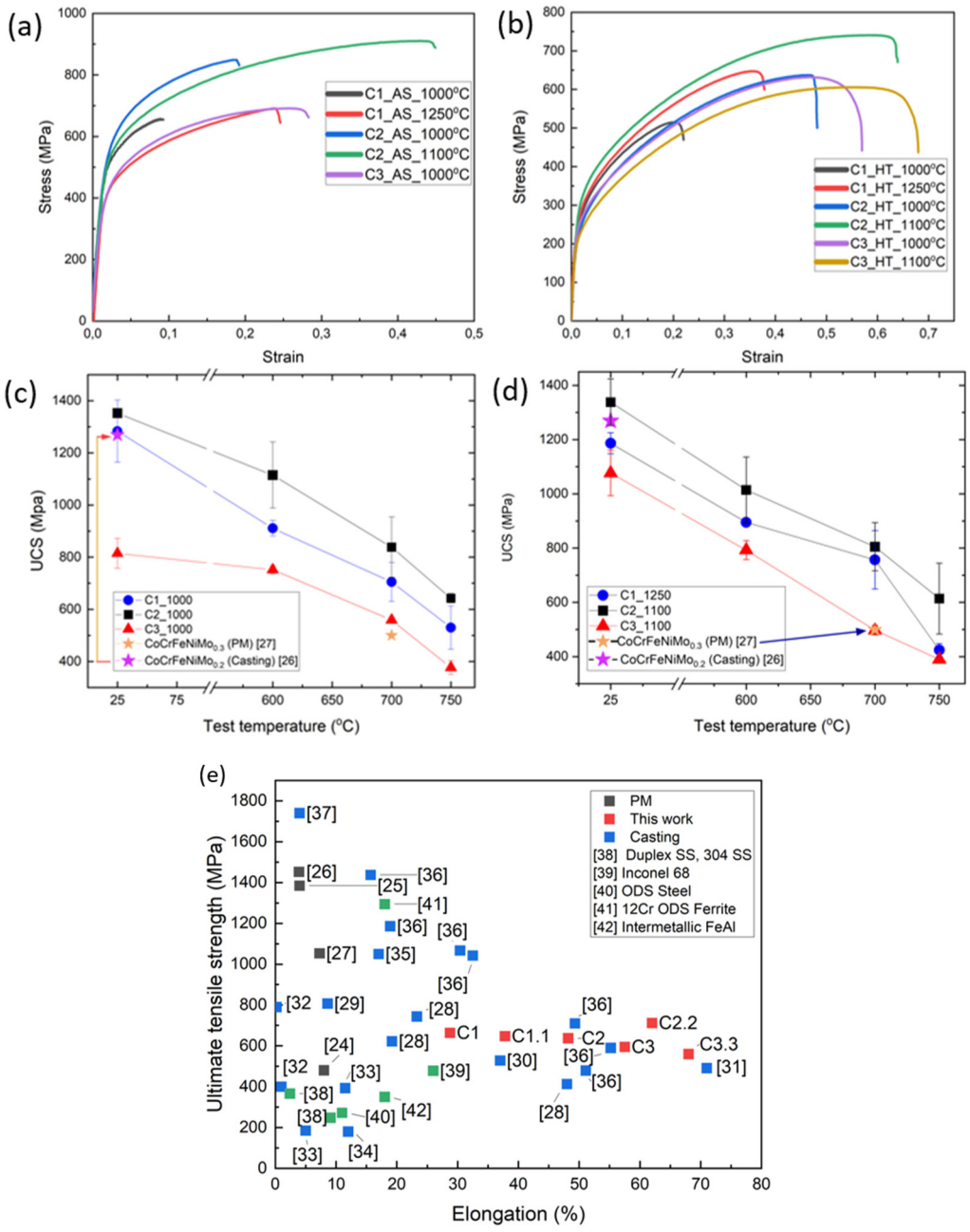

Fig. 4.21: Tensile stress-strain diagram of (a) as-sintered alloys (AS), (b) heat-treated alloys (HT); Ultimate compressive strength values at various temperatures of HT samples sintered at (c) 1000°C and (d) 1100°C. C1 alone was sintered at 1250°C instead of 1100°C. (e) Ultimate tensile strength vs elongation at fracture for different HEAs produced by powder metallurgy (PM) and casting along with other traditional alloys. UCS refers to Ultimate compressive strength. C1 – Sintered at 1000°C, C1.1 – Sintered at 1250°C, C2 – sintered at 1000°C, C2.2 – sintered at 1100°C, C3 – sintered at 1000°C, C3.3 - sintered at 1100°C [3]

TABLE 4.2: TENSILE PROPERTIES OF C1, C2, AND C3 ALLOYS IN THE AS-SINTERED AND HEAT-TREATED STATE

Condition	Alloys	Yield strength (MPa)	Ultimate tensile strength (MPa)	Ductility (%)
As-sintered	C1_1000ºC	397.5	657.59	10.2
	C1_1250ºC	311	691.07	25
	C2_1000ºC	400	848.98	20
	C2_1100ºC	418	894	42.75
	C3_1000ºC	315	667.5	28
Heat-treated at 1200ºC for 24 hours	C1_1000ºC	322	663.75	28.75
	C1_1250ºC	234	647.5	37.8
	C2_1000ºC	190	637.4	48.2
	C2_1100ºC	257.5	712	62
	C3_1000ºC	200	595	57.5
	C3_1100ºC	167.5	560	68
	$CoCrFeNiMo_{0.1}$[20]	198.8	479	51.1
	$CoCrFeNiMo_{0.2}$[20]	254.7	589.6	55.2
	CoCrFeNiMn[22]	200	600	39

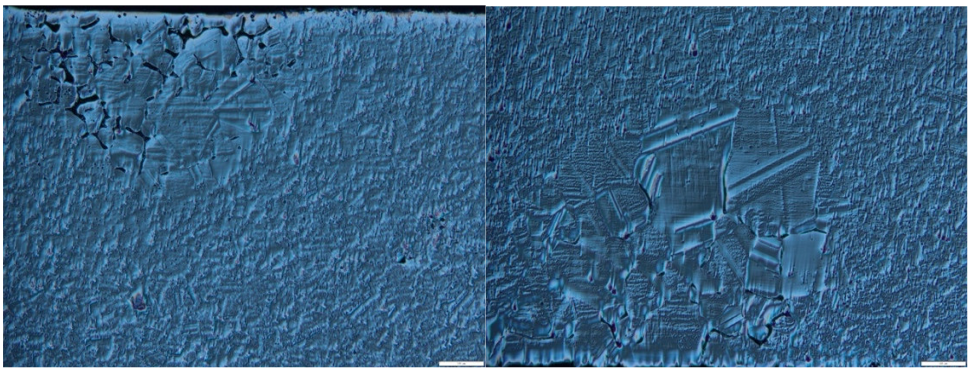

Fig. 4.22*:* Optical microscope images of C1 alloy sintered at 1250ºC and annealed at 1200ºC for 24 hours [3]

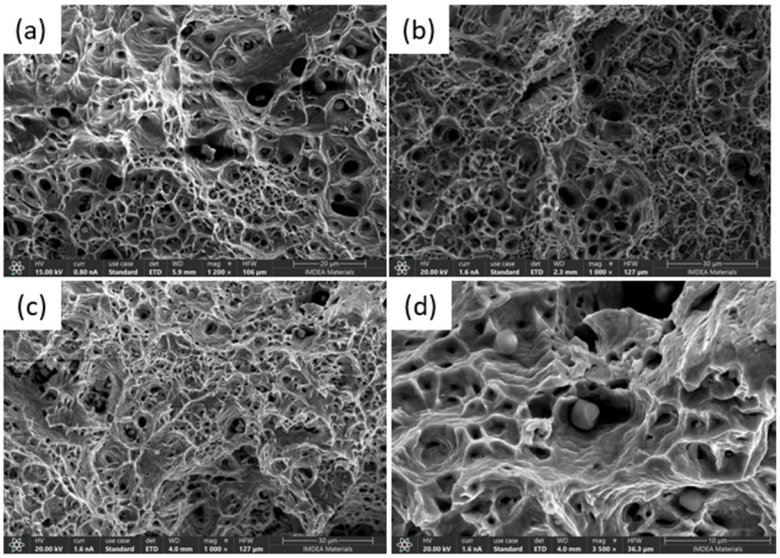

Fig. 4.23: SEM images of fracture surfaces of (a) C1, (b) C2, (c) C3, (d) C3 at higher magnification, sintered at 1000ºC and annealed at 1200ºC for 24 hours subjected to tensile testing [3]

TABLE 4.3: HOT COMPRESSION PROPERTIES OF C1, C2 AND C3 TESTED AT VARIOUS TEMPERATURES IN THE AS-SINTERED STATE

Temperature (ºC)	**Mechanical Property**	**C1 1000ºC AS**	**C1 1250ºC AS**	**C2 1000ºC AS**	**C2 1100ºC AS**	**C3 1000ºC AS**	**C3 1100ºC AS**
RT	YS (MPa)	370	268.8	572.3	506	501.7	335
	UTS (Mpa)	1242.5	1351.3	1547	1847.7	1134.4	1184
	Ductility (%)	31.5	33.7	31	37	35.8	39.2
600	YS (MPa)	310	335.8	394	320	277.6	210
	UTS (MPa)	715.7	780.5	1039.2	1042.3	634	697
	Ductility (%)	20.1	28.45	25.6	30	29.9	35.2
700	YS (MPa)	272.5	211.5	353	211.09	227.6	188.9
	UTS (MPa)	525.2	663.4	802	806.3	446	503
	Ductility (%)	28.1	35.85	35.9	42.75	37	38.5
750	YS (MPa)	213	188	300	274.6	166	160.5
	UTS (MPa)	352.5	410.8	488.7	>596	265	313.8
	Ductility (%)	31	31.4	45	>37.7	34.8	43.7

TABLE 4.4: HOT COMPRESSION PROPERTIES OF C1, C2 AND C3 TESTED AT VARIOUS TEMPERATURES IN THE HEAT-TREATED STATE

Temperature (ºC)	**Mechanical Property**	**C1 1000ºC HT**	**C1 1250ºC HT**	**C2 1000ºC HT**	**C2 1100ºC HT**	**C3 1000ºC HT**	**C3 1100ºC HT**
RT	YS (MPa)	310	211	330	242.7	205	183.6
	UTS (Mpa)	1224	1202.5	1352.5	1337.6	871.5	1076.6
	Ductility (%)	>44	>42	>41	>46.1	>39	>39
600	YS (MPa)	120	190	129	155.9	163.6	134
	UTS (MPa)	911	895	1115	1096	751.6	792.3
	Ductility (%)	>41.6	>37.6	>39.3	>41.9	>35.5	>34.7
700	YS (MPa)	122.5	127.3	132	163.5	113.5	145.8
	UTS (MPa)	705	683	757.5	859	549.7	497.4
	Ductility (%)	>41.7	>39.3	>37.9	39.7	>35.5	>36.8
750	YS (MPa)	164	132.2	142	176	90	120.5
	UTS (MPa)	530	424	642.2	613.5	376.6	390
	Ductility (%)	>37.5	>34	>44.1	36.6	>35.9	>33.7

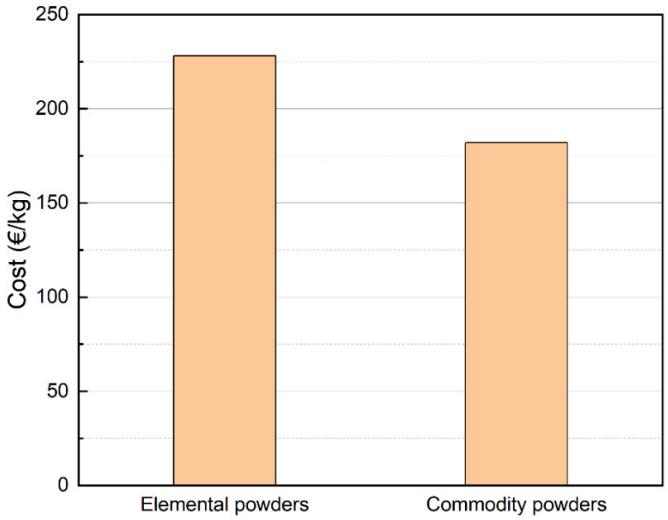

Fig. 4.24: Raw material cost comparison of manufacturing C2 alloy using elemental powders vs commodity powders [3]

4.1.6 Conclusions

The conclusions for the development of HEAs through FAHP and SPS with blended commodity powders are as follows:

1. Three non-equiatomic HEAs, labelled as C1, C2 and C3, were designed and developed by FAHP and SPS using a simple blend of commodity powders namely, Ni 625, Invar36, CoCrF75, 316L, and Fe49Ni. Post-sintering, in both the FAHP and SPS samples, the microstructures consisted of individual alloy powder particles with multiple phases including FCC, HCP and BCC and after an annealing treatment at 1200^{o}C for 24 hours, it resulted in a typical HEA microstructure with an FCC single phase. Prototype samples were prepared using FAHP for preliminary analysis and later bulk samples were manufactured using SPS to investigate the mechanical properties.

2. The best mechanical properties were exhibited by $Co_{23.28}Cr_{28.57}Fe_{25.03}Ni_{21.01}Mo_{2.1}$ HEA sintered at 1100^{o}C due to the higher amount of Mo. It had a tensile strength of 712 MPa with a ductility of 62%. Also, it had a compression strength of 1352.5 MPa at room temperature and 642.3 MPa at 750^{o}C exhibiting no fracture even up to 45% elongation.

3. This work proves that HEAs can be developed by these commodity powders without the need for expensive pre-alloying processes like mechanical alloying, thus avoiding contamination and paving way for an efficient, cost-effective and flexible way for industrial implementation and commercialization. So, the use of commodity alloy scraps as raw materials to manufacture HEAs using both casting and PM routes is a viable alternative, avoiding the direct use of critical metals like Co and Ni, due to both its toxicity and lack of availability.

4.2 Fabrication of HEAs via in-situ alloying commodity powders using laser powder bed fusion

This section consists of the work published in Ref. [4] (Paper 4 in appendix).

Laser powder bed fusion (PBF-LB/M) involves selectively melting layers of metallic powder using a high-energy laser, building up complex 3D parts layer by layer, allowing for the creation of intricate geometries. By integrating HEA powder feedstocks into the PBF-LB/M process, it becomes possible to produce fully dense, near-net-shaped components with customized compositions and properties tailored to specific application requirements. In a powder bed process like the PBF-LB/M, the feedstock should be spherical with a size distribution between 15-63 μm [33] to ensure proper spreadability and fully pre-alloyed by, e.g., gas-atomization or plasma spheroidizing to avoid elemental segregation. This process of pre-alloying for HEAs, which starts from traditional melting and casting to gas-atomizing, is expensive and time-consuming as HEAs involve four or five principal elements, where some of which, like Co [34], are also critical metals. Critical raw metals are those which lack in availability and possess serious concerns about its availability in the future as detailed in the European Union report [35–37] which included metals like Co, Mo and Nb among others. Therefore, this method is rigid and restricts the development and exploration of next-generation materials like HEAs via PBF-LB/M.

In recent years, the integration of in situ alloying with PBF-LB/M has emerged as a promising strategy to expand the capabilities by enabling the creation of multi-component alloys directly during the manufacturing process. The concept of in-situ alloying involves the simultaneous melting and mixing of elemental powders to produce alloys with controlled compositions and microstructures within the PBF-LB/M build chamber. In this regard, the feasibility of using

commercial commodity powders as a feedstock to produce novel HEAs using PBF-LB/M, C1 and C2, was explored in this work.

4.2.1 Powder flowability

For additive manufacturing processes, the flowability/spreadability of the powders is crucial to obtain a dense part. A flowability test was performed for the C1 and C2 powders using the Hall flowmeter along with calculating the apparent and tap density. The apparent density defines the state of loose packing of the powder, whereas the tapped density represents its random dense packing. The packing properties of a powder can affect operations critical to solid dosage manufacturing, including bulk storage, powder flow, and compaction.

The hall flow rate, apparent density and tapped density of C1 and C2 mix, calculated as a mean of three measurements is shown in Table 4.5.

TABLE 4.5: POWDER CHARACTERISTICS OF C1 AND C2 POWDER BLEND

Feedstock powder	**Flowability (s/50g)**	**Apparent density (g/cm^3)**	**Tapped density (g/cm^3)**
C1	14.54	4.36	4.67
C2	14.23	4.43	4.85

When the powders are loosely packed, they form bridges due to the inter-particle cohesive forces. These bridges are collapsed upon tapping, decreasing the volume and increasing the powder density. So, a large difference between apparent and tapped density indicate higher cohesiveness and hence, a poor flowability. Thus, another means of characterizing the powder flow is Hausner ratio and compressibility index. Hausner ratio is the ratio of the tapped density to the apparent density, whereas the relative difference between them is defined as the compressibility index. These values for C1 and C2 are shown in Table 4.6.

Carr R. L. [38] devised a scale of flowability, which determines the character of powder flow based upon the respective values of the Hausner ratio and the compressibility index, as indicated in Table 4.7. Comparing the values of Hausner ratio and Compressibility index of our feedstock powders in Table 4.6 with the reference scale in Table 4.7, it can be concluded that C1 and C2 powders are suitable to be used in SLM process.

TABLE 4.6: HAUSNER RATIO AND COMPRESSIBILITY INDEX OF C1 AND C2 POWDERS

Feedstock powders	Hausner ratio	Compressibility index (%)
C1	1.071	6.6
C2	1.095	8.6

TABLE 4.7: SCALE OF FLOWABILITY

Hausner ratio	Flow character	Compressibility index (%)
1.0 - 1.11	Excellent	<10
1.12-1.18	Good/free flow	11-15
1.19-1.25	Fair	16-20
1.26-1.34	Passable	21-25
1.35 – 1.45	Poor/Cohesive	26-31
1.46 – 1.59	Very poor/very cohesive	32-37
>1.6	Very very poor	>38

4.2.2 Powder morphology

C1 - a blend of Ni625, CoCrF75 and Invar36, and C2 – a blend of Ni625, 316L and CoCrF75 were observed in the SEM which showed good sphericity thus ensuring good flowability/spreadability.

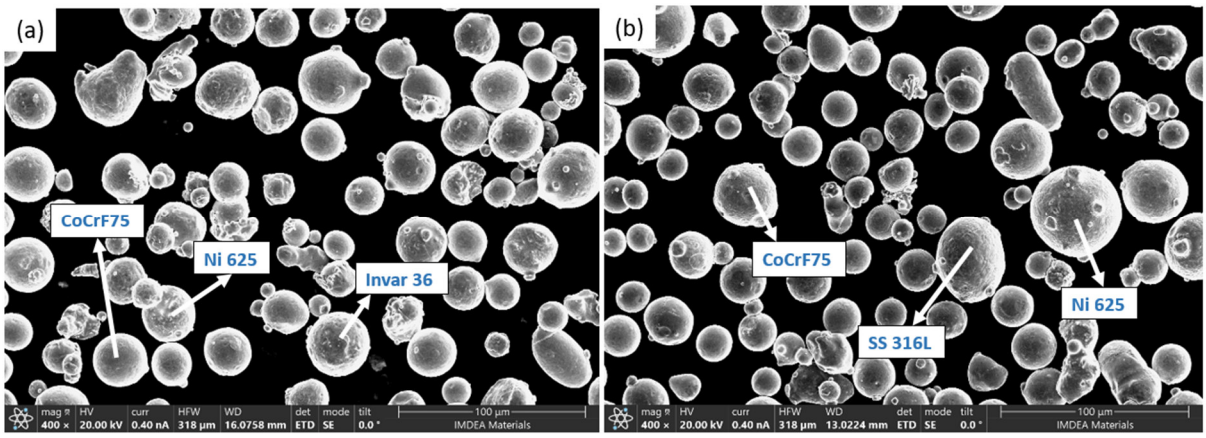

Fig. 4.25: SEM image of (a) C1 and (b) C2 mix of powders [4]

4.2.3 Porosity analysis

Porosity analysis was carried out first in the C2 alloy fabricated by SLM. Based on literature study of the commercial powders used, for the initial screening design, a volumetric energy density (VED) of 68 – 200 J/mm^3 was analyzed with laser power (P) in the range of 100-300W and scan speed (s) in the range from 500 - 1000 mm/s. The layer thickness (t) and hatch distance (h) were kept constant at 30µm and 70µm, respectively. The hatch distance of 70 µm was chosen as a base due to the same value of laser spot size of the Renishaw AM 400 machine. The VED is calculated as $\frac{P}{S* t* h}$. Two additional hatch distances of 50 and 60 µm were used at select combinations to try to reduce the porosities further. The porosity values in percentages for C2 alloy are shown in Fig. 4.26 (c). The general trend observed was that the porosity amount increased with laser power at a given scanning speed due to over-melting as seen from the spherical gas pores in Fig. 4.26 (e) and (f), whereas too low a power of 100W also increased the porosity amount due to insufficient melting causing lack of fusion pores as seen in Fig. 4.26 (a) and (b). Since the C2 samples achieved high relative densities, the second experimental trial for C2 was used as a starting point for C1 since the compositions were similar, to reduce the iterations and it followed a similar trend. The final optimized parameters of C1 and C2 HEA are listed in Table 4.8. Such reduced porosity levels prove that this HEA system is so well suited to be processed with PBF-LB/M via in-situ alloying commercial powders.

4.2.4 Structural and microstructural analysis

The as-built samples of C1 and C2 were etched to reveal the melt pool boundaries and substructures as shown in Fig. 4.27 (a) and (b) respectively. The grain growth here is an epitaxial growth in the maximum temperature gradient direction, typically observed in PBF-LB/M processes. As observed in the literature and discussed in Section 2.3.3.2, the boundaries of the substructures might be enriched in heavy elements like Mo and Nb [39] and possess a high density of dislocations [40], which restricts dislocation movement and enhances the strength of the alloy. The high dislocation density can be attributed to the rapid cooling process in PBF-LB/M.

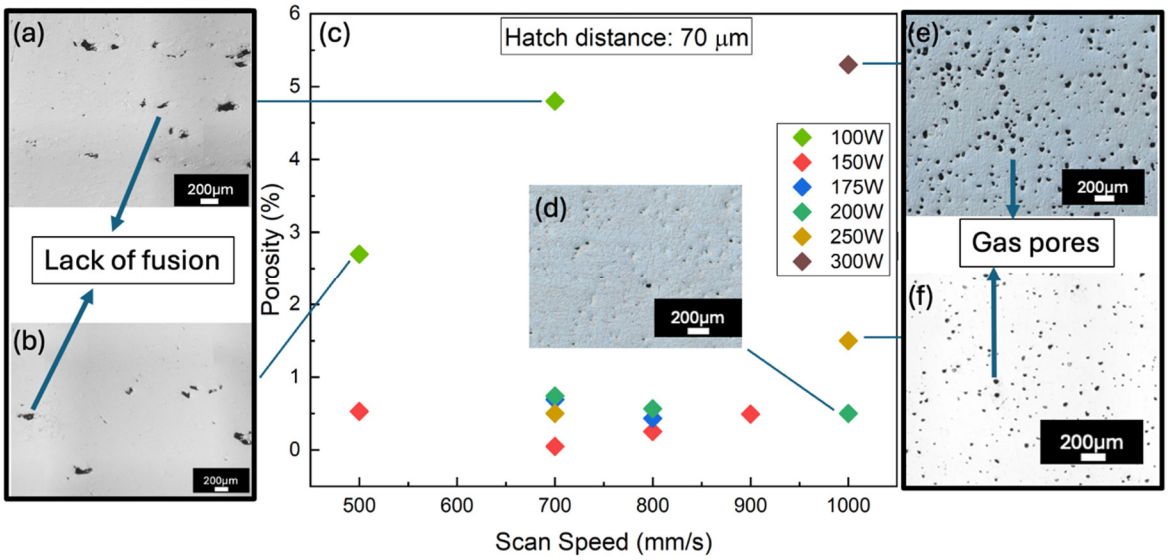

Fig. 4.26: Optical micrograph (OM) of C2 sample printed at 100W and (a) 700 mm/s and (b) 500 mm/s, (c) Porosity percentage plotted against scan speed for various laser powers, OM of C2 sample printed at 1000 mm/s and (d) 200W, (e) 250 W, and (f) 300W [4]

TABLE 4.8: PBF-LB/M PARAMETERS USED TO PRINT C1 AND C2 SAMPLES

Alloy	**Laser power (W)**	**Hatch distance (µm)**	**Scan Speed (mm/s)**	**Layer thickness (µm)**	**Porosity (%)**
C1	150	70	900	30	0.05 ± 0.008
C2	150	60	900	30	0.13 ± 0.017

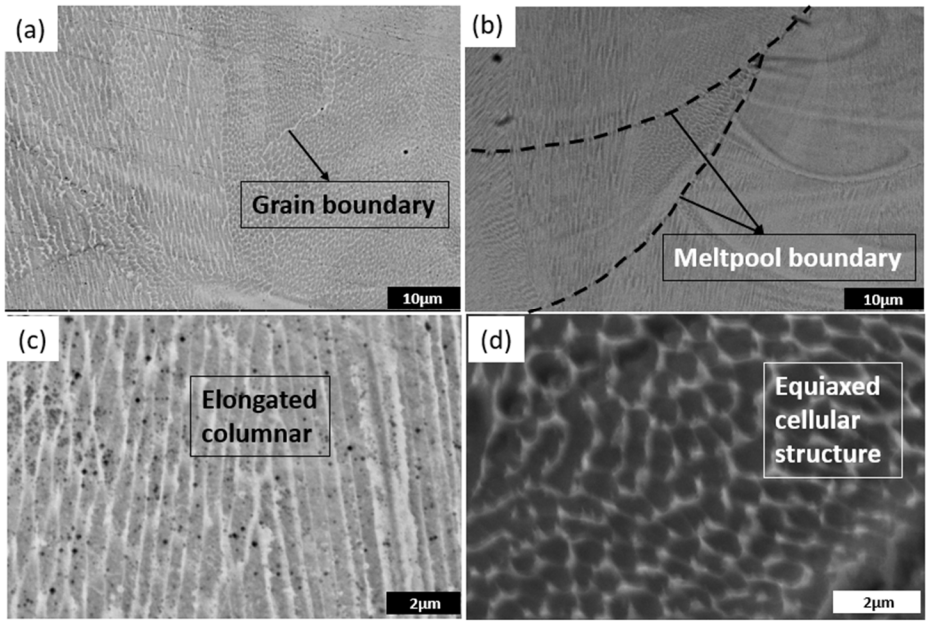

Fig. 4.27: BSE-SEM image of (a) C1 alloy, (b) C2 alloy, magnified view of substructures in analogous regions of (c) C1 alloy and (d) C2 alloy [4]

The success of this method of in-situ alloying lies in the fact that if the microstructure is single solid solution phase and the elemental distribution is homogenous. In that regard, X-ray analysis was performed on the as-built samples to study the phases and as shown in Fig. 4.28 (a). As discussed in [4] (Paper 4 in appendix), controlling segregations by in-situ alloying remains a challenge due to the random mixture of powders in the feedstock and lack of time for proper homogenization in the micro-sized melt pool at such high cooling rates, due to which it is difficult to predict the composition at any point in the blend and inside the melt pool as well. To this regard, reducing the number of elemental powders by using a mix of commodity powders to produce HEAs offers a better solution since most of the elements are already alloyed. To this regard, reducing the number of elemental powders by using a mix of commodity powders to produce HEAs offers a better solution since most of the elements are already alloyed. As shown in Fig. 4.28 (b) for C1 alloy and Fig. 4.28 (c) for C2 alloy, even when the feedstock is a blend of powders, the processed alloys show almost a homogenous elemental distribution with remarkably high relative densities of 99.9%, proving the feasibility of this novel method of using commodity powders. Some minor heterogeneities are observed along the melt pool boundaries for C1 alloy as shown in Fig. 4.28 (b) which is quite negligible compared with common in-situ

alloyed microstructures with a single melt [41,42]. However, this can be fixed by a short homogenization treatment, which could be a potential future study. To further confirm the phases, EBSD analysis was performed, and the results are shown in Fig. 4.29. Both C1 and C2 alloys had a single FCC phase in the as-built state, which shows that the developed alloys are indeed a HEA as predicted by the empirical calculations showing high entropies of mixing in Table 4 of Ref [4] (Paper 4 in appendix). The grain morphology is columnar along the build direction, as expected in the PBF-LB/M process. Both the alloys had the same average grain size of 20μm as measured from the EBSD with a critical misorientation angle of 10º, which shows that the higher amount of Mo and Cr in C2 alloy did not affect the grain size.

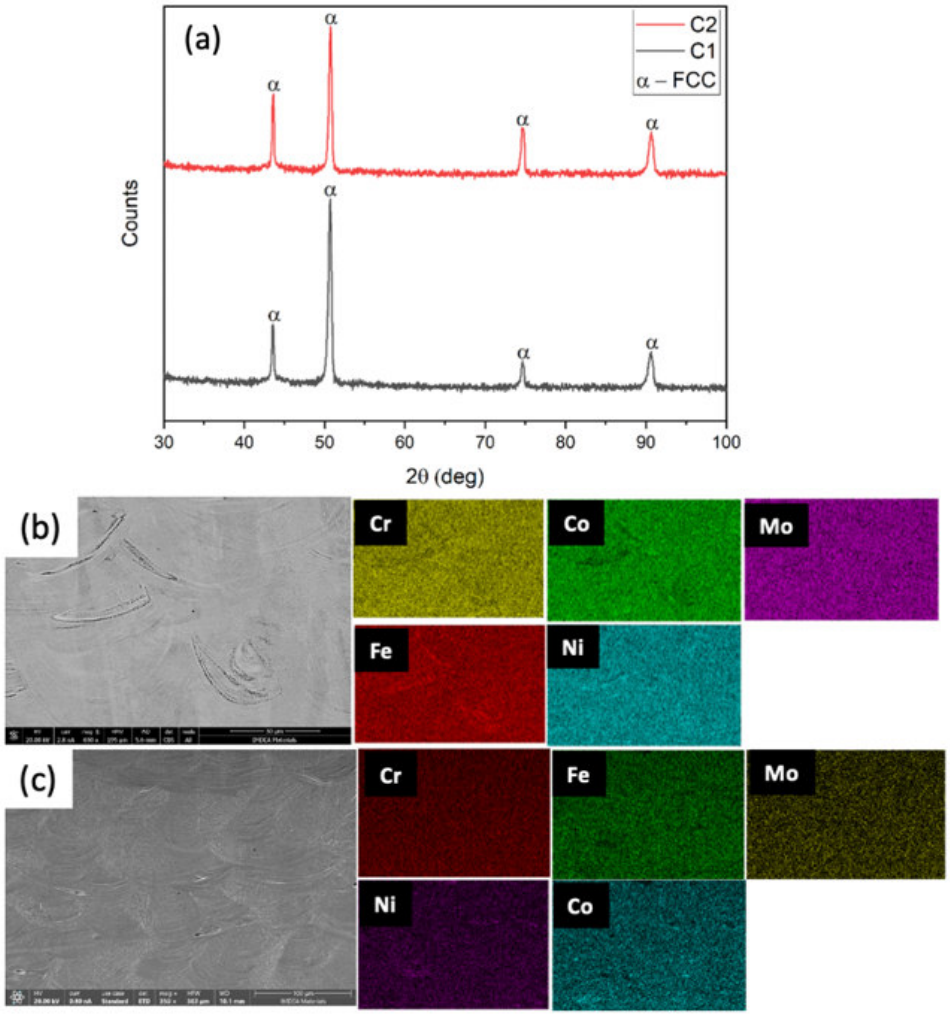

Fig. 4.28: (a) XRD peaks of C1 and C2 alloy, elemental distribution map of as-built (b) C1 and (C) C2 along the build direction [4]

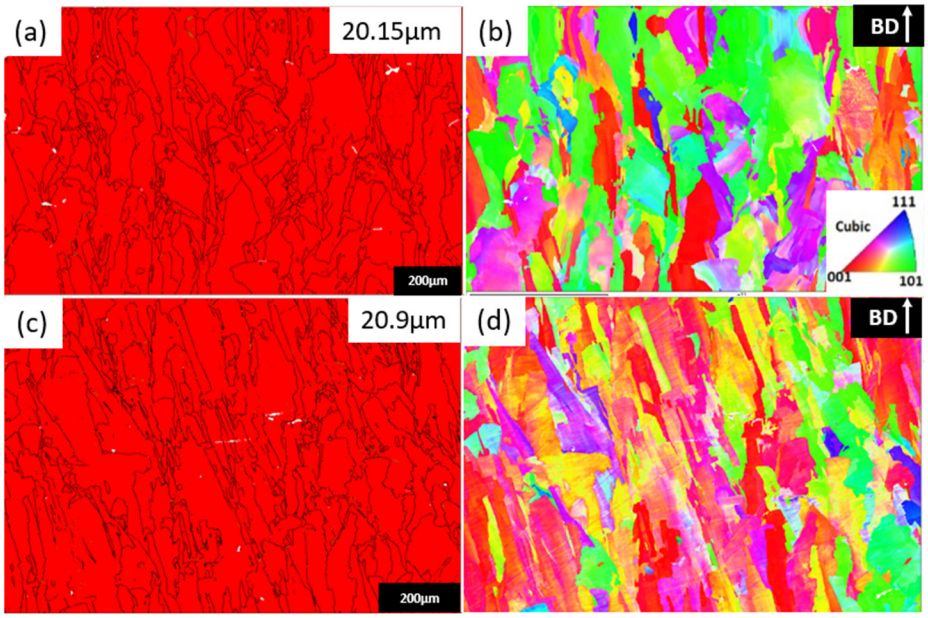

Fig. 4.29: Phase map of (a) C1 and (C) C2 and inverse pole figure in the Z direction of (b) C1 and (d) C2 parallel to the building direction [4]

4.2.5 Mechanical properties

Tensile tests were conducted on the as-built samples, oriented parallel to the build direction, to ascertain the minimum strength achievable with the alloys, recognizing that mechanical properties tend to improve after heat treatment and when tested perpendicular to the build direction. The yield strength (YS) and ultimate tensile strength (UTS) of C1 and C2, derived from the tensile test, are juxtaposed with those of similar high entropy alloys (HEAs) primarily obtained via vacuum arc melting (VAM) with an FCC phase in Fig. 4.30. The impact of Mo and Nb dissolution in C1 and C2 alloys, processed by PBF-LB/M, on strength is discernible from this plot. Notably, the strength values of C1 and C2 surpass those achieved through SPS in previous research, underscoring the superiority of PBF-LB/M. Both the YS and UTS of C1 and C2 decrease with temperature, a phenomenon expected due to dynamic softening at elevated temperatures, with C2 exhibiting higher yield and ultimate tensile strength than C1 at room and elevated temperatures owing to its elevated Mo, Nb, and Cr content, which induces local lattice distortion, thereby impeding dislocation movement. The highest strength is achieved by the C2 alloy, with a YS and UTS ranging from 539.6 MPa and 752 MPa at room temperature to 203.5 MPa and 272 MPa at 900°C, respectively. The summary of mechanical properties, including elongation, is presented in Table 4.9. Fig. 4.30 also demonstrates that C1 and C2 exhibit superior

mechanical behavior at both room and elevated temperatures compared to analogous HEAs containing Al and Mo [43–48], some of which feature eutectic microstructures, thus demonstrating the feasibility of achieving competitive mechanical properties at a reduced cost through this approach.

4.2.6 Fracture behaviour

As seen in Table 4.9, C1 alloy exhibits a sudden drop in ductility at 900°C. To explore this further, the gauge region of the tensile samples after fracture at high temperatures was examined in SEM to observe the microstructural changes. It can be seen from Fig. 4.31 (a) and (b) that the grains and substructures were elongated as expected due to the tensile loading. Notably, in Fig. 4.31 (c_2), there are precipitates shown in white along the grain boundaries in the sample tested at 900°C. An XRD analysis of the fractured samples did not show any peaks other than FCC due to the low volume fraction of precipitates, but an EDS line scan revealed that they are rich in Mo and Nb. Mo and Nb are known to form secondary intermediate phases in high entropy alloys when their quantities exceed the solid solubility limit [49]. Specifically, Fan et al. [50] found that a Nb and Mo-enriched hexagonal close-packed structure Laves phase was formed upon alloying Nb and Mo to CoCrFeNi via arc melting. Thus, the precipitation happening at high temperatures in the C1 and C2 alloys could well be the laves phase. Evidently, the cracks initiated from these precipitates and propagated rapidly along the grain boundaries, as seen in Fig. 4.31 (c_3) resulting in embrittlement. This explains the sudden drop in elongation of C1 alloy tested at 900°C as seen in Table 4.9, and is consistent with the cleavage fracture morphology, as shown in Fig. 4.32 (a_4). So, at 900°C, the fracture changes from ductile to brittle fracture. At other temperatures tested, the C1 alloy exhibits promising elongation along with very high strength for an FCC phase, which corresponds well with the ductile fracture morphology with dimples, as shown in Fig. 4.32 (a_1-a_3).

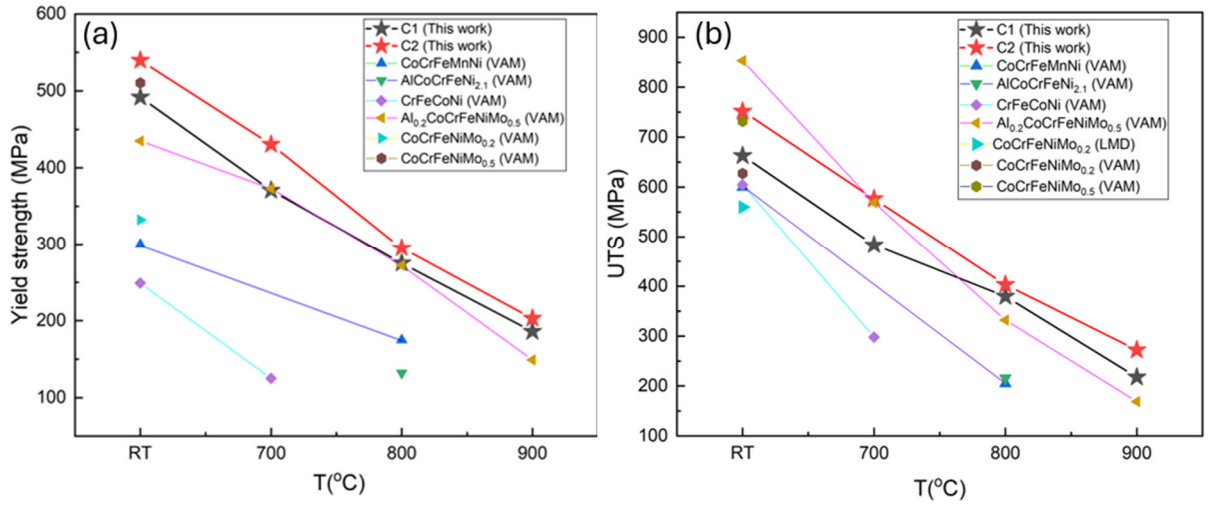

Fig. 4.30: Plots showing (a) Yield strength, (b) Ultimate tensile strength plotted against temperature for C1 and C2 alloys compared with various HEAs [4]; SPS- Spark plasma sintering, VAM—Vacuum Arc Melting, LMD—Laser metal deposition. C1 SPS [3], C2 SPS [3], CoCrFeMnNi (VAM) [43], $AlCoCrFeNi_{2.1}$ (VAM) [44], CrFeCoNi (VAM) [45], $Al_{0.2}CoCrFeNiMo_{0.5}$ (VAM) [46], $CoCrFeNiMo_{0.2}$ (LMD) [47], $CoCrFeNiMo_{0.2}$ (VAM) [48], $CoCrFeNiMo_{0.2}$ (VAM) [48]

TABLE 4.9: MECHANICAL PROPERTIES OF C1 AND C2 ALLOY TESTED ALONG THE BUILD DIRECTION

	C1			C2		
Temperature (°C)	**YS (MPa)**	**UTS (MPa)**	**e (%)**	**YS (MPa)**	**UTS (MPa)**	**e (%)**
RT	491.6 ± 22.85	663 ± 12.8	35.4 ± 0.03	539.6 ± 16.2	752 ± 14.26	37.6 ± 0.02
700	370.67 ± 36.85	483.3 ± 51.33	15.7 ± 4.73	430.3 ± 26.27	576.7 ± 20.2	15.67 ± 4.73
800	275 ± 49.95	379.3 ± 42.6	17 ± 5.57	295 ± 8.66	403.3 ± 7.23	18.33 ± 5.13
900	186 ± 12.73	218.5 ± 6.36	7 ± 1.41	203.5 ± 3.54	272 ± 4.24	27 ± 5.65

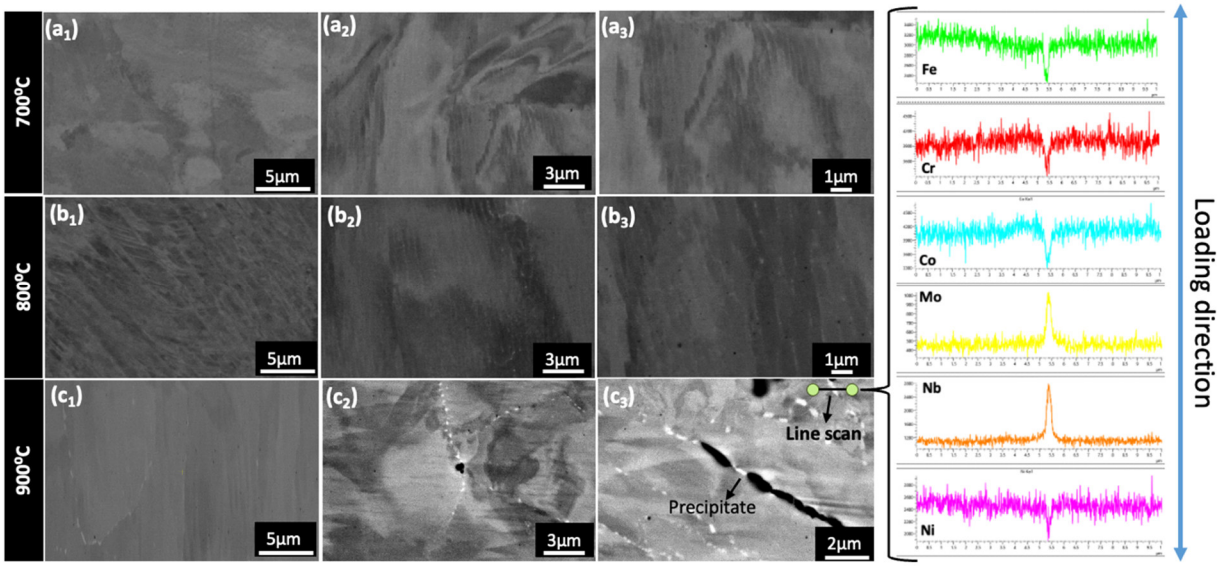

Fig. 4.31: SEM backscattered images of the gauge region of C1 alloy close to the fracture tested at (a_1-a_3): 700°C, (b_1-b_3): 800°C, (c_1-c_3): 900°C. On the right is the EDS line scan profile of the precipitate from (c_3), which are Mo and Nb-rich laves phase [4]

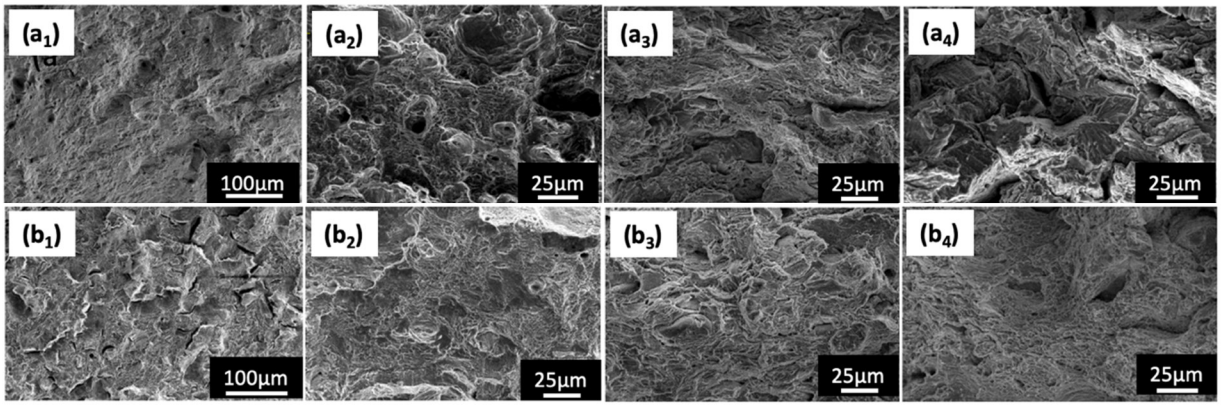

Fig. 4.22: Fracture surfaces of C1 alloy at: (a_1-a_4) Room Temperature, 700°C, 800°C and 900°C respectively, and of C2 alloy at: (b_1-b_4) Room Temperature, 700°C, 800°C and 900°C respectively [4]

In the C2 alloy, the volume fraction and size of Mo and Nb-rich precipitates exhibit a gradual increase from 700°C to 900°C, as illustrated in Fig. 4.33 (a-c). At 900°C, nano-precipitates are uniformly dispersed throughout the C2 alloy, contrasting with C1, where precipitates were solely present along grain boundaries. Consequently, C2 demonstrates superior elongation and a ductile fracture morphology, as depicted in Fig. 4.33 (b1-b4). Beyond enhanced solid solution strengthening, precipitation hardening significantly contributes to C2 alloy's superior strength

compared to C1 above 700°C, as seen in Table 4.9. Notably, C2, characterized by higher Mo and Nb content, exhibits greater strength than C1 at all temperatures without compromising ductility. A study by Wei et al [51] explored the increment in yield strength in CoCrFeNi-based HEA through small additions of Si, maintaining ductility. The simultaneous increase in strength and ductility was attributed to a decrease in stacking fault energy, the formation of deformation nanotwins, and possible short-range order. Therefore, future research can focus on investigating similar effects resulting from small additions of Mo and Nb to these alloys, along with an examination of precipitate formation at high temperatures, aspects beyond the current scope of this study.

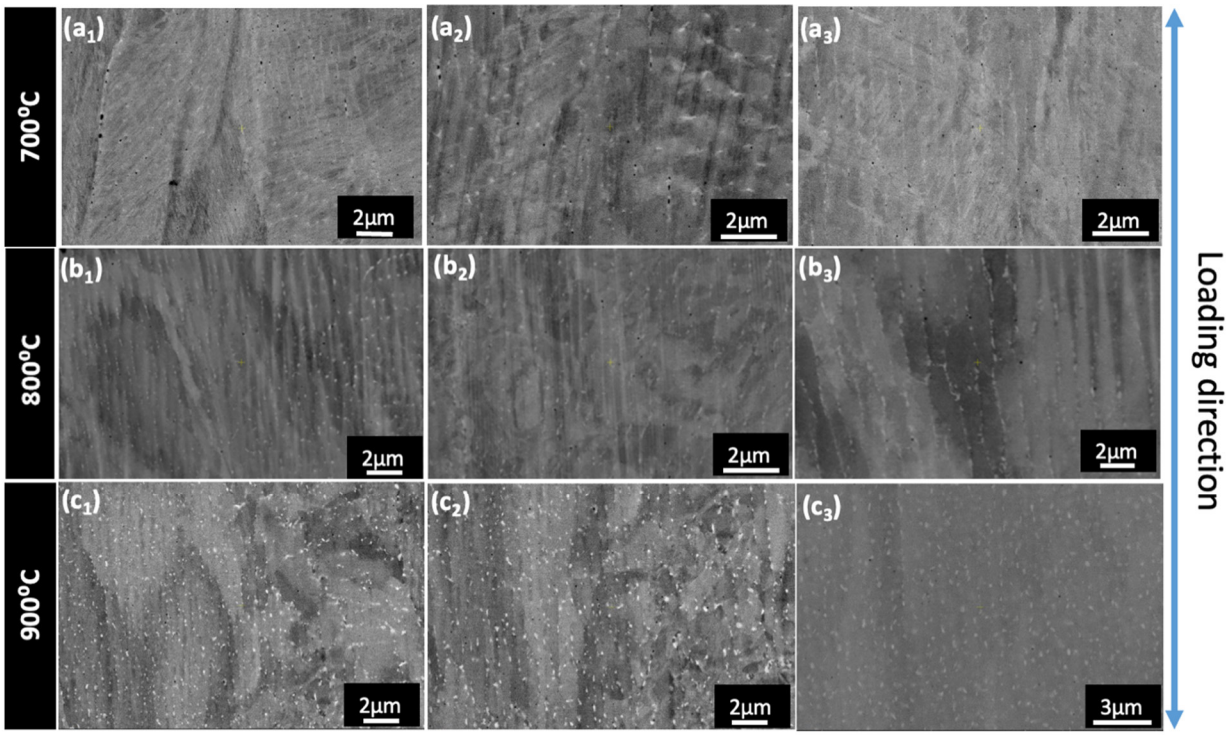

Fig. 4.33: SEM backscattered images of the gauge region of C2 alloy close to the fracture tested at (a_1-a_3): 700ºC, (b_1-b_3): 800ºC, (c_1-c_3): 900ºC. The white regions are Mo and Nb-rich Laves phase. [4]

4.2.7 Conclusions

Two low-cost non-equiatomic HEAs based on $CoCrFeNiMo_xNb_y$ were designed and processed by PBF-LB/M via in situ alloying commercial powders like Ni superalloy and stainless steel. Its processability, microstructure, and mechanical properties in rooms and at high temperatures were

evaluated in this study. The main conclusions regarding the success of mixing commodity compositions and the alloys designed are as follows:

1. The designed alloy compositions C1 and C2 achieved excellent printability after optimization, reaching densities close to 99.9% with no defects. In the as-built state, the alloys had a complete FCC matrix with almost a homogenous distribution of elements with no deleterious secondary phases.
2. Both C1 and C2 alloys achieved competitive mechanical properties, with C2 alloys exhibiting better strength from room temperature to 900 °C than C1 due to the former´s higher Mo and Nb content, enabling higher lattice distortion. Considering that no microstructure homogenization treatment has been carried out yet to improve the properties further, this approach to manufacturing HEAs through the hypothesis of pre-alloyed powder mixing is indeed promising.
3. Both the alloys exhibited good ductility at all temperatures except for C1 at 900 °C which suffered embrittlement due to the presence of Nb and Mo-rich laves precipitates along the grain boundaries, as opposed to C2, where the precipitates were dispersed throughout the matrix.

4.3 Role of mixing Al to the commercial feedstocks to fabricate HEAs via in-situ alloying in laser powder bed fusion

This section entails the work published in Ref. [5] (Paper 5 in appendix). This work was carried out in collaboration with Center for Additive Manufacturing – Metals (CAM2), Chalmers university of technology, Göteburg, Sweden.

As discussed in Section 4.2, the use of a blend of commercial commodity powders with similar density levels to develop high entropy alloys using laser powder bed fusion was feasible. So, the next step was to explore the possibility to blend lower dense powders to develop dual phase HEAs. As seen in Section 2.2.2.1, to improve the strength of CoCrFeNi HEA, Al and Mo 10are preferentially added. Al acts as a BCC stabilizer in HEAs, and with the increase in the aluminium concentration in the alloy, the final structure changes from FCC to FCC + BCC. With further increase in the Al content, full BCC will be stabilized albeit with a higher strength but lower ductility [52]. In this work, a mix of commercial commodity powders and Al powders were used as feedstock in PBF-LB/M to study the effect of the different powders and laser parameters on

the relative density and elemental distribution of the bulk HEAs. The commercial powders used were Ni625, Invar36, and CoCrF75, to obtain HEA with composition of Co-Cr-Fe-Ni-Mo-Al. The processability of this feedstock was explored by adding varying amounts of fine Al powder and studying its effect on the density.

4.3.1 Powder morphology

For the base composition, a mix of Ni625, Invar36, and CoCrF75 powders was used to fabricate CoCrFeNiMo. Two more compositions were designed by adding pure Al powders of 3.5 wt.% and 4.5 wt. % to the initial mix, hereafter referred to as 3.5Al and 4.5Al. The powders were mixed in a roller mixer for 1 hour. The morphology along with the EDS maps of the powders after mixing is shown in Fig. 4.34.

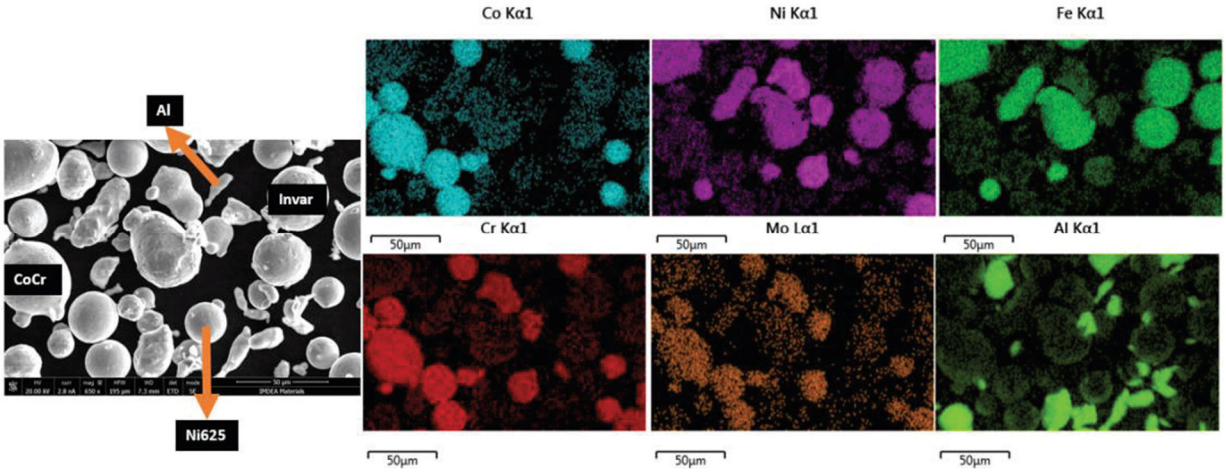

Fig. 4.34: SEM image of the powder mix with 3.5wt% Al and its corresponding EDS maps showing the elemental distribution [5]

4.3.2 Process parameter optimization

The relative density (RD) of 0Al, 3.5Al and 4.5Al samples printed for the initial screening is shown in Fig. 4.35 plotted with respect to the volume energy density (VED), which is calculated by E/vht, where E is the laser power (W), v is the scanning speed (mm/s), h is the hatch distance (mm) and t is the layer thickness (mm). The 0Al sample achieved a maximum density of 99.93%. The sample consisted of mostly fine pores with very few large pores. It was noted that the RD gradually decreased with Al addition and the maximum densities were observed in the VED range of 50-90 J/mm^3. Typically, in PBF-LB/M processes, lower VED leads to irregular lack of fusion defects due to low molten pool temperature and poor melt fluidity. A higher VED might cause over melting resulting in keyhole porosity [53] [54].

The Analysis of Variance (ANOVA) table for the initial screening is given in Table 4.10. The null hypothesis significance testing parameter, the p-value, measures the degree of significance for statistical correlations between data pairs. P-values that are less than 0.05 typically indicate strong evidence against the null hypothesis [55] [56], meaning there is a statistically significant correlation for that data pair. Based on the p-values, the model was significant, and the factor h and the interaction h*v were found to be the most significant factors that influence the RD. A contour plot between hatch distance and scanning speed is shown in Fig. 4.36, for the three Al contents for a laser power of 140W where it can be seen that the RD increases with lower h and higher v in all three cases. On increasing Al to 4.5 wt%, the dense region moves towards higher scanning speed for a fixed hatch distance and laser power, which implies a lower volume energy density. Inhomogeneities in the layer and meltpool is highly likely when adding Al to the mixed feedstocks due to its lower density and melting point, which expands the solidification range of the alloy. These inhomogeneities could cause porosity and cracks in the microstructure. Based on this result, a second DoE was performed, setting the VED limit between 50-100 J/mm^3, and a scanning speed greater than 900 mm/s, for 3.5Al and 4.5Al samples, and the relative densities were calculated. The resulting optimized parameters for all three alloys are shown in Table 4.11. The parameters were also checked for reproducibility, and their RDs obtained were close to 99.9%.

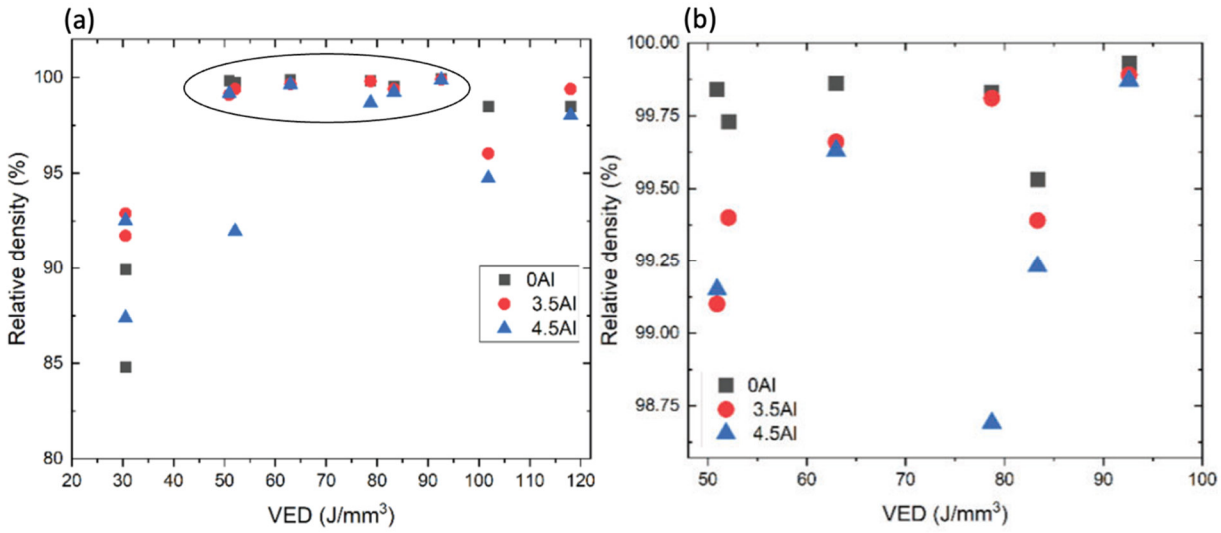

Fig. 4.35: Plot of relative density against volume energy density (VED) from (a) 20 to 120 J/mm^3 and (b) magnified plot of the encircled region between a VED of 50 to 100 J/mm^3 [5]

TABLE 4.10: ANALYSIS OF VARIANCE TABLE OF THE INITIAL SCREENING PARAMETERS (A - LASER POWER (E), B - SCANNING SPEED (v), C - HATCH DISTANCE (h), AND D - AL CONTENT (Al))

Source	F-Value	p-value
Model	7.57	0.0001 (significant)
A - E	0.51	0.485
B - v	2.18	0.1568
C - h	9.1	0.0074
D - Al	0.38	0.5442
AB	3.71	0.0702
AC	8.9	0.008
AD	0.23	0.638
BC	13.34	0.0018
BD	0.1	0.751
CD	1.54	0.23

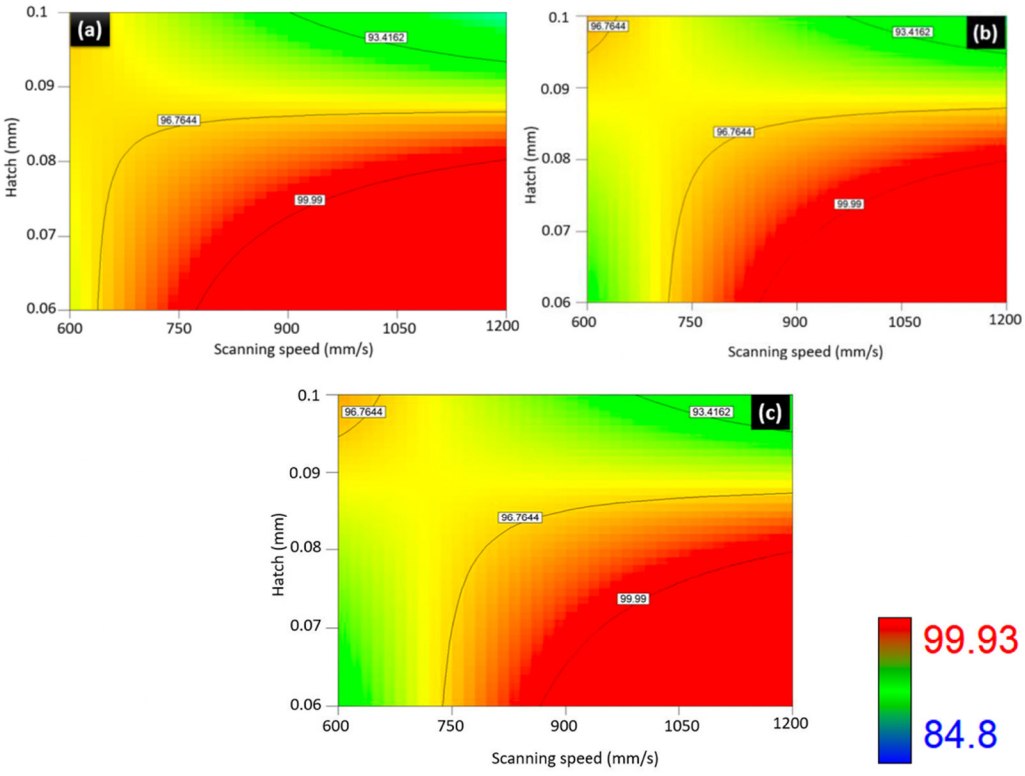

Fig. 4.36: Contour plots of relative densities showing the interaction between hatch and scanning speed for a laser power of 140W and layer thickness of 30µm for (a) 0Al, (b) 3.5Al and (c) 4.5Al sample [5]

TABLE 4.11: OPTIMIZED PARAMETERS FOR 0AL, 3.5AL AND 4.5AL WITH A LAYER THICKNESS OF 30MM

Alloy	Laser Power (W)	Scanning Speed (mm/s)	Hatch distance (mm)	Relative density (%)
0Al	150	900	0.06	99.93
3.5Al	140	1050	0.06	99.92
4.5Al	140	1050	0.06	99.91

4.3.3 Microstructural characterization and mechanical properties

The SEM backscattered image and elemental distribution of 0Al samples are shown in Fig. 4 of Paper 5 in the Appendix [5]. The distribution is almost homogenous except for localized segregations and depletions along the swirls of some of the melt pools. Similarly, the 3.5Al samples show a nearly homogenous distribution of elements, as shown in Fig. 5 (a) of paper 5 in the Appendix [5]. However, micro-cracks caused due to solidification cracking could be observed in certain regions where there was a prominent segregation, which usually happened to be along the melt pool boundaries, as shown in Fig. 5 (b) in Paper 5 in the appendix [5]. The segregation is caused by CoCrF75 powder particles as the enrichment in Co and Cr was observed near the crack. When the Al content was increased to 4.5 wt%, the Al segregation was observed to be more prominent as shown in Fig. 6 in Paper 5 in the appendix [5]. This figure shows a backscatter SEM image where the light grey regions are Al and Fe rich, and the dark region is even more enriched in Al. It is also worth noting that the darker Al enriched region is on the edge of the melt pool, which belong to the heat-affected zone with lesser heat input due to which perhaps the alloying in-situ was not complete. As mentioned in Section 4.2.4, it is challenging to control segregations during in-situ alloying due to the random mixture of powder feedstock. But in this case, blending a fine powder of Al with the commercial powders feedstock has worked well considering the resulting relative density of over 99.9%.

The Vickers hardness measured along the horizontal and vertical cross sections of the as-printed samples is shown in Table 4.12. The hardness increases with the increase in Al content due to the solid solution strengthening and lattice distortion effect due to the higher atomic size of Al compared to other elements in the HEA [57]. The 4.5Al alloy shows the maximum hardness of

293 HV along the horizontal cross-section. This matches well with the hardness of similar alloys like $Al_{0.5}CoCrFeNi$ fabricated by PBF-LB/M which was about 270HV [58,59]. The same alloy, when fabricated by vacuum arc melting had a hardness of 180 HV due to a coarser grain size [59] which shows the effectiveness of the PBF-LB/M process in both fabrication of complex alloy systems as well as achieving better mechanical properties.

TABLE 4.12: VICKER´S HARDNESS OF THE ALLOYS (HV_1)

Alloy	Hardness of horizontal cross-section (HV_1)	Hardness of vertical cross-section (HV_1)
0Al	240	260
3.5Al	290	284
4.5Al	293	291.2

4.3.4 Conclusions

The following conclusions can be made regarding the role of adding Al to the commercial feedstocks for fabricating HEAs via in-situ alloying in laser powder bed fusion:

1. The possibility of manufacturing HEAs via in-situ alloying pure Al powders, which has a much lower density and melting point, with Ni625, Invar36 and CoCrF75 was studied in this work.
2. Up to 4.5 wt.% Al was added to the studied HEA system based on $CoCrFeNiMo_xAl_y$, where near full density samples were obtained with relative densities close to 99.9%. Upon increasing Al content, it was observed that the optimum region for higher density moved towards higher scanning speeds for a fixed hatch and laser power, implying a lower VED. The distribution of elements was nearly homogenous with exception of some localized regions where some segregations and depletions were observed in the swirls of some of the meltpools. A small percentage of microcracks were present which were due to solidification cracking and some of them were due to elemental segregation. The fraction of microcracks increased with Al addition, contributing to the reduction in RD. Possibility to eliminate micro-cracking and improving microstructure homogeneity by subsequent HIP should be exploited.

3. The hardness of the alloys increased with Al addition due to solid solution strengthening and lattice distortion effect, with the maximum hardness of 293 HV achieved with 4.5 wt.% Al addition.
4. This work shows that there is a potential of adding elemental powders of different densities to the commercial commodity powders to achieve microstructural modifications to make new HEAs using laser powder bed fusion.

Bibliography

[1] J.M. Torralba, S. Venkatesh Kumarán, Development of competitive high-entropy alloys using commodity powders, Mater Lett 301 (2021) 130202. https://doi.org/10.1016/J.MATLET.2021.130202.

[2] S. Venkatesh Kumaran, D. Garbiec, J.M. Torralba, Development of High Entropy alloys using field assisted sintering and gas atomized commodity powders as raw materials, in: EuroPM, European Powder Metallurgy Association, 2021. ISBN:0A978-1-899072-54-5.

[3] S. Venkatesh Kumaran, D. Garbiec, J.M. Torralba, A novel and sustainable method to develop non-equiatomic CoCrFeNiMox high entropy alloys via spark plasma sintering using commercial commodity powders and evaluation of its mechanical behaviour, Materials Science and Engineering: A 878 (2023) 145207. https://doi.org/10.1016/J.MSEA.2023.145207.

[4] S.V. Kumaran, J.M. Torralba, Laser Powder Bed Fusion Processing of Low Cost CoCrFeNiMo x Nb y High Entropy Alloys with Promising High-Temperature Properties via In Situ Alloying Commercial Powders, Metals, (2024).

[5] Venkatesh Kumaran, B. Malladi, E. Hryha, J.M. Torralba, Effect of laser process paramaters on non-equiatomic $CoCrFeNiMo_xAl_y$ HEAs manufactured by PBF-LB/M via in-situ alloying, European powder metallurgy association (EPMA), Euro Powder Metallurgy 2023 proceedings, DOI: 10.59499/EP235762606

[6] J.W. Yeh, Recent progress in high-entropy alloys, Annales de Chimie Science Des Matériaux 31 (2006) 633–648. https://doi.org/10.3166/acsm.31.633-648.

[7] A. Takeuchi, A. Inoue, Quantitative evaluation of critical cooling rate for metallic glasses, Materials Science and Engineering: A 304–306 (2001) 446–451. https://doi.org/https://doi.org/10.1016/S0921-5093(00)01446-5.

[8] X. Yang, Y. Zhang, Prediction of high-entropy stabilized solid-solution in multi-component alloys, Mater Chem Phys 132 (2012) 233–238. https://doi.org/https://doi.org/10.1016/j.matchemphys.2011.11.021.

[9] Z. Wang, Y. Huang, Y. Yang, J. Wang, C.T. Liu, Atomic-size effect and solid solubility of multicomponent alloys, Scr Mater 94 (2015) 28–31. https://doi.org/https://doi.org/10.1016/j.scriptamat.2014.09.010.

[10] A.K. Singh, N. Kumar, A. Dwivedi, A. Subramaniam, A geometrical parameter for the formation of disordered solid solutions in multi-component alloys, Intermetallics (Barking) 53 (2014) 112–119. https://doi.org/https://doi.org/10.1016/j.intermet.2014.04.019.

[11] S. GUO, C.T. LIU, Phase stability in high entropy alloys: Formation of solid-solution phase or amorphous phase, Progress in Natural Science: Materials International 21 (2011) 433–446. https://doi.org/10.1016/S1002-0071(12)60080-X.

[12] S. Guo, C. Ng, J. Lu, C.T. Liu, Effect of valence electron concentration on stability of fcc or bcc phase in high entropy alloys, J Appl Phys 109 (2011) 103505. https://doi.org/10.1063/1.3587228.

[13] J.M. Torralba, P. Alvaredo, A. García-Junceda, High-entropy alloys fabricated via powder metallurgy. A critical review, Powder Metallurgy 62 (2019) 84–114. https://doi.org/10.1080/00325899.2019.1584454.

[14] X.A. Hu, G. Le Zhao, F.C. Liu, W.X. Liu, Microstructure and mechanical behavior of Inconel 625 alloy processed by selective laser melting at high temperature up to 1000 °C, Rare Metals 39 (2020) 1181–1189. https://doi.org/10.1007/S12598-019-01321-3/TABLES/2.

[15] Ö. Özgün, R. Yilmaz, H. Özkan Gülsoy, F. Findik, The effect of aging treatment on the fracture toughness and impact strength of injection molded Ni-625 superalloy parts, Mater Charact 108 (2015) 8–15. https://doi.org/10.1016/j.matchar.2015.08.006.

[16] A. Mostafaei, E.L. Stevens, E.T. Hughes, S.D. Biery, C. Hilla, M. Chmielus, Powder bed binder jet printed alloy 625: Densification, microstructure and mechanical properties, Mater Des 108 (2016) 126–135. https://doi.org/10.1016/j.matdes.2016.06.067.

[17] Ö. Özgün, H. Özkan Gülsoy, R. Yilmaz, F. Findik, Injection molding of nickel based 625 superalloy: Sintering, heat treatment, microstructure and mechanical properties, J Alloys Compd 546 (2013) 192–207. https://doi.org/10.1016/j.jallcom.2012.08.069.

[18] H. Carpenter, S. Tamura, The formation of twinned nanocrystals, 113 (1926). https://doi.org/https://doi.org/10.1098/rspa.1926.0144.

[19] C. Dai, Y. Fu, Y. Pan, Y. Yin, C. Du, Z. Liu, Microstructure and mechanical properties of FeCoCrNiMo0.1 high-entropy alloy with various annealing treatments, Mater Charact 179 (2021) 111313. https://doi.org/10.1016/J.MATCHAR.2021.111313.

[20] W.H. Liu, Z.P. Lu, J.Y. He, J.H. Luan, Z.J. Wang, B. Liu, Y. Liu, M.W. Chen, C.T. Liu, Ductile CoCrFeNiMox high entropy alloys strengthened by hard intermetallic phases, Acta Mater 116 (2016) 332–342. https://doi.org/10.1016/j.actamat.2016.06.063.

[21] H. Ma, C.H. Shek, Effects of Hf on the microstructure and mechanical properties of CoCrFeNi high entropy alloy, J Alloys Compd 827 (2020) 154159. https://doi.org/10.1016/J.JALLCOM.2020.154159.

[22] A. Gali, E.P. George, Tensile properties of high- and medium-entropy alloys, Intermetallics (Barking) 39 (2013) 74–78. https://doi.org/10.1016/j.intermet.2013.03.018.

[23] J. Li, Y. Cao, B. Gao, Y. Li, Y. Zhu, Superior strength and ductility of 316L stainless steel with heterogeneous lamella structure, J Mater Sci 53 (2018) 10442–10456. https://doi.org/10.1007/s10853-018-2322-4.

[24] F.K. Yan, G.Z. Liu, N.R. Tao, K. Lu, Strength and ductility of 316L austenitic stainless steel strengthened by nano-scale twin bundles, Acta Mater 60 (2012) 1059–1071. https://doi.org/10.1016/j.actamat.2011.11.009.

[25] A.B. Kale, A. Bag, J.H. Hwang, E.G. Castle, M.J. Reece, S.H. Choi, The deformation and fracture behaviors of 316L stainless steels fabricated by spark plasma sintering technique under uniaxial tension, Materials Science and Engineering A 707 (2017) 362–372. https://doi.org/10.1016/j.msea.2017.09.058.

[26] W. Wang, M. Yang, D. Yan, P. Jiang, F. Yuan, X. Wu, Deformation mechanisms for superplastic behaviors in a dual-phase high specific strength steel with ultrafine grains,

Materials Science and Engineering: A 702 (2017) 133–141. https://doi.org/10.1016/J.MSEA.2017.07.011.

[27] T.T. Shun, L.Y. Chang, M.H. Shiu, Microstructure and mechanical properties of multiprincipal component CoCrFeNiMox alloys, Mater Charact 70 (2012) 63–67. https://doi.org/10.1016/J.MATCHAR.2012.05.005.

[28] J. Wang, Y. Liu, B. Liu, Y. Wang, Y. Cao, T. Li, R. Zhou, Flow behavior and microstructures of powder metallurgical CrFeCoNiMo0.2 high entropy alloy during high temperature deformation, Materials Science and Engineering: A 689 (2017) 233–242. https://doi.org/10.1016/J.MSEA.2017.02.064.

[29] X. Yang, Y. Zhang, Prediction of high-entropy stabilized solid-solution in multi-component alloys, Mater Chem Phys 132 (2012) 233–238. https://doi.org/10.1016/j.matchemphys.2011.11.021.

[30] Charles Kittel, Introduction to Solid State Physics Charles Kittel, 2005.

[31] K.Y. Tsai, M.H. Tsai, J.W. Yeh, Sluggish diffusion in Co-Cr-Fe-Mn-Ni high-entropy alloys, Acta Mater 61 (2013) 4887–4897. https://doi.org/10.1016/j.actamat.2013.04.058.

[32] Hunan Fushel Technology Limited, (n.d.). https://www.fusnano.com/ (accessed May 6, 2021).

[33] L. Cordova, M. Campos, T. Tinga, Revealing the Effects of Powder Reuse for Selective Laser Melting by Powder Characterization, Jom 71 (2019) 1062–1072. https://doi.org/10.1007/s11837-018-3305-2.

[34] Cobalt Infocard, European Chemicals Agency (n.d.). https://echa.europa.eu/substance-information/-/substanceinfo/100.028.325?_disssubsinfo_WAR_disssubsinfoportlet_backURL=https%3A%2F%2Fecha.europa.eu%2Finformation-on-chemicals%3Fp_p_id%3Ddisssimplesearchhomepage_WAR_disssearchportlet%26p_p_lifecycle%3D0%26.

[35] European Commission, Study on the Critical Raw Materials for the EU, 2023. https://op.europa.eu/en/publication-detail/-/publication/57318397-fdd4-11ed-a05c-01aa75ed71a1.

[36] European Commission, Proposal for a Regulation of the European Parliament and of the Council establishing a framework for ensuring a secure and sustainable supply of critical raw materials and amending Regulations (EU) 168/2013, (EU) 2018/858, 2018/1724 and (EU) 2019/1020, (2016) 1–23.

[37] European Commission, Proposal for a Regulation of the European Parliament and of the council, for establishing a framework for ensuring a secure and sustainable supply of critical raw materials and amending Regulations (EU) 168/2013, (EU) 2018/858, 2018/1724 and (EU) 2019/102, 0079 (2023) 1–23. https://doi.org/10.2760/386650.

[38] R.L. Carr, Evaluating Flow Properties of Solids, Chemical Engineering 2 (1965) 163–168.

[39] Y. Zhong, L. Liu, S. Wikman, D. Cui, Z. Shen, Intragranular cellular segregation network structure strengthening 316L stainless steel prepared by selective laser melting, Journal of Nuclear Materials 470 (2016) 170–178. https://doi.org/10.1016/j.jnucmat.2015.12.034.

[40] A.J. Birnbaum, J.C. Steuben, E.J. Barrick, A.P. Iliopoulos, J.G. Michopoulos, Intrinsic strain aging, Σ3 boundaries, and origins of cellular substructure in additively manufactured 316L, Addit Manuf 29 (2019) 100784. https://doi.org/10.1016/j.addma.2019.100784.

[41] D. Lin, L. Xu, X. Li, H. Jing, G. Qin, H. Pang, F. Minami, A Si-containing FeCoCrNi high-entropy alloy with high strength and ductility synthesized in situ via selective laser melting, Addit Manuf 35 (2020). https://doi.org/10.1016/j.addma.2020.101340.

[42] L. Farquhar, G. Maddison, L. Hardwick, F. Livera, I. Todd, R. Goodall, In-Situ Alloying of CoCrFeNiX High Entropy Alloys by Selective Laser Melting, Metals 2022, Vol. 12, Page 456 12 (2022) 456. https://doi.org/10.3390/MET12030456.

[43] J. Sun, W. Zhao, P. Yan, S. Li, Z. Dai, L. Jiao, T. Qiu, X. Wang, High temperature tensile properties of as-cast and forged CrMnFeCoNi high entropy alloy, Materials Science and Engineering: A 850 (2022) 143570. https://doi.org/10.1016/J.MSEA.2022.143570.

[44] Y. Zhang, X. Wang, J. Li, Y. Huang, Y. Lu, X. Sun, Deformation mechanism during high-temperature tensile test in an eutectic high-entropy alloy AlCoCrFeNi2.1, Materials Science and Engineering: A 724 (2018) 148–155. https://doi.org/10.1016/j.msea.2018.03.078.

[45] M.G. Jo, J.Y. Suh, M.Y. Kim, H.J. Kim, W.S. Jung, D.I. Kim, H.N. Han, High temperature tensile and creep properties of CrMnFeCoNi and CrFeCoNi high-entropy alloys, Materials Science and Engineering: A 838 (2022) 142748. https://doi.org/10.1016/j.msea.2022.142748.

[46] Y. Palguna, S. Kotla, R. Korla, High temperature deformation behavior of Al0.2CoCrFeNiMo0.5 high entropy alloy: Dynamic strain ageing, J Alloys Compd 930 (2023) 167422. https://doi.org/10.1016/j.jallcom.2022.167422.

[47] Q. Wang, A. Amar, C. Jiang, H. Luan, S. Zhao, H. Zhang, G. Le, X. Liu, X. Wang, X. Yang, J. Li, CoCrFeNiMo0.2 high entropy alloy by laser melting deposition: Prospective material for low temperature and corrosion resistant applications, Intermetallics (Barking) 119 (2020) 106727. https://doi.org/10.1016/J.INTERMET.2020.106727.

[48] Z. Niu, Y. Wang, C. Geng, J. Xu, Y. Wang, Microstructural evolution, mechanical and corrosion behaviors of as-annealed CoCrFeNiMox (x = 0, 0.2, 0.5, 0.8, 1) high entropy alloys, J Alloys Compd 820 (2020) 153273. https://doi.org/10.1016/J.JALLCOM.2019.153273.

[49] W.H. Liu, T. Yang, C.T. Liu, Precipitation hardening in CoCrFeNi-based high entropy alloys, Mater Chem Phys 210 (2018) 2–11. https://doi.org/10.1016/j.matchemphys.2017.07.037.

[50] R. Fan, L. Wang, L. Zhao, L. Wang, S. Zhao, Y. Zhang, B. Cui, Synergistic effect of Nb and Mo alloying on the microstructure and mechanical properties of CoCrFeNi high entropy alloy, Materials Science and Engineering: A 829 (2022) 142153. https://doi.org/10.1016/j.msea.2021.142153.

[51] D. Wei, W. Gong, T. Tsuru, I. Lobzenko, X. Li, S. Harjo, T. Kawasaki, H.S. Do, J.W. Bae, C. Wagner, G. Laplanche, Y. Koizumi, H. Adachi, K. Aoyagi, A. Chiba, B.J. Lee, H.S.

Kim, H. Kato, Si-addition contributes to overcoming the strength-ductility trade-off in high-entropy alloys, Int J Plast 159 (2022) 103443. https://doi.org/10.1016/j.ijplas.2022.103443.

[52] C.J. Tong, Y.L. Chen, S.K. Chen, J.W. Yeh, T.T. Shun, C.H. Tsau, S.J. Lin, S.Y. Chang, Microstructure characterization of AlxCoCrCuFeNi high-entropy alloy system with multiprincipal elements, Metall Mater Trans A Phys Metall Mater Sci 36 (2005) 881–893. https://doi.org/10.1007/s11661-005-0283-0.

[53] D. Vogiatzief, A. Evirgen, M. Pedersen, U. Hecht, Laser powder bed fusion of an Al-Cr-Fe-Ni high-entropy alloy produced by blending of prealloyed and elemental powder: Process parameters, microstructures and mechanical properties, J Alloys Compd 918 (2022) 165658. https://doi.org/10.1016/J.JALLCOM.2022.165658.

[54] F. Yang, L. Wang, Z. Wang, Q. Wu, K. Zhou, X. Lin, W. Huang, Ultra strong and ductile eutectic high entropy alloy fabricated by selective laser melting, J Mater Sci Technol 106 (2022) 128–132. https://doi.org/10.1016/J.JMST.2021.08.015.

[55] Jay L. Devore, Probability and Statistics for Engineering and the Sciences, Eighth edition, Cengage learning, Boston, MA (2011)

[56] H. Akoglu, User´s guide to correlation coefficients, Turk. J. Emerg. Med., 18 (2018), pp. 91-93, https://doi.org/10.1016/j.tjem.2018.08.001

[57] F.J. Wang, Y. Zhang, G.L. Chen, Atomic packing efficiency and phase transition in a high entropy alloy, J Alloys Compd 478 (2009) 321–324. https://doi.org/10.1016/J.JALLCOM.2008.11.059.

[58] K. Sun, W. Peng, L. Yang, L. Fang, Effect of SLM processing parameters on microstructures and mechanical properties of al0.5 CoCrFeNi high entropy alloys, Metals (Basel) 10 (2020) 292. https://doi.org/10.3390/met10020292.

[59] W.R. Wang, W.L. Wang, J.W. Yeh, Phases, microstructure and mechanical properties of AlxCoCrFeNi high-entropy alloys at elevated temperatures, J Alloys Compd 589 (2014) 143–152. https://doi.org/10.1016/J.JALLCOM.2013.11.084.

CHAPTER 5

Conclusions and future work

5.1 Conclusions

The present work aims to offer new approaches to the manufacturing of high entropy alloys (HEAs) with regards to powder metallurgy and additive manufacturing. On this note, multiple manufacturing techniques and materials were utilized to explore the feasibility of using a blend of commercial powders, termed as commodity powders in this work, as a raw material feedstock. The developed HEAs using this method show promising performance and open a new avenue to explore next generation materials in a sustainable, efficient, and cost-effective manner. The major tasks involved composition design, alloy fabrication using field assisted hot pressing, spark plasma sintering and laser powder bed fusion, microstructural characterization, and mechanical property evaluation.

From the above tasks carried out, it can be concluded that high entropy alloys have been successfully obtained, which belong nearly to the cantor alloy family, using the commodity type alloys, manufactured by field assisted sintering processes and laser powder bed fusion, with promising performance. And from the mechanical properties analyzed at room and at high temperatures, it can be stated that the alloys developed using this sustainable methodology are competitive with some nickel-based superalloys designed to work at high temperatures.

The general conclusion above is further broken down into partial conclusions that correspond to the specific objectives of this thesis work:

1. The alloys developed were $Co_{25.56}Cr_{20.7}Fe_{26.92}Ni_{25.2}Mo_{1.6}$, $Co_{23.28}Cr_{28.57}Fe_{25.03}Ni_{21.01}Mo_{2.1}$, $Co_{29.07}Cr_{17.2}Fe_{28.22}Ni_{24.45}Mo_{1.06}$, which were labeled as C1, C2, and C3 respectively. C1 – with a blend of Ni625, Invar36 and CoCrF75, C2 - a blend of Ni625, 316L and CoCrF75, C3 – with a blend of Fe49Ni and CoCrF75. Firstly, prototyped samples of C1, C2 and C3 were developed by Field assisted Hot pressing (FAHP) at a temperature of 1000ºC, pressure of 50 MPa and a dwell time of 15 minutes. All three samples attained near-full density except C2, due to the increased quantity of high melting point element Cr. All three alloys consisted of FCC, BCC and HCP phases after sintering, whereas after a homogenization heat treatment at 1200ºC for 24 hours, the microstructure converted to a single FCC phase with slight grain growth, proving that this method is feasible to obtain a high entropy alloy microstructure.

2. Bulk samples of the three alloys were manufactured using spark plasma sintering (SPS) at two different temperatures of 1000ºC and 1100ºC to investigate the mechanical properties. Tensile and hot compression testing were performed on the samples. The strength of the alloys was related directly with the amount of Mo content. The best mechanical properties were exhibited by $Co_{23.28}Cr_{28.57}Fe_{25.03}Ni_{21.01}Mo_{2.1}$ HEA sintered at 1100ºC due to the higher amount of Mo, inducing more lattice distortion. It had a tensile strength of 712 MPa with a ductility of 62%. Also, it had a compression strength of 1352.5 MPa at room temperature and 642.3 MPa at 750ºC exhibiting no fracture even up to 45% elongation. Mo enhanced the sluggish diffusion effect in the HEAs as it increases the activation energy for high temperature deformation and thus the compression strength decreased with temperature with respect to the amount of Mo, in the order, C2, C1 and C3 in both the sintering temperature, 1000ºC and 1100ºC. In addition, a raw materials cost analysis was performed which showed a 20% decrease in cost when using commercial powders compared to when using pure elemental powders.

3. The same method of blending commercial commodity powders was extended to laser powder bed fusion where C1 and C2 alloys were fabricated. A process parameter optimization was carried out and both the alloys had reduced porosities of less than 0.1%. An EDS elemental distribution map revealed almost a homogenous distribution, and an EBSD phase map revealed a complete FCC phase with no deleterious secondary phases even in the as-built state which proved the feasibility of this method. To evaluate

the tensile properties, tensile testing was carried out at room temperature, and at 700ºC, 800ºC and 900ºC. C2 achieved better mechanical properties than C1 due to the higher Mo and Nb content, enabling higher lattice distortion. C2 exhibited a tensile strength of 752 MPa at room temperature and 272 MPa at 900ºC. Both the alloys exhibited good ductility at all temperatures except for C1 at 900 °C which suffered embrittlement due to the presence of Nb and Mo-rich laves precipitates along the grain boundaries, as opposed to C2, where the precipitates were dispersed throughout the matrix.

4. Since the feedstock of a blend of commercial powders to manufacture single FCC phase HEAs proved to be feasible with good mechanical properties, the next effort was to explore the poosibility of developing dual phase HEAs by adding pure Al powders to the mix. Al was added to the C1 mix in 3.5 wt% and 4.5 wt%. A detailed design of experiments was carried out by adding Al as a factor. After optimization, remarkably high relative densities upto 99.9% was reached. Upon increasing Al content, it was observed that the optimum region for higher density moved towards higher scanning speeds for a fixed hatch and laser power, implying a lower VED. The distribution of elements was nearly homogenous with exception of some localized regions where some segregations and depletions were observed in the swirls of some of the meltpools. A small percentage of microcracks were present which were due to solidification cracking and some of them were due to elemental segregation, which can be healed using Hot Isostatic Pressing (HIP). The hardness of the alloys increased with Al addition due to solid solution strengthening and lattice distortion effect, with the maximum hardness of 293 HV achieved with 4.5 wt.% Al addition. This work shows that there is a potential of adding elemental powders of different densities to the commercial commodity powders to achieve microstructural modifications to make new HEAs using laser powder bed fusion.

5. Overall, the research carried out for this PhD thesis aimed to approach the manufacturing of powder metallurgy HEAs (PMHEAs) from a cost-effective, sustainable, and high-throughput manner enabling its commercialization. It is cost-effective because it avoids the use of pure elemental powders, which are very expensive, and it avoids the cost from mechanical alloying/gas atomization, by using a blend of commercial mass-produced powders which can be a commodity for

manufacturing HEAs. It is sustainable because using such commodity compositions can result in the use of steel and superalloy scraps to produce HEAs or powders made from such scraps to produce PMHEAs. It is a high-throughput technique because it offers a flexible and rapid way to explore new HEA compositions instead of mechanical alloying/gas atomizing each promising composition.

5.2 Future work

New avenues have been opened for the manufacturing of powder metallurgy HEAs using the approach in this thesis which has been shown to be successful with different material compositions and manufacturing techniques. But this has also opened multiple lines of research for further exploration described below.

5.2.1 Materials

The materials developed in this work started with readily available commercial powders. However, there are plenty of other commercial powders available which can be made use of to produce interesting HEAs tailored to a specific application. This thesis focused on 3D transition HEAs with additions of Mo and Nb for higher strength at room and high temperature. Other types of HEAs can be produced by mixing commercial alloys like Ti6Al4V or lightweight HEAs can be produced by using Al alloys and Mg alloys.

5.2.2 Methodologies

In this work, the manufacturing techniques used were field assisted hot pressing, spark plasma sintering and laser powder bed fusion. Beyond this, there are several other fabrication techniques which can utilized. For example, metal injection moulding (MIM) is a promising technology that can be used to make HEAs by mixing commodity powders with suitable binders and not much work has been done in this regard so far. Additionally, "feedstock-based" 3D printing methods (such as composite extrusion modelling) require similar optimization methods to those used in MIM. When it comes to laser powder bed fusion, the processability of the HEAs can be compared between a pulsed wave and a continuous wave emission of the lasers especially for the Al based HEAs as it is more crack-prone. Hot Isostatic Pressing (HIP) can be optimized for the parts printed with PBF-LB/M to heal any cracks and fix the slight inhomogeneities in the elemental distribution due to in-situ alloying.

Having demonstrated the feasibility of 3D methods based on laser powder bed fusion, direct energy deposition (DED) methods are perfectly applicable with our methodology, since in

DED, alloys can be easily constructed from powders of different compositions without having to optimise at the same extremes as in PBF-LB/M.

5.2.3 Properties

A variety of properties beyond tensile can be tested for the materials developed in this work. Firstly, since the HEAs contain Mo, it enhances the pitting corrosion resistance. A detailed corrosion study can be conducted on the different HEAs and can be compared with respect to the manufacturing processes i.e., SPS and PBF-LB/M. The same goes for fatigue, creep, and fracture mechanics.
Moreover, heat treatments must be tailored to explore the possibility of precipitating dual phases in the Al based HEAs and analysing their mechanical properties.

In this thesis work we have focused on mechanical properties at room temperature and at high temperature, but high entropy alloys of the same family as those developed have demonstrated high capabilities in other areas such as oxidation and corrosion resistance. A work developed in parallel to this thesis work, where the C2 alloy fabricated by PBF-LB/M has been used, has shown excellent hydrogen embrittlement behaviour (work yet to be published), opening up the possibility of hydrogen storage applications.

Appendix

The five publications under the purview of this thesis is appended in this section.

Paper 1

JM Torralba, S Venkatesh Kumaran, Development of competitive high-entropy alloys using commodity powders, Materials letters, (2021), Vol. 301, 130202, https://doi.org/10.1016/j.matlet.2021.130202

Materials Letters 301 (2021) 130202

Contents lists available at ScienceDirect

Materials Letters

journal homepage: www.elsevier.com/locate/matlet

Development of competitive high-entropy alloys using commodity powders

José M. Torralba [a,b,*], S. Venkatesh Kumarán [b]

[a] Universidad Carlos III de Madrid, IMDEA Materials Institute, 28911 Leganes, Madrid, Spain
[b] IMDEA Materials Institute, 28906 Getafe, Madrid, Spain

ARTICLE INFO

Keywords:
High-entropy alloys
Powder metallurgy
Commercial powders
Field assisted sintering

ABSTRACT

One of the main drawbacks of the powder metallurgy route for High-Entropy Alloys (HEAs) is the unavailability of fully pre-alloyed powders in the market. Using commodity powders (commercial Ni, Fe and Co base fully pre-alloyed powders, fully available in large quantities and at competitive prices) to produce HEAs presents a completely new and competitive scenario for obtaining viable alloys for high-performance applications.

1. Introduction

Since the concept of "high-entropy alloys" (HEAs) was introduced in 2004 [1,2], extensive research on this family of alloys has resulted in >4000 papers, according to the Scopus database. Despite ingot metallurgy is the most common way to develop and manufacture HEAs, powder metallurgy (PM) has shown high potential for manufacturing HEAs. PM has provided an alternative technology for HEA development that achieves significantly higher compositional accuracy than other methods, while preventing segregation and achieving superior microstructural control [3]. Powder metallurgy high-entropy alloys (PMHEAs) have been developed using three different classes of powders to date: fully prealloyed powders (usually gas-atomized), pure elemental powders and mechanically alloyed powders (which are fabricated from elemental powders). The source of the powders depends on the PM manufacturing route selected. The cost and availability of powders limit the use of PM for fabricating HEAs. There are no fully prealloyed powders on the market with the specific compositions of even the most extensively studied HEAs and pure powders are usually expensive and can be difficult to manage. However, many grades of powder are available on the market that belong to the families of metals on which many HEAs are based: Ni, Cr, Fe, Co, Ti, Al, etc. These grades are all fully commercially available (the compositions of these powders are widely used in the industry) from several manufacturers and can be delivered in large quantities within short times at competitive prices. These families of available alloys in mass production are designated by the term "commodity", for which the following hypothesis is presented in this paper: is it feasible to produce a HEA using a mix of commodity powders as raw materials? We investigate this hypothesis by predicting the HEA formation from mixing properly fully prealloyed commodity powders Ni625, INVAR36, CoCrF75 (62%Co-32%Cr-4%Mo-Co bal.wt.%), Fe49Ni and 316L. We also validate the hypothesis by manufacturing by PM route one of the proposed compositions.

2. Materials and methods

The selected alloys are available on the market as gas-atomized powders from different providers (the Co base powders from VDM Metals (Germany) and the rest from Sandvick Osprey (UK). Table 1 presents the role and compositional features of each alloy in the target HEA. Table 2 shows the proposed weight percentages mixed in the alloys to produce the final composition, shown in atomic percentages. Can a "real" HEA be obtained using these powder mixes?

This novel class of materials known as high-entropy alloys were first defined as those containing five or more elements in relatively high (5–35 at.%) or even equiatomic concentrations [1,4]. This composition-based definition was later modified [5]. That is, HEAs are no longer required to be equimolar and can contain minor elements used to modify the properties of the base HEA [6]. Our proposed HEA based on three commodity powders would not fall within existing definitions of HEAs. However, a definition based on the magnitude of the entropy has been considered since the earliest development of these alloys. The configurational mixing entropy ΔS_{mix} can be used to classify alloys as low ($\Delta S_{mix,\,ideal} < 0.69R$), where $\Delta S_{mix,\,ideal}$ is the total configurational molar entropy in an ideal solid solution and R is the gas constant), medium ($0.69R < \Delta S_{mix,\,ideal} < 1.61R$) and high ($\Delta S_{mix,\,ideal} > 1.61R$) entropy alloys [6]. The value of the configurational mixing entropy ΔS_{mix} can be easily obtained [7]. Also the value of the enthalpy of

* Corresponding author.
E-mail addresses: torralba@ing.uc3m.es, josemanuel.torralba@imdea.org (J.M. Torralba).

https://doi.org/10.1016/j.matlet.2021.130202
Received 2 March 2021; Received in revised form 19 April 2021; Accepted 3 June 2021
Available online 6 June 2021

Table 1
Proposed "commodity" alloys and their role in the target HEA.

			wt. (%)				
Alloy	Size (d90) (μm)	Role	Ni	Fe	Cr	Mo	Co
Ni625	45	Source of Ni, Cr, Fe and Mo	61,54	5,35	25,26	5,6	–
INVAR 36	5	Source of Fe and Ni	34,8	65,14	–	–	–
CoCrF75	53	Source of Co, Cr and Mo	0,51	0,8	32,57	3,72	62,41
316L	22	Source of Fe, Cr, Ni and Mo	11.82	67.77	18.9	1.51	
Fe49Ni	22	Source of Fe, Ni	47.76	52.24			

Table 2
Proposed mixes of commodity powders used to develop different possible HEAs.

	Weight %					Atomic %				
Alloy	Ni625	INVAR 36	CoCrF75	316L	Fe49Ni	Ni	Fe	Cr	Mo	Co
C1	20	38	42			25,45	27,42	20,44	1,59	25,1
C2	28		38	33		21.18	24.42	25.92	3.6	23.11
C3			48		52	24.44	27.55	15.63	1.79	29.96

Table 3
Different assessment parameters for HEAs.

	Obtained value				
Parameter	C1	C2	C3	Threshold values	Reference
ΔS_{mix}^{conf}	1.44R	1.48R	1.43R	> 1.61R	[6]
ΔH_{mix} (kJ/Mol)	−6.3727	−6.2822	−6.636	$-11.6 < \Delta H_{mix} < 3.2$	[15]
Ω/1000	3.52	3.7	3.3	≥1.1	[16]
100δ	1.69	2.24	1.85	<6.6	[16]
γ	1.1324	1.1333	1.1328	<1,175	[11]
Λ	4.19	9.58	9.21	>0.96	[13]
VEC	8.32	7.92	8.38	>8 for FCC	[17]

mixing for a multicomponent alloy system with n elements can be determined to predict the formation of the HEA [8].

Other criteria have been introduced to predict the formation of a single solid solution (SSS) HEA [9]. A recent study provided an extensive classification of such alloys, including an analysis of the compositional accuracy and the factors that significantly impact this accuracy [10], including the parameters, Ω and δ, defined in [18] to assess the forming ability of a simple solid solution. Ω reflects the relative strength of the entropy and the enthalpy, and δ is a measure of the atomic size difference in the alloy. Thus, a simple solid solution forms when the entropy is large relative to the enthalpy and there is a small atomic size difference in the alloy. A novel parameter, γ, was proposed in [11] as a measure of the atomic size difference [12]. Singh et al. [13] proposed another single-parameter model by defining $\Lambda = \Delta Smix/\delta 2$. SSS formation was

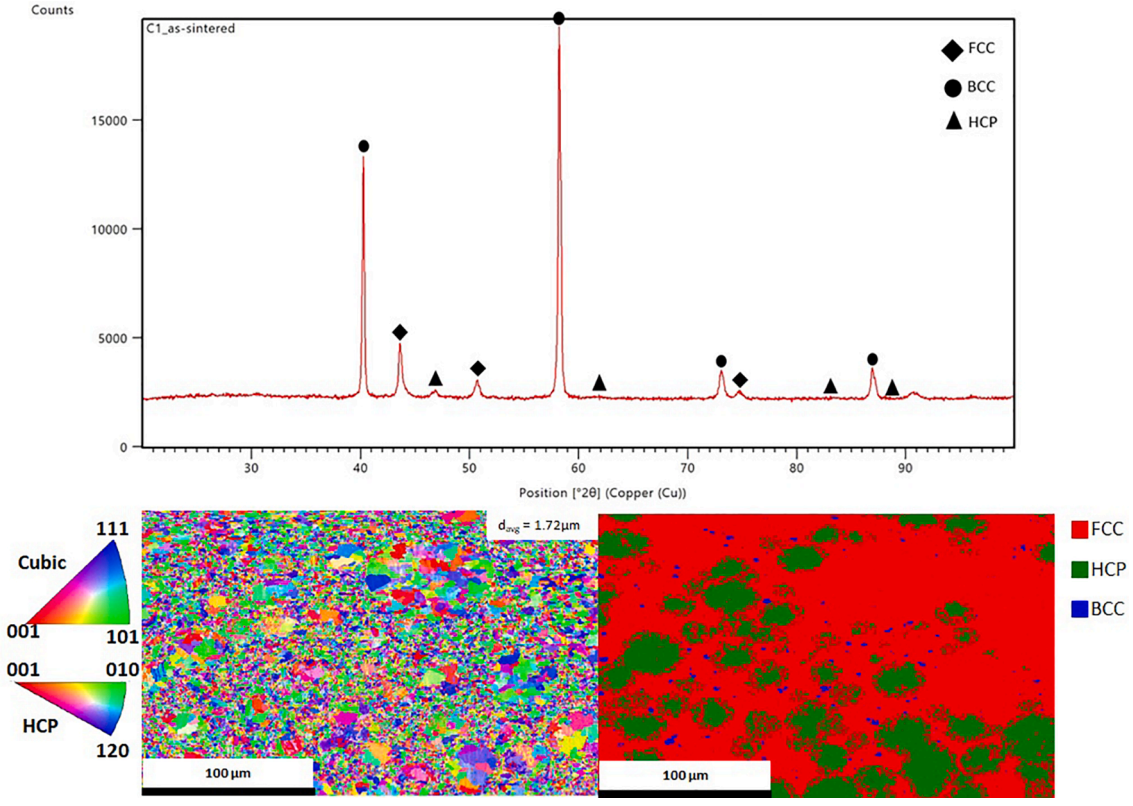

Fig. 1. Up, XRD pattern and, down, EBSD inverse pole figure (IPF-Z) map of the alloy and EBSD phase map of the as-sintered sample.

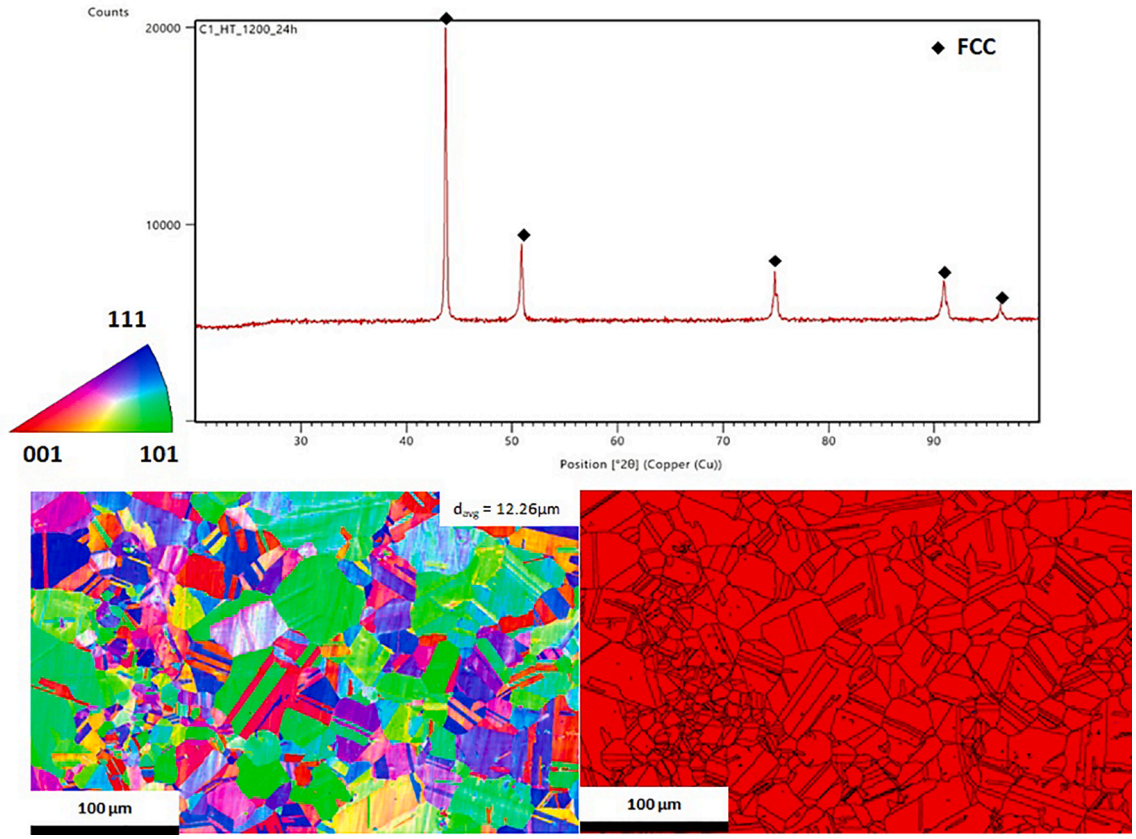

Fig. 2. Up, XRD pattern of the as-sintered sample. Down, EBSD inverse pole figure (IPF-Z) map of the alloy and EBSD phase map.

reported to be favored for $\Lambda > 0.96$, i.e., a large configurational entropy and a small atomic size difference. Atomic size differences play a central role in this model.

The valence electron concentration (VEC) can be used to determine the suitability of an FCC or BCC alloy as an HEA [14]. The VEC plays a decisive role in determining whether an HEA exists as a FCC- or BCC-type solid solution, that is, a large VEC ($\geq$8) favors the formation of FCC-type solid solutions, whereas a small VEC (<6.87) favors the formation of BCC-type solid solutions.

Once we assess the prediction that the proposed alloy compositions can form a simple solid solution, we have fabricated one of the alloys (C1) as a bulk material by manual mixing followed by field-assisted hot pressing and annealing. The three commodity powders were used as the raw materials (the quantity of each powder in the mix are shown in Table 1). Field-assisted hot pressing was performed using a Gleeble3800 at 50 MPa and 1000 °C for 15 min. The obtained density of the sintered samples was 94% of the theoretical density. Annealing was performed in vacuum at 1200 °C for 24 h. A phase analysis was performed using the PANalytical X-ray diffractometer with a Cu Kα source. The microstructures were observed via double-beam scanning electron microscopy (Helios Nanolab 600i) equipped with an electron backscatter diffraction (EBSD) device.

3. Results and discussion

Table 3 shows the calculated values of the aforementioned parameters for the proposed alloys, as well as the threshold values. The calculated parameter values for the proposed alloys suggest that PMHEAs can be feasibly obtained using mixes of commodity powders, and according these predictions the alloys C1 and C3 will produce a FCC single phase and C2 a mix of BCC and FCC.

Fig. 1 (down) shows an EBSD inverse pole figure (IPF) map of the as-sintered alloy. The average grain size was measured as 1.72 µm. The EBSD phase map shows three main phases (the FCC phase is shown in red, the HCP phase is shown in green and the BCC phase is shown in blue), which were also detected by XRD (Fig. 1, up).

The HEA was fully developed after annealing (Fig. 2), and only the FCC phase can be observed in both the XRD pattern and the EBSD phase map. The microstructure shows only FCC grains (Fig. 2, down). The average grain size in the annealed sample is 12.26 µm. There is an slightly increase in the grain size due to the higher annealing temperature/time.

4. Conclusions

The results of this preliminary study show that powder metallurgy presents a promising way to produce HEAs using commodity powders, which are inexpensive raw materials (in comparison with gas-atomized powders tailored to specific HEA compositions or elemental powders) that are fully commercially available in large quantities. This study identifies new opportunities for the development of HEAs and their implementation in industry.

CRediT authorship contribution statement

José M. Torralba: Conceptualization, Formal analysis, Funding acquisition, Investigation, Methodology, Project administration, Supervision, Validation, Visualization, Writing - original draft, Writing - review & editing. **S. Venkatesh Kumarán:** Data curation, Formal analysis, Investigation, Validation, Visualization, Writing - review & editing.

Declaration of Competing Interest

The authors declare that they have no known competing financial interests or personal relationships that could have appeared to influence

the work reported in this paper.

Acknowledgments

Authors wish to thank to IMDEA Materials Institute for the financial support to this research.

References

[1] J.-W. Yeh, S.-K. Chen, S.-J. Lin, J.-Y. Gan, T.-S. Chin, T.-T. Shun, C.-H. Tsau, S.-Y. Chang, Nanostructured high-entropy alloys with multiple principal elements: Novel alloy design concepts and outcomes, Adv. Eng. Mater. 6 (2004) 299–303, https://doi.org/10.1002/adem.200300567.
[2] B. Cantor, I.T.H.T.H. Chang, P. Knight, A.J.B.J.B. Vincent, Microstructural development in equiatomic multicomponent alloys, 375–377 (2004) 213–218.
[3] J.M. Torralba, P. Alvaredo, A. García-Junceda, High-entropy alloys fabricated via powder metallurgy. A critical review, Powder Metall. 62 (2019), https://doi.org/10.1080/00325899.2019.1584454.
[4] E.P. George, D. Raabe, R.O. Ritchie, High-entropy alloys, Nat. Rev. Mater. 4 (8) (2019) 515–534, https://doi.org/10.1038/s41578-019-0121-4.
[5] D.B.B. Miracle, O.N.N. Senkov, A critical review of high entropy alloys and related concepts, Pergamon, 2017.
[6] J.-W. Yeh, Recent progress in high-entropy alloys, Ann. Chim. Sci. Des Matériaux. 31 (6) (2006) 633–648, https://doi.org/10.3166/acsm.31.633-648.
[7] W. Steurer, Single-phase high-entropy alloys – A critical update, Mater. Charact. 162 (2020), 110179, https://doi.org/10.1016/j.matchar.2020.110179.
[8] F.R. de Boer, W.C.M. Mattens, R. Boom, A.R. Miedema, A.K. Niessen, Cohesion in metals, North-Holland, Netherlands, 1988 http://inis.iaea.org/search/search.aspx?orig_q=RN:20078890.
[9] M.C. Troparevsky, J.R. Morris, P.R.C. Kent, A.R. Lupini, G.M. Stocks, Criteria for predicting the formation of single-phase high-entropy alloys, Phys. Rev. X. 5 (2015) 11041, https://doi.org/10.1103/PhysRevX.5.011041.
[10] J.-H. Li, M.-H. Tsai, Theories for predicting simple solid solution high-entropy alloys: Classification, accuracy, and important factors impacting accuracy, Scr. Mater. 188 (2020) 80–87, https://doi.org/10.1016/j.scriptamat.2020.06.064.
[11] Z. Wang, Y. Huang, Y. Yang, J. Wang, C.T. Liu, Atomic-size effect and solid solubility of multicomponent alloys, Scr. Mater. 94 (2015) 28–31, https://doi.org/10.1016/j.scriptamat.2014.09.010.
[12] Z. Yuan, W. Tian, F. Li, Q. Fu, Y. Hu, X. Wang, Microstructure and properties of high-entropy alloy reinforced aluminium matrix composites by spark plasma sintering, J. Alloys Compd. (2019), https://doi.org/10.1016/j.jallcom.2019.07.185.
[13] A.K. Singh, N. Kumar, A. Dwivedi, A. Subramaniam, A geometrical parameter for the formation of disordered solid solutions in multi-component alloys, Intermetallics. 53 (2014) 112–119, https://doi.org/10.1016/j.intermet.2014.04.019.
[14] S. Guo, C. Ng, J. Lu, C.T. Liu, Effect of valence electron concentration on stability of fcc or bcc phase in high entropy alloys, J. Appl. Phys. 109 (2011), 103505, https://doi.org/10.1063/1.3587228.
[15] A. Takeuchi, A. Inoue, Quantitative evaluation of critical cooling rate for metallic glasses, Mater. Sci. Eng. A. 304–306 (2001) 446–451, https://doi.org/10.1016/S0921-5093(00)01446-5.
[16] X. Yang, Y. Zhang, Prediction of high-entropy stabilized solid-solution in multi-component alloys, Mater. Chem. Phys. 132 (2-3) (2012) 233–238, https://doi.org/10.1016/j.matchemphys.2011.11.021.
[17] S. Guo, C.T. Liu, Phase stability in high entropy alloys: Formation of solid-solution phase or amorphous phase, Prog. Nat. Sci. Mater. Int. 21 (2011) 433–446, https://doi.org/10.1016/S1002-0071(12)60080-X.

Paper 2

JM Torralba, S Venkatesh Kumaran, “Development of High Entropy alloys using field assisted sintering and gas atomized commodity powders as raw materials”, European powder metallurgy association (EPMA), Euro Powder Metallurgy 2021 proceedings, ISBN: 978-189907254-5

Manuscript refereed by Mr Peter Kjeldsteen (Sintex a|s, Denmark)

Development of competitive high-entropy alloys using commodity powders

José M. Torralba[1]; S. Venkatesh Kumaran[2]
[1] torralba@ing.uc3m.es Universidad Carlos III de Madrid, IMDEA Materials Institute, 28911 Leganes, Madrid, Spain
[2] venkatesh.sivagnana@imdea.org IMDEA Materials Institute, 28906 Getafe, Madrid, Spain

Abstract

High-Entropy Alloys (HEAs) are undoubtedly currently one of the most rapidly emerging materials, and the powder metallurgy routes are an interesting possibility for manufacturing HEAs. One of the main drawbacks of the powder metallurgy route is the unavailability of fully pre-alloyed powders in the market, which makes powder route development an expensive alternative to the ingot metallurgy route. The possibility using commodity powders (which are fully available in large quantities and at competitive prices) to produce HEAs presents a completely new and competitive scenario for obtaining viable alloys for high-performance applications.

Since the concept of “high-entropy alloys” (HEAs) was introduced first by Yo [1] in 2000 and again in 2004 [2,3], extensive research on this family of alloys has resulted in more than 4000 papers, according to the Scopus database. Most of the studies related to HEAs have involved the development of processing methods based on ingot metallurgy. Arc melting has been proven as a highly efficient technique among the processing methods available and involves melting over five metals, some of which have high melting points, followed by solidification to produce alloys with a good level of solubility and without segregation. However, the drawbacks of ingot metallurgy limit its potential application for fabricating alloys with a complex composition, such as HEAs. Within this context, powder metallurgy (PM) has shown high potential for manufacturing HEAs. The first papers on the use of PM to develop HEAs appeared a few years after HEAs were first introduced [4–6]. PM has provided an alternative technology for HEA development that achieves significantly higher compositional accuracy than other methods, while preventing segregation and achieving superior microstructural control (including the formation of nanocrystalline materials), resulting in facile production of metal matrix composites. PM offers two additional advantages over other forming techniques: (1) PM can be applied to metals with dissimilar densities and can therefore be used to fabricate lightweight HEAs [7] or even eutectic HEAs[8]; and (2) PM can be applied when many metals with extremely high melting points are involved and can therefore be used to fabricate so-called refractory HEAs[9]. Powder metallurgy high-entropy alloys (PMHEAs) have been developed using three different classes of powders to date: fully prealloyed powders (usually gas-atomized), pure elemental powders and mechanically alloyed powders (which are fabricated from elemental powders)[10]. The source of the powders depends on the PM manufacturing route selected. The cost and availability of powders limit the use of PM for fabricating HEAs. There are no fully prealloyed powders in the market with the specific compositions of even the most extensively studied HEAs. There are many problems associated because the level of interstitial contamination must be maintained, and pure powders are usually expensive and can be difficult to manage. However, many grades of powder are available on the market that belong to the families of metals on which many HEAs are based: Ni, Cr, Fe, Co, Ti, Al, etc. These grades are all fully commercially available (the compositions of these powders are widely used in the industry) from several manufacturers and can be delivered in large quantities within short times at competitive prices. These families of available alloys in mass production are designated by the term “commodity”, for which the following hypothesis is presented in this paper: it is feasible to produce a HEA using a mix of commodity powders as raw materials. We investigate this hypothesis by using the PM route to produce different HEAs from Ni625, INVAR36, F75 CoCr, Fe49Ni and 316L. These alloys are available on the market as gas-atomized powders from different providers (the Co base powders used in this study were obtained from VDM Metals (Germany) and the rest from Sandvick Osprey (UK)). Table 1 presents the role and compositional features of each alloy in the target HEA.

Table 1. Proposed “commodity” alloys and their role in the target HEA.

			wt. (%)				
Alloy	Size (d90) (µm)	Role	Ni	Fe	Cr	Mo	Co
Ni625	45	Source of Ni, Cr, Fe and Mo	61,54	5,35	25,26	5,6	-
INVAR 36	5	Source of Fe and Ni	34,8	65,14	-	-	-
CoCrF75	53	Source of Co, Cr and Mo	0,51	0,8	32,57	3,72	62,41
316L	22	Source of Fe, Cr, Ni and Mo	11.82	67.77	18.9	1.51	
Fe49Ni	22	Source of Fe, Ni	47.76	52.24			

Table 2 shows the proposed weight percentages mixed in the alloys to produce the final composition, shown in atomic percentages. Can a “real” HEA be obtained using this powder mix? Many criteria (associated with forming a unique solid solution and phases) must be satisfied to establish the suitability of a mix of elements for fabricating an HEA with the desired characteristics.

Table 2. Proposed mixes of commodity powders used to develop different possible HEAs.

	Weight %					Atomic %				
Alloy	Ni625	INVAR 36	CoCrF75	316L	Fe49Ni	Ni	Fe	Cr	Mo	Co
C1	20	38	42			25,45	27,42	20,44	1,59	25,1
C2	28		38	33		21.18	24.42	25.92	3.6	23.11
C3			48		52	24.44	27.55	15.63	1.79	29.96

This novel class of materials known as high-entropy alloys were first defined as those containing five or more elements in relatively high (5–35 at.%) or even equiatomic concentrations [2,11]. This composition-based definition was later modified [12]. That is, HEAs are no longer required to be equimolar and can contain minor elements used to modify the properties of the base HEA [13]. Most definitions of HEAs do not refer to the magnitude of the entropy or the presence of a single-phase solid solution. Our proposed HEA based on three commodity powders would not fall within existing definitions of HEAs. However, a definition based on the magnitude of the entropy has been considered since the earliest development of these alloys. The configurational mixing entropy ΔS_{mix} can be used to classify alloys as low- ($\Delta S_{mix,\ ideal} < 0.69R$, where $\Delta S_{mix,\ ideal}$ is the total configurational molar entropy in an ideal solid solution and R is the gas constant), medium-($0.69R < \Delta S_{mix,\ ideal} < 1.61R$) and high-($\Delta S_{mix,\ ideal} > 1.61R$) entropy alloys[13]. The value of the configurational mixing entropy ΔS_{mix} can be approximated as follows [14]:

$$\Delta S_{mix} = -R \sum_{i=1}^{n} C_i ln C_i \quad (1),$$

where R is the gas constant, 8.314 J $K^{-1}mol^{-1}$, and C_i is the mole fraction of the i^{th} of N components (different chemical elements). ΔS_{mix} is always positive and maximal for an alloy with an equiatomic chemical composition and a random distribution of N components on the lattice sites. However, it is important that HEAs are in a single phase, and many criteria have been introduced to predict the formation of single-phase high-entropy alloys [15]. A recent study provided an extensive classification of such alloys, including an analysis of the compositional accuracy and the factors that significantly impact this accuracy[16].

The enthalpy of mixing for a multicomponent alloy system with n elements can be determined using the following equation[17]:

$$\Delta H_{mix} = \sum_{i=1,\ i \neq j}^{n} 4\Delta H_{ij}^{mix} C_i C_j \quad (2),$$

where ΔH_{ij}^{mix} is the mixing enthalpy of a binary liquid $i_{50}j_{50}$ alloy.

Many other parameters were introduced (see in Table 3 how to obtain them and in Table 4 the threshold values) by different authors to predict the suitability of forming a HEA. Ω and δ, were defined

in [18] to assess the forming ability of a simple solid solution. Ω reflects the relative strength of the entropy and the enthalpy, and δ is a measure of the atomic size difference in the alloy. Thus, a simple solid solution forms when the entropy is large relative to the enthalpy and there is a small atomic size difference in the alloy. A novel parameter, γ, was proposed in [20] as a measure of the atomic size difference[21]. Singh et al.[22] proposed another single-parameter model by defining $\Lambda = \Delta S_{mix}/\delta^2$. SSS formation was reported to be favored for Λ> 0.96, i.e., a large configurational entropy and a small atomic size difference. This model is the unique among current models in that the effect of the enthalpy is not considered. The configurational entropy is relatively insensitive to the HEA composition. Atomic size differences play a central role in this model.

The valence electron concentration (VEC) can be used to determine the suitability of an FCC or BCC alloy as an HEA [23]. The VEC plays a decisive role in determining whether an HEA exists as a FCC- or BCC-type solid solution, that is, a large VEC (≥8) favors the formation of FCC-type solid solutions, whereas a small VEC (<6.87) favors the formation of BCC-type solid solutions. See also Table 3 to see the way to calculate VEC [24].

Table 3. Different proposed parameters regarding the forming suitability for a HEA.

$\Omega = \frac{T_m \Delta S_{mix}}{\lvert \Delta H_{mix} \rvert}$ (*)	$\delta = \sqrt{\sum_{i=1}^{n} C_i \left(1 - \frac{r_i}{\bar{r}}\right)^2}$ (**)	$\Lambda = \Delta S_{mix}/\delta^2$	$VEC = \sum_{i=1}^{n} C_i (VEC)_i$ (**)
$\gamma = \omega_s/\omega_L = \left(1 - \sqrt{\frac{(r_s+\bar{r})^2 - \bar{r}^2}{(r_s+\bar{r})^2}}\right) / \left(1 - \sqrt{\frac{(r_L+\bar{r})^2 - \bar{r}^2}{(r_l+\bar{r})^2}}\right)$ (*)			
(*) ω_S and ω_L are the solid angles of the smallest and the largest atoms, respectively, with respect to the surrounding atoms. T_m is the rule-of-mixtures (ROM) melting point of the alloy, $\bar{r}$ is the average atomic radius in the alloy obtained by ROM and r_i is the atomic radius of the i^{th} element. The atomic radii in [18] were used to calculate r_i.			
(**)$(VEC)_i$ and c_i are the VEC and the atomic percentage of the i^{th} component, respectively			

Table 4 shows the calculated values of the aforementioned parameters for the proposed alloys, as well as the threshold values required to form a SSS.

Table 4. Different assessment parameters for HEAs.

	Obtained value				
Parameter	C1	C2	C3	Threshold values	Reference
ΔS_{mix}^{conf}	1.44R	1.48R	1.43R	> 1.61R	[13]
ΔH_{mix} (kJ/Mol)	-6.3727	-6.2822	-6.636	$-11.6 < \Delta H_{mix} < 3.2$	[25]
Ω/1000	3.52	3.7	3.3	≥1.1	[19]
100δ	1.69	2.24	1.85	<6.6	[19]
γ	1.1324	1.1333	1.1328	<1,175	[20]
Λ	4.19	9.58	9.21	>0.96	[22]
VEC	8.32	7.92	8.38	>8 for FCC	[24]

The calculated parameter values for the proposed alloys shown in Table 4 suggest that PMHEAs can be feasibly obtained using mixes of commodity powders. Figure 1 shows graphs from [24] and [23] for the alloys analyzed in this study: these approximations show that the three proposed alloys can form a single solid solution, and two of the alloys can form a simple FCC structure.

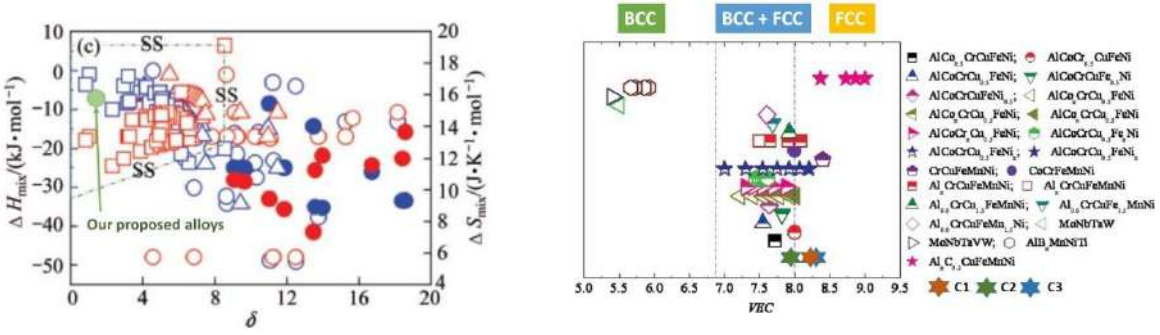

Figure 1. Left, prediction for forming a single solid solution based on thermodynamical values and the δ parameter [24], and, right, prediction for forming BCC or FCC phases based on the VEC [23].

Motivated by the prediction that the proposed alloy compositions can form a simple solid solution, we fabricated all the alloys (C1, C2, and C3) as a bulk material by simple mixing followed by field-assisted hot pressing and annealing. The proposed methodology is shown in Fig. 2. The commodity powders were used as the raw materials (the chemical composition and quantity of each powder in the mixes are shown in Table 2). The maximum size of each class of powders is presented in Table 1. Field-assisted hot pressing was performed using a Gleeble3800 at 50 MPa and 1000 °C for 15 minutes. The density of the sintered C1, C2 and C3 samples were 94%, 88.26%, and 93% of the theoretical density. Annealing was performed in vacuum at 1200 °C for 24 hours. A microstructural analysis was performed on the sintered and annealed samples. A phase analysis was performed using the PANalytical X-
ray diffractometer with a Cu Kα source. The microstructures were observed via double-beam scanning electron microscopy (Helios Nanolab 600i) equipped with an electron backscatter diffraction (EBSD) device.

The XRD and EBSD results of C1 alloy are shown in Fig. 3. In the as-sintered alloy, FCC, HCP and BCC phases are present as seen in the EBSD phase map in Fig 3(c). The inverse pole figure (IPF) map of the alloy in the Z-direction is shown in Fig. 3(b). After annealing, the HEA was fully developed into a single solid solution with just the FCC phase as seen in the EBSD phase map in Fig. 3(e). The observed phases match the ones obtained by XRD analysis shown in Fig. 3(a).

Similarly, results of C2 and C3 alloys are shown in Figs. 4 and 5 respectively. It follows the same pattern like C1, where the as-sintered alloy has FCC, BCC, and HCP phases, whereas the annealed ones have only the FCC phase. The C2 alloy was not fully sintered at the given temperature and time as evident by the black spots in Fig 4(b) and (c). This is probably due to the higher quantity of high melting point elements, chromium and molybdenum in the C2 mixture compared to C1 and C3.

The average grain size in the annealed samples is larger than the as-sintered ones for all the three alloys due to the higher annealing temperature/time.

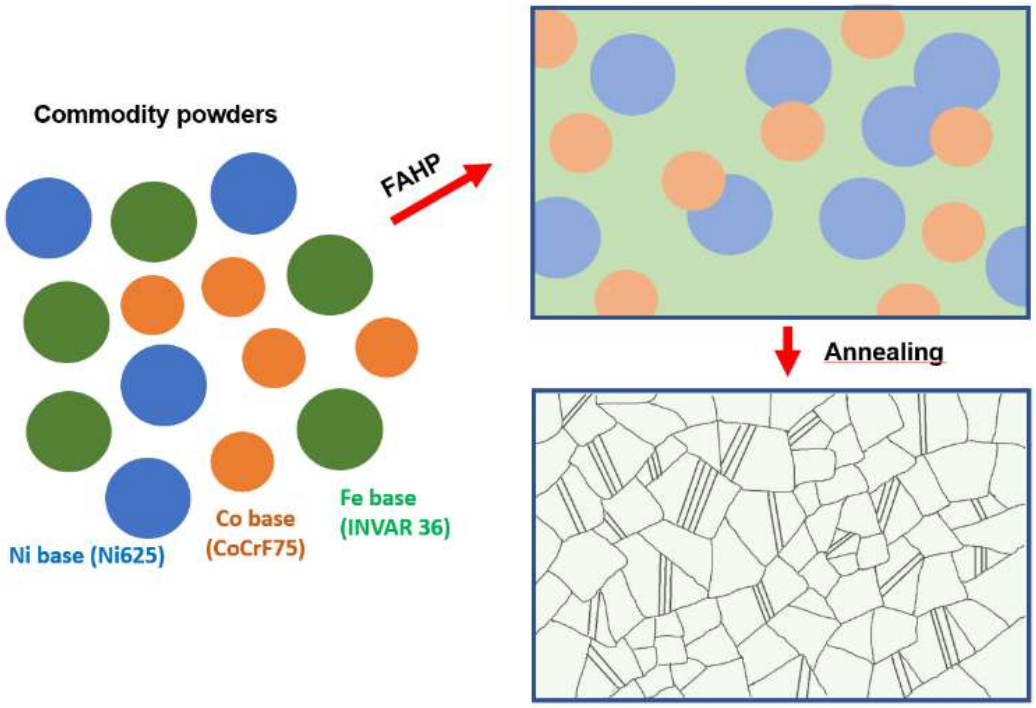

Fig. 2. Proposed methodology

The results of this preliminary study show that powder metallurgy presents a promising way to produce HEAs using commodity powders, which are inexpensive raw materials (in comparison with gas-atomized powders tailored to specific HEA compositions or elemental powders) that are fully commercially available in large quantities. This study identifies new opportunities for the development of HEAs and their implementation in industry.

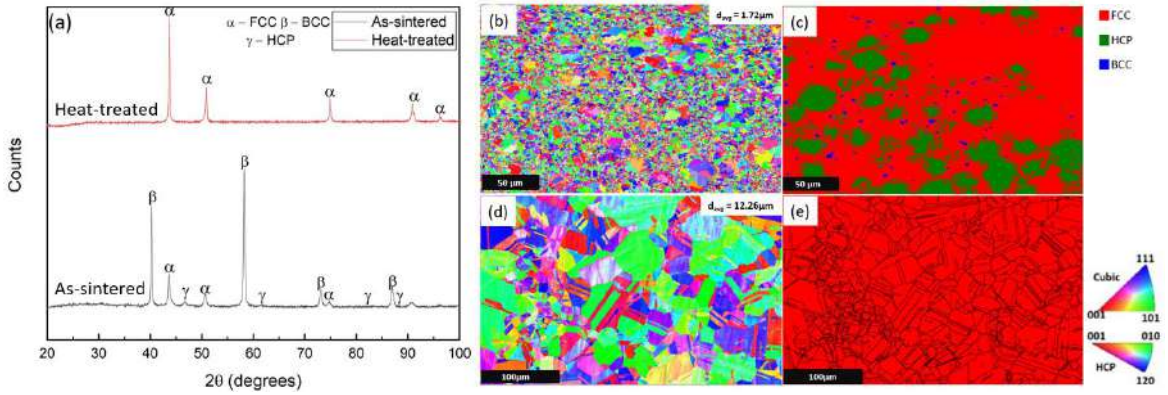

Fig. 3. (a) XRD pattern of C1 As-sintered and Heat-treated sample, and (b), (c) EBSD inverse pole figure (IPF-Z) map and EBSD phase map of the as-sintered and (d), (e) heat-treated C1 sample.
5

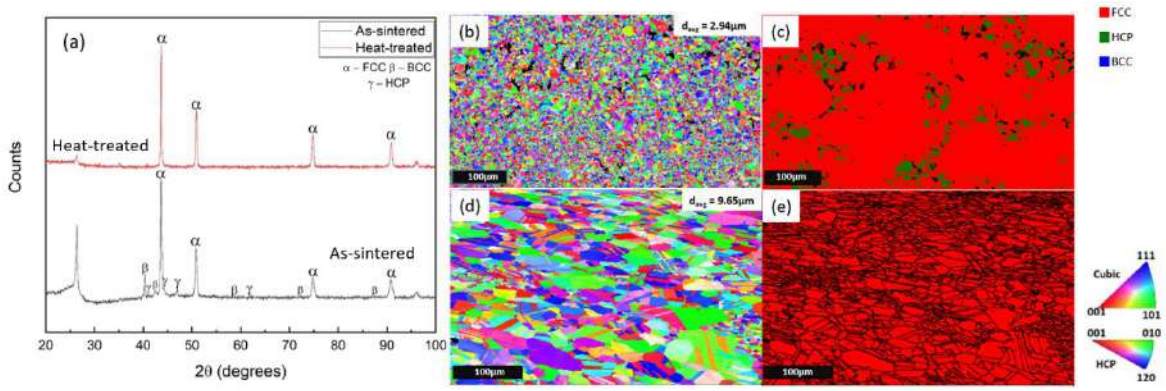

Fig. 4. (a) XRD pattern of C2 As-sintered and Heat-treated sample, and (b), (c) EBSD inverse pole figure (IPF-Z) map and EBSD phase map of the as-sintered and (d), (e) heat-treated C2 sample

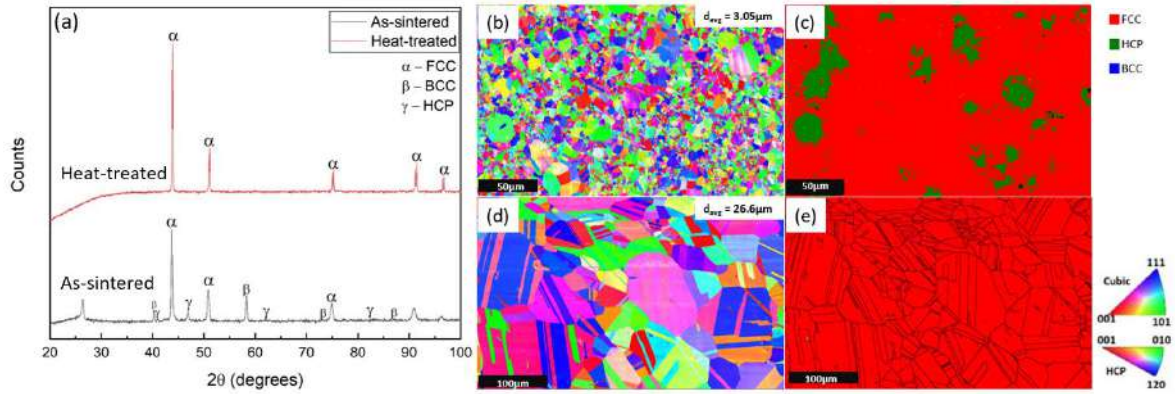

Fig. 5. (a) XRD pattern of C3 As-sintered and Heat-treated sample, and (b), (c) EBSD inverse pole figure (IPF-Z) map and EBSD phase map of the as-sintered and (d), (e) heat-treated C3 sample

Acknowledgements

Authors wish to thank IMDEA Materials Institute for their financial support to this research.

References

[1] K. Yo, High entropy multicomponent alloy, JP2002173732A, 2000.
[2] J.-W. Yeh, S.-K. Chen, S.-J. Lin, J.-Y. Gan, T.-S. Chin, T.-T. Shun, C.-H. Tsau, S.-Y. Chang, Nanostructured High-Entropy Alloys with Multiple Principal Elements: Novel Alloy Design Concepts and Outcomes, Adv. Eng. Mater. 6 (2004) 299–303. https://doi.org/10.1002/adem.200300567.
[3] B. Cantor, I.T.H.T.H. Chang, P. Knight, A.J.B.J.B. Vincent, Microstructural development in equiatomic multicomponent alloys, 375–377 (2004) 213–218.
[4] S. Varalakshmi, M. Kamaraj, B.S. Murty, Synthesis and characterization of nanocrystalline AlFeTiCrZnCu

high entropy solid solution by mechanical alloying, J. Alloys Compd. 460 (2008) 253–257.
[5] K.B. Zhang, Z.Y. Fu, J.Y. Zhang, J. Shi, W.M. Wang, H. Wang, Y.C. Wang, Q.J. Zhang, Nanocrystalline CoCrFeNiCuAl high-entropy solid solution synthesized by mechanical alloying, J. Alloys Compd. 485 (2009) L31–L34. https://doi.org/10.1016/j.jallcom.2009.05.144.
[6] Y.-L. Chen, Y.-H. Hu, C.-W. Tsai, C.-A. Hsieh, S.-W. Kao, J.-W. Yeh, T.-S. Chin, S.-K. Chen, Alloying behavior of binary to octonary alloys based on Cu–Ni–Al–Co–Cr–Fe–Ti–Mo during mechanical alloying, J. Alloys Compd. 477 (2009) 696–705. https://doi.org/10.1016/J.JALLCOM.2008.10.111.
[7] A. Kumar, M. Gupta, An Insight into Evolution of Light Weight High Entropy Alloys: A Review, Metals. 2016; 6(9):199. https://doi.org/10.3390/met6090199.
[8] Y. Lu, Y. Dong, S. Guo, L. Jiang, H. Kang, T. Wang, B. Wen, Z. Wang, J. Jie, Z. Cao, H. Ruan, T. Li, A Promising New Class of High-Temperature Alloys: Eutectic High-Entropy Alloys, Sci Rep 4, 6200 (2014). https://doi.org/10.1038/srep06200.
[9] O.N. Senkov, G.B. Wilks, D.B. Miracle, C.P. Chuang, P.K. Liaw, Refractory high-entropy alloys, Intermetallics. 18 (2010) 1758–1765. https://doi.org/10.1016/j.intermet.2010.05.014.
[10] J.M. Torralba, P. Alvaredo, A. García-Junceda, High-entropy alloys fabricated via powder metallurgy. A critical review, Powder Metallurgy, 62 (2019) 84-114, DOI: 10.1080/00325899.2019.1584454.
[11] E.P. George, D. Raabe, R.O. Ritchie, High-entropy alloys, Nat. Rev. Mater. 4 (2019) 515–534. https://doi.org/10.1038/s41578-019-0121-4.
[12] D.B.B. Miracle, O.N.N. Senkov, A critical review of high entropy alloys and related concepts, Acta Materialia 122 (2017) 448-511. https://doi.org/10.1016/j.actamat.2016.08.081.
[13] J.-W. Yeh, Recent progress in high-entropy alloys, Ann. Chim. Sci. Des Matériaux. 31 (2006) 633–648. https://doi.org/10.3166/acsm.31.633-648.
[14] W. Steurer, Single-phase high-entropy alloys – A critical update, Mater. Charact. 162 (2020) 110179. https://doi.org/10.1016/j.matchar.2020.110179.
[15] M.C. Troparevsky, J.R. Morris, P.R.C. Kent, A.R. Lupini, G.M. Stocks, Criteria for Predicting the Formation of Single-Phase High-Entropy Alloys, Phys. Rev. X. 5 (2015) 11041. https://doi.org/10.1103/PhysRevX.5.011041.
[16] J.-H. Li, M.-H. Tsai, Theories for predicting simple solid solution high-entropy alloys: Classification, accuracy, and important factors impacting accuracy, Scr. Mater. 188 (2020) 80–87. https://doi.org/https://doi.org/10.1016/j.scriptamat.2020.06.064.
[17] F.R. de Boer, W.C.M. Mattens, R. Boom, A.R. Miedema, A.K. Niessen, Cohesion in metals, North-Holland, Netherlands, 1989. 103–637. http://inis.iaea.org/search/search.aspx?orig_q=RN:20078890.
[18] C. Kittel, Introduction to solid state physics. Fifth edition. United Kingdom: N. p., 1976.
[19] X. Yang, Y. Zhang, Prediction of high-entropy stabilized solid-solution in multi-component alloys, Mater. Chem. Phys. 132 (2012) 233–238. https://doi.org/https://doi.org/10.1016/j.matchemphys.2011.11.021.
[20] Z. Wang, Y. Huang, Y. Yang, J. Wang, C.T. Liu, Atomic-size effect and solid solubility of multicomponent alloys, Scr. Mater. 94 (2015) 28–31. https://doi.org/https://doi.org/10.1016/j.scriptamat.2014.09.010.
[21] Z. Yuan, W. Tian, F. Li, Q. Fu, Y. Hu, X. Wang, Microstructure and properties of high-entropy alloy reinforced aluminum matrix composites by spark plasma sintering, J. Alloys Compd. (2019). https://doi.org/10.1016/j.jallcom.2019.07.185.
[22] A.K. Singh, N. Kumar, A. Dwivedi, A. Subramaniam, A geometrical parameter for the formation of disordered solid solutions in multi-component alloys, Intermetallics. 53 (2014) 112–119. https://doi.org/https://doi.org/10.1016/j.intermet.2014.04.019.
[23] S. Guo, C. Ng, J. Lu, C.T. Liu, Effect of valence electron concentration on stability of fcc or bcc phase in high entropy alloys, J. Appl. Phys. 109 (2011) 103505. https://doi.org/10.1063/1.3587228.
[24] S. Guo, C.T. Liu, Phase stability in high entropy alloys: Formation of solid-solution phase or amorphous phase, Prog. Nat. Sci. Mater. Int. 21 (2011) 433–446. https://doi.org/10.1016/S1002-0071(12)60080-X.
[25] A. Takeuchi, A. Inoue, Quantitative evaluation of critical cooling rate for metallic glasses, Mater. Sci. Eng. A. 304–306 (2001) 446–451. https://doi.org/https://doi.org/10.1016/S0921-5093(00)01446-5.

Paper 3

S Venkatesh Kumaran, D Garbiec, JM Torralba, "A novel and sustainable method to develop non-equiatomic $CoCrFeNiMo_x$ high entropy alloys via spark plasma sintering using commercial commodity powders and evaluation of its mechanical behavior", Materials Science & Engineering A, (2023), Vol 878, 145207, https://doi.org/10.1016/j.msea.2023.145207

Materials Science & Engineering A 878 (2023) 145207

Contents lists available at ScienceDirect

Materials Science & Engineering A

journal homepage: www.elsevier.com/locate/msea

A novel and sustainable method to develop non-equiatomic $CoCrFeNiMo_x$ high entropy alloys via spark plasma sintering using commercial commodity powders and evaluation of its mechanical behaviour

S. Venkatesh Kumaran [a,b,*], Dariusz Garbiec [c], José Manuel Torralba [a,b]

[a] IMDEA Materials Institute, Madrid, 28906, Spain
[b] Universidad Carlos III de Madrid, Leganes, 28911, Spain
[c] Łukasiewicz Research Network, Poznań Institute of Technology, 6 Ewarysta Estkowskiego St., 61-755, Poznan, Poland

A B S T R A C T

A novel approach to developing high entropy alloys (HEAs) using spark plasma sintering (SPS) was explored in this work where a mix of commercial commodity powders like Ni625, CoCrF75, and 316L was used instead of pre-alloyed powders avoiding the expensive pre-alloying steps like mechanical alloying or gas atomizing. Three non-equiatomic HEAs, based on Co, Cr, Fe, Ni, and Mo were designed and developed by blending the powders which were sintered via SPS and resulted in a single FCC phase after homogenization. The HEAs were microstructurally and mechanically characterized with tensile and hot compression tests up to a temperature of 750 °C showing excellent properties. The maximum room temperature tensile strength and ductility demonstrated was 712 MPa and 62% respectively, by the alloy $Co_{23.28}Cr_{28.57}Fe_{25.03}Ni_{21.01}Mo_{2.1}$. Moreover, the same alloy exhibited a compression strength greater than 640 MPa with a ductility above 45% at a temperature of 750 °C. Also, this study paves the way for a novel fabrication route that offers more flexibility to develop new HEAs cost-effectively and efficiently which is crucial for the discovery of new materials over high-throughput techniques. Using such commodity alloys also opens the possibility of developing ingot casting from recycled scraps avoiding the direct use of critical metals.

1. Introduction

High Entropy Alloys (HEAs) have garnered significant research interest in the past decade since the advent of cantor and cantor based alloys [1,2], due to their unconventional alloying approach which results in exceptional mechanical properties, such as high strength [3,4], wear resistance [5], corrosion resistance [6–8], and thermal stability [9] among others. Despite ingot metallurgy being the most common method to manufacture HEAs, powder metallurgy (PM) has also shown great potential in manufacturing HEAs. This is mainly because PM can achieve significantly higher compositional accuracy, prevent segregation, and achieve superior microstructural control [10]. Powder metallurgy high-entropy alloys (PMHEAs) have been developed using three different classes of powders to date: fully pre-alloyed gas-atomized powders, pure elemental powders, and fully pre-alloyed mechanically alloyed powders (which are also fabricated from elemental powders). However, some of the main limitations in PM routes to fabricate HEAs are the cost and availability of the powders. Firstly, there are no fully pre-alloyed powders in the market to fabricate even the most extensively used HEAs today. Thus, there is always a need to start from expensive elemental powders (>99% purity) to proceed with either mechanical alloying to produce pre-alloyed powders or by using critical metals as raw materials to produce powders by gas atomizing, both of which are time-consuming and expensive. Moreover, pure elemental powders can also be difficult to handle. For instance, in the commonly studied cantor alloy (CoCrFeMnNi), Cr has a high affinity towards oxygen forming chromium oxides, whereas, Ni and Co are considered hazardous by the REACH regulations [11,12]. However, as described in our previous work [13], there are many grades of powder available in the market that belong to the families of metals on which many HEAs are based: Ni, Cr, Fe, Co, Ti, Al, etc. These grades are all commercially available from several manufacturers and can be delivered in large quantities within short times at competitive prices. So, in this work, we explore the possibility of using these families of available alloys in mass production, designated by the term 'commodity', as raw materials to develop HEAs. As these commodity powders are usually mass-produced, their cost is relatively low and are easily available in the market, due to which, they offer a highly convenient way for the development of engineering materials by the PM route.

In our previous work [13], the focus was to develop a prototype model using field-assisted hot pressing to analyze the microstructure which proved that developing HEAs using commercial commodity

* Corresponding author. IMDEA Materials Institute, Madrid, 28906, Spain.
E-mail address: venkatesh.sivagnana@imdea.org (S. Venkatesh Kumaran).

https://doi.org/10.1016/j.msea.2023.145207
Received 7 February 2023; Received in revised form 5 May 2023; Accepted 25 May 2023
Available online 27 May 2023

powders was very much feasible. The composition was designed based on calculating the thermodynamic parameters to ensure a single solid solution as detailed in our previous work [13]. In our current work, we developed three different non-equiatomic HEAs using the available commercial commodity powders using Spark Plasma Sintering (SPS). Tensile and hot compression tests were performed to evaluate the mechanical behavior. The alloys developed were $Co_{25.56}Cr_{20.7}Fe_{26.92}Ni_{25.2}Mo_{1.6}$, $Co_{23.28}Cr_{28.57}Fe_{25.03}Ni_{21.01}Mo_{2.1}$, $Co_{29.07}Cr_{17.2}Fe_{28.22}Ni_{24.45}Mo_{1.06}$, which were labeled as C1, C2, and C3 respectively. Today, the use of critical metals is controversial, and this can be an obstacle in developing HEAs as many of them contain Co and Ni. So, with this work, a new possibility is opened to manufacture HEAs both by casting and powder metallurgy with commodity alloy powders or scraps as raw material and thus avoiding the direct use of critical metals.

Recently, single-phase FCC-type HEAs have been widely studied, such as CoCrFeNi alloy due to their exceptional ductility and fracture toughness [14]. However, they possess lower strengths at ambient and elevated temperatures making them unsuitable for structural applications. In this regard, many alloying elements have been added to the CoCrFeNi system to improve the mechanical properties. Specifically, Mo improves the room and high-temperature strength owing to its high melting point and elastic modulus [15]. So, motivated by this, Mo was included through the commodity powders to develop three different alloys with varying Mo content and the mechanical properties were tested both at room and at high temperatures.

2. Materials and methods

In this work, three non-equiatomic $CoCrFeNiMo_x$ alloys were prepared using commercial commodity powders. The commodity powders used were Ni 625, SS 316L, Invar 36, CoCr F75, and Fe49Ni. The CoCr alloy powders were provided by VDM Metals (Germany) and the rest were from Sandvick Osprey (UK). All the powders used were commercial grades, ready to be used for other applications. The particle size distribution and the composition of the powders are listed in Table 1. From these above powders, three different alloy combinations were designed and were simply mixed in the appropriate proportion as shown in Table 2. The alloys are labeled C1, C2, and C3. The composition was designed to keep Ni, Fe, Cr, and Co fairly equiatomic with minor Mo addition. The morphology of the C1, C2, and C3 powder mixes are shown in Fig. 1. In C1, as shown in Fig. 1 (a) and (b), Ni 625 consists of an irregular shape with a d50 of 60 μm, which is much larger than the other powder particles. These powders are relatively spherical, but due to a non-optimized gas atomization process, it has led to clusters of satellites. As seen in Fig. 1 (d), the 316L powder particles in the C2 mix are adhered to each other forming large agglomerates. This is attributed to the smaller particle size distribution (PSD) of 316L. In C3, the Fe49Ni particles are highly irregular and adhered to each other and also to the CoCrF75 powder particles as shown in Fig. 1 (e). Once the powders were mixed, the SPS consolidation was carried out in HP D 25/3 SPS furnace (FCT system, Germany) at Siec Badawcza Lukasiewicz, Poznan, Poland. A tungsten foil was placed between the powders and the graphite die to avoid carbon diffusion. The die had a cylindrical shape with 60 mm diameter and 15 mm height. The sintering was carried out at two different temperatures for each alloy, 1000 °C, and 1100 °C with a heating rate of 100 °C/min with a 50 MPa pressure for 10 min. Initially, based on the previous works in the literature [10], the temperatures were chosen to be 1000 °C and 1250 °C. When C1 was being consolidated, a liquid phase was formed at around 1140 °C and removed from the tools due to which the consolidation temperature for C2 and C3 was reduced to 1100 °C. After sintering, the bulk samples were annealed at 1200 °C for 24 h in a metal muffle furnace (Carbolite CWF 13/23) to homogenize the microstructure. All the samples were vacuum encapsulated in a glass tube to avoid oxidation. Both the as-sintered (AS) and heat-treated (HT) samples were manually ground and polished up to a colloidal silica solution of 0.04 μm. The microstructural characterization of the sintered samples was performed by a dual-beam Helios Nanolab 600i SEM equipped with Energy dispersive spectroscopy (EDS) and Electron backscattered diffraction (EBSD) detector. Phase identification was performed by X-ray diffraction (XRD) in a PANalytical diffractometer with a Cu $K\alpha_1$ radiation source. The XRD peaks obtained were analyzed using HighScore plus software. Vickers hardness tests were carried out with a load of 1 Kgf for a period of 25s with a Shimizu hardness tester.

The tensile tests of all the samples were carried out at room temperature using a Kammrath and Weiss GmbH micro-tensile machine which can also be placed inside an SEM for in-situ testing. The tensile speed was 10^{-3} s^{-1} and the samples were machined to a flat dog-bone shape with gauge dimensions of 4 x 1 × 1 mm. For each material, the average was calculated from two tests. Compression tests were performed on both the as-sintered (AS) and heat-treated samples at room temperature and at temperatures of 600 °C, 700 °C, and 750 °C in an Instron 3384 machine equipped with a 30 kN load cell. The sample dimensions were 2 x 2 × 4 mm. For each material, three tests were performed at a strain rate of 10^{-3}/s and the average was calculated.

Table 1
Proposed commodity alloys and their role in the target HEA.

Alloy	Size (d50) (μm)	Role	wt. (%)				
			Ni	Fe	Cr	Mo	Co
Ni625[a]	60	Source of Ni, Cr, Fe and Mo	61.54	5.35	25.26	5.6	–
INVAR 36	3.8	Source of Fe and Ni	34.8	65.14	–	–	–
CoCrF75	30	Source of Co, Cr and Mo	0.51	0.8	32.57	3.72	62.41
316L	11.5	Source of Fe, Cr, Ni and Mo	11.82	67.77	18.9	1.51	–
Fe49Ni	15	Source of Fe, Ni	47.76	52.24	–	–	–

[a] Ni625 consists of ~3 wt% Nb.

3. Results and discussion

3.1. X-ray diffraction

The XRD peaks obtained for C1, C2 and C3 both in the as-sintered and heat treated state are shown in Fig. 2 (a) and (c) respectively. C1 in the as-sintered state contains both Face centered cubic (FCC) and Hexagonal close-packed (HCP) peaks, whereas after annealing at 1200 °C for 24 h, only FCC peaks remain. The same goes for C2 and C3, except that in C2 alloy sintered at 1100 °C and C3 alloy sintered at 1000 °C and 1100 °C, no HCP peaks were detected in XRD but as shown in Fig. S6, Fig. S7 from the supplementary data and Fig. 6, HCP phases were present on the phase maps obtained by EBSD. The HCP phase is linked to the Co base powders and Co is highly concentrated in very specific areas in the as-sintered samples which makes it suitable to be detected by EBSD but not easily by XRD, thus, making the HCP peaks too weak. Both C2 and C3 alloy at both temperatures converted to a single FCC phase after annealing. Since all the alloys in the as-sintered state is just a mix of different commodity powders, there is no single FCC phase throughout with the same lattice parameters. This is the reason why there are multiple peaks as shown in Fig. 2(b), which is the region from the boundary marked in Fig. 2(a), representing FCC phases with different but very close lattice parameters. After the annealing process, the multiple small peaks change to one sharper and narrower peak indicating a single FCC phase with the same lattice parameters. Moreover, as seen in Fig. 2 (d), which shows the peaks of alloys after annealing, the slight shift in peaks between C1, C2 and C3 indicate slight

Table 2
Proposed mixes of commodity powders used to develop different possible HEAs.

Alloy	wt. %					at. %				
	Ni625	INVAR 36	CoCrF75	316L	Fe49Ni	Ni	Fe	Cr	Mo	Co
C1[a]	20	38	42			25.21	26.92	20.7	1.61	25.56
C2[a]	28		38	34		21.01	25.03	28.56	2.1	23.28
C3			48		52	24.45	28.22	17.2	1.06	29.07

[a] C1 and C2 contain trace amounts of Nb.

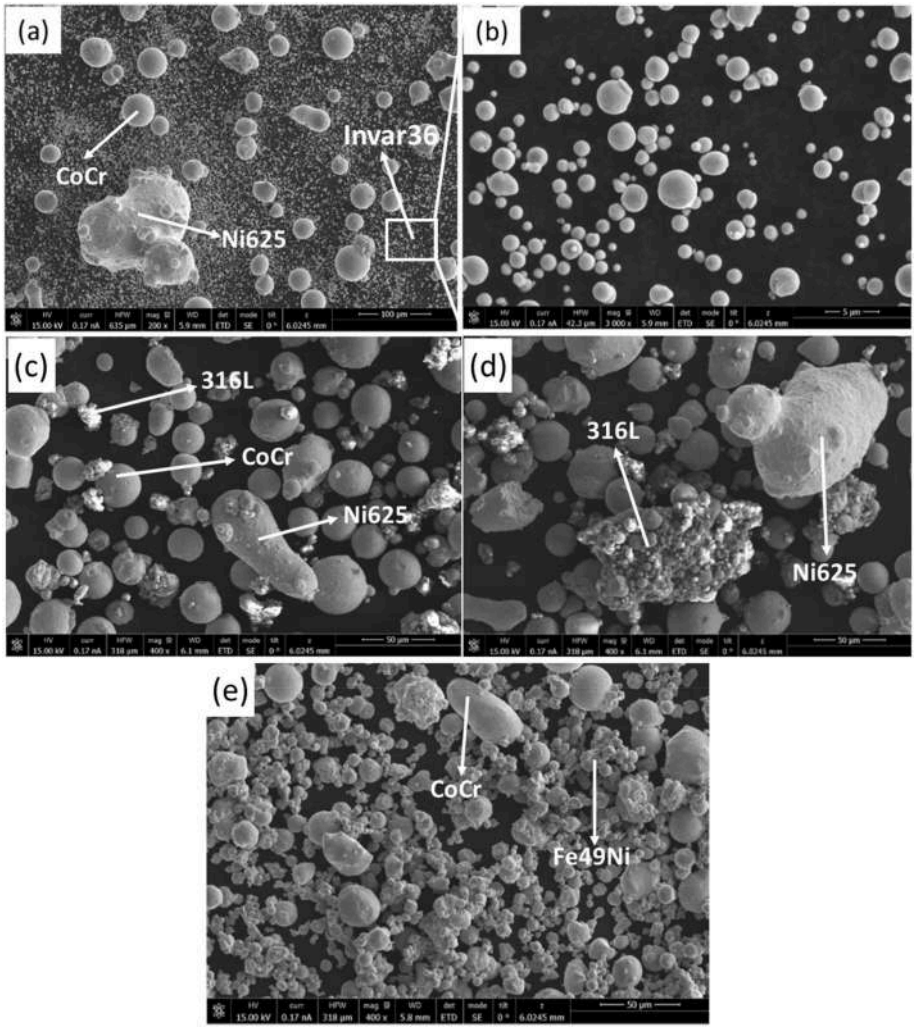

Fig. 1. SEM images showing the powder morphology of (a) C1 mix; (b) magnified SEM image of Invar36 powders in the inset; (c) and (d) powder morphology of C2 mix; (e) powder morphology of C3 mix.

change in lattice parameters as expected due to the varying compositions between the alloys.

3.2. Microstructural analysis

The elemental distribution map obtained by EDS for C1 alloy in the as-sintered (sintered at 1000 °C) and annealed state are shown in Fig. 3 and Fig. 4 respectively. The individual powder particles of C1, i.e., Ni625, Invar36, and CoCrF75 are clearly visible in the as-sintered state. The Invar36 powders formed the matrix here as its smaller particle size distribution enabled it to achieve higher sinterability. However, when the same alloy was annealed at 1200 °C for 24 h, the elemental distribution became homogenous, resulting in a typical HEA microstructure as shown in Fig. 4. The same pattern was followed for C2 and C3 alloys as well.

The microstructures of the as-sintered and annealed alloys sintered at 1000 °C and 1100 °C along with the porosity values are shown in Fig. S1 and Fig. S2 in the supplementary data. In the as-sintered microstructures, the individual powders can be seen whereas they are homogenized after annealing giving a typical HEA microstructure. In Fig. S1, it can be observed that the porosity decreases with higher sintering temperatures. The C2 mix of powders are not fully sintered well at the given parameters (1000 °C, 50 MPa, 10 min) due to the higher amount of large particle sized powders, which is Ni625, with a d50 of 60 μm. However, the same mix of powders were properly sintered at a temperature of 1100 °C.

In highly localized regions, there were small white precipitates in C1 and C2 alloy after annealing but were absent in C3 alloy. A line scan of a

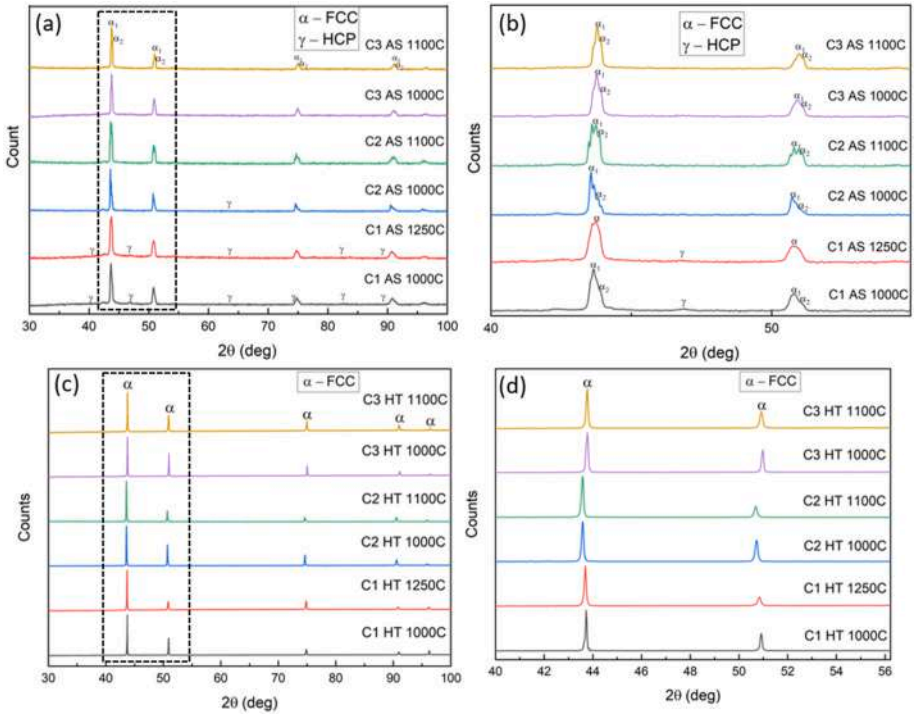

Fig. 2. XRD peaks of the alloys in the (a) as-sintered condition sintered at different temperatures and (b) closer view of the marked region from (a), (c) XRD peaks of the alloys sintered at different temperatures after annealing at 1200 °C for 24 h and (d) closer view of the marked region from (c).

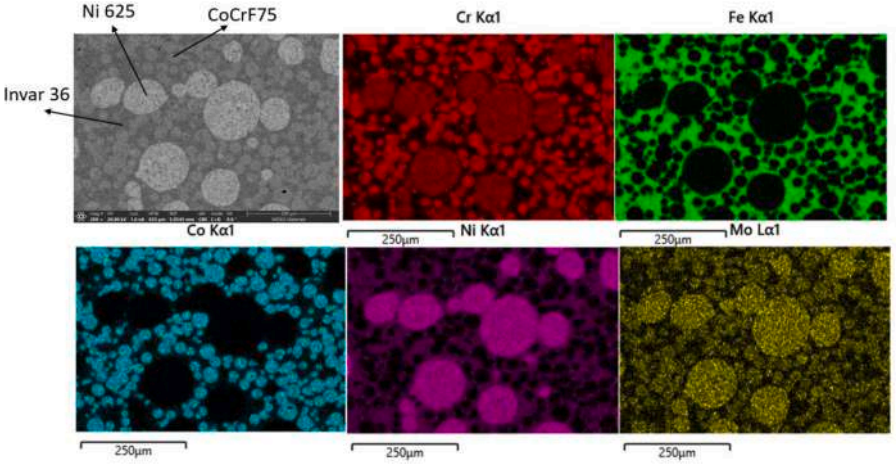

Fig. 3. Elemental distribution map of C1 alloy as-sintered via SPS at 1000 °C.

precipitate is shown in Fig. S3 for C1 alloy sintered at 1000 °C and annealed at 1200 °C for 24 h which shows that the precipitates are rich in Nb and Mo. As mentioned earlier, Nb is present in Ni625 alloy in small amounts which is mixed in C1 and C2. Due to its very low fraction in the microstructure, perhaps they were not identifiable by XRD. It is known that in Ni625 alloy, many intermetallic phases (like Ni_3Nb) and carbides (MC, M_6C and $M_{23}C_6$) may precipitate after long-time annealing [16–19]. Also shown in Fig. S3 are some oxide inclusions which were confirmed by EDS showing chromium and oxygen peaks. As these were absent in the as-sintered alloys, it can be implied that they were picked up during the long-time annealing process. Regardless, these precipitates and oxides did not significantly influence the mechanical properties due to their low volume fraction as discussed in Section 4.3.2.

To study the phases after sintering and annealing, EBSD was performed on all the samples. The C1 alloy in the as-sintered state sintered at 1000 °C consists of FCC, HCP and minor amount of body centered cubic (BCC) phases as shown in Fig. 5 (b). After annealing at 1200 °C for 24 h, it results in a single FCC phase as shown in Fig. 5 (d). The same C1 alloy when sintered at a higher temperature of 1250 °C, consists of FCC but with much lesser amounts of HCP and BCC phases compared to when it was sintered at 1000 °C as shown in Fig. S4 (b). This is attributed to the fact that at higher temperatures, the atomic diffusion is faster which enables more homogeneity to occur. When this alloy was annealed at 1200 °C for 24 h, a single FCC phase was obtained as shown in Fig. S4 (d). The C2 alloy was sintered at 1000 °C and 1100 °C, referred to as C2_1000 and C2_1100 respectively. Both of them consisted of a majority of FCC phase and some amounts of BCC and HCP in the as-sintered condition as shown in Fig. S5 (b) and Fig. S6(b), respectively. However, after annealing, a single FCC phase was obtained in both the cases as shown in Fig. S5(d) for C2_1000 and Fig. S6(d) for C2_1100. The C3 alloy

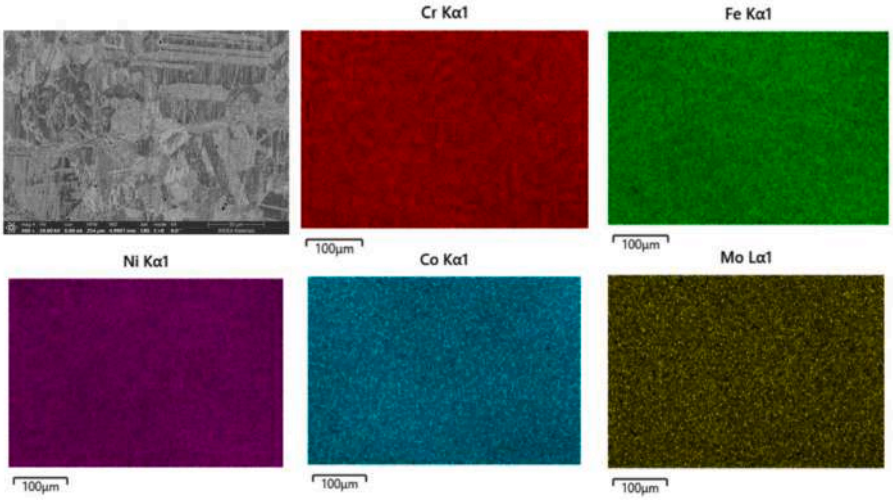

Fig. 4. Elemental distribution map of C1 alloy annealed for 24 h.

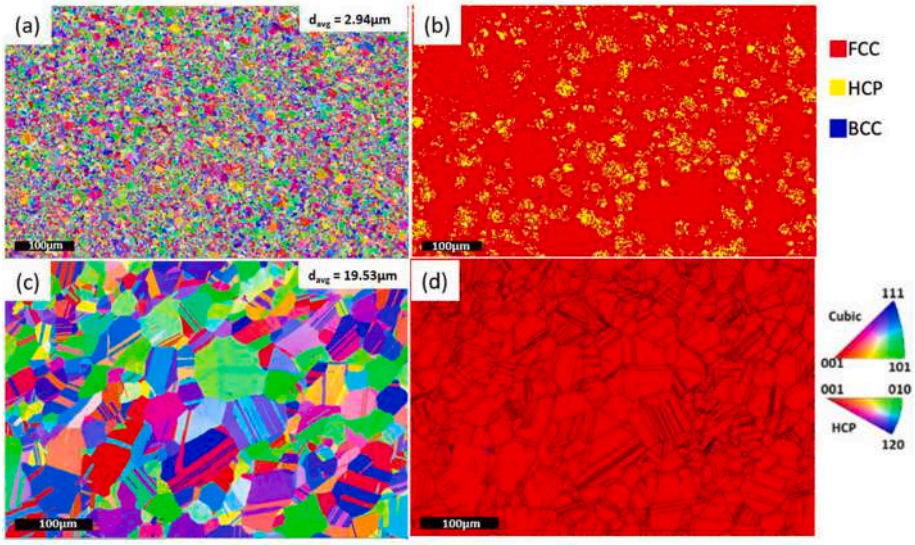

Fig. 5. IPF and phase map of C1 alloy sintered at 1000 °C in the as-sintered state (a, b) and after annealing at 1200 °C for 24hrs (c, d).

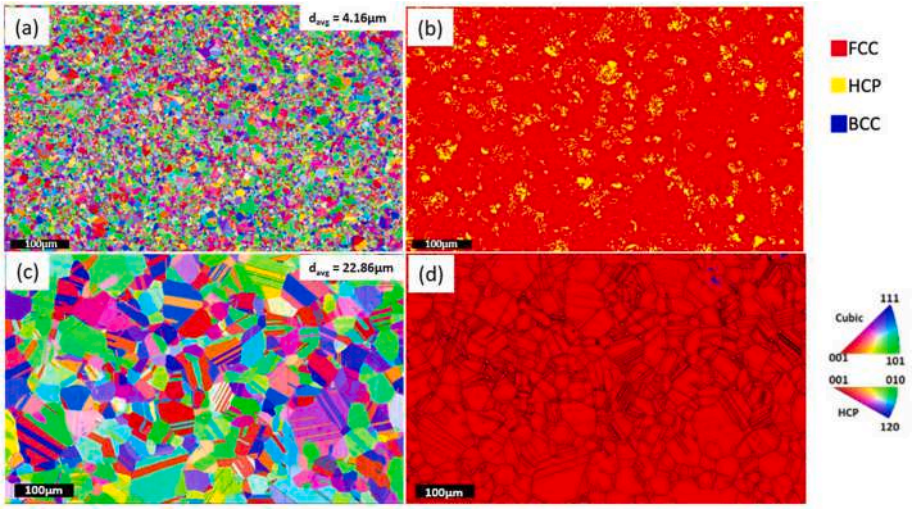

Fig. 6. IPF and phase map of C3 alloy sintered at 1000 °C in the as-sintered state (a, b) and after annealing at 1200 °C for 24hrs (c, d).

was also sintered at 1000 °C and 1100 °C. In both cases, the as-sintered samples consisted of FCC and HCP phases as shown in Fig. 6 (b) and Fig. S7 (b), respectively. After annealing at 1200 °C for 24 h, the microstructure changed to a single FCC phase as shown in Fig. 6 (c) for C3_1000 and Fig. S7(d) for C3_1100. In all the alloys, after heat treatment, numerous annealing twins can be observed in the inverse pole figure maps suggesting low stacking fault energies as commonly found in recrystallized FCC metals [20].

It is interesting to note that despite the high temperature and times used for annealing, the grain growth is only slight due to the very small grains obtained due to the fast heating rates and short dwell times in SPS. The grain sizes obtained after sintering and annealing in all the alloys are shown in Fig. 7. These grains are much smaller than the equivalent alloys obtained from ingot casting. For example, FeCoCrNiMo0.1 had a grain size of 75 μm when annealed at 1050 °C for 60 min [21] which shows that powder metallurgy routes have great potential in improving the mechanical properties of new alloys.

3.3. Mechanical properties

3.3.1. Hardness

The vicker's hardness of the annealed alloys is shown in Fig. 8. The trend in hardness can be explained by the amount of Mo content. Hardness increases with Mo content as it aids in the local lattice distortion effect in alloys [22]. Thus, C2 has the highest hardness followed by C1 and C3. These values are consistent with other similar PMHEAs like CoCrFeNi, where the obtained hardness was 194 Hv [23].

3.3.2. Tensile properties

Micro-tensile tests were performed on the as-sintered and annealed samples. The as-sintered samples do not exactly represent HEAs as they are a mix of different powder particles and the composition is not uniform. But for comparative purposes, the tensile results were studied for the as-sintered samples also as shown in Fig. 9(a).

The tensile test results of annealed samples are shown in Fig. 9(b) and the summary of the mechanical properties of both as-sintered and annealed samples are shown in Table 3. The ultimate tensile strength (UTS) is lesser and the ductility is higher for all heat treated samples compared to the as-sintered ones due to the presence of a single FCC phase and larger grains in the former. All the alloys exhibit a reasonably high UTS and ductility for a single FCC phase, with C2 alloy exhibiting the maximum UTS of 712 MPa due to higher amounts of Mo. As mentioned earlier, the alloying of Mo causes local distortion in the FCC structure [22], which contributes to the strengthening.

Unfortunately, not a lot of work has been reported so far on tensile

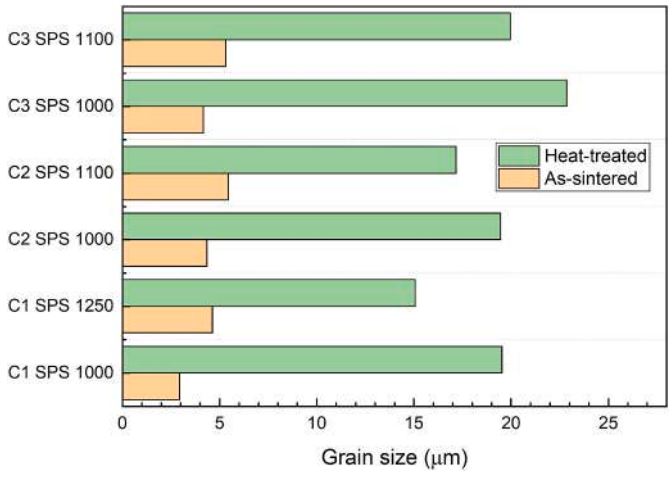

Fig. 7. Plot comparing the grain size of as-sintered and annealed samples obtained via SPS and FAHP.

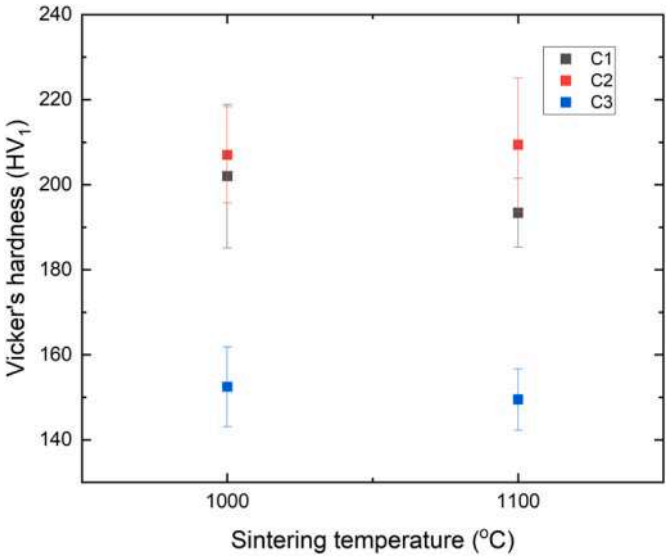

Fig. 8. Vicker's hardness values of C1, C2, and C3 alloys processed by SPS at various temperatures and annealed at 1200 °C for 24 h. It should be noted that the C1 alloy was sintered at 1250 °C instead of 1100 °C.

properties of PMHEAs, especially by SPS. Liu et al. [22] investigated the tensile properties of Mo alloyed as-cast CoCrFeNi and reported a UTS of 479 MPa with 51.1% ductility for $CoCrFeNiMo_{0.1}$ and 589.6 MPa with 55.2% ductility for $CoCrFeNiMo_{0.2}$. Similar FCC based alloys like CoCrFeNiMn had a yield strength of 200 MPa and a UTS of 600 MPa after arc-melting and hot rolling [24]. Fig. 9(e) shows a comparison plot of tensile strength vs. elongation at fracture of different HEAs developed via powder metallurgy and casting, and other structural alloys. The HEAs developed in this work using commodity powders exhibit a much higher elongation than many other alloys and possess promising tensile strength for a single FCC phase which emphasizes the novelty of this method.

As seen in Tables 3 and in the as-sintered samples, the UTS increases with increasing sintering temperature as there is a shrinkage in porosity, even though there is a slight increase in the grain sizes. Among the heat treated samples, the C2 alloy shows an expected trend, where the YS and UTS increase with increasing sintering temperatures due to the reduction in porosity, but not in the case of C1 and C3. As mentioned earlier, C1 experienced melting when it was sintered at 1250 °C, and produced a liquid phase which resulted in irregular porosities as shown in Fig. S8 and might have reduced the strength of the alloy. This is the same trend as seen from the values of vickers hardness as well where C1 sintered at 1250 °C has lesser hardness than the one sintered at 1000 °C. It should be noted that C3 alloy has the lowest YS and UTS, due to its lower quantity of Mo and absence of Nb, which reduced the lattice distortion effect. This shows that Mo and Nb have a significant effect in strengthening HEAs even in small quantities.

Despite the lower ductility of C1 alloy sintered at 1000 °C and annealed at 1200 °C for 24 h (10.2%), the fracture surfaces of all samples subjected to the tensile test shown in Fig. 10 present a typical micro-ductile fracture. All three samples exhibit micro-fracture with similar small dimples with large ductility signs. As shown in Fig. 10(d), some inclusions are present inside the larger dimples which upon EDS analysis showed two types of oxides, which were Mn–Cr rich and some Si-rich. The commodity powders used consists of trace amounts of Mn and Si which might have resulted in the formation of oxides after the long time annealing. However, no trends were observed between the oxide volume fraction and mechanical properties which shows that the oxides did not affect the mechanical properties significantly. Moreover, no Nb and Mo rich precipitates were found on the fracture surfaces of C1 and C2 alloys again indicating their insiginificant impact on the mechanical

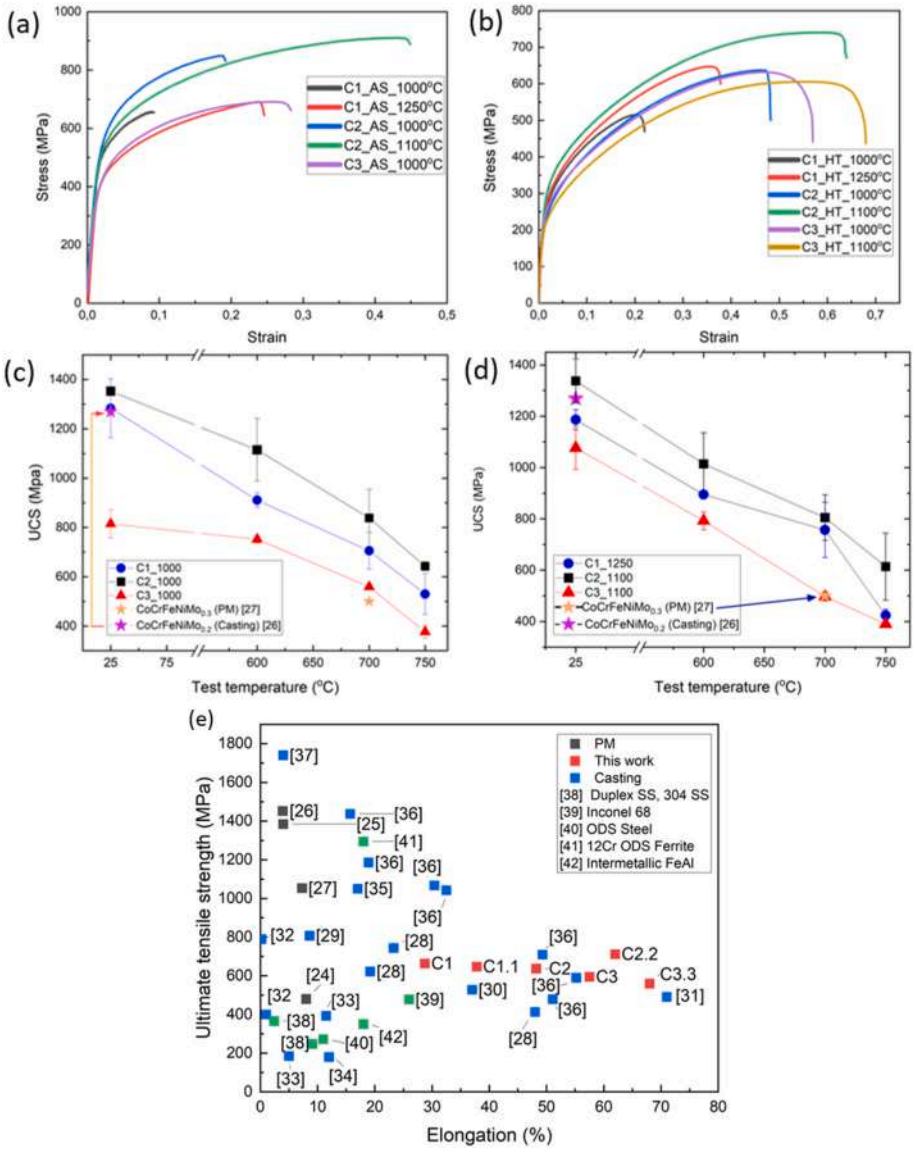

Fig. 9. Tensile stress-strain diagram of (a) as-sintered alloys (AS), (b) heat-treated alloys (HT); Ultimate compressive strength values at various temperatures of HT samples sintered at (c) 1000 °C and (d) 1100 °C. C1 alone was sintered at 1250 °C instead of 1100 °C. (e) Ultimate tensile strength vs elongation at fracture for different HEAs produced by powder metallurgy (PM) and casting along with other traditional alloys. UCS refers to Ultimate compressive strength. C1 – Sintered at 1000 °C, C1.1 – Sintered at 1250 °C, C2 – sintered at 1000 °C, C2.2 – sintered at 1100 °C, C3 – sintered at 1000 °C, C3.3 - sintered at 1100 °C [32–50].

properties.

3.3.3. Hot compression test

The ultimate compression strength of the annealed alloys tested at various temperatures up to 750 °C obtained by hot compression test is shown in Fig. 9(c) for samples sintered at 1000 °C and Fig. 9 (d) for samples sintered at 1100 °C. The summary of the yield strength (YS), ultimate compression strength (UCS) and ductility of both as-sintered (AS) and annealed samples (HT) are presented in Table S1 in the supplementary data. The AS alloys in general exhibit better strength and lesser ductility than HT alloys due to the presence of harder and stronger HCP and BCC phases, and the fine grain sizes obtained in the former.

As expected, in all the alloys, the UCS decreases with increasing temperatures as shown in Fig. 9 (c) and (d) due to the dynamic softening that occurs at higher temperatures due to the improved thermal activation process [25]. It is to be noted that all the heat treated samples experienced no fracture at any of the test temperatures even after the strain reached more than 40% indicating a remarkable ductility of the FCC phase. For example, at RT, the C2_HT alloy sintered at 1000 °C exhibited a UCS of 1352.5 MPa with a ductility >40%. The same alloy at 750 °C, had a UCS of 642.3 MPa with a ductility of >44%. Comparing similar alloys reported in the literature, $CoCrFeNiMo_{0.3}$ developed by casting, showed a UCS of 1269 MPa with a ductility of 58% at room temperature [26]. In another work, $CoCrFeNiMo_{0.2}$ HEA when developed by PM route had a UCS of 500 MPa at 700 °C [27] which is lower than that of the HEAs studied in this work.

Various strengthening mechanisms exist in conventional alloys including solid solution strengthening, precipitation strengthening, grain boundary strengthening, and dispersion strengthening. However, in HEAs, strengthening occurs also due to lattice distortion, which is more severe than conventional alloys due to the different atomic size of elements and their near-equal proportion, and sluggish diffusion at high temperatures which increases the activation energy. The strengthening due to lattice distortion is more relevant than solid solution strengthening in HEAs, as there are no definite criteria to differentiate a solute from a solvent. For C1 and C2, Mo and Nb contribute to severe lattice distortion due to their large atomic radius compared to the rest of the elements while for C3, it is only Mo. It is also to be noted that C1 and C2 consisted of Mo and Nb rich precipitates in certain localised regions both on the grain boundary and within the grains as shown in Fig. S3, which might have also contributed to high compression strength. This is evident by the lower UCS for C3 alloy compared to C1 and C2 at all temperatures. C2 alloy exhibited higher UCS at all temperatures than C1. The atomic size difference, δ defined in Ref. [28], was calculated for

Table 3
Tensile properties of C1, C2, and C3 alloys in the as-sintered and heat treated state.

Condition	Alloys	Yield strength (MPa)	Ultimate tensile strength (MPa)	Ductility (%)
As-sintered	C1_1000 °C	397.5	657.59	10.2
	C1_1250 °C	311	691.07	25
	C2_1000 °C	400	848.98	20
	C2_1100 °C	418	894	42.75
	C3_1000 °C	315	667.5	28
Heat-treated at 1200°C for 24 h	C1_1000 °C	322	663.75	28.75
	C1_1250 °C	234	647.5	37.8
	C2_1000 °C	190	637.4	48.2
	C2_1100 °C	257.5	712	62
	C3_1000 °C	200	595	57.5
	C3_1100 °C	167.5	560	68
	$CoCrFeNiMo_{0.1}$ [22]	198.8	479	51.1
	$CoCrFeNiMo_{0.2}$ [22]	254.7	589.6	55.2
	CoCrFeNiMn [24]	200	600	39

the alloys from the equation shown below:

$$\delta = \sqrt{\sum_{i=1}^{n} C_i \left(1 - \frac{r_i}{\bar{r}}\right)^2} \quad (1)$$

C_i is the mole fraction of the i^{th} of N components, $\bar{r}$ is the average atomic radius in the alloy obtained by rule of mixtures and r_i is the atomic radius of the i^{th} element. The atomic radii in Ref. [29] were used to calculate r_i. C2 had the highest atomic size difference at 2.24 compared to 1.7 for C1 which emphasizes the role played by Mo to distort the lattice and increase the strength by restricting the dislocation movement. Along with being a high radius element, Mo also has a melting point, which has been known to increase the activation energy (Q) for high temperature deformation [27]. In addition, Tsai et al. [30] showed that a higher the normalized activation energy (Q/T_m, where T_m is the melting point), the slower the diffusion rate, which implies that Mo enhances the sluggish diffusion effect in HEAs. This corroborates well with the compression test results, as the strength decreases with temperature with respect to the amount of Mo, in the order, C2, C1 and C3 in both the sintering temperatures, 1000 °C and 1100 °C.

4. Cost analysis

A cost analysis was conducted to compare the fabrication route by pure elemental powders and commercial commodity powders. Based on the quote by raw materials provider Hunan Fushel Technology Limited [31], a bar chart is shown in Fig. 11, comparing the cost of C2 alloy. It can be seen that by using commercial powders, there is a 20% reduction in raw material costs than when using pure elemental powders. In addition, it should be noted that when using elemental powders, there are added costs of pre-alloying steps like mechanical alloying or gas atomization, which will add to the total manufacturing cost and time. Hence, this method of using commodity powders offers a feasible way for the commercialization and industrial implementation of HEAs.

5. Conclusions

Bulk samples of HEAs using a simple blend of commodity powders namely, Ni 625, Invar36, CoCrF75, 316L, and Fe49Ni were fabricated by SPS at 1000 °C and 1100 °C. Post-sintering, the microstructure consisted of individual alloy powder particles with multiple phases including FCC, HCP and BCC and after an annealing treatment at 1200 °C for 24 h, it resulted in a typical HEA microstructure with an FCC phase.

1. Three non-equiatomic HEAs were prepared by blending different combinations of the commercial powders. The best mechanical properties were exhibited by $Co_{23.28}Cr_{28.57}Fe_{25.03}Ni_{21.01}Mo_{2.1}$ HEA sintered at 1100 °C due to the higher amount of Mo. It had a tensile strength of 712 MPa with a ductility of 62%. Also, it had a compression strength of 1352.5 MPa at room temperature and 642.3 MPa at 750 °C exhibiting no fracture even up to 45% elongation.
2. This work proves that HEAs can be developed by these commodity powders without the need for expensive pre-alloying processes like

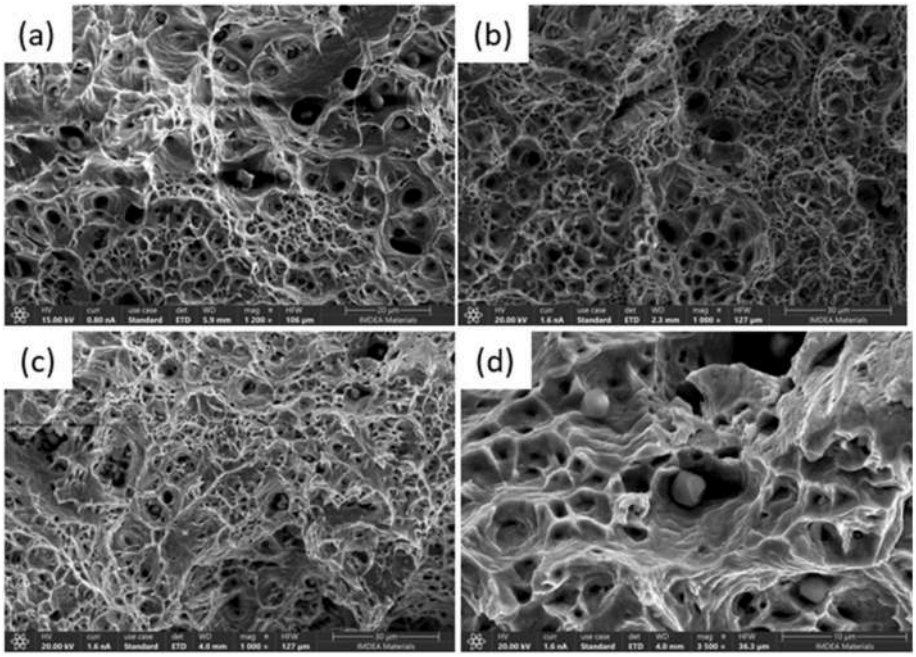

Fig. 10. SEM images of fracture surfaces of (a) C1, (b) C2, (c) C3, (d) C3 at higher magnification, sintered at 1000 °C and annealed at 1200 °C for 24 h subjected to tensile testing.

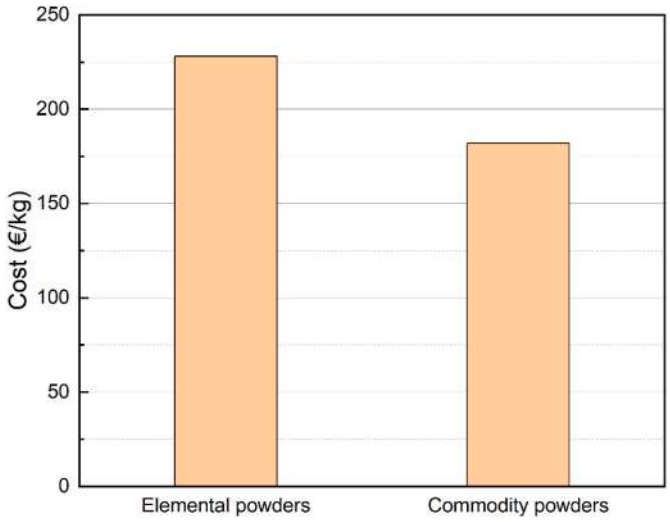

Fig. 11. Raw material cost comparison of manufacturing C2 alloy using elemental powders vs commodity powders.

mechanical alloying, thus avoiding contamination and paving way for an efficient, cost-effective and flexible way for industrial implementation and commercialization. So, the use of commodity alloy scraps as raw materials to manufacture HEAs using both casting and PM routes is a viable alternative, avoiding the direct use of critical metals like Co and Ni, due to both its toxicity and lack of availability.

CRediT authorship contribution statement

S. Venkatesh Kumaran: Writing – original draft, Investigation, Methodology, Conceptualization. **Dariusz Garbiec:** Resources, Investigation. **José Manuel Torralba:** Conceptualization, Supervision, Writing – review & editing.

Declaration of competing interest

The authors declare that they have no known competing financial interests or personal relationships that could have appeared to influence the work reported in this paper.

Data availability

Data will be made available on request.

Acknowledgements

The authors would like to thank VDM Metals, Germany for providing the powders for free. This work was funded by IMDEA Materials Institute, Madrid, Spain.

Appendix A. Supplementary data

Supplementary data to this article can be found online at https://doi.org/10.1016/j.msea.2023.145207.

References

[1] B. Cantor, I.T.H. Chang, P. Knight, A.J.B. Vincent, Microstructural development in equiatomic multicomponent alloys, Mater. Sci. Eng. 375–377 (1–2) (Jul. 2004) 213–218, https://doi.org/10.1016/j.msea.2003.10.257. SPEC. ISS.
[2] B. Cantor, Multicomponent high-entropy Cantor alloys, Prog. Mater. Sci. 120 (October 2020) (2021), 100754, https://doi.org/10.1016/j.pmatsci.2020.100754.
[3] B. Gludovatz, A. Hohenwarter, D. Catoor, E.H. Chang, E.P. George, R.O. Ritchie, A fracture-resistant high-entropy alloy for cryogenic applications, Science 345 (6201) (2014) 1153–1158, Sep, https://doi.org/10.1126/science.1254581, 1979.
[4] J. Ren, et al., Strong yet ductile nanolamellar high-entropy alloys by additive manufacturing, Nature 608 (7921) (Aug. 2022) 62–68, https://doi.org/10.1038/S41586-022-04914-8.
[5] M.H. Chuang, M.H. Tsai, W.R. Wang, S.J. Lin, J.W. Yeh, Microstructure and wear behavior of AlxCo1.5CrFeNi1.5Tiy high-entropy alloys, Acta Mater. 59 (16) (Sep. 2011) 6308–6317, https://doi.org/10.1016/J.ACTAMAT.2011.06.041.
[6] M.A. Melia, et al., Mechanical and corrosion properties of additively manufactured CoCrFeMnNi high entropy alloy, Addit. Manuf. 29 (Oct. 2019) 100833, https://doi.org/10.1016/J.ADDMA.2019.100833.
[7] Y. Shi, B. Yang, X. Xie, J. Brechtl, K.A. Dahmen, P.K. Liaw, Corrosion of Al xCoCrFeNi high-entropy alloys: Al-content and potential scan-rate dependent pitting behavior, Corrosion Sci. 119 (May 2017) 33–45, https://doi.org/10.1016/j.corsci.2017.02.019.
[8] W. Wang, J. Wang, H. Yi, W. Qi, Q. Peng, Effect of molybdenum additives on corrosion behavior of (CoCrFeNi)100-xMox high-entropy alloys, Entropy 20 (12) (Dec. 2018), https://doi.org/10.3390/e20120908.
[9] Y.D. Wu, et al., A refractory Hf25Nb25Ti25Zr25 high-entropy alloy with excellent structural stability and tensile properties, Mater. Lett. 130 (Sep. 2014) 277–280, https://doi.org/10.1016/j.matlet.2014.05.134.
[10] J.M. Torralba, P. Alvaredo, A. García-Junceda, High-entropy alloys fabricated via powder metallurgy. A critical review, Powder Metall. 62 (2) (Mar. 15, 2019) 84–114, https://doi.org/10.1080/00325899.2019.1584454. Taylor and Francis Ltd.
[11] Nickel Infocard, European chemicals agency. https://echa.europa.eu/substance-information/-/substanceinfo/100.028.283.
[12] Cobalt Infocard, European chemicals agency. https://echa.europa.eu/substance-information/-/substanceinfo/100.028.325?_disssubsinfo_WAR_disssubsinfoportlet_backURL=https%3A%2F%2Fecha.europa.eu%2Finformation-on-chemicals%3Fp_p_id%3Ddisssimplesearchhomepage_WAR_disssearchportlet%26p_p_lifecycle%3D0%26.
[13] J.M. Torralba, S. Venkatesh Kumarán, Development of competitive high-entropy alloys using commodity powders, Mater. Lett. 301 (Oct. 2021) 130202, https://doi.org/10.1016/J.MATLET.2021.130202.
[14] W.H. Liu, T. Yang, C.T. Liu, Precipitation hardening in CoCrFeNi-based high entropy alloys, Mater. Chem. Phys. 210 (May 2018) 2–11, https://doi.org/10.1016/J.MATCHEMPHYS.2017.07.037.
[15] C.Y. Hsu, C.C. Juan, S.T. Chen, T.S. Sheu, J.W. Yeh, S.K. Chen, Phase diagrams of high-entropy alloy system Al-Co-Cr-Fe-Mo-Ni, JOM 65 (12) (Dec. 2013) 1829–1839, https://doi.org/10.1007/s11837-013-0773-2.
[16] X.A. Hu, G. le Zhao, F.C. Liu, W.X. Liu, Microstructure and mechanical behavior of Inconel 625 alloy processed by selective laser melting at high temperature up to 1000 °C, Rare Met. 39 (10) (2020) 1181–1189, Oct, https://doi.org/10.1007/S12598-019-01321-3/TABLES/2.
[17] Ö. Özgün, R. Yilmaz, H. Özkan Gülsoy, F. Findik, The effect of aging treatment on the fracture toughness and impact strength of injection molded Ni-625 superalloy parts, Mater. Char. 108 (2015) 8–15, https://doi.org/10.1016/j.matchar.2015.08.006.
[18] A. Mostafaei, E.L. Stevens, E.T. Hughes, S.D. Biery, C. Hilla, M. Chmielus, Powder bed binder jet printed alloy 625: densification, microstructure and mechanical properties, Mater. Des. 108 (2016) 126–135, https://doi.org/10.1016/j.matdes.2016.06.067.
[19] Ö. Özgün, H. Özkan Gülsoy, R. Yilmaz, F. Findik, Injection molding of nickel based 625 superalloy: sintering, heat treatment, microstructure and mechanical properties, J. Alloys Compd. 546 (2013) 192–207, https://doi.org/10.1016/j.jallcom.2012.08.069.
[20] H. Carpenter, S. Tamura, The formation of twinned nanocrystals 113 (763) (1926), https://doi.org/10.1098/rspa.1926.0144.
[21] C. Dai, Y. Fu, Y. Pan, Y. Yin, C. Du, Z. Liu, Microstructure and mechanical properties of FeCoCrNiMo0.1 high-entropy alloy with various annealing treatments, Mater. Char. 179 (Sep. 2021) 111313, https://doi.org/10.1016/J.MATCHAR.2021.111313.
[22] W.H. Liu, et al., Ductile CoCrFeNiMox high entropy alloys strengthened by hard intermetallic phases, Acta Mater. 116 (Sep. 2016) 332–342, https://doi.org/10.1016/j.actamat.2016.06.063.
[23] H. Ma, C.H. Shek, Effects of Hf on the microstructure and mechanical properties of CoCrFeNi high entropy alloy, J. Alloys Compd. 827 (Jun. 2020) 154159, https://doi.org/10.1016/J.JALLCOM.2020.154159.
[24] Y. Brif, M. Thomas, I. Todd, The use of high-entropy alloys in additive manufacturing, Scripta Mater. 99 (Apr. 2015) 93–96, https://doi.org/10.1016/j.scriptamat.2014.11.037.
[25] I. Moravcik, et al., Microstructure and mechanical properties of Ni1,5Co1,5CrFeTi0,5 high entropy alloy fabricated by mechanical alloying and spark plasma sintering, Mater. Des. 119 (2017) 141–150, https://doi.org/10.1016/j.matdes.2017.01.036.
[26] C. Sun, P. Li, S. Xi, Y. Zhou, S. Li, X. Yang, A new type of high entropy alloy composite Fe18Ni23Co25Cr21Mo8WNb3C2 prepared by mechanical alloying and hot pressing sintering, Mater. Sci. Eng. 728 (Jun. 2018) 144–150, https://doi.org/10.1016/J.MSEA.2018.05.022.
[27] S. Xie, et al., Effect of phase transformation on densification kinetics and properties of spark plasma sintered Al0.7CoCrFeNi high-entropy alloy, Mater. Char. 160 (October 2019) 2020, https://doi.org/10.1016/j.matchar.2019.110098.
[28] W.H. Liu, J.Y. He, H.L. Huang, H. Wang, Z.P. Lu, C.T. Liu, Effects of Nb additions on the microstructure and mechanical property of CoCrFeNi high-entropy alloys, Intermetallics 60 (2015) 1–8, https://doi.org/10.1016/J.INTERMET.2015.01.004.

[29] S.G. Ma, et al., Superior high tensile elongation of a single-crystal CoCrFeNiAl0.3 high-entropy alloy by Bridgman solidification, Intermetallics 54 (Nov. 2014) 104–109, https://doi.org/10.1016/J.INTERMET.2014.05.018.
[30] G.A. Salishchev, et al., Effect of Mn and V on structure and mechanical properties of high-entropy alloys based on CoCrFeNi system, J. Alloys Compd. 591 (Apr. 2014) 11–21, https://doi.org/10.1016/J.JALLCOM.2013.12.210.
[31] A.V. Kuznetsov, D.G. Shaysultanov, N.D. Stepanov, G.A. Salishchev, O.N. Senkov, Tensile properties of an AlCrCuNiFeCo high-entropy alloy in as-cast and wrought conditions, Mater. Sci. Eng. 533 (2012) 107–118, https://doi.org/10.1016/j.msea.2011.11.045.
[32] Z. Tang, et al., Tensile ductility of an AlCoCrFeNi multi-phase high-entropy alloy through hot isostatic pressing (HIP) and homogenization, Mater. Sci. Eng., A 647 (Oct. 2015) 229–240, https://doi.org/10.1016/J.MSEA.2015.08.078.
[33] C.W. Tsai, M.H. Tsai, J.W. Yeh, C.C. Yang, Effect of temperature on mechanical properties of Al0.5CoCrCuFeNi wrought alloy, J. Alloys Compd. 490 (1–2) (Feb. 2010) 160–165, https://doi.org/10.1016/J.JALLCOM.2009.10.088.
[34] I.S. Wani, et al., Ultrafine-Grained AlCoCrFeNi2.1 Eutectic High-Entropy Alloy, vol. 4, Mar. 2016, pp. 174–179, https://doi.org/10.1080/21663831.2016.1160451. http://mc.manuscriptcentral.com/tmrl, 3.
[35] Y. Dong, X. Gao, Y. Lu, T. Wang, T. Li, A multi-component AlCrFe2Ni2 alloy with excellent mechanical properties, Mater. Lett. 169 (Apr. 2016) 62–64, https://doi.org/10.1016/J.MATLET.2016.01.096.
[36] W.H. Liu, et al., Ductile CoCrFeNiMox high entropy alloys strengthened by hard intermetallic phases, Acta Mater. 116 (Sep. 2016) 332–342, https://doi.org/10.1016/J.ACTAMAT.2016.06.063.
[37] F. Otto, A. Dlouhý, C. Somsen, H. Bei, G. Eggeler, E.P. George, The influences of temperature and microstructure on the tensile properties of a CoCrFeMnNi high-entropy alloy, Acta Mater. 61 (15) (2013) 5743–5755, Sep, https://doi.org/10.1016/J.ACTAMAT.2013.06.018.
[38] J. Chen, B. Young, Stress–strain curves for stainless steel at elevated temperatures, Eng. Struct. 28 (2) (Jan. 2006) 229–239, https://doi.org/10.1016/J.ENGSTRUCT.2005.07.005.
[39] V. Venkatesh, H.J. Rack, Elevated temperature hardening of INCONEL 690, Mech. Mater. 30 (1) (Sep. 1998) 69–81, https://doi.org/10.1016/S0167-6636(98)00020-9.
[40] R. Schaeublin, T. Leguey, P. Spätig, N. Baluc, M. Victoria, Microstructure and mechanical properties of two ODS ferritic/martensitic steels, J. Nucl. Mater. 307–311 (1 SUPPL) (Dec. 2002) 778–782, https://doi.org/10.1016/S0022-3115(02)01193-5.
[41] A. Chauhan, D. Litvinov, J. Aktaa, High temperature tensile properties and fracture characteristics of bimodal 12Cr-ODS steel, J. Nucl. Mater. 468 (Jan. 2016) 1–8, https://doi.org/10.1016/J.JNUCMAT.2015.11.013.
[42] R.S. Sundar, S.C. Deevi, High-temperature strength and creep resistance of FeAl, Mater. Sci. Eng., A 357 (1–2) (Sep. 2003) 124–133, https://doi.org/10.1016/S0921-5093(03)00261-2.
[43] A. Gali, E.P. George, Tensile properties of high- and medium-entropy alloys, Intermetallics 39 (2013) 74–78, https://doi.org/10.1016/j.intermet.2013.03.018.
[44] W. Wang, M. Yang, D. Yan, P. Jiang, F. Yuan, X. Wu, Deformation mechanisms for superplastic behaviors in a dual-phase high specific strength steel with ultrafine grains, Mater. Sci. Eng., A 702 (Aug. 2017) 133–141, https://doi.org/10.1016/J.MSEA.2017.07.011.
[45] T.T. Shun, L.Y. Chang, M.H. Shiu, Microstructure and mechanical properties of multiprincipal component CoCrFeNiMox alloys, Mater. Char. 70 (Aug. 2012) 63–67, https://doi.org/10.1016/J.MATCHAR.2012.05.005.
[46] J. Wang, et al., Flow behavior and microstructures of powder metallurgical CrFeCoNiMo0.2 high entropy alloy during high temperature deformation, Mater. Sci. Eng., A 689 (Mar. 2017) 233–242, https://doi.org/10.1016/J.MSEA.2017.02.064.
[47] X. Yang, Y. Zhang, Prediction of high-entropy stabilized solid-solution in multi-component alloys, Mater. Chem. Phys. 132 (2–3) (Feb. 2012) 233–238, https://doi.org/10.1016/j.matchemphys.2011.11.021.
[48] Introduction to Solid State Physics, Charles Kittel, 2005.
[49] K.Y. Tsai, M.H. Tsai, J.W. Yeh, Sluggish diffusion in Co-Cr-Fe-Mn-Ni high-entropy alloys, Acta Mater. 61 (13) (2013) 4887–4897, https://doi.org/10.1016/j.actamat.2013.04.058.
[50] Hunan Fushel Technology Limited. https://www.fusnano.com/. (Accessed 6 May 2021).

Supplementary data

A novel and sustainable method to develop non-equiatomic $CoCrFeNiMo_x$ high entropy alloys via spark plasma sintering using commercial commodity powders and evaluation of its mechanical behaviour

S Venkatesh Kumaran[1,2], Dariusz Garbiec[3], José Manuel Torralba[1,2]

1. IMDEA Materials Institute, Madrid, Spain, 28906
2. Universidad Carlos III de Madrid, Leganes, Spain, 28911
3. Łukasiewicz Research Network – Poznań Institute of Technology, 6 Ewarysta Estkowskiego St., 61-755, Poznan, Poland

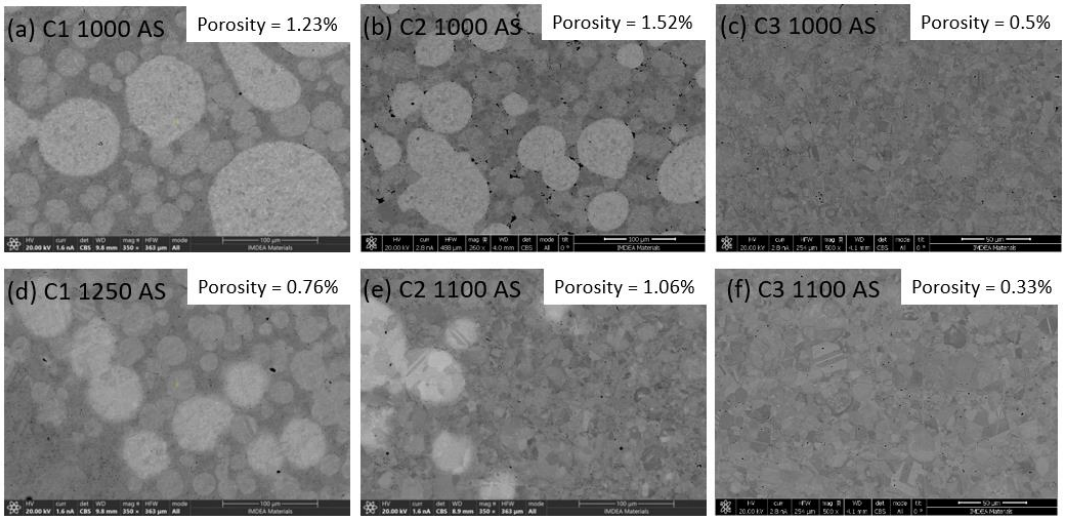

Fig. S 1: SEM images of as-sintered samples via SPS; C1 sintered at (a) 1000°C, (d) 1250°C, and C2 sintered at (b) 1000°C, (e) 1100°C, and C3 sintered at (c) 1000°C, (f) 1100°C

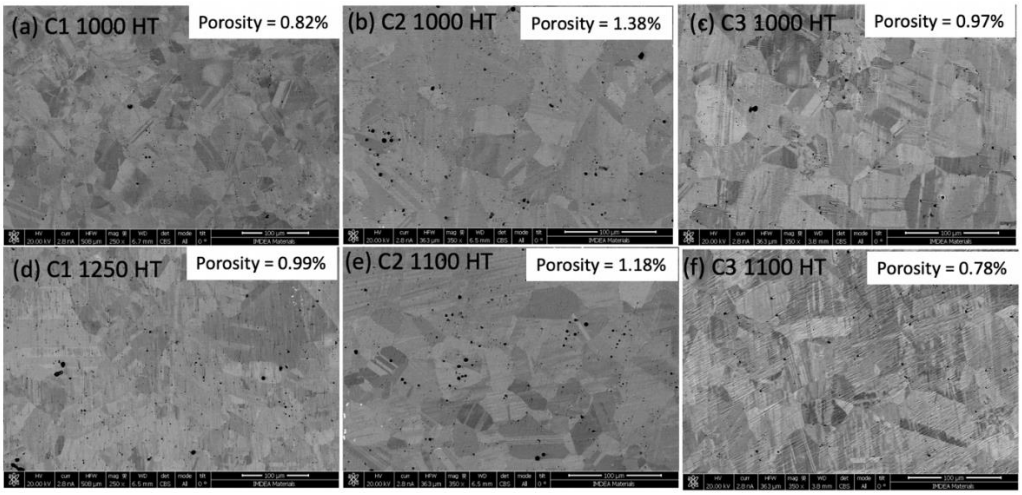

Fig. S 2: SEM images of samples sintered at various temperatures via SPS and annealed at 1200°C for 24 hours; C1 sintered at (a) 1000°C, (d) 1250°C, and C2 sintered at (b) 1000°C, (e) 1100°C, and C3 sintered at (c) 1000°C, (f) 1100°C

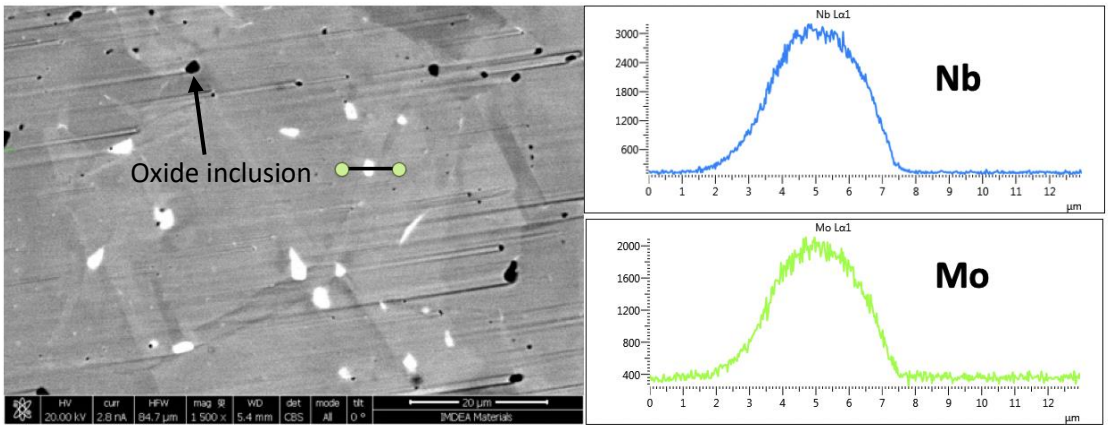

Fig. S 3: SEM BSE image of C1 alloy sintered at 1000°C and annealed at 1200°C for 24 hours with a line scan on a precipitate showing the distribution of Nb and Mo. The black arrow points at an oxide inclusion

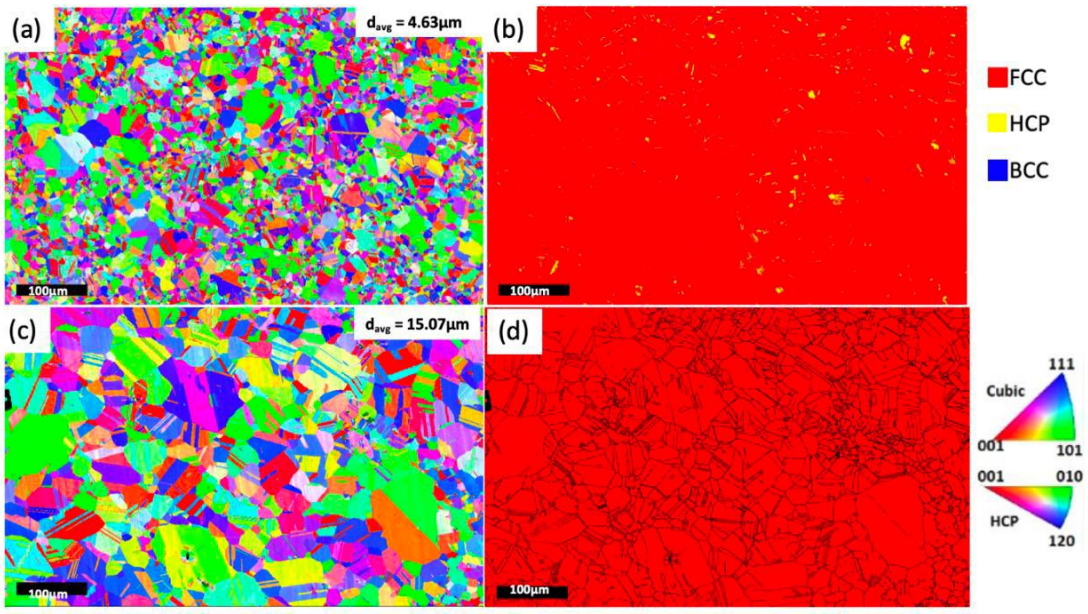

Fig. S 4: IPF and phase map of C1 alloy sintered at 1250°C in the as-sintered state (a, b) and after annealing at 1200°C for 24hrs (c, d)

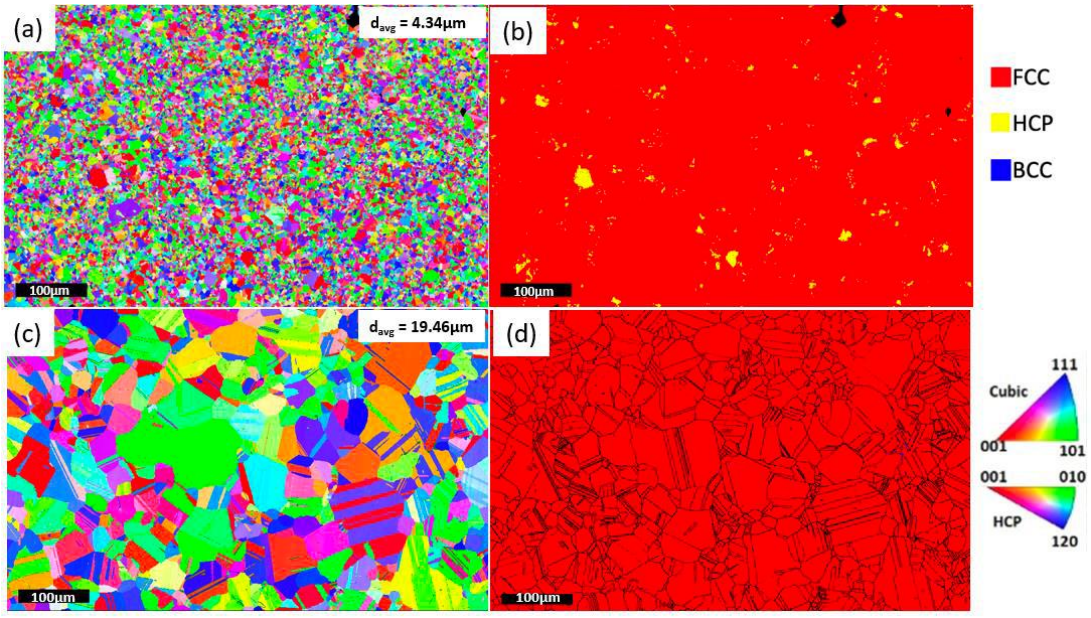

Fig. S 5. IPF and phase map of C2 alloy sintered at 1000°C in the as-sintered state (a, b) and after annealing at 1200°C for 24hrs (c, d)

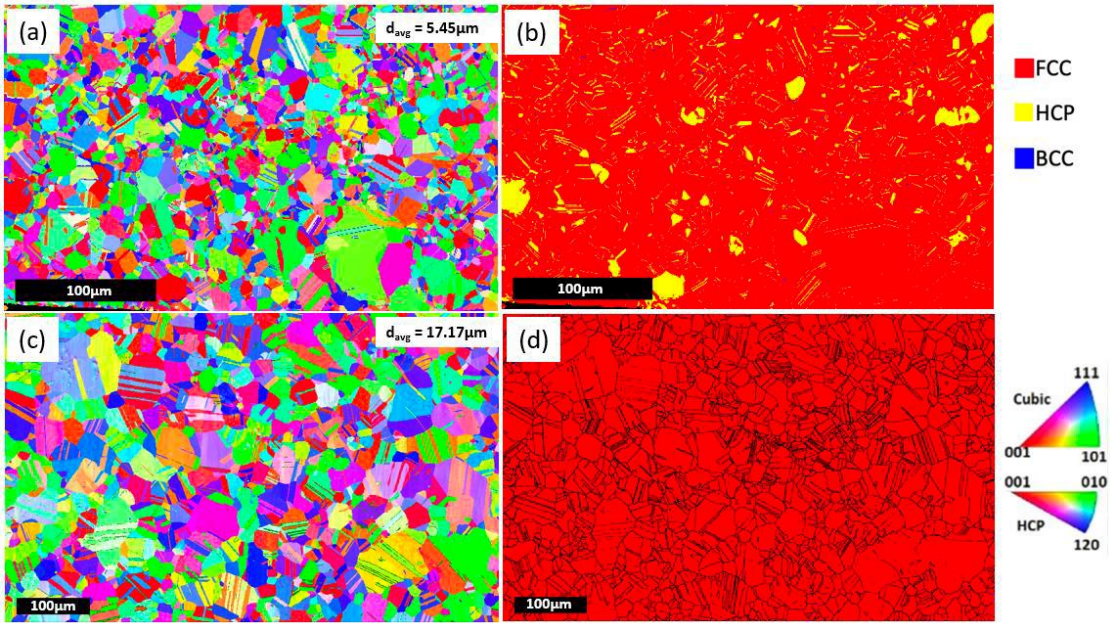

Fig. S 6. IPF and phase map of C2 alloy sintered at 1100°C in the as-sintered state (a, b) and after annealing at 1200°C for 24hrs (c, d)

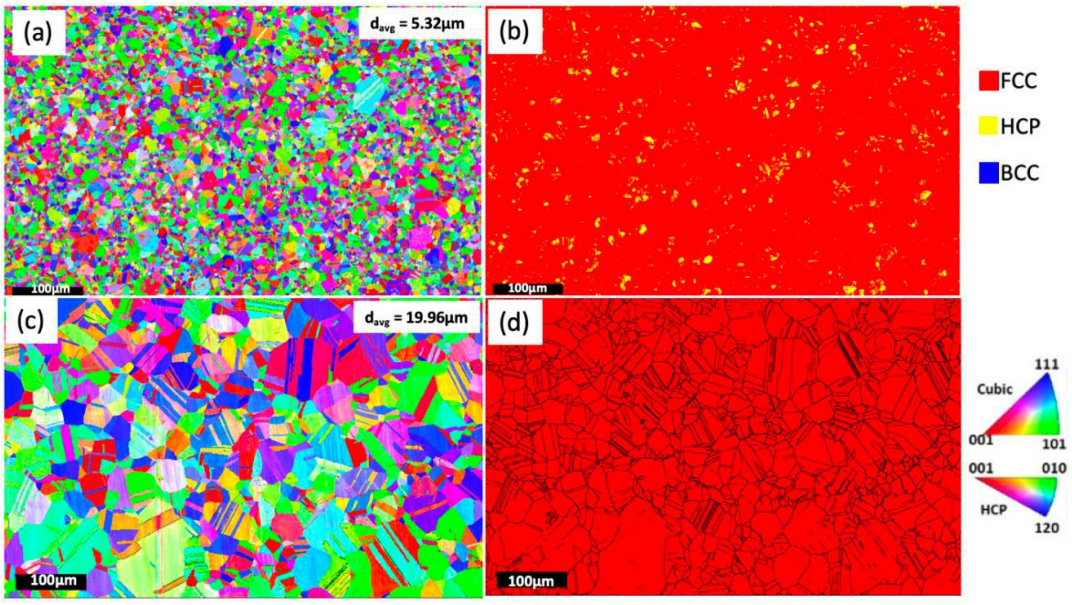

Fig. S 7. IPF and phase map of C3 alloy sintered at 1100°C in the as-sintered state (a, b) and after annealing at 1200°C for 24 hrs (c, d)

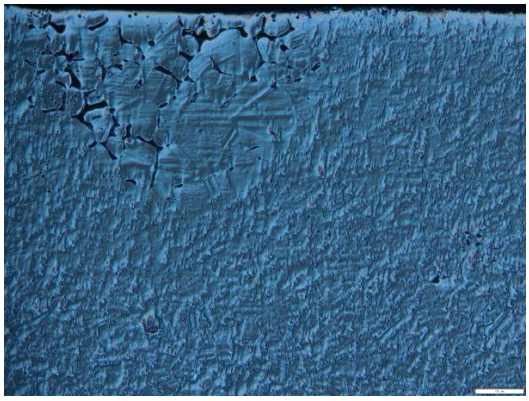

Fig. S 8. Optical microscope images of C1 alloy sintered at 1250°C and annealed at 1200°C for 24 hours

Table S1: Results of hot compression properties of C1, C2 and C3 alloys in the as-sintered (AS) and heat-treated (HT) condition from room temperature to 750°C

Temperature (°C)	Mechanical Property	C1 1000°C AS	C1 1250°C AS	C2 1000°C AS	C2 1100°C AS	C3 1000°C AS	C3 1100°C AS	C1 1000°C HT	C1 1250°C HT	C2 1000°C HT	C2 1100°C. HT	C3 1000°C HT	C3 1000°C HT
RT	YS (MPa)	370	268.8	572.3	506	501.7	335	310	211	330	242.7	205	183.6
	UTS (Mpa)	1242.5	1351.3	1547	1847.7	1134.4	1184	1224	1202.5	1352.5	1337.6	871.5	1076.6
	Ductility (%)	31.5	33.7	31	37	35.8	39.2	>44	>42	>41	>46.1	>39	>39
600	YS (MPa)	310	335.8	394	320	277.6	210	120	190	129	155.9	163.6	134
	UTS (MPa)	715.7	780.5	1039.2	1042.3	634	697	911	895	1115	1096	751.6	792.3
	Ductility (%)	20.1	28.45	25.6	30	29.9	35.2	>41.6	>37.6	>39.3	>41.9	>35.5	>34.7
700	YS (MPa)	272.5	211.5	353	211.09	227.6	188.9	122.5	127.3	132	163.5	113.5	145.8
	UTS (MPa)	525.2	663.4	802	806.3	446	503	705	683	757.5	859	549.7	497.4
	Ductility (%)	28.1	35.85	35.9	42.75	37	38.5	>41.7	>39.3	>37.9	>39.7	>35.5	>36.8
750	YS (MPa)	213	188	300	274.6	166	160.5	164	132.2	142	176	90	120.5
	UTS (MPa)	352.5	410.8	488.7	>596	265	313.8	530	424	642.2	613.5	376.6	390
	Ductility (%)	31	31.4	45	>37.7	34.8	43.7	>37.5	>34	>44.1	>36.6	>35.9	>33.7

Table S2: Tensile properties of different HEAs and some traditional alloys. The reference numbers shown are according to the original article. For convenience, the references are also listed here in the end with the original numbers.

Alloy	Process	$\sigma_{0.2}$ (MPa)	σ_{max} (MPa)	ε (%)	Reference
CoCrFeNi	AM (PBF-LB)	402	480	8	[24]
$Ni_{1.5}Co_{1.5}CrFeTi_{0.5}$	SPS	1308	1384	4	[25]
$Fe_{18}Ni_{23}Co_{25}Cr_{21}Mo_8WNb_3C_2$	Hot pressing		1452	3.9	[26]
$Al_{0.7}$CoCrFeNi	SPS		1053	7.3	[27]
C1 1000 HT (This work)	SPS	322	663.75	28.75	
C1 1250 HT (This work)	SPS	234	647.5	37.8	
C2 1000 HT (This work)	SPS	190	637.5	48.2	
C2 1100 HT (This work)	SPS	257.5	712	62	
C3 1000 HT (This work)	SPS	200	595	57.5	
C3 1100 HT (This work)	SPS	167.5	560	68	
CoCrFeNi	Arc melted	147	413	48	[28]
$CoCrFeNiNb_{0.103}$	Arc melted	317	622	19.2	[28]
$CoCrFeNiNb_{0.155}$	Arc melted	321	744	23.3	[28]
$CoCrFeNiNb_{0.206}$	Arc melted	402	807	8.6	[28]
$Al_{0.3}$CoCrFeNi	Arc melted	275	528	37	[29]
CoCrFeMnNi	Arc melted	215	491	71	[30]
AlCoCrCuFeNi	Arc melted and homogenized	790	790	0.2	[31]
AlCoCrFeNi	As-cast	395	400	1	[32]
AlCoCrFeNi	As cast+HIP	295	393	11.5	[32]
$Al_{0.5}$CoCrCuFeNi	Rolled	180	185	5	[33]
$Al_{0.5}$CoCrCuFeNi	Rolled+annealed	160	180	12	[33]
$AlCoCrFeNi_{2.1}$	As cast	620	1050	17	[34]
$AlCrFe_2Ni_2$	As cast	796	1437	15.7	[35]
$CoCrFeNiMo_{0.1}$	As cast	199	479	51.1	[36]
$CoCrFeNiMo_{0.2}$	As cast	255	590	55.2	[36]

$CoCrFeNiMo_{0.3}$	As cast	305	710	49.3	[36]
$CoCrFeNiMo_{0.3}$	Rolled	815	1186	18.9	[36]
$CoCrFeNiMo_{0.3}$	Rolled	647	1042	32.5	[36]
$CoCrFeNiMo_{0.3}$	Rolled+annealed	684	1067	30.4	[36]
CoCrFeNiMn	High Pressure Torsion	1400	1740	4	[37]
Duplex Stainless Steel		329	366	2.4	[38]
304 Stainless Steel		179	248	9.1	[38]
Inconel 680		150	478	26	[39]
ODS Steel+0.3%Ytria		210	272	11	[40]
12Cr-ODS ferritic		1200	1294	18	[41]
Intermetallic FeAl		345	350	18	[42]

References

[24] Y. Brif, M. Thomas, and I. Todd, “The use of high-entropy alloys in additive manufacturing,” Scr Mater, vol. 99, pp. 93–96, Apr. 2015, doi: 10.1016/j.scriptamat.2014.11.037.

[25] I. Moravcik et al., “Microstructure and mechanical properties of Ni1,5Co1,5CrFeTi0,5 high entropy alloy fabricated by mechanical alloying and spark plasma sintering,” Mater Des, vol. 119, pp. 141–150, 2017, doi: 10.1016/j.matdes.2017.01.036.

[26] C. Sun, P. Li, S. Xi, Y. Zhou, S. Li, and X. Yang, “A new type of high entropy alloy composite Fe18Ni23Co25Cr21Mo8WNb3C2 prepared by mechanical alloying and hot pressing sintering,” Materials Science and Engineering A, vol. 728, pp. 144–150, Jun. 2018, doi: 10.1016/J.MSEA.2018.05.022.

[27] S. Xie et al., “Effect of phase transformation on densification kinetics and properties of spark plasma sintered Al0.7CoCrFeNi high-entropy alloy,” Mater Charact, vol. 160, no. October 2019, 2020, doi: 10.1016/j.matchar.2019.110098.

[28] W. H. Liu, J. Y. He, H. L. Huang, H. Wang, Z. P. Lu, and C. T. Liu, “Effects of Nb additions on the microstructure and mechanical property of CoCrFeNi high-entropy alloys,” Intermetallics (Barking), vol. 60, pp. 1–8, 2015, doi: 10.1016/J.INTERMET.2015.01.004.

[29] S. G. Ma et al., “Superior high tensile elongation of a single-crystal CoCrFeNiAl0.3 high-entropy alloy by Bridgman solidification,” Intermetallics (Barking), vol. 54, pp. 104–109, Nov. 2014, doi: 10.1016/J.INTERMET.2014.05.018.

[30] G. A. Salishchev et al., “Effect of Mn and V on structure and mechanical properties of high-entropy alloys based on CoCrFeNi system,” J Alloys Compd, vol. 591, pp. 11–21, Apr. 2014, doi: 10.1016/J.JALLCOM.2013.12.210.

[31] A. V. Kuznetsov, D. G. Shaysultanov, N. D. Stepanov, G. A. Salishchev, and O. N. Senkov, “Tensile properties of an AlCrCuNiFeCo high-entropy alloy in as-cast and wrought conditions,” Materials Science and Engineering A, vol. 533, pp. 107–118, 2012, doi: 10.1016/j.msea.2011.11.045.

[32] Z. Tang et al., “Tensile ductility of an AlCoCrFeNi multi-phase high-entropy alloy through hot isostatic pressing (HIP) and homogenization,” Materials Science and Engineering: A, vol. 647, pp. 229–240, Oct. 2015, doi: 10.1016/J.MSEA.2015.08.078.

[33] C. W. Tsai, M. H. Tsai, J. W. Yeh, and C. C. Yang, “Effect of temperature on mechanical properties of Al0.5CoCrCuFeNi wrought alloy,” J Alloys Compd, vol. 490, no. 1–2, pp. 160–165, Feb. 2010, doi: 10.1016/J.JALLCOM.2009.10.088.

[34] I. S. Wani et al., “Ultrafine-Grained AlCoCrFeNi2.1 Eutectic High-Entropy Alloy,” http://mc.manuscriptcentral.com/tmrl, vol. 4, no. 3, pp. 174–179, Mar. 2016, doi: 10.1080/21663831.2016.1160451.

[35] Y. Dong, X. Gao, Y. Lu, T. Wang, and T. Li, “A multi-component AlCrFe2Ni2 alloy with excellent mechanical properties,” Mater Lett, vol. 169, pp. 62–64, Apr. 2016, doi: 10.1016/J.MATLET.2016.01.096.

[36] W. H. Liu et al., “Ductile CoCrFeNiMox high entropy alloys strengthened by hard intermetallic phases,” Acta Mater, vol. 116, pp. 332–342, Sep. 2016, doi: 10.1016/J.ACTAMAT.2016.06.063.

[37] F. Otto, A. Dlouhý, C. Somsen, H. Bei, G. Eggeler, and E. P. George, “The influences of temperature and microstructure on the tensile properties of a CoCrFeMnNi high-entropy alloy,” Acta Mater, vol. 61, no. 15, pp. 5743–5755, Sep. 2013, doi: 10.1016/J.ACTAMAT.2013.06.018.

[38] J. Chen and B. Young, “Stress–strain curves for stainless steel at elevated temperatures,” Eng Struct, vol. 28, no. 2, pp. 229–239, Jan. 2006, doi: 10.1016/J.ENGSTRUCT.2005.07.005.

[39] V. Venkatesh and H. J. Rack, “Elevated temperature hardening of INCONEL 690,” Mechanics of Materials, vol. 30, no. 1, pp. 69–81, Sep. 1998, doi: 10.1016/S0167-6636(98)00020-9.

[40] R. Schaeublin, T. Leguey, P. Spätig, N. Baluc, and M. Victoria, “Microstructure and mechanical properties of two ODS ferritic/martensitic steels,” Journal of Nuclear Materials, vol. 307–311, no. 1 SUPPL., pp. 778–782, Dec. 2002, doi: 10.1016/S0022-3115(02)01193-5.

[41] A. Chauhan, D. Litvinov, and J. Aktaa, “High temperature tensile properties and fracture characteristics of bimodal 12Cr-ODS steel,” Journal of Nuclear Materials, vol. 468, pp. 1–8, Jan. 2016, doi: 10.1016/J.JNUCMAT.2015.11.013.

[42] R. S. Sundar and S. C. Deevi, “High-temperature strength and creep resistance of FeAl,” Materials Science and Engineering: A, vol. 357, no. 1–2, pp. 124–133, Sep. 2003, doi: 10.1016/S0921-5093(03)00261-2.

Paper 4

S Venkatesh Kumaran, JM Torralba, “Laser powder bed fusion processing of low cost $CoCrFeNiMo_xNb_y$ high entropy alloys with promising high-temperature properties via in-situ alloying commercial powders: Inconel, CoCrF75, 316L, and INVAR”, Metals, (2024), 14(5), 500, https://doi.org/10.3390/met14050500

metals

MDPI

Article

Laser Powder Bed Fusion Processing of Low Cost $CoCrFeNiMo_xNb_y$ High Entropy Alloys with Promising High-Temperature Properties via In Situ Alloying Commercial Powders

S. Venkatesh Kumaran [1,2,*] and José Manuel Torralba [1,2]

[1] IMDEA Materials Institute, 28906 Madrid, Spain; torralba@ing.uc3m.es
[2] Department of Materials Science and Engineering, Universidad Carlos III de Madrid, 28911 Leganes, Spain
* Correspondence: s.venkateshk@gmail.com

Abstract: A blend of only commercial powders, including Ni625, CoCrF75, and 316L, were used as the raw material for fabricating non-equiatomic $CoCrFeNiMo_xNb_y$ high entropy alloys (HEAs) through laser powder bed fusion (PBF-LB/M) via in situ alloying, instead of using pure elemental powders, thus reducing the raw materials cost. The rapid cooling inherent in the PBF-LB/M process facilitated the dissolution of Mo and Nb, resulting in a single FCC phase characterized by high relative densities. High-temperature tensile tests were conducted at room temperature, 700 °C, 800 °C, and 900 °C, revealing mechanical properties that surpassed those reported in existing HEA literature. The remarkable strength of the HEAs developed in this study primarily stemmed from the incorporation of Mo and Nb, leading to the precipitation of Mo and Nb-rich lave phases at elevated temperatures. While constraining elongation when confined to grain boundaries, these precipitates enhanced strength without compromising elongation when distributed throughout the matrix. This work is a feasibility study to explore the usage of commodity compositions from the market to develop HEAs using PBF-LB/M, which opens the possibility of using scraps to further the development of new materials. Consequently, this study presents a rapid and cost-effective approach for HEA development, improving efficiency and sidestepping the direct utilization of critical raw metals for sustainable manufacturing. Moreover, this work also underscores the outstanding mechanical performance of these HEAs at high temperatures, paving the way for the design of innovative alloys for future high-temperature applications.

Keywords: high entropy alloy; laser powder bed fusion; in-situ alloying; commercial powders; high temperature properties

Citation: Venkatesh Kumaran, S.; Torralba, J.M. Laser Powder Bed Fusion Processing of Low Cost $CoCrFeNiMo_xNb_y$ High Entropy Alloys with Promising High-Temperature Properties via In Situ Alloying Commercial Powders. *Metals* **2024**, *14*, 500. https://doi.org/10.3390/met14050500

Academic Editor: Eric Hug

Received: 15 March 2024
Revised: 16 April 2024
Accepted: 22 April 2024
Published: 25 April 2024

1. Introduction

Since the advent of high entropy alloys (HEAs) in 2004 [1,2], they have attracted significant attention due to the possibility of adding multiple principal elements to obtain unique microstructures and the possibility to fine-tune the properties, which results in high mechanical strength, good ductility, wear resistance, oxidation resistance, and corrosion resistance [3]. These properties result from the four core effects of HEAs, namely, (i) high entropy, (ii) severe lattice distortion, (iii) sluggish diffusion, and (iv) cocktail effect [4]. The definition of HEAs, initially stated as alloys consisting of more than five elements of composition range between 5 and 35 at% [1], has been modified to alloys with a configurational mixing entropy, $\Delta S_{mix} > 1.5$ R, where R is the gas constant [5].

The most common method used to manufacture HEAs has been casting or arc melting [1] due to its convenience and efficiency when more than five elements need to be solidified. However, due to its ultra-high cooling rate, powder metallurgy routes and

additive manufacturing have recently shown great potential in developing HEAs with remarkable properties [6,7]. The most prominent additive manufacturing techniques to produce HEAs have been through powder bed systems, either with a laser beam (PBF-LB/M) or with an electron beam (PBF-EB/M), and powder feed systems like laser metal deposition (LMD) [6]. In a powder bed process like the PBF-LB/M, the feedstock should be spherical with a size distribution between 15–63 μm [8] to ensure proper spreadability and fully pre-alloyed by, e.g., gas-atomization or plasma spheroidizing to avoid elemental segregation. This process of pre-alloying for HEAs, which starts from traditional melting and casting to gas-atomizing, is expensive and time-consuming as HEAs involve four or five principal elements, where some of which, like Co [9], are also critical metals. Critical raw metals lack availability and possess serious concerns about its availability in the future, as detailed in the European Union report [10–12], which included metals like Co, Mo, and Nb, among others. Therefore, this method is rigid and restricts the development and exploration of next-generation materials like HEAs via PBF-LB/M.

The concept of in situ alloying has been introduced recently in PBF-LB/M, where the constituent elements are alloyed simultaneously during consolidation. For instance, Simonelli et al. explored different feedstocks to print Ti-6Al-4V in PBF-LB/M by simply mixing elemental powders and by using a novel technique called satellite mixing, where the powders were wet mixed with polyvinyl alcohol [13]. Compared to the simply mixed feedstock, the segregations were observed to be significantly reduced with the satelliting technique. In a similar work, Ewald et al. used powder blends to produce HEAs based on Al-C-Co-Fe-Mn-Ni to enable rapid alloy development in PBF-LB/M [14]. The effects of process parameters on the homogeneity and mechanical properties were studied, and it was concluded that an optimized energy input results in a homogenous elemental distribution in the printed parts. In the study by Chen et al. [15], Mn powders were blended with pre-alloyed CoCrFeNi powder. Good printability with a nearly homogenous Mn distribution in the as-printed parts was observed with a high VED of 259.3 J/mm^3. Similarly, Sun et al. [16] fabricated CoCrFeNiMn by using elemental powders, and it exhibited slightly lower ultimate tensile strength but higher ductility than the HEA fabricated by fully prealloyed CoCrFeNi powder mixed with Mn elemental powders [15]. In another study by Hou et al. [17], the strength and hardness of CoCrFeNi HEA fabricated by pre-alloyed powders and by elemental powders were comparable, even though a higher energy input was necessary to obtain excellent performance in the case of elemental powders. Unmelted Cr particles were also observed in the overlapping regions of melt pools due to the very high melting point of Cr compared to the rest of the elements.

Since HEAs have four or five elements in almost equiatomic proportions, it is quite difficult to obtain a homogenous elemental distribution by using pure elemental powders, especially when there is a notable difference in the melting points of elements, densities, and a positive enthalpy of mixing between pairs of elements. This is observed in a study by Farquhar et al. [18], where Ti powders were unmelted due to the high melting point, and severe segregations of Cu were found due to its positive enthalpy of mixing with other elements in the HEA. Moreover, pure elemental powders can also be challenging to handle. For instance, in the most widely studied cantor alloy (CoCrFeMnNi), Cr has a high tendency to form chromium oxides, whereas Ni and Co are considered hazardous by the REACH regulations [9,19]. As a solution to this problem, in this work, a blend of commercial powders, which are cheaper and widely available in the market, are explored as a feedstock in PBF-LB/M. As described in our previous works, where this approach was used to develop HEAs using field-assisted hot pressing [20] and spark plasma sintering [21], there are many grades of powders available in the market that belong to the families of metals on which many HEAs are based: Ni, Cr, Fe, Co, Ti, Al, etc. These powders are mass-produced by several manufacturers and can be delivered in large quantities quickly at competitive prices. We term these powders as 'commodity' in this work. Recently, Knieps et al. investigated the effect of powder morphology on in situ alloying in PBF-

LB/M to enable the selection of correct powder feedstock by using a blend of commercial powders and elemental powders [22]. It was concluded that a multimodal particle size distribution (PSD) increases packing density and enhances process performance. However, no microstructural studies or evaluations of mechanical properties were carried out. After validating the work based on commercial powders for developing cost-effective HEAs [20,21], there have been studies using a similar approach but with the casting technique [23–25].

So, in this investigation, The main objectives of this research work are (a) avoiding the use of fully pre-alloyed powders for HEAs which need special atomizing by using critical raw materials which increases the cost, (b) as a solution to (a), to explore the feasibility of using widely available and cheaper commercial commodity powders thus easing the exploration of new HEAs, (c) to facilitate a higher level of recycling of scraps from such commodity alloys paving the way for sustainable manufacturing of HEAs and other next-generation materials. Coming to the choice of materials in this study, CoCrFeNi, being the most studied HEA due to its exceptional ductility and fracture toughness [26], was used as a basis to which high atomic size elements Mo and Nb were incorporated into it through the commercial powders. Mo and Nb are recognized for their ability to augment both room and high-temperature strength in the alloy [27,28]. Corresponding commercial powders were carefully selected and blended in precise proportions, yielding two distinct HEAs: $Co_{25.45}Cr_{19.2}Fe_{26.6}Ni_{25.2}Mo_3Nb_{1.65}$ and $Co_{21.4}Cr_{26.62}Fe_{24.8}Ni_{21.4}Mo_{3.9}Nb_{2.5}$. Similar alloys were previously developed in our earlier work using spark plasma sintering, revealing the presence of precipitates rich in Mo and Nb [21]. The literature indicates that large-sized atoms such as Mo and Nb tend to induce the formation of topologically closed packed phases (TCP), including σ, μ, and Laves phases, thereby compromising alloy ductility [29]. However, ultra-high cooling processes like PBF-LB/M have demonstrated the capability to suppress the occurrence of these TCP phases. Consequently, this prevents the reduction in ductility by increasing the solubility of Mo and Nb. The resulting elevated lattice distortion enhances the mechanical properties of the alloys, a phenomenon further explored in this study.

2. Materials and Methods

The gas-atomized powders used in this work were Ni 625, CoCrF75, 316L, and Invar36. Ni 625 and CoCrF75 powders were provided by VDM metals (Werdohl, Germany), 316L powders by Carpenter additive (Widnes, UK), and Invar36 by Sandvik Osprey (Neath, UK). The particle size range of all the powders was between 15 and 45 μm. The average particle sizes and compositions of powders are given in Table 1. It was important to keep the average particle size of the powders closer to each other to ensure good spreadability during PBF-LB/M processing, ensuring high densities.

Table 1. Proposed commodity alloys and their role in the target HEA.

Alloy	Size (d50) (μm)	Role	wt. (%)					
			Ni	Fe	Cr	Mo	Co	Nb
Ni625	32	Source of Ni, Cr, Fe, Mo	56.87	5	22	10	1	3.8
INVAR 36	29.9	Source of Fe and Ni	36	63.28	-	-	-	-
CoCrF75	30	Source of Co, Cr, and Mo	0.41	0.75	30	7	60.41	-
316L	31.6	Source of Fe, Cr, Ni, Mo	12.55	65.85	17.68	2.33	-	-

Based on the composition of the powders, two different alloys, labeled as C1 and C2, were designed to keep them reasonably equiatomic. The powders were simply mixed in appropriate proportions, as given in Table 2, where the final composition of the alloys is also shown. All the powders had good sphericity, as confirmed in the SEM image of the mix of powders shown in Figure 1. To ensure the formation of a solid solution for these

compositions, empirical parameters for C1 and C2 alloys were calculated in our previous work [20], which ensured the formation of the FCC phase.

Table 2. Proposed mixes of commodity powders used to develop different possible HEAs.

Alloy	wt. %				at. %					
	Ni625	INVAR 36	CoCrF75	316L	Ni	Fe	Cr	Mo	Co	Nb
C1	20	38	42	-	25.2	26.6	19.2	3	25.45	1.65
C2	30	-	37	33	21.4	24.8	26.62	3.9	22.6	2.5

The bulk samples were fabricated by laser beam powder bed fusion system AM 400 from Renishaw (UK) with a focused beam of a diameter of 70 µm. It should be noted that this machine uses a pulsed laser, where the point distance and exposure time calculate the scan speed. The material of the build plate utilized was S 275 steel. Cuboidal samples of 3 × 7 × 7 mm were built for process parameter optimization by varying the laser power, scan speed, and hatch distance with a constant layer thickness of 30 µm. Porosity analysis was carried out by optical microscope and ImageJ to determine the best combination of parameters. The samples were cut along the build direction, polished up to 1 µm diamond paste, and a collage of the whole surface of the samples (7 × 7 mm) was captured at 5x magnification to calculate the porosity levels using ImageJ. To reveal the melt pools, the samples were etched with Aqua regia solution (HNO_3:HCl:H_2O = 1:3:2) for 5 s. The parameters with the least porosity for C1 and C2 were selected and tested again for reproducibility, which yielded similar porosity levels. The same parameters were selected to print the samples for tensile testing. The optimized parameters and the average porosity amount for C1 and C2 are shown in Table 3 and the results are discuss in Section 4. For tensile testing, solid blocks of samples were printed for both C1 and C2 with the optimized parameters from which flat dog-bone-shaped samples were machined. The gauge dimension of the tensile samples was 12.5 × 3 × 2.5 mm. The tensile tests were performed at room temperature in an Instron 5966 machine at a strain rate of 10^{-3}/s. The high-temperature tensile tests were carried out in a Universal testing machine, MTS 810, according to ASTM E21-20 standard [30]. The heating rate was 100 °C/min, and the exposure time was 30 min. The microstructural and compositional analysis was performed in a FEG-SEM (Apreo 2S LoVac) which is equipped with an EDS and EBSD detector. X-ray diffraction studies were carried out in a PANalytical X-ray diffractometer for phase identification, and the obtained peaks were analyzed with Highscore Plus software 4.9.

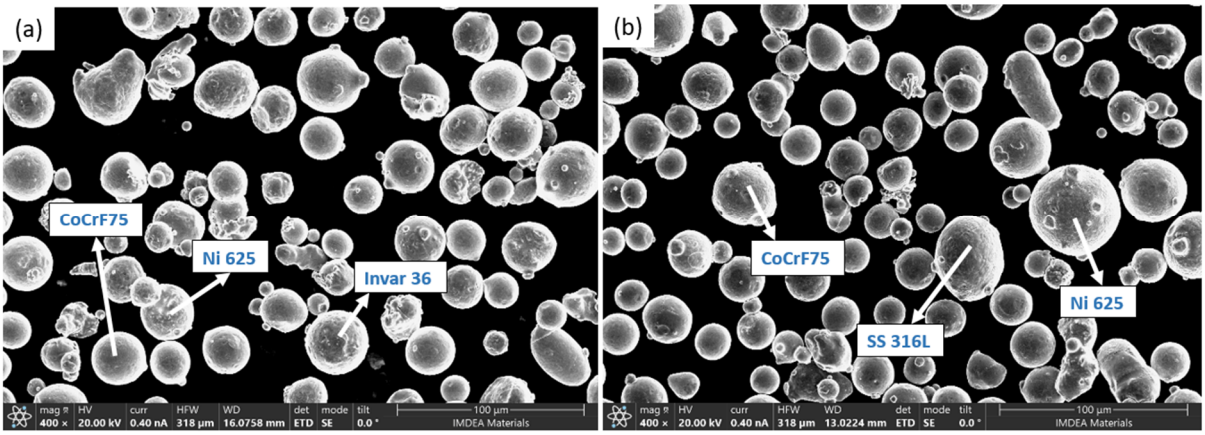

Figure 1. SEM image of (**a**) C1 and (**b**) C2 mix of powders.

Table 3. PBF-LB/M Parameters used to print C1 and C2 samples.

Alloy	Laser Power (W)	Hatch Distance (μm)	Scan Speed (mm/s)	Layer Thickness (μm)	Porosity (%)
C1	150	70	900	30	0.05 ± 0.008
C2	150	60	900	30	0.13 ± 0.017

3. Results and Discussion

3.1. Thermodynamic Predictions

There are certain empirical parameters that are used to predict the solid solution formation behavior of HEAs, given as follows:

Configurational entropy of mixing: $\Delta S_{mix} = -R\sum_{i=1}^{n} c_i ln c_i$

Enthalpy of mixing: $\Delta H_{mix} = \sum_{i=1, i\neq j}^{n} 4\Delta H_{ij}^{mix} c_i c_j$

Atomic size difference: $\delta = \sqrt{\sum_{i=1}^{n} c_i \left(1 - \frac{r_i}{\bar{r}}\right)^2}$, $\bar{r} = \sum_{i=1}^{n} c_i r_i$

Valence electron concentration: VEC = $\sum_{i=1}^{n} C_i (VEC)_i$

$$\Omega = \frac{T_{\bar{m}} \Delta S_{mix}}{|\Delta H_{mix}|}, \; T_{\bar{m}} = \sum_{i=1}^{n} c_i (T_m)_i$$

where n represents the number of elements, R is the gas constant, $\bar{r}$ is the average atomic radius of the alloy, r_i is the atomic radius of the constituent element and is obtained from [31], c_i is the atomic fraction of the alloy elements, and $T_{\bar{m}}$ is the melting point of the alloy calculated by the rule of mixtures. Ω is a new parameter defined in [32] to predict the formation of a solid solution (SS) phase that reflects the strength of entropy and enthalpy. The values of the empirical parameters for C1 and C2 alloy are calculated and tabulated in Table 4. These parameters, being most applicable to HEAs fabricated by casting/arc melting, might be unsuitable for additive manufacturing because of their rapid cooling rate and ability to suppress unfavorable compounds. However, they provide useful information for designing initial HEA compositions. Both C1 and C2 HEA satisfy all the parameters except ΔH_{mix} to form SS, i.e., FCC phase, according to the VEC. A large negative value of ΔH_{mix} Favours formation of an amorphous phase [33], but since both C1 and C2 exhibit FCC phase, as confirmed by XRD and EBSD, we conclude that this parameter model is not strictly applicable to these alloys.

Table 4. Various empirical parameters' values of C1 and C2 along with the threshold values for SS formation.

Alloy	ΔS_{mix}	ΔH_{mix}	δ (%)	VEC	Ω/1000
C1	−1.54 R	−12.46	1.28	8.36	1.685
C2	−1.58 R	−14.21	1.3	8.11	1.575
Threshold values	>1.5 R [5]	−11.6 < ΔH_{mix}< 3.2 [33]	<6.6 [33]	>8 for FCC [34]	≥1.1 [32]

3.2. Porosity Analysis

Porosity analysis was carried out first in the C2 alloy fabricated by SLM. Based on the literature study of the commercial powders used for the initial screening design, a volumetric energy density (VED) of 68–200 J/mm^3 was analyzed with laser power (P) in the range of 100–300 W and scan speed (s) in the range from 500–1000 mm/s. The layer thickness (t) and hatch distance (h) were kept constant at 30 μm and 70 μm, respectively. The hatch distance of 70 μm was chosen as a base due to the same value of laser spot size of the Renishaw AM 400 machine. The VED is calculated as $\frac{P}{S * t * h}$. Two additional hatch distances of 50 and 60 μm were used at select combinations to try to reduce the porosities further. The porosity values in percentages for C2 alloy are shown in Figure 2c. The general trend observed was that the porosity amount increased with laser power at a given scanning speed due to over-melting, as seen from the spherical gas pores in Figure 2e,f, whereas too low a power of 100 W also increased the porosity amount due to insufficient melting causing lack of fusion pores as seen in Figure 2a,b. Since the C2

samples achieved high relative densities, the second experimental trial for C2 was used as a starting point for C1 since the compositions were similar to reduce the iterations. The graph for the C1 alloy is included in the supplementary report in Figure S2, along with the C2 graph for the hatch distance of 50 µm. With a laser power of 150 W and a scan speed of 900 mm/s, a hatch distance of 60 µm worked slightly better for C2 alloys than a hatch distance of 70 µm but increased the porosity for C1 alloy. And with the same laser power and scanning speed, a 70 µm hatch distance, i.e., with a reduced VED, could reduce the porosities in C1 alloy. A lower VED perhaps worked better for C1 due to the lower quantity of high melting point elements Mo and Nb compared to C2. The final optimized parameters of C1 and C2 HEA are listed in Table 4. Such reduced porosity levels prove that this HEA system is so well suited to be processed with PBF-LB/M via in situ alloying commercial powders.

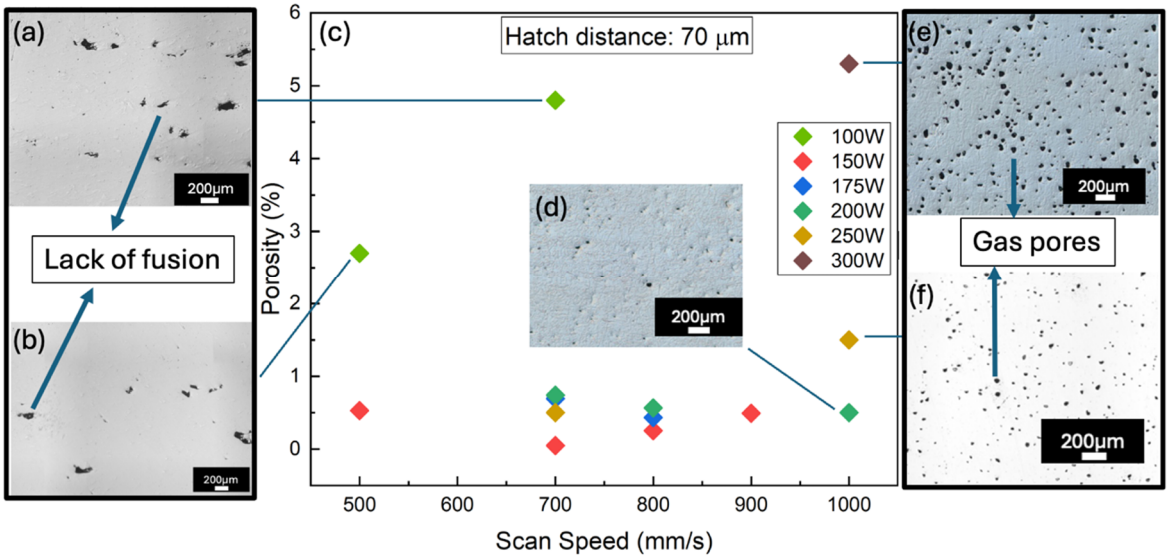

Figure 2. Optical micrograph (OM) of C2 sample printed at 100 W and (**a**) 700 mm/s and (**b**) 500 mm/s, (**c**) Porosity percentage plotted against scan speed for various laser powers, OM of C2 sample printed at 1000 mm/s and (**d**) 200 W, (**e**) 250 W, and (**f**) 300 W.

3.3. Microstructural Analysis

The microstructures of C1 and C2 alloys along the building direction were studied in SEM, as shown in Figure 3a,b. The microstructure reveals grain boundaries, melt pool boundaries, and various substructures, which are elongated columnar and equiaxed cellular, in the nanoscale within the grains. The grain growth here is typical epitaxial growth in the direction of the maximum temperature gradient, which is typically observed in PBF-LB/M processes. As observed in the literature, the boundaries of the substructures might be enriched in heavy elements like Mo and Nb [35] and possess a high density of dislocations [36], which restricts dislocation movement and enhances the strength of the alloy. The high dislocation density can be attributed to the rapid cooling process in PBF-LB/M.

X-ray diffraction was performed on the alloys to identify the phase structure. As shown in Figure 4a, both C1 and C2 alloys showed only FCC peaks confirming the single-phase solid solution structure in the as-built stage itself. Controlling segregations by in situ alloying remains a challenge due to the random mixture of powders in the feedstock and lack of time for proper homogenization in the micro-sized melt pool at such high cooling rates, due to which it is difficult to predict the composition at any point in the blend and inside the melt pool as well. Reducing the number of elemental powders by using a mix of commodity powders to produce HEAs offers a better solution since most of the elements are already alloyed. As shown in Figure 4b for C1 alloy and Figure 4c for

C2 alloy, even when the feedstock is a blend of powders, the processed alloys show almost a homogenous elemental distribution with remarkably high relative densities of 99.9%, proving the feasibility of this novel method of using commodity powders. Some minor heterogeneities are observed along the melt pool boundaries for C1 alloy, as shown in Figure 4b, which is quite negligible compared with common in in situ alloyed microstructures with a single melt [18,37]. However, this can be fixed by a short homogenization treatment, which is beyond the scope of the current feasibility study. To further confirm the phases, EBSD analysis was performed, and the results are shown in Figure 5. Both C1 and C2 alloys had a single FCC phase in the as-built state, which shows that the developed alloys, as predicted by the calculations in [20], are indeed HEA. The grain morphology is columnar along the build direction, as expected in the PBF-LB/M process. Both the alloys had the same average grain size of 20 μm as measured from the EBSD with a critical misorientation angle of 10^0, which shows that the higher amount of Mo and Cr in the C2 alloy had no effect on the grain size.

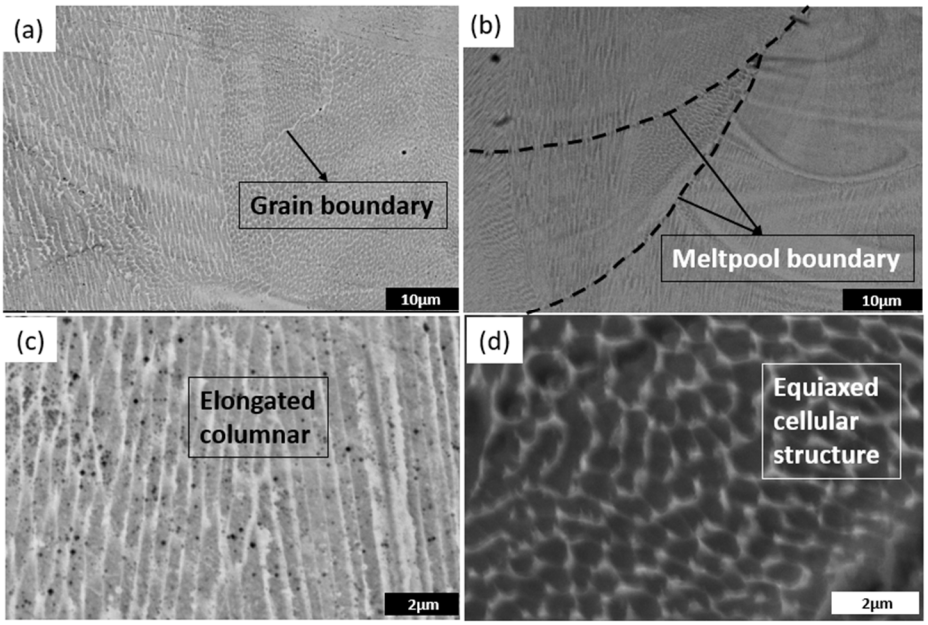

Figure 3. BSE-SEM image of (**a**) C1 alloy, (**b**) C2 alloy, magnified view of substructures in analogous regions of (**c**) C1 alloy and (**d**) C2 alloy.

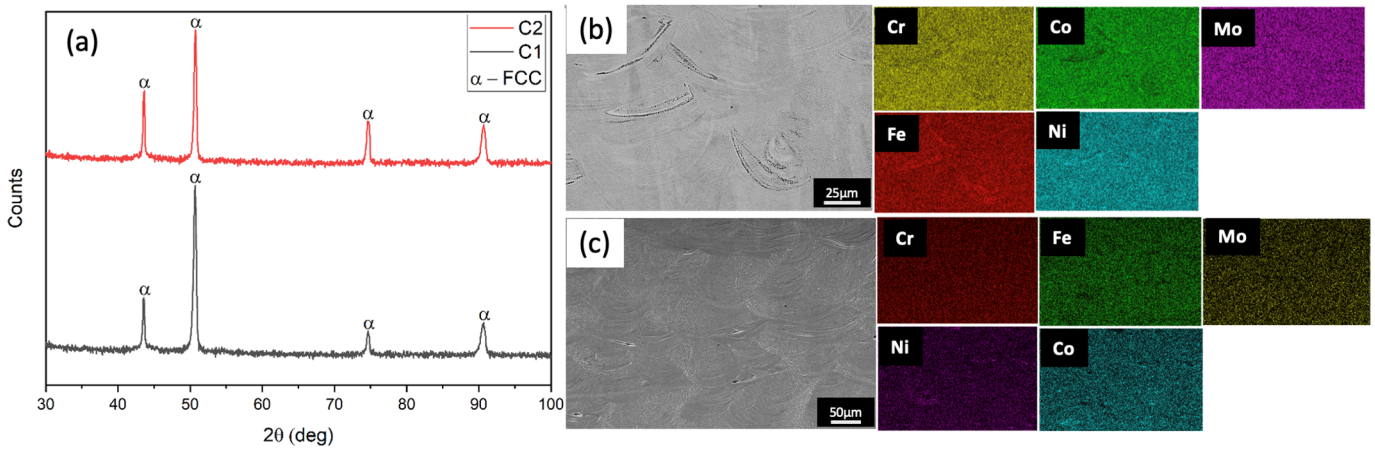

Figure 4. (**a**) XRD peaks of C1 and C2 alloy, elemental distribution map of as-built (**b**) C1 and (**c**) C2 along the build direction.

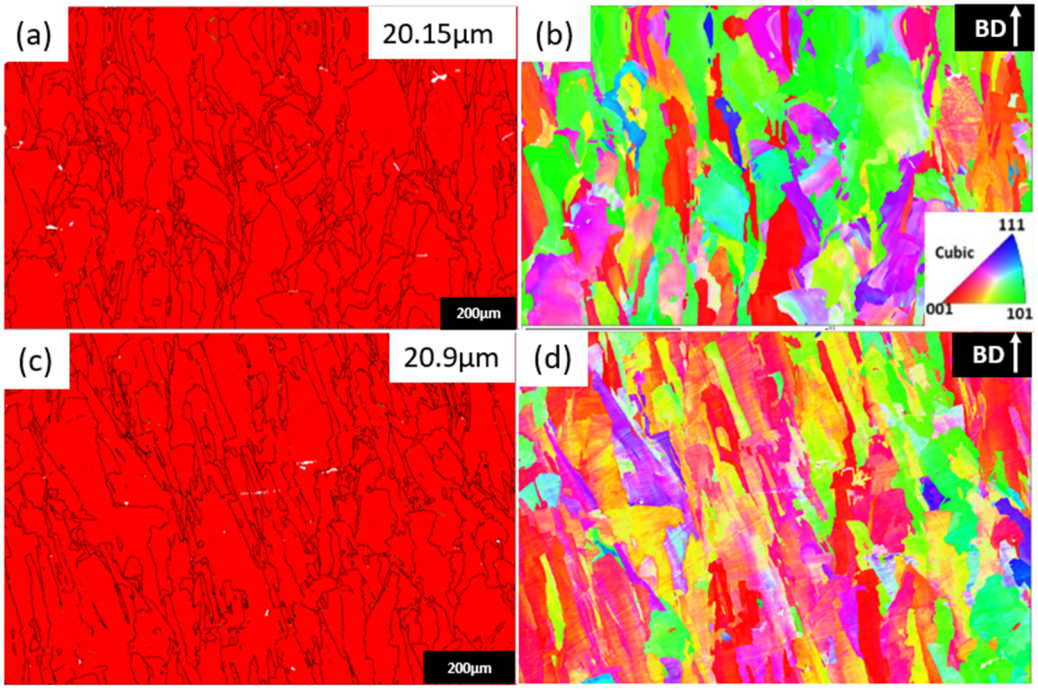

Figure 5. Phase map of (**a**) C1 and (**c**) C2 and inverse pole figure in the Z direction of (**b**) C1 and (**d**) C2 parallel to the building direction.

3.4. Mechanical Properties

Tensile tests were performed on the as-built samples and tested parallel to the build direction to obtain the minimum strength possible with the alloys as the mechanical properties would be better after heat treatment and, if tested, normal to the build direction. The yield strength (YS) and ultimate tensile strength (UTS) of C1 and C2 obtained from the tensile test are compared with similar HEAs mostly obtained by vacuum arc melting (VAM) with an FCC phase in Figure 6. The effect of Mo and Nb dissolution in C1 and C2 alloys processed by PBF-LB/M on the strength is clearly observed through this plot. Notably, the strength values of C1 and C2 are also higher than when they were processed by Spark plasma sintering (SPS) in our previous work [21], proving the superiority of PBF-LB/M. Both the YS and UTS of C1 and C2 decrease with temperature as expected due to dynamic softening occurring at high temperatures [38], and C2 exhibits a higher yield and ultimate tensile strength than C1 at room and high temperatures due to the former's higher Mo, Nb, and Cr content which induces local lattice distortion [39], thus hindering dislocation movement. As seen in Table 3, the atomic size difference, δ, is slightly higher for C2, which enables higher lattice distortion. The highest strength is attained by C2 alloy with a YS and UTS of 539.6 MPa and 752 MPa at room temperature to 203.5 MPa and 272 MPa at 900 °C, respectively. The summary of the mechanical properties, including elongation, is tabulated in Table 5. Figure 6 also shows that C1 and C2 exhibit better mechanical behavior at both room and high temperatures compared to similar HEAs containing Al and Mo [40–45], some of them even having eutectic microstructures, thus proving that by this method, it is possible to achieve competitive mechanical properties at lower cost. The cost savings considering only the raw materials amounted to 20% for the C2 alloy, as shown in Figure 7, as calculated in our previous work [21]. The calculation for elemental powders excludes the cost of ingot casting and gas atomizing, which will eventually amount to much higher savings.

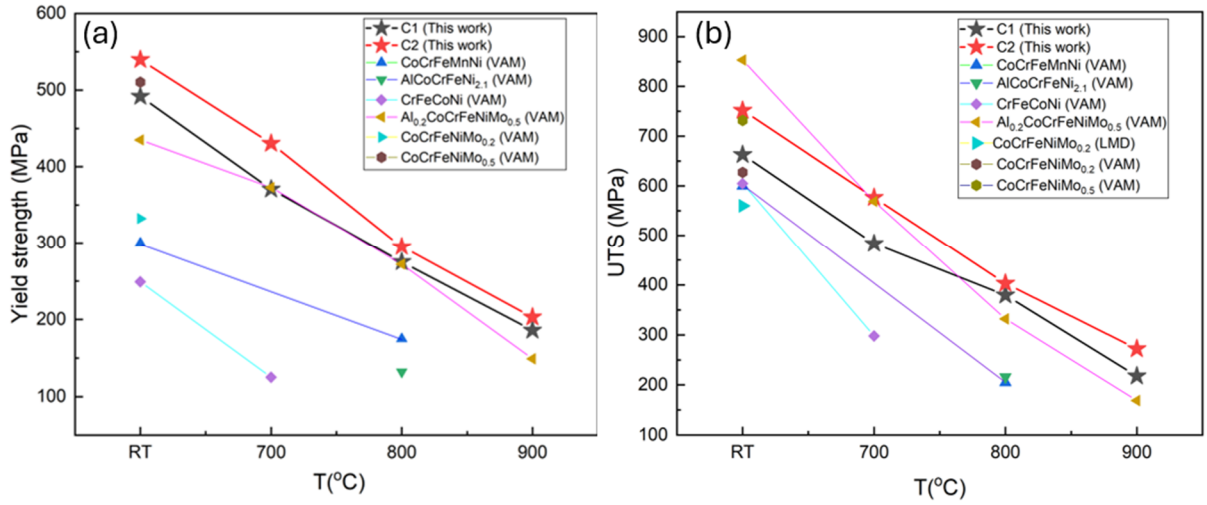

Figure 6. Plots showing (**a**) Yield strength, (**b**) Ultimate tensile strength plotted against temperature for C1 and C2 alloys compared with various HEAs; SPS- Spark plasma sintering, VAM—Vacuum Arc Melting, LMD—Laser metal deposition. C1 SPS reprinted from [18], C2 SPS reprinted from [18], CoCrFeMnNi (VAM) reprinted from [37], AlCoCrFeNi$_{2.1}$ (VAM) reprinted from [38], CrFeCoNi (VAM) reprinted from [39], Al$_{0.2}$CoCrFeNiMo$_{0.5}$ (VAM) reprinted from [40], CoCrFeNiMo$_{0.2}$ (LMD) reprinted from [41], CoCrFeNiMo$_{0.2}$ (VAM) reprinted from [42].

Table 5. Mechanical properties of C1 and C2 alloy tested along the build direction.

	C1			C2		
Temperature (°C)	**YS (MPa)**	**UTS (MPa)**	**e (%)**	**YS (MPa)**	**UTS (MPa)**	**e (%)**
RT	491.6 ± 22.85	663 ± 12.8	35.4 ± 0.03	539.6 ± 16.2	752 ± 14.26	37.6 ± 0.02
700	370.67 ± 36.85	483.3 ± 51.33	15.7 ± 4.73	430.3 ± 26.27	576.7 ± 20.2	15.67 ± 4.73
800	275 ± 49.95	379.3 ± 42.6	17 ± 5.57	295 ± 8.66	403.3 ± 7.23	18.33 ± 5.13
900	186 ± 12.73	218.5 ± 6.36	7 ± 1.41	203.5 ± 3.54	272 ± 4.24	27 ± 5.65

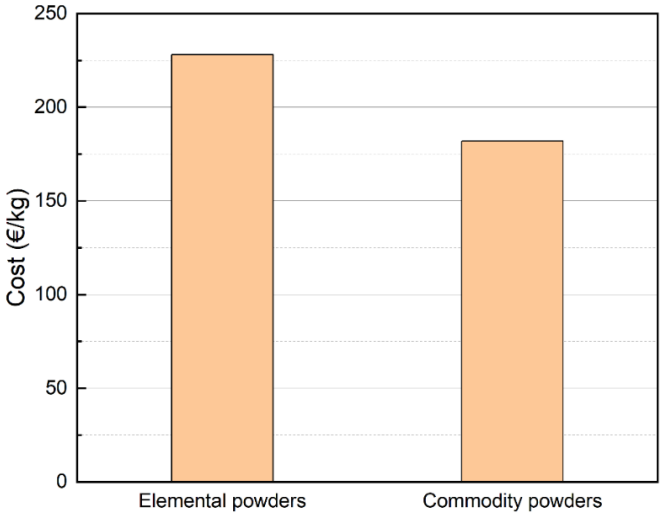

Figure 7. Raw material cost comparison of manufacturing C2 alloy using elemental powders vs commodity powders [21]. Reprinted with permission from ref. [21]. 2024 Elsevier.

3.5. Fracture Behaviour

As seen in Table 5, C1 alloy exhibits a sudden drop in ductility at 900 °C. To explore this further, the gauge region of the tensile samples after fracture at high temperatures was examined in SEM to observe the microstructural changes. It can be seen from Figure

8a,b that the grains and substructures were elongated as expected. Notably, in Figure 8(c2), there are precipitates shown in white along the grain boundaries in the sample tested at 900 °C. An XRD analysis of the fractured samples did not show any peaks other than FCC due to the low volume fraction of precipitates as shown in Figure S3 in the supplementary report, but an EDS line scan revealed that they are rich in Mo and Nb. Mo and Nb are known to form secondary intermediate phases in high entropy alloys when their quantities exceed the solid solubility limit [26]. Specifically, Fan et al. [46] found that a Nb and Mo-enriched hexagonal close-packed structure Laves phase was formed upon alloying Nb and Mo to CoCrFeNi via arc melting. Thus, the precipitation happening at high temperatures in the C1 and C2 alloys could well be the lave phase. Evidently, the cracks initiated from these precipitates and propagated rapidly along the grain boundaries, as seen in Figure 8(c3), resulting in embrittlement. This explains the sudden drop in elongation of C1 alloy tested at 900 °C, as seen in Table 5, and is consistent with the cleavage fracture morphology, as shown in Figure 9(a4). So, at 900 °C, the fracture changes from ductile to brittle fracture. At other temperatures tested, the C1 alloy exhibits promising elongation along with very high strength for an FCC phase, which corresponds well with the ductile fracture morphology with dimples, as shown in Figure 10(a1–a3).

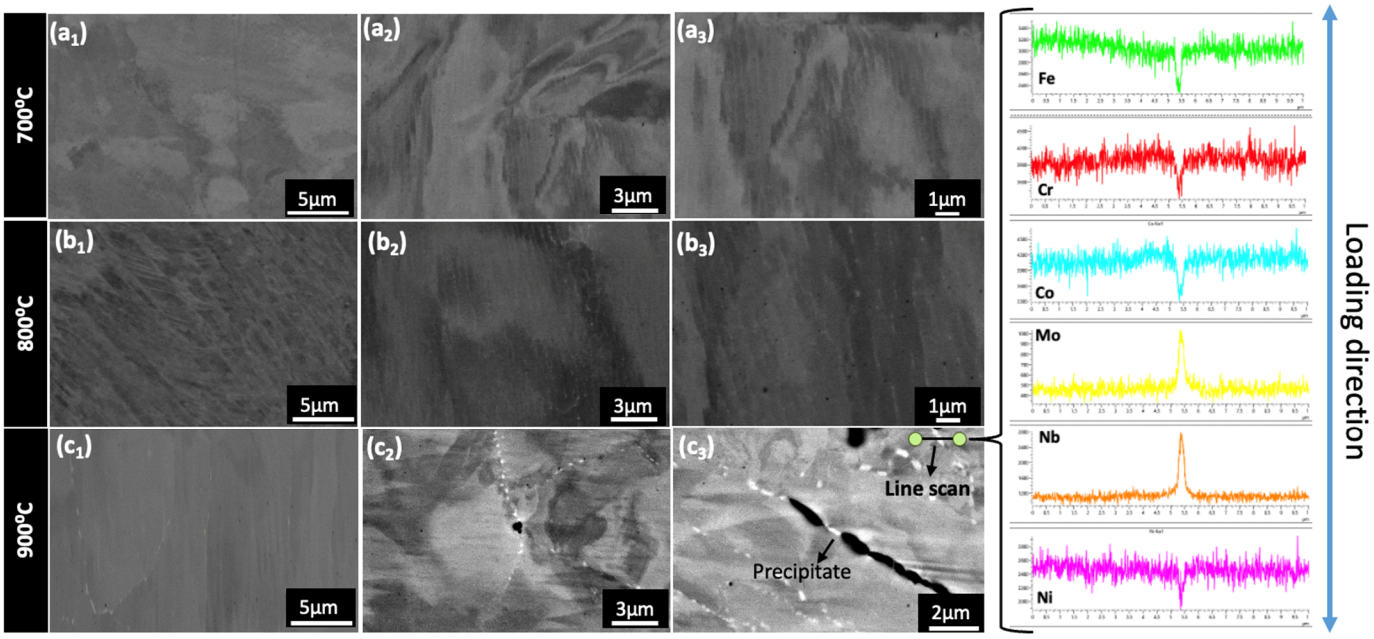

Figure 8. SEM backscattered images of the gauge region of C1 alloy close to the fracture tested at (**a1–a3**): 700 °C, (**b1–b3**): 800 °C, (**c1–c3**): 900 °C. On the right is the EDS line scan profile of the precipitate from (**c3**), which are Mo and Nb-rich laves phase.

In the C2 alloy, the volume fraction and size of Mo and Nb-rich precipitates exhibit a gradual increase from 700 °C to 900 °C, as illustrated in Figure 10 (a–c). At 900 °C, nano-precipitates are uniformly dispersed throughout the C2 alloy, contrasting with C1, where precipitates were solely present along grain boundaries. Consequently, C2 demonstrates superior elongation and a ductile fracture morphology, as depicted in Figure 10(b1–b3). Beyond enhanced solid solution strengthening, precipitation hardening significantly contributes to C2 alloy's superior strength compared to C1 above 700 °C, as seen in Table 4. Notably, C2, characterized by higher Mo and Nb content, exhibits greater strength than C1 at all temperatures without compromising ductility. A study by Wei et al. [47] explored the increment in yield strength in CoCrFeNi-based HEA through small additions of Si, maintaining ductility. The simultaneous increase in strength and ductility was attributed to a decrease in stacking fault energy, the formation of deformation nano twins, and possible short-range order. Therefore, our future research will focus on investigating

similar effects resulting from small additions of Mo and Nb to these alloys, along with an examination of precipitate formation at high temperatures, aspects beyond the current scope of this study.

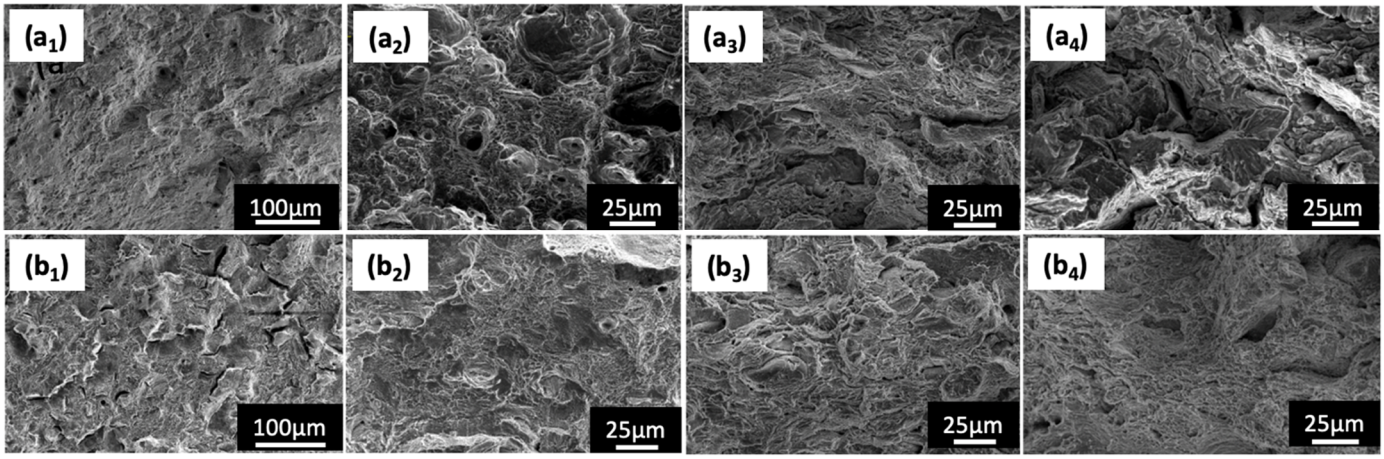

Figure 9. Fracture surfaces of C1 alloy at: (**a**1–**a**4) Room Temperature, 700 °C, 800 °C and 900 °C respectively, and of C2 alloy at: (**b**1–**b**4) Room Temperature, 700 °C, 800 °C and 900 °C respectively.

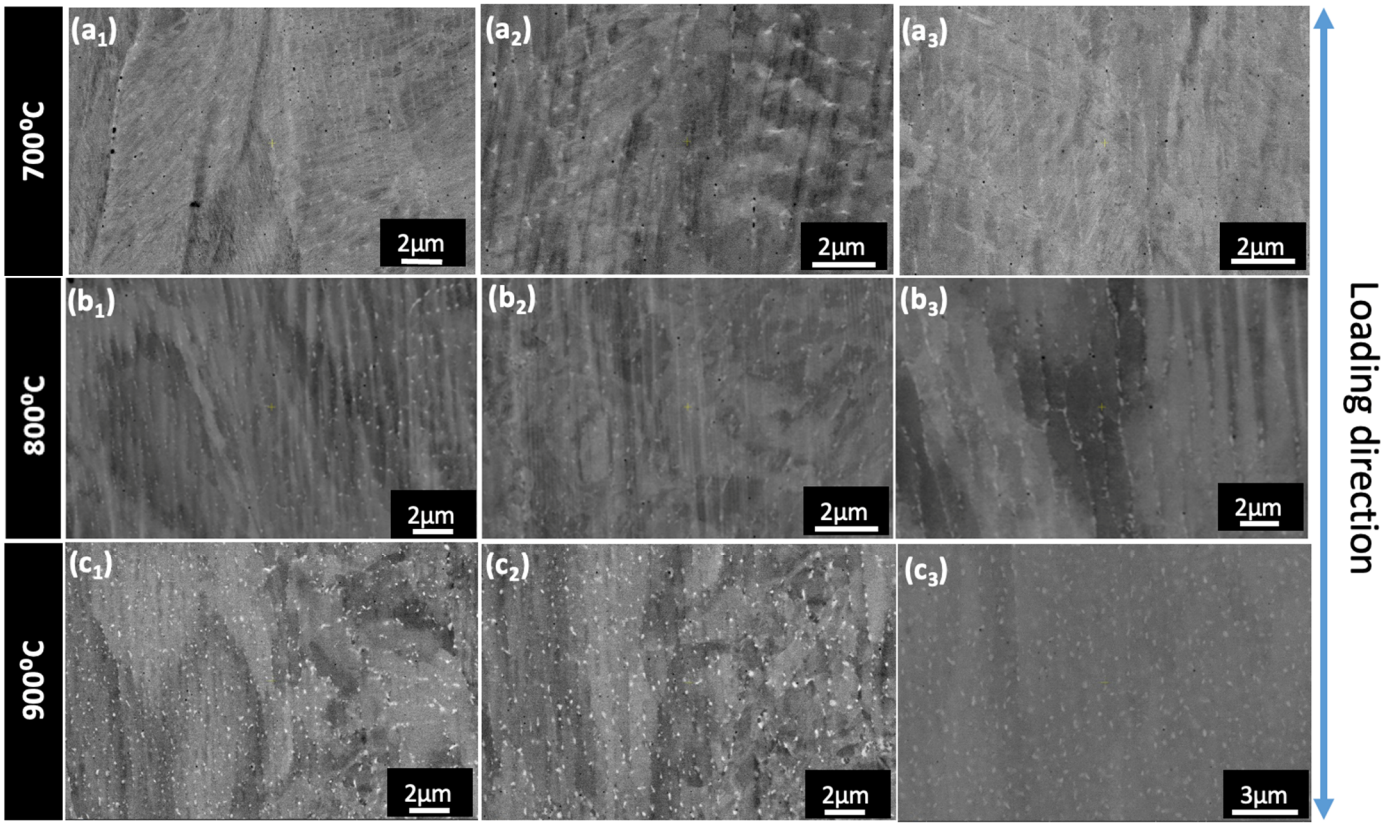

Figure 10. SEM backscattered images of the gauge region of C2 alloy close to the fracture tested at (**a**1–**a**3): 700 °C, (**b**1–**b**3): 800 °C, (**c**1–**c**3): 900 °C. The white regions are Mo and Nb-rich Laves phase.

4. Conclusions

In this work, two low-cost non-equiatomic HEAs based on $CoCrFeNiMo_xNb_y$ were designed and processed by PBF-LB/M via in situ alloying commercial powders like Ni superalloy and stainless steel. Its processability, microstructure, and mechanical properties in rooms and at high temperatures were evaluated in this study. The main

conclusions regarding the success of mixing commodity compositions and the alloys designed are as follows:

1. The designed alloy compositions C1 and C2 achieved excellent printability after optimization, reaching densities close to 99.9% with no defects. In the as-built state, the alloys had a complete FCC matrix with almost a homogenous distribution of elements with no deleterious secondary phases;
2. Both C1 and C2 alloys achieved competitive mechanical properties, with C2 alloys exhibiting better strength from room temperature to 900 °C than C1 due to the former´s higher Mo and Nb content, enabling higher lattice distortion. Considering that no microstructure homogenization treatment has been carried out yet to improve the properties further, this approach to manufacturing HEAs through the hypothesis of pre-alloyed powder mixing is indeed promising;
3. Both the alloys exhibited good ductility at all temperatures except for C1 at 900 °C which suffered embrittlement due to the presence of Nb and Mo-rich laves precipitates along the grain boundaries, as opposed to C2, where the precipitates were dispersed throughout the matrix;
4. Utilizing this approach resulted in a significant reduction in the cost of raw materials by 20%, not factoring in savings from ingot casting and gas atomization. Consequently, this method facilitates the commercialization of HEAs by providing an efficient and cost-effective avenue. Furthermore, it opens the possibility of employing scrap-based compositions to achieve a HEA microstructure.

Supplementary Materials:. The following supporting information can be downloaded at: https://www.mdpi.com/article/10.3390/met14050500/s1, Figure S1: Porosity percentage plotted against Scan speed for various laser powers printed with a hatch distance of 50 μm and layer thickness of 30 μm for C2 alloy; Figure S2: Porosity percentage plotted against Scan speed for various laser powers printed with a hatch distance of (a) 50 μm and (b) 70 μm and layer thickness of 30 μm for C1 alloy; Figure S3: XRD plot of C2 alloy after tensile testing at 900 °C at a step size of (a) 0.0262° and (b) 0.0131°.

Author Contributions: Conceptualization, S.V.K. and J.M.T.; Methodology, S.V.K. and J.M.T.; Investigation, S.V.K.; Writing—original draft, S.V.K.; Writing—review & editing, S.V.K. and J.M.T.; Supervision, J.M.T. All authors have read and agreed to the published version of the manuscript.

Funding: This research received no external funding.

Data Availability Statement: The original contributions presented in the study are included in the article/supplementary material, further inquiries can be directed to the corresponding authors.

Acknowledgments: The authors would like to thank the powder suppliers, VDM Metals (Germany), Sandvik Osprey (UK), Carpenter Additive (UK), and MIMETE (Italy) for providing the powders.

Conflicts of Interest:. The authors declare no conflicts of interest.

References

1. Yeh, J.W.; Chen, S.K.; Lin, S.J.; Gan, J.Y.; Chin, T.S.; Shun, T.T.; Tsau, C.H.; Chang, S.Y. Nanostructured high-entropy alloys with multiple principal elements: Novel alloy design concepts and outcomes. *Adv. Eng. Mater.* **2004**, *6*, 299–303. https://doi.org/10.1002/adem.200300567.
2. Cantor, B.; Chang, I.T.H.; Knight, P.; Vincent, A.J.B. Microstructural development in equiatomic multicomponent alloys. *Mater. Sci. Eng. A* **2004**, *375–377*, 213–218. https://doi.org/10.1016/j.msea.2003.10.257.
3. Chen, J.; Zhou, X.; Wang, W.; Liu, B.; Lv, Y.; Yang, W.; Xu, D.; Liu, Y. A review on fundamental of high entropy alloys with promising high–temperature properties. *J. Alloys Compd.* **2018**, *760*, 15–30. https://doi.org/10.1016/J.JALLCOM.2018.05.067.
4. Zhang, Y.; Zuo, T.T.; Tang, Z.; Gao, M.C.; Dahmen, K.A.; Liaw, P.K.; Lu, Z.P. Microstructures and properties of high-entropy alloys. *Prog. Mater. Sci.* **2014**, *61*, 1–93. https://doi.org/10.1016/j.pmatsci.2013.10.001.
5. Yeh, J.W. Alloy design strategies and future trends in high-entropy alloys. *JOM* **2013**, *65*, 1759–1771. https://doi.org/10.1007/s11837-013-0761-6.
6. Torralba, J.M.; Campos, M. High Entropy Alloys Manufactured by Additive Manufacturing. *Metals* **2020**, *10*, 639. https://doi.org/10.3390/MET10050639.

7. Torralba, J.M.; Alvaredo, P.; García-Junceda, A. High-entropy alloys fabricated via powder metallurgy. A critical review. *Powder Metall.* **2019**, *62*, 84–114. https://doi.org/10.1080/00325899.2019.1584454.
8. Cordova, L.; Campos, M.; Tinga, T. Revealing the Effects of Powder Reuse for Selective Laser Melting by Powder Characterization. *JOM* **2019**, *71*, 1062–1072. https://doi.org/10.1007/s11837-018-3305-2.
9. Cobalt Infocard, European Chemicals Agency. Available online: https://echa.europa.eu/substance-information/-/substanceinfo/100.028.325?_disssubsinfo_WAR_disssubsinfoportlet_backURL=https%3A%2F%2Fecha.europa.eu%2Finformation-on-chemicals%3Fp_p_id%3Ddisssimplesearchhomepage_WAR_disssearchportlet%26p_p_lifecycle%3D0%26 (accessed on 25 August 2021).
10. Grohol, D.M. Constanze Veeh, Study on the Critical Raw Materials for the EU, 2023. Available online: https://op.europa.eu/en/publication-detail/-/publication/57318397-fdd4-11ed-a05c-01aa75ed71a1 (accessed on 1 March 2024).
11. *Proposal for a Regulation of the European Parliament and of the Council Establishing a Framework for Ensuring a Secure and Sustainable Supply of Critical Raw Materials and Amending Regulations (EU) 168/2013, (EU) 2018/858, 2018/1724 and (EU) 2019/1020*; European Commission, Brussels, Belgiei, 2023; pp. 1–23.
12. *Annexes to the Proposal for a Regulation of the European Parliament and of the Council, for Establishing a Framework for Ensuring a Secure and Sustainable Supply of Critical Raw Materials and Amending Regulations (EU) 168/2013, (EU) 2018/858, 2018/1724 and (EU) 2019/1020, 0079*; European Commission, Brussels, Belgiei, 2023; pp. 1–23. https://doi.org/10.2760/386650.
13. Simonelli, M.; Aboulkhair, N.T.; Cohen, P.; Murray, J.W.; Clare, A.T.; Tuck, C.; Hague, R.J.M. A comparison of Ti-6Al-4V in-situ alloying in Selective Laser Melting using simply-mixed and satellited powder blend feedstocks. *Mater. Charact.* **2018**, *143*, 118–126. https://doi.org/10.1016/j.matchar.2018.05.039.
14. Ewald, S.; Kies, F.; Hermsen, S.; Voshage, M.; Haase, C.; Schleifenbaum, J.H. Rapid Alloy Development of Extremely High-Alloyed Metals Using Powder Blends in Laser Powder Bed Fusion. *Materials* **2019**, *12*, 1706. https://doi.org/10.3390/MA12101706.
15. Chen, P.; Li, S.; Zhou, Y.; Yan, M.; Attallah, M.M. Fabricating CoCrFeMnNi high entropy alloy via selective laser melting in-situ alloying. *J. Mater. Sci. Technol.* **2020**, *43*, 40–43. https://doi.org/10.1016/J.JMST.2020.01.002.
16. Sun, M.; Wang, B.; Zhang, J.; Lu, B. Intermetallics In-situ synthesis of CoCrFeMnNi high-entropy alloy by selective laser melting. *Intermetallics* **2023**, *156*, 107866. https://doi.org/10.1016/j.intermet.2023.107866.
17. Hou, Y.; Su, H.; Zhang, H.; Wang, X.; Wang, C. Fabricating Homogeneous FeCoCrNi High-Entropy Alloys via SLM In Situ Alloying. *Metals* **2021**, *11*, 942. https://doi.org/10.3390/MET11060942.
18. Farquhar, L.; Maddison, G.; Hardwick, L.; Livera, F.; Todd, I.; Goodall, R. In-Situ Alloying of CoCrFeNiX High Entropy Alloys by Selective Laser Melting. *Metals* **2022**, *12*, 456. https://doi.org/10.3390/MET12030456.
19. Nickel Infocard, European Chemicals Agency. Available online: https://echa.europa.eu/substance-information/-/substanceinfo/100.028.283 (accessed on 25 August 2021).
20. Torralba, J.M.; Kumarán, S.V. Development of competitive high-entropy alloys using commodity powders. *Mater. Lett.* **2021**, *301*, 130202. https://doi.org/10.1016/J.MATLET.2021.130202.
21. Kumaran, S.V.; Garbiec, D.; Torralba, J.M. A novel and sustainable method to develop non-equiatomic CoCrFeNiMox high entropy alloys via spark plasma sintering using commercial commodity powders and evaluation of its mechanical behaviour. *Mater. Sci. Eng. A* **2023**, *878*, 145207. https://doi.org/10.1016/J.MSEA.2023.145207.
22. Knieps, M.S.; Reynolds, W.J.; Dejaune, J.; Clare, A.T.; Evirgen, A. In-situ alloying in powder bed fusion: The role of powder morphology. *Mater. Sci. Eng. A* **2021**, *807*, 140849. https://doi.org/10.1016/j.msea.2021.140849.
23. Hariharan, K.; Sivaprasad, K. Sustainable Low-Cost Method for Production of High-Entropy Alloys from Alloy Scraps. *J. Sustain. Metall.* **2022**, *2*, 625–631. https://doi.org/10.1007/s40831-022-00523-x.
24. Navazani, M.; Kada, S.R.; Fabijanic, D.; Barnett, M. Increasing ductility via Cu addition in AlxCrFeMnNi: Towards a scrap-based high entropy alloy. *Intermetallics* **2024**, *164*, 108100. https://doi.org/10.1016/j.intermet.2023.108100.
25. Chao, Q.; Joseph, J.; Annasamy, M.; Hodgson, P.; Barnett, M.R.; Fabijanic, D. AlxCoCrFeNi high entropy alloys from metal scrap: Microstructure and mechanical properties. *J. Alloys Compd.* **2024**, *976*, 173002. https://doi.org/10.1016/j.jallcom.2023.173002.
26. Liu, W.H.; Yang, T.; Liu, C.T. Precipitation hardening in CoCrFeNi-based high entropy alloys. *Mater. Chem. Phys.* **2018**, *210*, 2–11. https://doi.org/10.1016/j.matchemphys.2017.07.037.
27. Hsu, C.Y.; Juan, C.C.; Chen, S.T.; Sheu, T.S.; Yeh, J.W.; Chen, S.K. Phase diagrams of high-entropy alloy system Al-Co-Cr-Fe-Mo-Ni. *JOM* **2013**, *65*, 1829–1839. https://doi.org/10.1007/s11837-013-0773-2.
28. Jiang, H.; Qiao, D.; Lu, Y.; Ren, Z.; Cao, Z.; Wang, T.; Li, T. Direct solidification of bulk ultrafine-microstructure eutectic high-entropy alloys with outstanding thermal stability. *Scr. Mater.* **2019**, *165*, 145–149. https://doi.org/10.1016/J.SCRIPTAMAT.2019.02.035.
29. Gao, X.; Liu, T.; Zhang, X.; Fang, H.; Qin, G.; Chen, R. Precipitation phase and twins strengthening behaviors of as-cast non-equiatomic CoCrFeNiMo high entropy alloys. *J. Alloys Compd.* **2022**, *918*, 165584. https://doi.org/10.1016/j.jallcom.2022.165584.
30. *ASTM E21-20 Standard*; Standard Test Methods for Elevated Temperature Tension Tests of Metallic Materials. ASTM International: West Conshohocken, PA, USA, 2021. https://doi.org/10.1520/E0021-20.
31. Kittel, C. *Introduction to Solid State Physics*, 8th ed.; John Wiley & Sons, Inc.: Hoboken, NJ, USA, 2005; ISBN 0-471-41526-X.

32. Yang, X.; Zhang, Y. Prediction of high-entropy stabilized solid-solution in multi-component alloys. *Mater. Chem. Phys.* **2012**, *132*, 233–238. https://doi.org/10.1016/j.matchemphys.2011.11.021.
33. Guo, S.; Hu, Q.; Ng, C.; Liu, C.T. More than entropy in high-entropy alloys: Forming solid solutions or amorphous phase. *Intermetallics* **2013**, *41*, 96–103. https://doi.org/10.1016/j.intermet.2013.05.002.
34. Guo, S.; Ng, C.; Lu, J.; Liu, C.T. Effect of valence electron concentration on stability of fcc or bcc phase in high entropy alloys. *J. Appl. Phys.* **2011**, *109*, 103505. https://doi.org/10.1063/1.3587228.
35. Zhong, Y.; Liu, L.; Wikman, S.; Cui, D.; Shen, Z. Intragranular cellular segregation network structure strengthening 316L stainless steel prepared by selective laser melting. *J. Nucl. Mater.* **2016**, *470*, 170–178. https://doi.org/10.1016/j.jnucmat.2015.12.034.
36. Birnbaum, A.J.; Steuben, J.C.; Barrick, E.J.; Iliopoulos, A.P.; Michopoulos, J.G. Intrinsic strain aging, Σ3 boundaries, and origins of cellular substructure in additively manufactured 316L. *Addit. Manuf.* **2019**, *29*, 100784. https://doi.org/10.1016/j.addma.2019.100784.
37. Lin, D.; Xu, L.; Li, X.; Jing, H.; Qin, G.; Pang, H.; Minami, F. A Si-containing FeCoCrNi high-entropy alloy with high strength and ductility synthesized in situ via selective laser melting. *Addit. Manuf.* **2020**, *35*, 101340. https://doi.org/10.1016/j.addma.2020.101340.
38. Moravcik, I.; Cizek, J.; Zapletal, J.; Kovacova, Z.; Vesely, J.; Minarik, P.; Kitzmantel, M.; Neubauer, E.; Dlouhy, I. Microstructure and mechanical properties of Ni1,5Co1,5CrFeTi0,5 high entropy alloy fabricated by mechanical alloying and spark plasma sintering. *Mater. Des.* **2017**, *119*, 141–150. https://doi.org/10.1016/j.matdes.2017.01.036.
39. Liu, W.H.; Lu, Z.P.; He, J.Y.; Luan, J.H.; Wang, Z.J.; Liu, B.; Liu, Y.; Chen, M.W.; Liu, C.T. Ductile CoCrFeNiMox high entropy alloys strengthened by hard intermetallic phases. *Acta Mater.* **2016**, *116*, 332–342. https://doi.org/10.1016/J.ACTAMAT.2016.06.063.
40. Sun, J.; Zhao, W.; Yan, P.; Li, S.; Dai, Z.; Jiao, L.; Qiu, T.; Wang, X. High temperature tensile properties of as-cast and forged CrMnFeCoNi high entropy alloy. *Mater. Sci. Eng. A* **2022**, *850*, 143570. https://doi.org/10.1016/J.MSEA.2022.143570.
41. Zhang, Y.; Wang, X.; Li, J.; Huang, Y.; Lu, Y.; Sun, X. Deformation mechanism during high-temperature tensile test in an eutectic high-entropy alloy AlCoCrFeNi2.1. *Mater. Sci. Eng. A* **2018**, *724*, 148–155. https://doi.org/10.1016/j.msea.2018.03.078.
42. Jo, M.G.; Suh, J.Y.; Kim, M.Y.; Kim, H.J.; Jung, W.S.; Kim, D.I.; Han, H.N. High temperature tensile and creep properties of CrMnFeCoNi and CrFeCoNi high-entropy alloys. *Mater. Sci. Eng. A* **2022**, *838*, 142748. https://doi.org/10.1016/j.msea.2022.142748.
43. Palguna, Y.; Kotla, S.; Korla, R. High temperature deformation behavior of Al0.2CoCrFeNiMo0.5 high entropy alloy: Dynamic strain ageing. *J. Alloys Compd.* **2023**, *930*, 167422. https://doi.org/10.1016/j.jallcom.2022.167422.
44. Wang, Q.; Amar, A.; Jiang, C.; Luan, H.; Zhao, S.; Zhang, H.; Le, G.; Liu, X.; Wang, X.; Yang, X.; et al. CoCrFeNiMo0.2 high entropy alloy by laser melting deposition: Prospective material for low temperature and corrosion resistant applications. *Intermetallics* **2020**, *119*, 106727. https://doi.org/10.1016/J.INTERMET.2020.106727.
45. Niu, Z.; Wang, Y.; Geng, C.; Xu, J.; Wang, Y. Microstructural evolution, mechanical and corrosion behaviors of as-annealed CoCrFeNiMox (x = 0, 0.2, 0.5, 0.8, 1) high entropy alloys. *J. Alloys Compd.* **2020**, *820*, 153273. https://doi.org/10.1016/J.JALLCOM.2019.153273.
46. Fan, R.; Wang, L.; Zhao, L.; Wang, L.; Zhao, S.; Zhang, Y.; Cui, B. Synergistic effect of Nb and Mo alloying on the microstructure and mechanical properties of CoCrFeNi high entropy alloy. *Mater. Sci. Eng. A* **2022**, *829*, 142153. https://doi.org/10.1016/j.msea.2021.142153.
47. Wei, D.; Gong, W.; Tsuru, T.; Lobzenko, I.; Li, X.; Harjo, S.; Kawasaki, T.; Do, H.S.; Bae, J.W.; Wagner, C.; et al. Kato, Si-addition contributes to overcoming the strength-ductility trade-off in high-entropy alloys. *Int. J. Plast.* **2022**, *159*, 103443. https://doi.org/10.1016/j.ijplas.2022.103443.

Paper 5

S Venkatesh Kumaran, Bala Malladi, Eduard Hryha, José Manuel Torralba, “Effect of laser process paramaters on non-equiatomic $CoCrFeNiMo_xAl_y$ HEAs manufactured by PBF-LB/M via in-situ alloying”, European powder metallurgy association (EPMA), Euro Powder Metallurgy 2023 proceedings, DOI: 10.59499/EP235762606

Euro PM2023 - Session 16 : AM Beam Based Technologies - AM High Entropy Alloys Keynote Paper Winner

Manuscript refereed by Dr Miren Aristizabal (Ceit-BRTA, Spain)

Effect Of Laser Process Parameters On Non-Equiatomic Cocrfenimo$_x$al$_y$ Heas Manufactured By PBF-LB/M Via In-Situ Alloying

S Venkatesh Kumaran[1,3]; Sri Bala Aditya Malladi[2]; Eduard Hryha[2]; Jose M Torralba[1,3]

[1]IMDEA Materials, Madrid, Spain
[2]Chalmers University of Technology, Göteborg, Sweden
[3]Universidad Carlos III de Madrid, Spain

Abstract

Manufacturing high entropy alloys (HEAs) using powder bed fusion-laser beam/Metal (PBF-LB/M) enables their production with minimal elemental segregation due to its inherently fast cooling rates resulting in excellent properties. So far, HEAs have been fabricated with fully pre-alloyed gas-atomized powders which makes it expensive and slower to explore new alloy compositions. In this work, for the first time, instead of pre-alloying, blended powders of CoCrF75, Ni625, Invar36, and pure Al powders were used as feedstock to develop a CoCrFeNiMo$_x$Al$_y$ HEA which consists of FCC phase in the metastable state. The process was successfully optimized, achieving relative densities greater than 99.8%. This method of mixing powders for PBF-LB/M enables rapid exploration of new HEAs and this work is expected to contribute to its successful application in the future.

Introduction

Since the advent of high entropy alloys (HEAs) in 2004 [1][2], they have attracted significant attention due to the possibility of adding multiple principal elements to obtain unique microstructures and the possibility to fine-tune the properties, which results in high mechanical strength, good ductility, wear resistance, oxidation resistance, and corrosion resistance [3]. The definition of HEAs, initially stated as alloys consisting of more than five elements of composition range between 5 and 35 at% [1], has been modified to alloys with a configurational mixing entropy, $\Delta S_{mix} > 1.5R$, where R is the gas constant [5].

The most common method used to manufacture HEAs has been casting or arc melting [1] due to its convenience and efficiency when more than five elements need to be solidified. However, powder metallurgy routes and additive manufacturing have recently shown great potential in developing HEAs with remarkable properties [5], [6]. The most prominent among the additive manufacturing techniques to produce HEAs have been through powder bed systems, either with a laser beam (PBF-LB/M) or with an electron beam (PBF-EB), and powder feed systems like laser metal deposition (LMD) [6]. In a powder bed process like the PBF-LB/M, the feedstock should be spherical with a size distribution between 15-63 µm to ensure proper spreadability and fully pre-alloyed by e.g. gas-atomization or plasma spheroidizing to avoid elemental segregation. This process of pre-alloying for HEAs, which starts from traditional melting and casting to gas-atomizing, is expensive and time-consuming as HEAs involve four or five principal elements. Therefore, this method is rigid and restricts developing and exploring next-generation materials like HEAs via PBF-LB/M.

The concept of in-situ alloying has been introduced recently in PBF-LB/M, where the constituent elements are alloyed simultaneously during consolidation. For instance, Sun et al [11] fabricated CoCrFeNiMn by using elemental powders, and it exhibited slightly lower ultimate tensile strength but higher ductility than the HEA fabricated by fully prealloyed CoCrFeNi powder mixed with Mn elemental powders [10]. In another study by Hou et al.[12], the strength and hardness of CoCrFeNi HEA fabricated by pre-alloyed powders and by elemental powders were comparable, even though a higher VED was necessary to obtain excellent performance in the case of elemental powders. Unmelted Cr particles were also observed in the overlapping regions of melt pools due to the very high melting point of Cr compared to the rest of the elements. Furthermore, Knieps et al. investigated the effect of powder morphology on in-situ alloying in PBF-LB/M to enable the selection of correct powder feedstock [13]. In this work, a blend of commercial alloy powders and elemental powders was used. It was concluded that a multimodal particle size distribution (PSD) increases packing density and enhances process performance. However, no post-processing heat treatments or microstructural studies were carried out. It should be noted that all the above works were based on developing FCC-based HEAs.

 https://doi.org/10.59499/EP235762606

The alloy CoCrFeNi is widely studied among FCC-based HEAs due to its remarkable ductility and toughness, even at cryogenic temperatures [14]. But its strength is not high enough for structural applications [15]. Thus, other elements are added to improve the mechanical properties by forming precipitates or other hard phases like BCC. Elements like Al and Mo act as strong contenders as alloying elements in HEAs. Specifically, Al acts as a BCC stabilizer in HEAs, and with the increase in the aluminum concentration in the alloy, the final structure changes from FCC to FCC+BCC. With further increase in the Al content, full BCC will be stabilized albeit with a higher strength but lower ductility [16]. Mo enhances the room and high-temperature strength owing to its high melting point and elastic modulus [17]. So, in this work, a mix of commercial commodity powders and Al powders were used as feedstock in PBF-LB/M to study the effect of the different powders and laser parameters on the relative density and elemental distribution of the bulk HEAs. The commercial powders used were Ni625, Invar36, and CoCrF75, to obtain HEA with composition of Co-Cr-Fe-Ni-Mo-Al. The processability of this feedstock was explored by adding varying amounts of fine Al powder and studying its effect on the density. This work is relevant to enable rapid exploration of next-generation materials through PBF-LB/M using in-situ alloying approach.

Experimental procedure

Feedstock preparation

For the base composition, a mix of Ni625, Invar36, and CoCrF75 powders was used to fabricate CoCrFeNiMo. The Ni625 powder was provided by VDM Metals (Germany), Invar36 powder was supplied by Sandvik Osprey (UK) and CoCrF75 was provided by MIMETE (Italy). All three powders had a particle size between 15-53 µm with a d50 of around 30µm. The composition was designed to keep Ni, Fe, Cr, and Co nearly equiatomic with minor amounts of Mo. Two more compositions were designed by adding pure Al powders of 3.5 wt.% and 4.5 wt. % to the initial mix, hereafter referred to as 3.5Al and 4.5Al. The pure Al powders had a finer PSD with a d50 of 20µm and d90 of 44µm. The powders were mixed in a roller mixer for 1 hour. The morphology along with the EDS maps of the powders after mixing is shown in *Figure 1***.**

Table 1: Proposed commodity alloys and their role in the target HEA

Alloy	Role	wt. %					
		Ni	Fe	Cr	Mo	Co	Al
Ni625	Source of Ni, Cr, Fe, and Mo	61.54	5.35	25.26	5.6	-	
INVAR 36	Source of Fe and Ni	34.8	65.14	-	-	-	
CoCrF75	Source of Co, Cr, and Mo	0.51	0.8	32.57	3.72	62.41	

Table 2: Proposed mixes of commodity and Al powders used to develop the HEAs

Alloy	wt. % of powders				at. % of final HEA					
	Ni625	INVAR 36	CoCrF75	Al	Ni	Fe	Cr	Mo	Co	Al
0Al	20	38	42	0	25.45	27.42	20.44	1.59	25.1	0
3.5Al	20	35	41.5	3.5	23.27	23.96	19.75	1.54	24.3	7.17
4.5Al	20	34	41.5	4.5	22.7	23.07	19.54	1.52	24.04	9.12

PBF-LB/M processing

The samples were manufactured in an EOS M100 machine equipped with a 200W Yb-fiber laser with a spot size of 40µm. The build chamber was purged with argon gas to reduce the amount of oxygen to 1000 ppm before process starts. Test samples were printed with a stripe scanning strategy with 5 mm stripe width and with a 0.1 mm overlap with adjacent stripes and a 67° scan rotation between the subsequent layers**.** Design of experiments (DOE) were carried out using the software *JMP pro* version 17 by SAS by varying the laser power from 110 - 170W, scan speed from 600 – 1200 mm/s, hatch distance from 0.06 – 0.1 mm and with a constant layer thickness of 30 µm. Based on the porosity percentage of the printed samples, a second DoE was performed by narrowing the process parameter window. In the end, ten cubes of 7mm were built for each material (0Al, 3.5Al, 4.5Al) and for each DoE.

 https://doi.org/10.59499/EP235762606

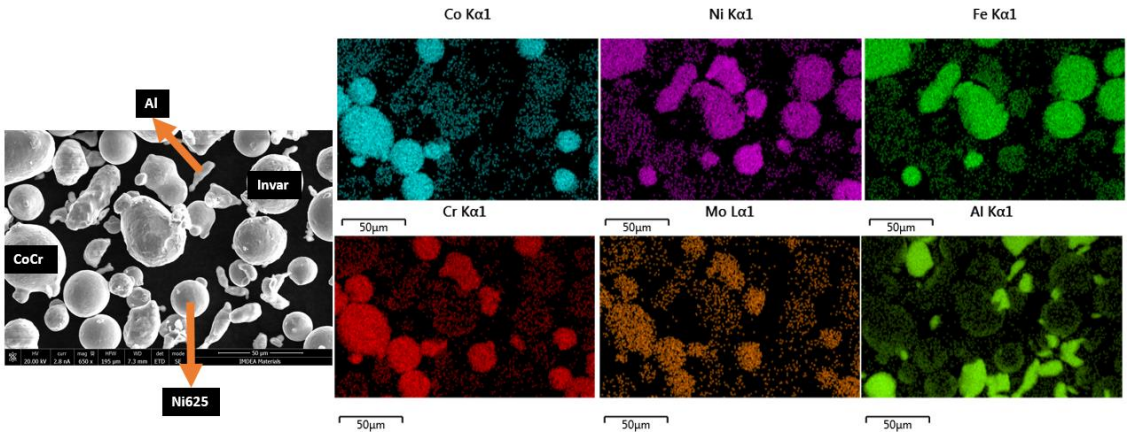

Figure 1. SEM image of the powder mix with 3.5wt% Al and its corresponding EDS maps showing the elemental distribution

Material characterization

The printed samples were cut from the baseplate with wire arc discharge machining and were cut longitudinally with a disc cutter to analyze the cross section in the as-built direction. All the samples were ground and polished up to 1 µm using diamond solution. The optical micrographs were taken with a Zeiss Axioscope 7. The porosity analysis was performed using the image threshold technique using ImageJ software. The 3.5Al and 4.5Al samples were electrochemically etched with oxalic acid for 5 seconds to reveal the meltpools. To study the microstructure, the samples were analyzed in FEG-SEM Apreo equipped with EDS to study the elemental distribution. Hardness was measured with a Vickers hardness tester with a load of 1 kg and a dwell time of 15 seconds per indent.

Results and discussion

Process parameter optimization

The relative density (RD) of 0Al, 3.5Al and 4.5Al samples printed for the initial screening is shown in Figure 2 plotted with respect to the volume energy density (VED), which is calculated by E/vht, where E is the laser power (W), v is the scanning speed (mm/s), h is the hatch distance (mm), and t is the layer thickness (mm). The 0Al sample achieved a maximum density of 99.93%. The sample consisted of mostly fine pores with very few large pores. It was noted that the RD gradually decreased with Al addition, and the maximum densities were observed in the range of 50-90 J/mm^3 VED. Typically, in PBF-LB/M processes, lower VED leads to an irregular lack of fusion defects due to low molten pool temperature and poor melt fluidity. A higher VED might cause over melting resulting in keyhole porosity [19], [20].

The Analysis of Variance (ANOVA) table for the initial screening is given in Table *3*, where the factors were laser power (LP), scanning speed (SS), hatch distance (H), and Al content (Al). Based on the p-values, the model was significant, and the factor H and the interaction H*SS were found to be the most significant factors that influence the RD. A contour plot between H and SS is shown in Figure 3, for the three Al contents for a laser power of 140W where it can be seen that the RD increases with lower H and higher SS in all three cases. On increasing Al to 4.5 wt%, the dense region moves towards higher SS for a fixed hatch distance and laser power, which implies a lower volume energy density. Based on this result, a second DoE was performed, setting the VED limit between 50-100 J/mm^3, and a scanning speed greater than 900 mm/s, for 3.5Al and 4.5Al samples, and the relative densities were calculated. The resulting optimized parameters for all three alloys are shown in Table 4. The parameters were also checked for reproducibility, and their RDs obtained were close to 99.9%. Upon increasing Al content, it was observed that the optimum region for higher density moved towards higher scanning speeds for a fixed hatch and laser power, implying a lower VED. As an elemental powder like Al is mixed in the feedstock, it is likely to increase the porosity and cracking mainly because of the lower melting point and density, which causes inhomogeneities in the layer and expands the solidification region.

 https://doi.org/10.59499/EP235762606

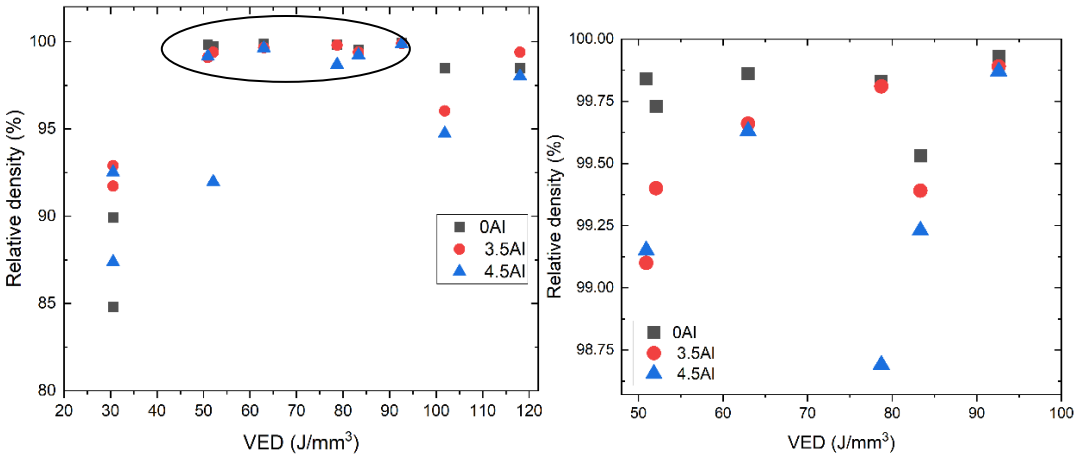

Figure 2. Plot of relative density against volume energy density (VED) from (a) 20 to 120 J/mm^3 and (b) magnified plot of the encircled region between a VED of 50 to 100 J/mm^3

Table 3: Analysis of variance (ANOVA) table of the initial screening parameters (A - laser power (LP), B - scanning speed (SS), C - hatch distance (H), and D - Al content (Al))

Source	F-value	p-value
Model	7.57	0.0001 (significant)
A-LP	0.51	0.485
B-SS	2.18	0.1568
C-H	9.1	0.0074
D-Al	0.38	0.5442
AB	3.71	0.0702
AC	8.9	0.008
AD	0.23	0.638
BC	13.34	0.0018
BD	0.1	0.7510
CD	1.54	0.23

https://doi.org/10.59499/EP235762606

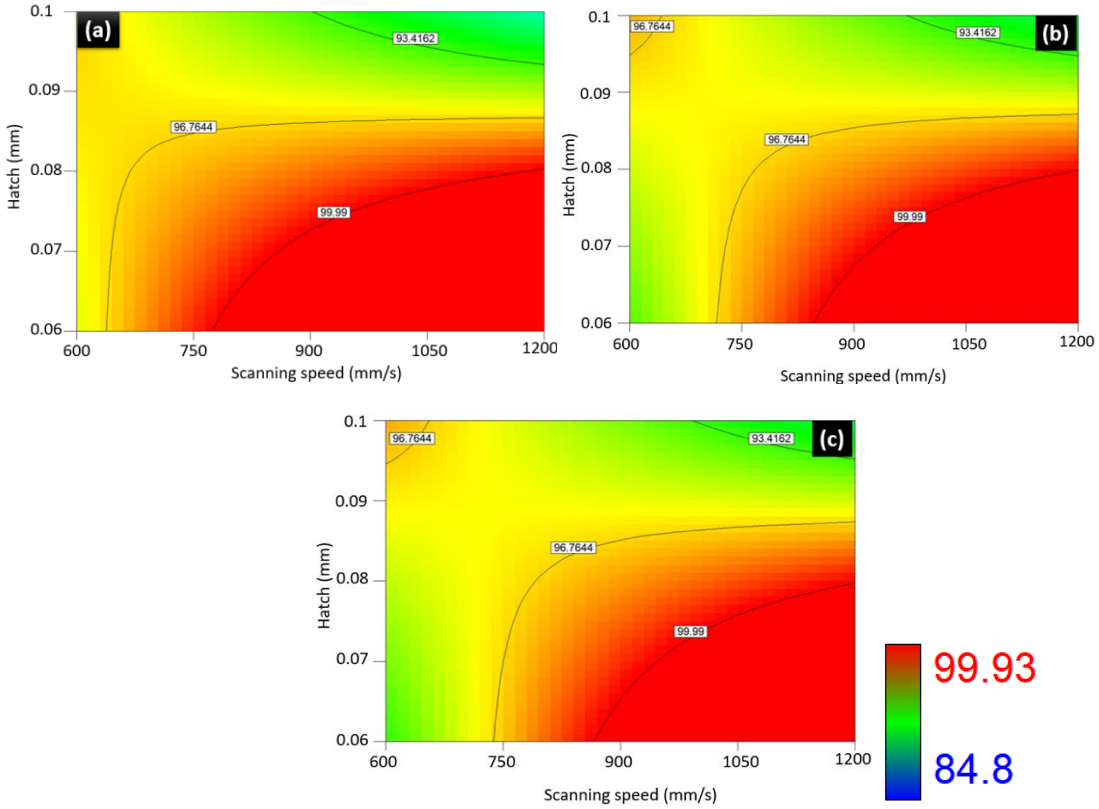

Figure 3. Contour plots of relative densities showing the interaction between hatch and scanning speed for a laser power of 140W and layer thickness of 30µm for (a) 0Al, (b) 3.5Al and (c) 4.5Al sample

Table 4: Optimized parameters for 0Al, 3.5Al and 4.5Al with a layer thickness of 30µm

Alloy	Laser power (W)	Scanning speed (mm/s)	Hatch distance (mm)	Relative density (%)
0Al	150	900	0.06	99.93
3.5Al	140	1050	0.06	99.92
4.5Al	140	1050	0.06	99.91

Microstructural characterization

The SEM backscattered image and elemental distribution of 0Al samples are shown in Figure 4 (a)**.** The distribution is almost homogenous except for localized segregations and depletions along the swirls of some of the melt pools. Similarly, the 3.5Al samples show a nearly homogenous distribution of elements, as shown in Figure 4 (c)**.** However, micro-cracks caused due to solidification cracking could be observed in certain regions where there was a prominent segregation, which usually happened to be along the melt pool boundaries, as shown in Figure 4 (d)**.** The segregation is caused by CoCrF75 powder particles as the enrichment in Co and Cr was observed near the crack. When the Al content was increased to 4.5 wt%, the Al segregation was more prominent as shown in Figure 4 (b). Figure 4(b) shows a backscatter SEM image where the light grey regions are Al and Fe rich, and the dark region is even more enriched in Al. It is also worth noting that the darker Al enriched region is on the edge of the melt pool, which belong to the heat-affected zone with lesser heat input due to which perhaps the alloying in-situ was not complete. Controlling segregations by in-situ alloying remains a challenge due to the random mixture of powders in the feedstock and lack of time for proper homogenization in the micro-sized melt pool at such a high cooling rates, due to which it is difficult to predict the composition at any

 https://doi.org/10.59499/EP235762606

point in the blend and inside the meltpool as well. To this regard, reducing the number of elemental powders by using a mix of commodity powders to produce HEAs offers a better solution since most of the elements are already alloyed. This is evident from the obtained relative densities of over 99.9%.

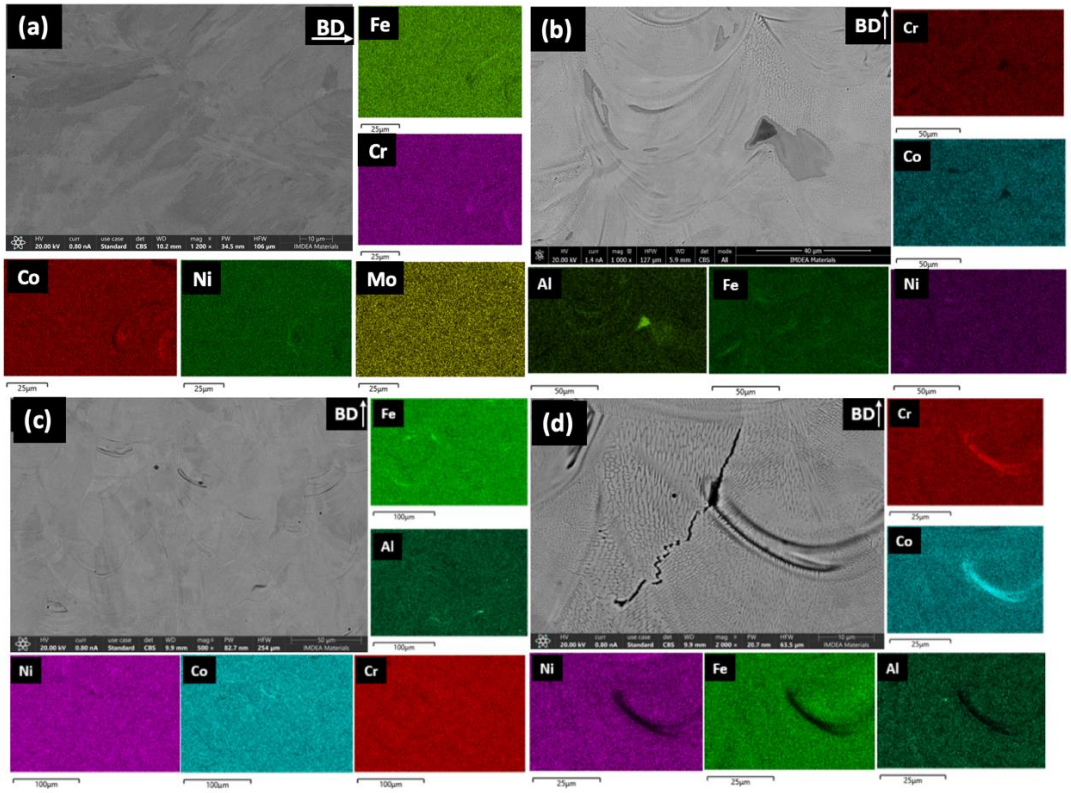

Figure 4. SEM backscatter image and EDS elemental distribution map of 0Al

Mechanical properties

The Vickers hardness measured along the horizontal and vertical cross sections of the as-printed samples is shown in **Table *5***. The hardness increases with the increase in Al content due to the solid solution strengthening and lattice distortion effect due to the higher atomic size of Al compared to other elements in the HEA [21]. The 4.5Al alloy shows the maximum hardness of 293 HV along the horizontal cross-section. This matches well with the hardness of similar alloys like $Al_{0.5}CoCrFeNi$ fabricated by PBF-LB/M which was about 270HV [22] The same alloy, when fabricated by vacuum arc melting had a hardness of 180 HV due to a coarser grain size [23] which shows the effectiveness of the PBF-LB/M process in both fabrication of complex alloy systems as well as achieving better mechanical properties.

Table 5: Vicker´s hardness of the alloys (HV_1)

Alloy	Hardness of horizontal cross section (HV_1)	Hardness of vertical cross-section (HV_1)
0Al	240	260
3.5Al	290	284
4.5Al	293	291.2

Conclusions

In this work, the possibility of manufacturing novel HEAs using PBF-LB/M via in-situ alloying using commercial commodity powders was explored. Particularly, the role of mixing pure Al powders, which has a much lower density and melting point than Ni-625, Invar36 and CoCrF75, was studied.

 https://doi.org/10.59499/EP235762606

Up to 4.5 wt.% Al was added to the studied HEA system based on $CoCrFeNiMo_xAl_y$, where near full density samples were obtained with relative densities close to 99.9%. Upon increasing Al content, it was observed that the optimum region for higher density moved towards higher scanning speeds for a fixed hatch and laser power, implying a lower VED. The distribution of elements was nearly homogenous with exception of some localized regions where some segregations and depletions were observed in the swirls of some of the meltpools.

A small percentage of microcracks were present which were due to solidification cracking and some of them were due to elemental segregation. The fraction of microcracks increased with Al addition, contributing to the reduction in RD. Possibility to eliminate micro-cracking and improving microstructure homogeneity by subsequent HIP should be exploited. In the future, annealing at various temperatures and times will be carried out to explore the possibility of precipitation of secondary phases like BCC, sigma and mu.

The hardness of the alloys increased with Al addition due to solid solution strengthening and lattice distortion effect, with the maximum hardness of 293 HV achieved with 4.5 wt.% Al addition.

This work is believed to enable rapid exploration of new-generation materials like HEAs avoiding the expensive preparation step of pre-alloyed powders. In addition, this shows that there is a potential of adding elemental powders of different densities to commercial commodity powders to achieve microstructural modifications.

Acknowledgements

This project was supported by IMDEA Materials, Madrid, Spain, and was conducted in the framework of the Centre for Additive Manufacturing – Metal (CAM^2), supported by the Swedish Governmental Agency of Innovation Systems (Vinnova) at Chalmers University of Technology, Gothenburg, Sweden.

References

[1] J. W. Yeh et al., "Nanostructured high-entropy alloys with multiple principal elements: Novel alloy design concepts and outcomes," Adv Eng Mater, vol. 6, no. 5, pp. 299–303, 2004, doi: 10.1002/adem.200300567.

[2] B. Cantor, I. T. H. Chang, P. Knight, and A. J. B. Vincent, "Microstructural development in equiatomic multicomponent alloys," Materials Science and Engineering A, vol. 375–377, no. 1-2 SPEC. ISS., pp. 213–218, Jul. 2004, doi: 10.1016/j.msea.2003.10.257.

[3] J. Chen et al., "A review on fundamental of high entropy alloys with promising high–temperature properties," J Alloys Compd, vol. 760, pp. 15–30, Sep. 2018, doi: 10.1016/J.JALLCOM.2018.05.067.

[4] J. W. Yeh, "Alloy design strategies and future trends in high-entropy alloys," JOM, vol. 65, no. 12, pp. 1759–1771, Dec. 2013, doi: 10.1007/s11837-013-0761-6.

[5] J. M. Torralba and M. Campos, "High Entropy Alloys Manufactured by Additive Manufacturing," Metals 2020, Vol. 10, Page 639, vol. 10, no. 5, p. 639, May 2020, doi: 10.3390/MET10050639.

[6] J. M. Torralba, P. Alvaredo, and A. García-Junceda, "High-entropy alloys fabricated via powder metallurgy. A critical review," Powder Metallurgy, vol. 62, no. 2. Taylor and Francis Ltd., pp. 84–114, Mar. 15, 2019. doi: 10.1080/00325899.2019.1584454.

[7] M. Sun, B. Wang, J. Zhang, and B. Lu, "Intermetallics In-situ synthesis of CoCrFeMnNi high-entropy alloy by selective laser melting," Intermetallics (Barking), vol. 156, no. February, p. 107866, 2023, doi: 10.1016/j.intermet.2023.107866.

[8] P. Chen, S. Li, Y. Zhou, M. Yan, and M. M. Attallah, "Fabricating CoCrFeMnNi high entropy alloy via selective laser melting in-situ alloying," J Mater Sci Technol, vol. 43, pp. 40–43, Apr. 2020, doi: 10.1016/J.JMST.2020.01.002.

[9] Y. Hou, H. Su, H. Zhang, X. Wang, and C. Wang, "Fabricating Homogeneous FeCoCrNi High-Entropy Alloys via SLM In Situ Alloying," Metals 2021, Vol. 11, Page 942, vol. 11, no. 6, p. 942, Jun. 2021, doi: 10.3390/MET11060942.

[10] M. S. Knieps, W. J. Reynolds, J. Dejaune, A. T. Clare, and A. Evirgen, "In-situ alloying in powder bed fusion: the role of powder morphology," Materials Science and Engineering: A, p. 140849, Jan. 2021, doi: 10.1016/j.msea.2021.140849.

 https://doi.org/10.59499/EP235762606

[11] B. Gludovatz, A. Hohenwarter, D. Catoor, E. H. Chang, E. P. George, and R. O. Ritchie, "A fracture-resistant high-entropy alloy for cryogenic applications," Science (1979), vol. 345, no. 6201, pp. 1153–1158, Sep. 2014, doi: 10.1126/science.1254581.

[12] A. J. Zaddach, R. O. Scattergood, and C. C. Koch, "Tensile properties of low-stacking fault energy high-entropy alloys," Materials Science and Engineering A, vol. 636, pp. 373–378, Jun. 2015, doi: 10.1016/J.MSEA.2015.03.109.

[13] C. J. Tong et al., "Microstructure characterization of AlxCoCrCuFeNi high-entropy alloy system with multiprincipal elements," Metall Mater Trans A Phys Metall Mater Sci, vol. 36, no. 4, pp. 881–893, 2005, doi: 10.1007/s11661-005-0283-0.

[14] C. Y. Hsu, C. C. Juan, S. T. Chen, T. S. Sheu, J. W. Yeh, and S. K. Chen, "Phase diagrams of high-entropy alloy system Al-Co-Cr-Fe-Mo-Ni," JOM, vol. 65, no. 12, pp. 1829–1839, Dec. 2013, doi: 10.1007/s11837-013-0773-2.

[15] D. Vogiatzief, A. Evirgen, M. Pedersen, and U. Hecht, "Laser powder bed fusion of an Al-Cr-Fe-Ni high-entropy alloy produced by blending of prealloyed and elemental powder: Process parameters, microstructures and mechanical properties," J Alloys Compd, vol. 918, p. 165658, Oct. 2022, doi: 10.1016/J.JALLCOM.2022.165658.

[16] F. Yang et al., "Ultra strong and ductile eutectic high entropy alloy fabricated by selective laser melting," J Mater Sci Technol, vol. 106, pp. 128–132, Apr. 2022, doi: 10.1016/J.JMST.2021.08.015.

[17] F. J. Wang, Y. Zhang, and G. L. Chen, "Atomic packing efficiency and phase transition in a high entropy alloy," J Alloys Compd, vol. 478, no. 1–2, pp. 321–324, Jun. 2009, doi: 10.1016/J.JALLCOM.2008.11.059.

[18] K. Sun, W. Peng, L. Yang, and L. Fang, "Effect of SLM processing parameters on microstructures and mechanical properties of al0.5 CoCrFeNi high entropy alloys," Metals (Basel), vol. 10, no. 2, p. 292, Feb. 2020, doi: 10.3390/met10020292.

[19] W. R. Wang, W. L. Wang, and J. W. Yeh, "Phases, microstructure and mechanical properties of AlxCoCrFeNi high-entropy alloys at elevated temperatures," J Alloys Compd, vol. 589, pp. 143–152, Mar. 2014, doi: 10.1016/J.JALLCOM.2013.11.084.

 https://doi.org/10.59499/EP235762606